

Technische Universität München
Fakultät für Physik



Max-Planck-Institut für Physik
(Werner-Heisenberg-Institut)



In cooperation with CERN
Supported by the Wolfgang Gentner
Programme



Doctoral Thesis

Instability and Seeded Self-Modulation of a Relativistic Proton Bunch in Plasma

Instabilität und angeregte Selbstmodulation eines Protonenpakets
in Plasma

Fabian Gregor Batsch

München, September 2021



TECHNISCHE UNIVERSITÄT MÜNCHEN
Fakultät für Physik

Instability and Seeded Self-Modulation of a Relativistic
Proton Bunch in Plasma

Fabian Gregor Batsch

Vollständiger Abdruck der von der Fakultät für Physik der Technischen Universität
München zur Erlangung des akademischen Grades eines

Doktors der Naturwissenschaften (Dr. rer. nat.)

genehmigten Dissertation.

Vorsitzende:

Prof. Dr. Laura Fabbietti

Prüfende der Dissertation:

1. Hon.-Prof. Dr. Allen C. Caldwell
2. Hon.-Prof. Dr. Frank Jenko

Die Dissertation wurde am 04.10.2021 bei der Technischen Universität München
eingereicht und durch die Fakultät für Physik am 29.11.2021 angenommen.

Abstract

In the Advanced Wakefield Experiment (AWAKE) at CERN, the self-modulation (SM) of a relativistic particle bunch in plasma is used to divide initially several-cm-long proton bunches into a train of mm-long micro-bunches. Because these micro-bunches are shorter than and separated by the plasma wavelength, they are well-suited to drive large-amplitude ($\sim \text{GV/m}$) plasma wakefields for the acceleration of externally injected electron bunches. However, deterministic and reproducible electron acceleration in these wakefield requires the reproducibility of and thus control over the phase of the modulation.

In this thesis, I study the variation in phase of the SM for various initial wakefield amplitudes provided by the relativistic ionization front of a short and intense laser pulse. With time-resolved streak camera images, I experimentally demonstrate the existence of two different SM regimes. For this purpose, I develop a diagnostic tool called laser reference signal to measure the phase and timing of micro-bunches on that images at the ps-time scale. I show that in a plasma created at the very front or ahead of the proton bunch, the SM grows as an instability from initial transverse wakefields driven by noise or by bunch irregularities at times later than that of the ionization front. As a consequence, the bunch self-modulates with the plasma frequency, but the micro-bunches appear at no particular time and their phase or timing with respect to the ionization front vary over the full range of a plasma period. This is the regime of the SM instability (SMI). I demonstrate that when the ionization front is placed closer to the bunch center, the larger initial transverse wakefields seed the modulation process. The bunch modulates again with the plasma frequency, but now the micro-bunches appear with essentially the same timing from event to event, i.e. their timing is reproducible. Using Fourier transforms, I show for the first time that the phase of the modulation is tied to the ionization front and varies only maximum 3% to 7% of 2π (rms) all along the bunch. This second regime is called seeded SM (SSM). I determine the transition point between the SMI and SSM regime in terms of timing of the ionization front and corresponding initial transverse wakefield amplitude. The fact that the phase of the SM, especially further along the bunch, can be controlled by providing sufficiently large ($\sim \text{MV/m}$) initial wakefield amplitudes allows for a deep understanding of the SM physics, which is very important for the conceptional design of future experiments. By determining the relative phase of micro-bunches with respect to each other, I show that the modulation frequency of the SM is constant along the whole modulated bunch. These

observations are obtained for a plasma density that is constant along the propagation path of the protons.

For the SSM regime, I additionally study the influence of linear plasma density gradients on the phase velocity of the wakefields and on the formation of the micro-bunches. I use gradients between $\pm 2\%/m$ along the 10 m of plasma. The results demonstrate the suitability of non-constant plasma density profiles as a tool to optimize the SM and acceleration processes by influencing the phase velocity of the wakefields. Theory predicts that with a constant plasma density, a difference between the phase velocity of the protons and of the wakefields causes the micro-bunches in the back of the bunch to be eventually defocused. I show that compared to the no-gradient case, negative gradients further decrease the phase velocity of the wakefields. This leads to an earlier defocusing of the micro-bunches, which reduces their number along the bunch train and decreases the charge per remaining micro-bunch. I also show experimentally that providing a positive gradient along the propagation path increases the phase velocity of the wakefields, thus allowing for an (at least) partial compensation of the dephasing. More micro-bunches with higher charge per bunch form. Since with gradients the plasma frequency is not constant along the propagation path, I analyze the modulation frequency of the micro-bunch train for different widths of the analysis window and for different radial positions. I also measure the relative phase along the bunch and its rms variation as a function of the gradient to show that gradients do not influence the seeding process and its phase reproducibility.

Contents

Abstract	v
1 Introduction to Plasma Wakefield Acceleration	1
1.1 The Development of Conventional Acceleration Techniques	1
1.2 Motivation for Novel Acceleration Schemes	3
1.3 Plasma-based Wakefield Acceleration and its Working Principles . .	5
1.4 The Different Wakefield Acceleration Schemes in Comparison	7
1.4.1 Laser-driven Wakefield Acceleration	8
1.4.2 Electron-driven Wakefield Acceleration	9
1.4.3 Proton-driven Wakefield Acceleration: AWAKE	9
1.5 Thesis Topic: Self-Modulation Instability, its Seeding and the Influence of Linear Plasma Gradients	10
1.6 Thesis Layout	15
2 Theory and Concepts	17
2.1 Plasma and its Properties	17
2.2 Plasma Waves and Linear Wakefield Theory	18
2.3 Initial Transverse Wakefield and Noise Amplitudes	22
2.4 The Phase Velocity of Wakefields	23
2.5 The Discrete Fourier Transform of a Periodic Signal	24
3 AWAKE and Experimental Setups	27
3.1 General Description of the AWAKE Experiment	27
3.2 The Experimental Structure and Location of Components	30
3.3 The Experimental Components in Detail	31
3.3.1 The Proton Beam Line	31
3.3.2 The Ionizing Laser System	32
3.3.3 The Rb Vapor Source and Plasma Density Parameter Control	34
3.3.4 The SC/OTR Diagnostic	37
3.3.5 Other SM Diagnostics	39
3.3.6 The Electron Line	40
3.3.7 The Electron Spectrometer	40
3.4 Development of Experimental Diagnostics	41
3.4.1 The Rb Vapor Density Diagnostic	41

3.4.2	Calculation of the Rb Vapor Density	45
3.4.3	The Laser Reference Signal	51
3.5	AWAKE Run 2	56
4	Analysis Tools and Procedures	59
4.1	Image Processing	59
4.1.1	Background Subtraction	59
4.1.2	Saturated Pixel Treatment	61
4.1.3	Linearization of the Temporal Axis	62
4.2	Localization of the LRS	63
4.3	Superposition and Stitching of SC Images	65
4.4	Modulation Frequency and Phase Determination	66
4.4.1	Determination of the Time Profile	66
4.4.2	The DFT of the Time Profile	68
4.4.3	Determination of the Modulation Frequency and Phase	70
5	Characterization of the Laser Reference Signal	73
5.1	The Identification and Determination of Uncertainties	73
5.1.1	Trigger System Jitter between Laser and SC	74
5.1.2	Uncertainty on the Temporal Position of the LRS	75
5.1.3	Timing Jitter between Laser Pulse and LRS	76
5.1.4	Uncertainty on Translation Stage Movements	77
5.2	The Total Measurement Uncertainty	78
6	Instability and Seeding of the Self-Modulation	81
6.1	Observation of Different SM Regimes	82
6.1.1	The Self-Modulation Instability Regime	82
6.1.2	The Seeded Self-Modulation Regime	87
6.2	Transition between SMI and SSM	89
6.3	Phase Variation along the Modulated Bunch with Seeding	92
6.4	Relative Modulation Phase and Frequency along the Bunch	95
6.5	Summary	98
7	Experimental Studies of SM with Linear Density Gradients	99
7.1	Observation of the Micro-Bunch Train as a Function of the Density Gradient	100
7.2	Modulation Frequency as a Function of Plasma Gradient	105
7.3	Frequency Dependency on Transverse Position	108
7.4	Phase Reproducibility with Plasma Gradients	109
7.5	Relative Modulation Phase and Frequency with Plasma Gradients	111
7.6	Summary	112

8 Conclusion and Outlook	115
Acknowledgments	119
Appendices	121
A Supplemental Material	123
B Publications	133
Glossary	153
List of Figures	157
Bibliography	161

Chapter 1

Introduction to Plasma Wakefield Acceleration

1.1 The Development of Conventional Acceleration Techniques

Linear and circular particle accelerators using radio-frequency (RF)-based techniques were the key to success for the fundamental research known to us today as they allowed for most of the discoveries in particle physics such as the exploration of the standard model. The development of the different conventional accelerator types happened over approximately the last 115 years, starting with the first electron beams produced by cathode ray tubes at the end of the 19th century [1], and peaking at tens of kilometers long accelerators such as the Large Hadron Collider (LHC, [2]) at the European Organization for Nuclear Research (CERN, short for *Organization européenne pour la recherche nucléaire*). The first linear accelerators such as the Van de Graaff generator [1, 3] used high continuous voltages to reach energies on the MeV scale, which allowed for example for studies of nuclear reactions. In 1932, E. Cockcroft and J. Walton demonstrated the world's first conversion of lithium to helium using a 400 keV proton beam that passed through a voltage-multiplier cascade, nowadays called Cockcroft-Walton generator [1, 4]. The energy gain per particle and meter achievable with these accelerator types usually cannot exceed the MeV/m scale due to limitation in the fields that can be sustained and in the size of the accelerating structure. The main limitation for the accelerating gradient, also for more recent accelerator types, are corona discharges or voltage breakdown when the space inside the cavities is ionized and arcs form.

Higher energies, on the order of 100 MeV, were achieved by circulating the particles through the accelerating structure multiple times and using an alternating voltage (AC) to adapt to the high frequencies with which the electric fields have to alternate for effective acceleration [1]. The development of these circular machines was initiated by E. O. Lawrence and his development of the cyclotron from 1929 onward. In a cyclotron, as explained in a publication by him and M. S. Livingston in [5] in 1932, the particles move inside two flat metallic structures and perpendicular to a constant

magnetic field, resulting in a spiral-like path. Every half revolution, the particles experience acceleration through a high-frequency AC voltage, i.e., a RF voltage. The resonant frequency of the cyclotron is constant as it is independent of the radius of the beam path. Also CERN's first accelerator, the Synchro-Cyclotron, was of this type and accelerated protons to 600 MeV [6]. The difference from a normal cyclotron is that at these relativistic energies the frequency had to be adapted with increasing energy to account for the increasing relativistic mass when the protons approach the speed of light [1].

In these accelerators the highest achievable energy (on the order of several 100 MeV) is also limited by the size of the structures, as well as by the strength of their magnetic field. Again, a new accelerator type had to be developed to overcome the limitations, leading to the development of the synchrotron. The synchrotron became the workhorse in modern particle physics until today as it can not only be used as an accelerator, but also as a storage ring for colliders. In these machines, the particles propagate on a closed, circular path with fixed radius, i.e., the magnets increase their field strength with increasing particle energy. Because of the possibility to build chains of accelerators with successively increasing radii, the maximum energy limit was raised by several orders of magnitude up to the TeV scale and huge acceleration complexes such as CERN were built. With the LHC, center-of mass collision energies of up to 13 TeV (6.5 TeV per proton) were reached, and as a consequence the existence of the Higgs boson was confirmed in 2012 [7].

Even though this meant the (preliminary) completion of the standard model, possible discoveries of new physics in the context of dark matter search, neutrino properties, the matter-antimatter asymmetry, etc. call for even higher collision energies. Collisions of particles that are constituted of quarks (such as hadrons/protons) underlie all four fundamental interactions (gravitation, electromagnetism, weak and strong interaction) cannot be considered point-like and the event reconstructions involve complex hadronic cascade processes. Protons and ions are composite particles, whereas leptons are elementary particles. As a consequence, the current trend in particle physics is working toward the construction of lepton accelerators that access the TeV range. Leptons are (besides gravitation and electromagnetism) only subject to the weak interaction, but not the strong interaction, leading to collision events with much clearer signatures and therefore possibly allowing for significantly more precise studies of new particles and their properties.

However, nowadays circular accelerators only access the TeV energy scale for hadrons because of significantly smaller synchrotron radiation losses when compared to leptons. The power loss per charged particle due to this specific type of bremsstrahlung is proportional to $(1/m_0)^4$ [1], with m_0 the rest mass of the particle. As the rest mass of the electron is ≈ 1836 times smaller than that of the proton, the synchrotron losses of an electron with equal beam path and energy are $\approx 10^{13}$ times larger. Therefore, linear accelerators were and still are the standard for lepton

acceleration¹. The largest linear accelerator so far was located at the SLAC National Accelerator Laboratory in the United States and delivered 50 GeV electrons and positrons after 3.2 km of acceleration length [9]. To reach the electron-TeV scale, the two linear colliders projects with the highest prospects of success are the Compact Linear Collider (CLIC) planned to be constructed at CERN [10] and the International Linear Collider (ILC) studied by Japan [11]. While a collision energy of 3 TeV is foreseen to be reached in an in total 48 km long accelerator complex of CLIC, ILC is aiming to reach a collision energy of 500 GeV in a 31 km long accelerator. The maximal foreseen accelerating gradients are 100 MeV/m and 30 MeV/m, respectively.

The maybe most ambitious plans for an electron-electron collider are part of the plans for the Future Circular Collider (FCC) at CERN [12]. The FCC is planned to use the LHC as pre-injector and to accelerate hadrons in a 100-km-circumference ring to energies of 100 TeV (called FCC-hh, [13]). Before that, it is foreseen to operate as a luminosity-frontier electron-positron collider (called FCC-ee) with 182.5 GeV per particle in each beam [14]. The resulting collision energy of 365 GeV is above the top quark pair-production threshold of ≈ 350 GeV [15], and therefore allowing for precise studies of its properties. Experiments on the neutrino mass and dark matter are also foreseen.

For completeness, we also want to mention a possible muon collider. This collider is in the stage of conceptional design, with the main challenges in the short lifetime of muons of $\approx 2 \mu\text{s}$ and the fact that they are only produced in natural or artificial high-energy collisions. However, they are of interest because of their rest mass which is 206.8 times larger than that of the electron. The synchrotron losses would accordingly be $206.8^4 = 1.8 \times 10^9$ times smaller when compared to circular electron accelerators (or "only" ≈ 6217 times larger when compared to proton accelerators), while still providing the advantages of a lepton-lepton collider.

1.2 Motivation for Novel Acceleration Schemes

One characteristic has been present through this entire period of conventional particle accelerators until today: the research on new particles and their properties eventually required significantly higher collision energies than that achievable with the accelerators of that time. Consequently, larger accelerators or even new types of accelerators with new acceleration techniques and stronger bending magnets had to be developed. Especially an energy increase by several orders of magnitude usually requires significant amounts of pioneering work. This constant demand for larger accelerators is slowly reaching constructional and financial limits. The previously

¹Even though some circular machines were built, e.g. the Large Electron-Positron Collider (LEP) at CERN that used the same 27-km-circumference tunnel infrastructure as the LHC today and that reached particle energies of 104.5 GeV per electron [8].

mentioned projects of ILC, CLIC and FCC with lengths of tens of kilometers or 100 km circumference are projected to cost between 6 and 21 billion Euros [16]. Costs for the operation and their energy consumption are herein not even included. Even though there are strong efforts to mitigate these consequences by increasing the magnetic field strength, e.g. with new superconducting magnets [17] or by bringing the accelerating gradients close to breakdown voltage limits (as it is planned for CLIC with X-band structures [18]), the achievable improvements concerning the accelerator sizes, performance and costs are not sufficient.

Novel accelerators using the concept of plasma-based wakefield acceleration are therefore intensively studied at many research facilities around the globe. These wakefield accelerators do not utilize the electro-magnetic fields of conventional RF cavities, but the fields sustained by plasma waves. Using a plasma as cavity has the advantage that it is possible to overcome the breakdown voltage limit of ≈ 100 MV/m as a plasma already consists of ionized matter, i.e., it is (so to speak) already "broken down". The highest available field in a plasma is on the order of the wave breaking field E_{WB} [19]:

$$E_{WB} = (m_e c / e) \omega_{pe} . \quad (1.1)$$

Here, m_e is the electron rest mass¹, c the speed of light in vacuum and

$$\omega_{pe} = (n_{e0} e^2 / \epsilon_0 m_e)^{1/2} \quad (1.2)$$

is the plasma electron angular frequency [20] with n_{e0} the plasma electron density and ϵ_0 the vacuum permittivity. By combining Eq. 1.1 and 1.2, the wave breaking field can be estimated by $E_{WB} \approx 96 \text{ V/m} \sqrt{n_{e0} [\text{cm}^{-3}]}$. For densities around $n_{e0} \sim 10^{18} \text{ cm}^{-3}$, the limit is thus $\approx 96 \text{ GV/m}$. Indeed, accelerating fields of tens of GV/m have been reached, e.g. demonstrated at SLAC where trailing electrons of a 42 GeV-per-particle electron bunch doubled their energy over only 85 cm, equivalent to a gradient of 52 MeV/m [21]. When compared to conventional accelerators, this represents an increase in accelerating gradient of three orders of magnitude. As a result, these novel accelerators have the potential to reach the same energy over only a small fraction of the length needed with conventional acceleration techniques. The financial and spatial requirements for accelerator facilities are consequently supposed to decrease as well.

Because of the huge potential of saving resources, a broad field of possible applications is under investigation and development. These applications range from small ion and proton accelerators for medical applications like cancer irradiation, over high-energy electron sources for free-electron-lasers as high-brightness X-ray sources, to lepton accelerators that function as booster or main acceleration structures in future particle colliders. Depending on the application, different plasmas, plasma

¹An overview of all constants and variables is given in the glossary at the end of this thesis.

sources and ways to drive the plasma waves are used, as I briefly explain in the following paragraph.

1.3 Plasma-based Wakefield Acceleration and its Working Principles

Different schemes of wakefield acceleration exist, which are classified according to the way the plasma waves are excited. In principle two different types of so-called drivers can be used: a high-intensity, short-duration laser pulse (intensity $> 10^{18}$ W/cm² [22]) or relativistic, charged particle bunches [23]. Thereby, the effective driving of wakefields requires the length of the driver in longitudinal direction σ_z to be smaller than the plasma wavelength $\lambda_{pe} = 2\pi c/\omega_{pe}$: $\sigma_z < \lambda_{pe}$ [24]. Since the pulse or bunch must also fit transversely within the wakefields, its radius σ_r must be similarly small: $\sigma_r \leq 1/k_{pe} = c/\omega_{pe}$ [25], with k_{pe} the plasma electron wavenumber. The scheme of laser-driven systems is called laser wakefield acceleration (LWFA), schemes with beam-driven plasma wakefields are summarized under the term plasma wakefield acceleration (PWFA).

Independent of its type, the driver provides an essentially transverse force that excites the plasma wave along its path through the plasma. In the case of an intense laser pulse, the force comes from the ponderomotive force, in case of a particle bunch from its electric field. A schematic of the working principle of plasma-based wakefield acceleration with a laser pulse or a negatively charged, relativistic bunch in a laboratory frame of reference is displayed in Fig. 1 (the case of a positively charge bunch is discussed later in this chapter, see Fig. 2). The driver (black ellipse, the arrow indicates the propagation direction) enters a longitudinally extended, initially neutral plasma (Fig. 1(a)). Along its path, due to the transverse electric field of the driver, the plasma electrons (shown as red cloud) start moving transversely to the propagation axis (Fig. 1(b)). On the short timescales in which the driver passes by, the plasma ions remain at rest due to their higher mass. The lighter electrons are expelled from the axis, i.e. a surplus of ions (black plus symbol) remains. After the driver has passed, the positive charge on axis now attracts the electrons that accumulated away from the axis. As shown in Fig. 1(c), the electrons continue by moving back towards the axis. When the electrons reach the propagation axis, the negative charge density on axis is increased. Due to their kinetic energy, the electrons continue to move and overshoot. A periodic oscillation around the axis at the plasma electron frequency $f_{pe} = \omega_{pe}/2\pi$ forms as the electron motion continues as it started when the driver passed. In a co-moving frame, a plasma wave forms behind the driver. Its "bubbles" represent the accelerator cavities, in which, due to the charge separation, high-amplitude electro-magnetic fields (the so-called wakefields) provide the accelerating gradients on the GeV/m level. An electron bunch (orange ellipse

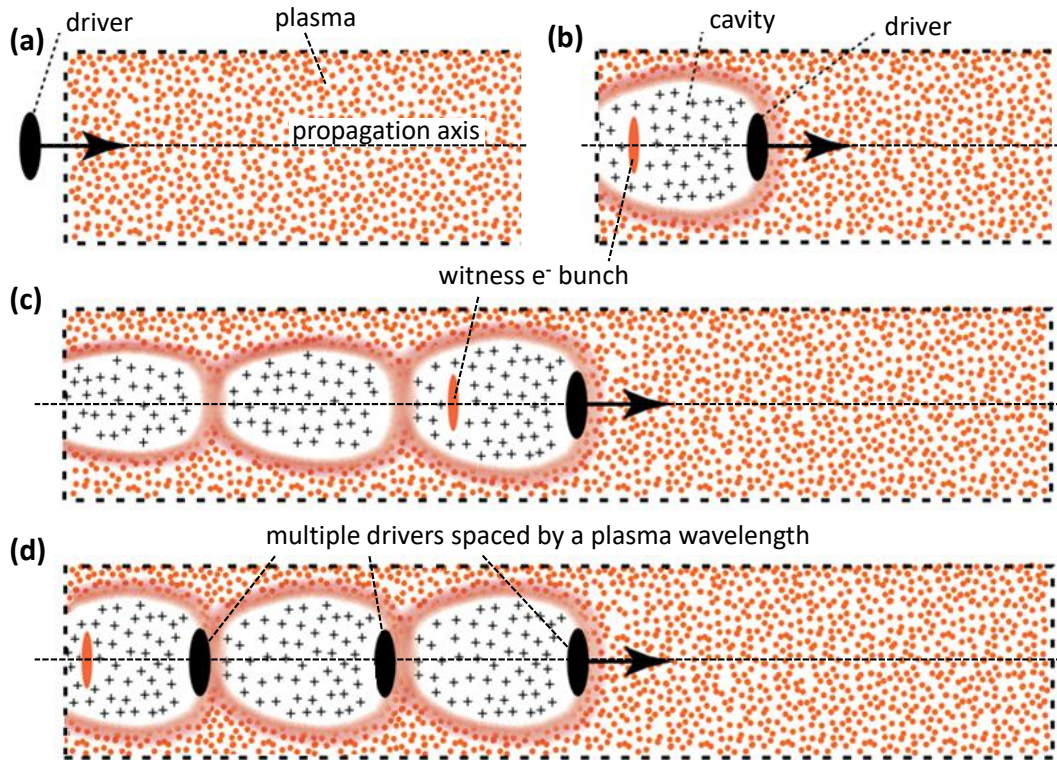


Figure 1: Schematic of plasma-based wakefield acceleration. (a) A short driver (black ellipse) enters a plasma (orange). (b,c) The driver deflects the plasma electrons. Cavities with a surplus of positive charge (black '+') inside and of negative charge (red) around it form behind the driver and around the propagation axis. A witness electron bunch is accelerated. (d) Multiple drivers spaced by a plasma wavelength can be used to coherently drive larger wakefields. From: [26], modified.

in Fig. 1) that co-propagates at the correct position inside the cavity, i.e. with the surplus of negative charge in its back and the positive charge in front is then accelerated to high energies (a full explanation of the distribution of electric fields in the wake follows after the discussion of this figure). As shown in Fig. 1(d), it is also possible to have multiple drivers that follow each other with a spacing of λ_{pe} [27]. In this case, the wakefields add coherently, and higher accelerating gradients can be achieved behind the multiple drivers.

With positively charged drivers such as short proton [28] or positron bunches [29], the driver does not expel electrons from the axis, but attracts them towards it. Despite the direction in which the electrons begin to move, the process that forms the

plasma wave is identical to that in Fig. 1, only shifted in phase. The corresponding schematic is shown in Fig. 2. In the vicinity of the proton driver, the electrons (indicated as blue minus symbol) move transversely towards the axis. Again, this leads to an increased negative charge on axis. The electrons overshoot, move away from the axis, and only the inert plasma ions remain on axis. The process continues exactly like in Fig. 1 and a plasma wave with high-amplitude wakefields forms behind the driver, as seen before.

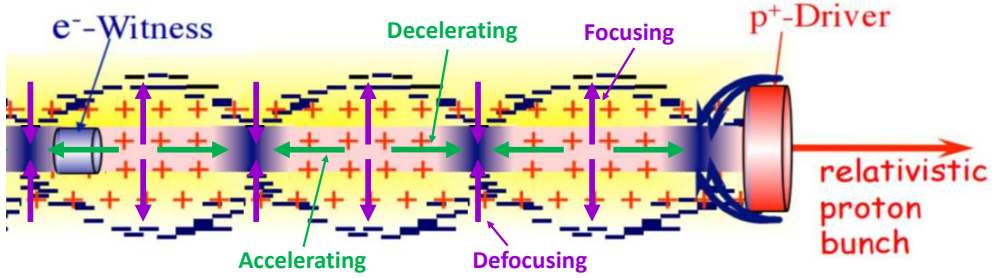


Figure 2: Schematic of proton-driven wakefield acceleration. A proton bunch shorter than the plasma wavelength drives wakefields that are accelerating or decelerating longitudinally (electric field lines as green arrows) and focusing or defocusing transversely (purple arrows). A witness electron bunch propagates in the accelerating and focusing part of the wakefield to be accelerated. From [30], modified.

We use this example to explain the different phases of the wakefields in a plasma cavity. In general, the electric field lines point away from the middle of the cavities and to the knots of the electron wave. For electrons on axis, the fields in longitudinal direction are consequently accelerating in the back half of a cavity and decelerating in the front half (green arrows). The transverse fields (purple arrows) are focusing in the middle of cavity and defocusing at their knots. As shown by the schematic¹, the longitudinal and transverse wakefields are shifted relative to each other by a quarter plasma wavelength. This means that only a quarter of a plasma wavelength is accelerating and focusing at the same time and thus suited for deterministic acceleration of externally injected electron bunches (see witness electron bunch in Fig. 2).

1.4 The Different Wakefield Acceleration Schemes in Comparison

Particles are accelerated because the plasma transfers energy from the driver to the witness bunch. The maximum achievable acceleration or energy gain is thus limited

¹but also by Eq. 2.11 and 2.12 in Chapter 2.2.

by the energy of the driver. For relativistic drive and witness bunches, the length over which particles are accelerated is also limited by the energy depletion of the driver [31] where its phase velocity decreases, i.e. particles transit to the defocusing parts of the wakefields.

This reveals the challenges of wakefield acceleration. The presence of strong defocusing fields (Fig. 2) that might act on bunches together with different phase velocities of the driver beams and wakefields is a significant difference from conventional accelerations. A main focus of LWFA and PWFA is therefore not only on maximizing the energy gain, but also on the preservation of the beam quality. This includes a low energy spread, a low emittance and a high population per bunch, e.g. as it is required to provide sufficiently high luminosity for collision experiments.

Since accelerators rely on very precise timing, all machine and beam parameters are usually described in the time domain, which is also done for this thesis. The previously mentioned requirement of $\sigma_z < \lambda_{pe}$ thus translates into the requirement that the duration of the driver σ_t is shorter than a plasma period: $\sigma_t < 1/\omega_{pe}$. As an example, an accelerating field of > 1 GV/m (which is obtained for plasma densities $n_{e0} = (\varepsilon_0 m_e / e^2) (1/\sigma_t^2) > 10^{14} \text{ cm}^{-3}$) requires pulses or bunches with $\sigma_t < 2$ ps and radii σ_r smaller 600 μm . The first step in the design process of a wakefield accelerator (for both LWFA and PWFA) is therefore the matching of all beam and plasma parameters.

1.4.1 Laser-driven Wakefield Acceleration

The concept of LWFA-based accelerators by T. Tajima and J. M. Dawson [22] initiated the development of all plasma wakefield acceleration schemes. Until sufficiently short laser pulses became available, pulses that were self-modulated through Raman scattering were used for this scheme [31]. The change to short pulses was, among others, triggered by the lack of control over the self-modulation (SM) process and thus over the phases of the wakefields. The creating of short pulses is nowadays realized through chirped pulse amplification (CPA) [32] which has, as a side-note, revolutionized not only plasma-based wakefield acceleration, but the whole field of laser physics and was therefore awarded the Nobel Prize in Physics 2018. With pulse durations of a few tens of femtoseconds and an energy of usually < 10 J per pulse, lasers in current laser-driven plasma wakefield accelerators have powers in the tera- to petawatt regime [33]. As a consequence, a broad field with various types of plasmas (e.g. capillary discharges and ionized gas jets), electron injection methods (e.g. shock-front injection, self-injection) and dielectric media instead of plasma developed. Possible applications are not only for particle physics, but also for ultra-bright X-ray sources. All these are routinely presented on conferences such as the European Advanced Accelerator Concepts Workshop (EAAC, see e.g. [34]). Over all years, accelerating gradients > 100 GeV/m [35], energy gains of 8 GeV [36], low energy

spreads (i.e., at the percent level) [37, 38, 39] and low-emittance beams [40] have been demonstrated separately, and also together [41]. Proton and ion acceleration usually uses target normal sheath acceleration (TNSA) [42]. Because lasers are comparably cheaper and easier to implement as drive beams than particle beams, LWFA has also a great perspective for applications in medical irradiation and X-ray facilities. However, as already mentioned, the energy stored in these laser pulse is typically small, <100 J. Particle beams as they are used in PWFA-based accelerators can carry significantly larger amount of energy.

1.4.2 Electron-driven Wakefield Acceleration

Until recently, beam-driven plasma wakefield accelerator experiments operated with bunch and plasma such that $\sigma_t \leq 1/\omega_{pe}$ to reach high accelerating fields. Short (pico- to femtoseconds-long), high-energy electron bunches are commonly produced. In this case, wakefields are tied to the short driver and deterministic, external injection is possible, as it was demonstrated in the original experiment [43]. The experiment of the previously mentioned ≈ 42 GeV energy gain by I. Blumenfeld et al. [21] functioned as an "afterburner"-like accelerator, i.e. a single electron bunch that was longer than the plasma wavelength ($\sigma_t = 50$ fs $> 1/\omega_{pe} = 34$ fs) was used and the front drove wakefields that accelerated a fraction of the electrons in its back. Acceleration of a full electron bunch by 9 GeV has been demonstrated [44]. High-efficiency acceleration with $\sim 30\%$ energy transfer efficiency from the drive to the accelerated bunch and 0.7% energy spread are reported in [45]. Also acceleration of positrons has been achieved [46], with energy gains of 5 GeV and energy spread at the percent level [47].

However, electron or positron bunches do not carry energies above ~ 100 J (the electron bunch of [21] carried 42 GeV/electron times 1.8×10^{10} electrons = 121 J). Thus, the energy provided by the drive bunch to the system for acceleration is limited in a similar way than with LWFA. A possibility to reach higher energies is the so-called staging, where the accelerated bunch traverses a chain of plasma wakefield accelerators with multiple, short plasmas and drivers.

1.4.3 Proton-driven Wakefield Acceleration: AWAKE

Proton bunches are available with notably higher energies per particle, but also bring a much higher mass (see paragraph 1.1). As a result, the bunches carry total energies that are several orders of magnitude higher than that of laser pulses or electron bunches. An example for these high-energy proton beams is the Super Proton Synchrotron (SPS) at CERN [48]. With 400 GeV/proton and a bunch population of $N_b = 3 \times 10^{11}$, each bunch provides 19.2 kJ. A bunch at 6.5 TeV in the LHC even possess 125 kJ. Such proton bunches carrying tens to hundreds of kilojoules of energy can be used to drive GV/m wakefields in a single, long plasma (hundreds to

thousands of meters) and accelerate electrons with a SM-based scheme to the TeV energy scale, as posited by simulation results [28].

The SM is thereby required because currently available proton bunches are too long when compared to the short plasma wavelength or period required for driving GeV/m accelerating gradients. Instead of the required hundreds of micrometers to ~ 1 mm, these bunches have lengths of several centimeters. Bunches of the SPS are between 6 cm and 12 cm long. Without SM, but still to fulfil $\sigma_z < \lambda_{pe}$, the plasma electron density would have to be significantly lower, around $n_{e0} \sim 10^{11} \text{ cm}^{-3}$. According to Eq. 1.1, the highest achievable field would be around $E_{WB} = 32 \text{ MV/m}$, i.e. only in the range of conventional RF cavities. As the world's first and up to now only proton-driven plasma wakefield experiment, AWAKE [49, 50] (short for "Advanced Wakefield Experiment") demonstrated that the SM indeed turns a long proton bunch into a train of short micro-bunches which is modulated at the plasma electron frequency [51]. The AWAKE experiment is described in detail in terms of working principle and setup in Chapter 3. In addition, it also demonstrated the acceleration of electrons to up to 2 GeV in the wakefields of these micro-bunches [52]. The SM-based and proton-driven acceleration scheme therefore promises applications in high-energy physics [53].

1.5 Thesis Topic: Self-Modulation Instability, its Seeding and the Influence of Linear Plasma Gradients

The focus of this thesis is on the SMM of the proton bunch as it represents a fundamental beam-plasma interaction. The proton bunch self-modulates because of an axi-symmetric instability that evolves transversely when it propagates through a plasma: the SM instability (SMI) [24]. In a preformed plasma, the head of the (Gaussian) proton bunch drives small initial transverse wakefields, as illustrated in Fig. 3. These in the beginning mainly focusing wakefields (blue arrows in Fig. 3(a)) are spaced by λ_{pe} and act back on the proton bunch. This initializes a modulation of the charge density of the bunch, which resonantly reinforces the wakefields. Focusing and defocusing wakefields grow to large amplitude as an instability and form on axis short (i.e. $\sigma_z < \lambda_{pe}$) micro-bunches that are spaced by λ_{pe} . The protons in between leave the axis (Fig. 3(b)). For long enough propagation distances, this leads to a deep modulation along the whole proton bunch. The train of micro-bunches then resonantly drives the wakefields for electron acceleration, as shown in the schematic of Fig. 1(d).

The challenge of exploiting a growing instability comes with its intrinsic property of usually being uncontrolled. The SM might grow from shot noise [55] or small

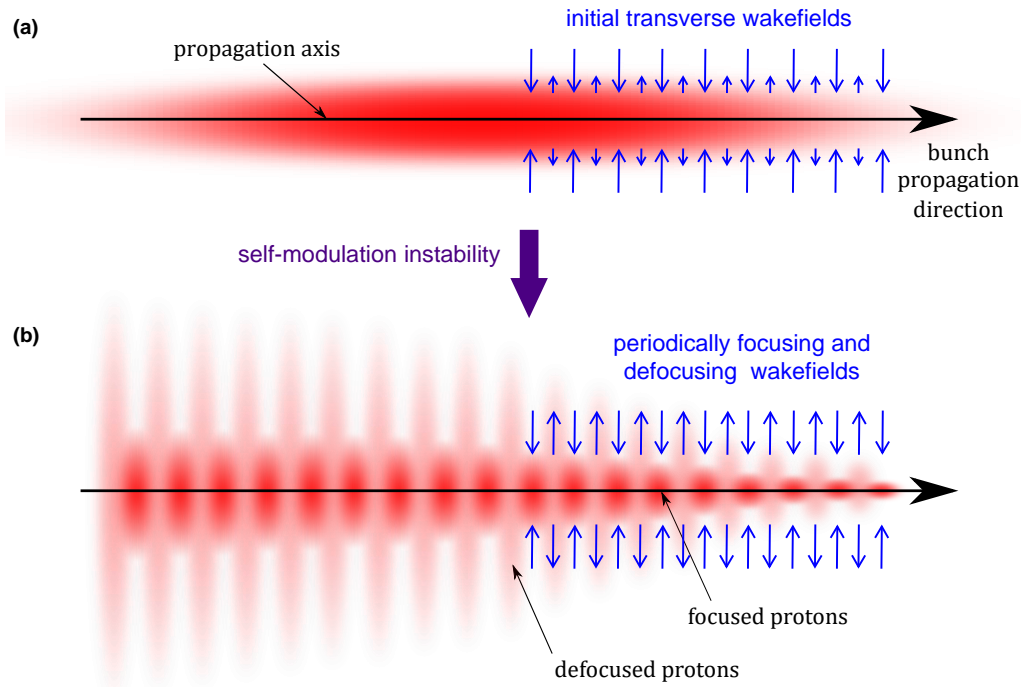


Figure 3: Schematic of the self-modulation instability of a long proton bunch in plasma (a). Resonantly growing focusing and defocusing wakefields modulate the bunch radially at the plasma electron frequency. This produces a train of micro-bunches with the protons in between being defocused (b). Modified plot from [54].

bunch irregularities¹. However, control over the SM, especially in terms of the relative phase or timing of the micro-bunches, is a key requirement for deterministic and reproducible electron injection into the focusing and accelerating quarter of the plasma period (see Fig. 2). This is not only important for AWAKE, but also for future, AWAKE-based accelerators for collision experiments [53].

The start of the SM can be triggered, which one refers to as seeding. In this case the SM does not start from shot noise or small bunch irregularities, but from an initial transverse wakefield that is provided through an external source, and we call it seeded self-modulation (SSM). Seeding can for example be induced by a cut in the proton bunch charge distribution [50] where the sharp edge in the charge density provides initial wakefields much larger than that of the noise or charge density irregularities. However, cutting the 400 GeV proton bunches transversely and perpendicularly to

¹Also other instabilities might evolve, such as the hosing instability. A detailed study of this instability is reported in [54].

the propagation axis would require a number of very large-size equipments that are not available.

In AWAKE, one therefore seeds the SMI with the sharp and relativistic ionization front (RIF) of an intense laser pulse. The process is illustrated in Fig. 4. The laser

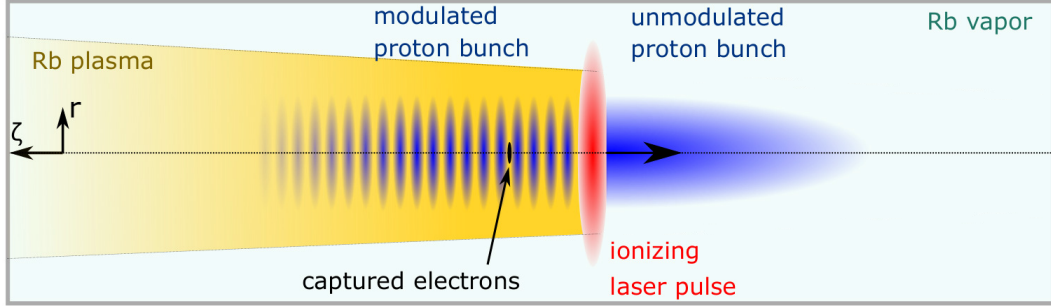


Figure 4: Schematic of seeded self-modulation. An intense laser pulse provides a relativistic ionization front that creates a sudden onset of the plasma inside the co-propagating proton bunch. From: [56].

pulse and the proton bunch co-propagate in rubidium (Rb) vapor. Thereby, the laser pulse travels close to the center of proton bunch where the charge density is close to its maximum. The RIF ionizes the vapor and forms a plasma column. The first half of the bunch therefore travels in Rb vapor only, which does not interact with the proton bunch. For the second half, the sudden increase in plasma density triggers large initial transverse wakefields that cause the SM to start at the position of the RIF. A train of micro-bunch that is modulated at the plasma frequency forms behind the RIF, as demonstrated in [51].

The effect of seeding is more clearly illustrated in Fig. 5. A time-resolved image of the ≈ 1 ns long proton bunch without plasma is shown Figure 5(a). The white dashed line represents the Gaussian distributed charge density on axis. This image is to be compared with Fig. 5(b), which shows the proton bunch after propagating through 10 m of plasma and with the RIF placed at $t = -130$ ps (indicated by the vertical, yellow dashed line; $t = 0$ marks the bunch center). A clear effect of the RIF and plasma on the bunch and the charge density on axis (blue line) is visible. After $t = -130$ ps, the charge on axis is decreased and defocused protons are visible away from the axis. A zoomed view of Fig. 5(b) is depicted in Fig. 5(c). Behind the RIF ($t = -130$ ps), a clear and periodic bunch train formed due to the seeding. Also the defocused protons from in between the micro-bunches are visible off-axis.

However, no studies of the effect of seeding on the relative phase or timing of the micro-bunches with respect to the RIF and its reproducibility have been reported

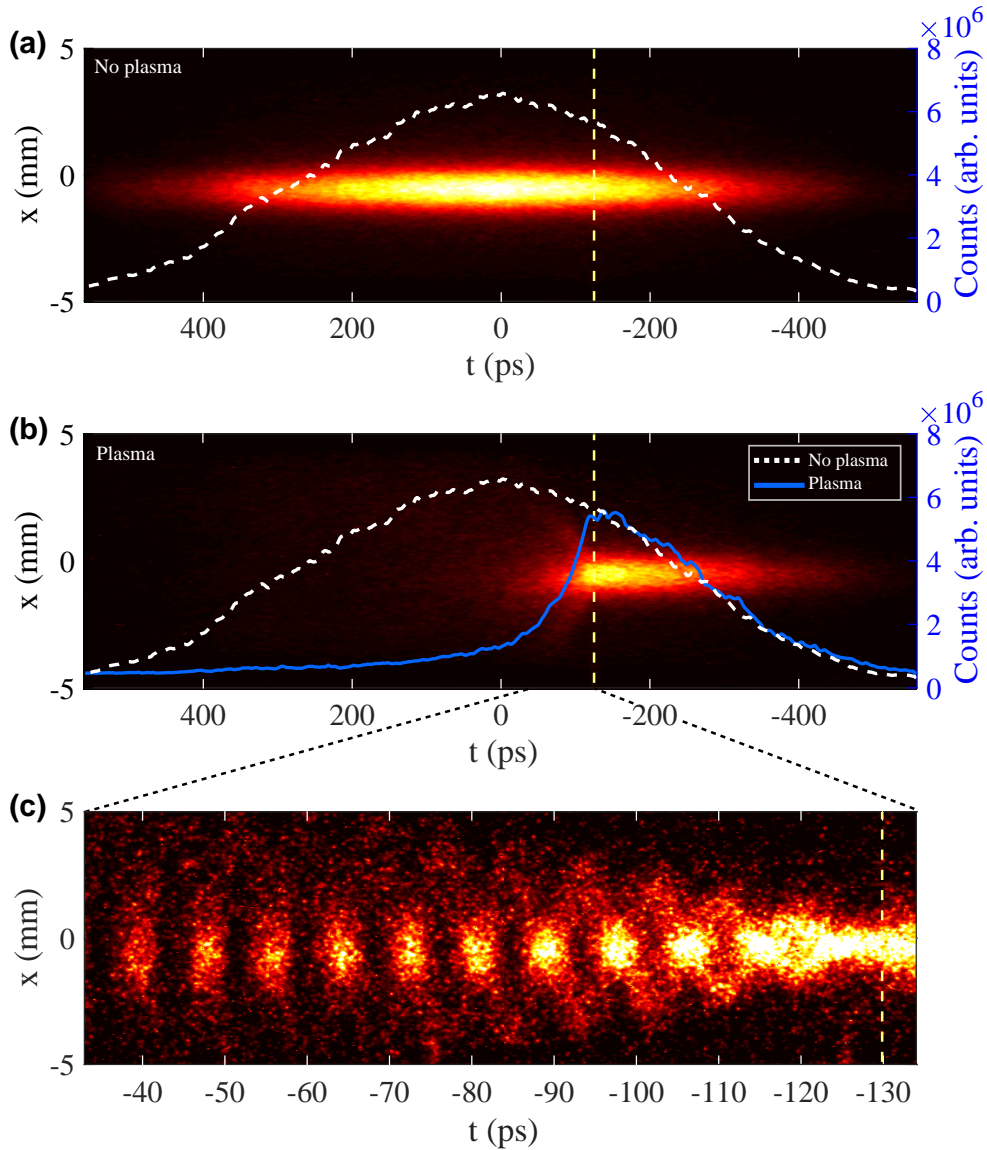


Figure 5: (a) Stitched and time-resolved image of the proton bunch without plasma. White, dashed line represents the on-axis proton distribution. Time $t = 0$ marks the bunch center, x the radial position. Front of the bunch on the right side. (b) Similar image with a co-propagating, intense laser pulse at time $t = -130$ ps ahead of the bunch center (not visible, indicated by the vertical dashed line in (a,b,c)). Corresponding on-axis proton distribution as blue line. Plasma density $n_{e0} = 1.81 \times 10^{14} \text{ cm}^{-3}$. (c) Image with higher time resolution showing the micro-bunch train and defocused protons behind the RIF.

before the work presented in this thesis. Neither (at least not to my knowledge) has the phase reproducibility been investigated for unseeded SM (SMI). From simulations, one expects no phase reproducibility for the SMI regime and phase reproducibility for the SSM regime. In its **first main part**, I therefore study the phase variation of the self-modulation of a relativistic proton bunch in a plasma with constant density while providing various initial transverse wakefield amplitudes for the seeding. The goal is to prove the existence of two distinct SM regimes in terms of variation in modulation phase and to observe the transition between them, i.e. the minimal required initial wakefield amplitude that overcomes any noise or bunch irregularities in the system. The transition point is critical as it provides very useful information about the reproducibility of the seeding and acceleration processes, required for the planing of future experimental run periods of AWAKE. For these studies, I use time-resolved streak camera (SC) images such as that of Fig. 5(c). For this purpose, I developed an experimental tool which is also presented: the so-called laser reference signal (LRS). This signal provides relative timing signals on the time-resolved images of the proton bunch to determine and compare that phase and timing of individual micro-bunches, despite any timing jitters in the system (see Chapters 3.4.3 and 5).

A **second main part** focuses on the preservation of the SM and its micro-bunches. As stated in [28, 57], in the case of a constant density profile the SMI continues to grow, which eventually defocuses the micro-bunches. Simulations show that changing the profile of the plasma can stop this process and preserves the micro-bunch structure and thus high wakefield amplitudes. The second part therefore experimentally investigates the influence of positive and negative linear density gradients on the SM. From time resolved images that display the entire modulated proton bunch, I compare the length of the micro-bunch train and the charge that remains on axis. As with density gradients the plasma electron frequency changes with n_{e0} along the propagation axis, I study the modulation frequency of the distributions of the micro-bunches and of the defocused protons to suggest at which position along the plasma the SM and defocusing takes place. It is also to mention that this experimental analysis led to the simulation studies of the SM under the influence of plasma density gradients presented in [58].

1.6 Thesis Layout

With the just mentioned perspectives, the detailed structure of this thesis reads as follows:

Chapter 2 summarizes the theory and physical concepts that are required for the interpretation of the SM measurements.

In Chapter 3, I explain AWAKE's working principle, its experimental setup and diagnostics in more detail. This includes an overview of the CERN accelerator complex and the components in AWAKE that are in particular important for this thesis. To its end, I present two diagnostics that I developed in the context of the phase variation and gradient measurements. The first one is the implementation of a live Rb vapor density and gradient measurement based on the method of [59]. The second diagnostic is the LRS which provides a timing signal on the time-resolved images.

Chapter 4 includes the determination of the temporal position of the LRS on images and the image processing and analysis procedure that determines the phase of the modulated bunch train with respect to the laser pulse.

In Chapter 5, I present a detailed analysis of the characteristics of the LRS, such as timing jitters and its measurement errors, which are essential for a correct interpretation of the phase variations measured.

The results of phase variation measurements are presented in Chapter 6. I measure the variation in modulation phase for different positions of the ionizing laser within the proton bunch. The LRS is also used to create high-resolution images of the entire modulated bunch train. Last, I determine the relative phase of micro-bunches along the bunch to reveal information about the modulation frequency along the proton bunch.

Chapter 7 presents the measurements of the self-modulation with linear plasma density gradients. I investigate the influence of these gradients on the micro-bunches and the on-axis charge. I explain how gradients influence the modulation frequency, also for different radial positions within the bunch. The measurements of the modulation frequency and phase, and its variation, are repeated while keeping the seed position constant and only changing the gradient.

In the last Chapter 8, I summarize the key results of this thesis, and their meaning and importance for future measurement campaigns foreseen in AWAKE. To complete the outlook, I suggest possible, complementary measurements to further investigate the transition point and how these measurements can serve as a guidance for similar measurements where electron bunches are used to seed the self-modulation.

Publications

The results of this thesis were reported in the following publications, which can also be found in Appendix B:

- *Transition between Instability and Seeded Self-Modulation of a Relativistic Particle Bunch in Plasma*, in F. Batsch, P. Muggli et al. (AWAKE Collaboration), Phys. Rev. Lett. 126, 164802 (2021),
- *Setup and Characteristics of a Timing Reference Signal with sub-ps Accuracy for AWAKE*, in F. Batsch, J. Phys. Conf. Ser. 1596, 012006 (2020),
- *Interferometer-based high-accuracy white light measurement of neutral rubidium density and gradient at AWAKE*, in F. Batsch, M. Martyanov, E. Öz, J. Moody, E. Gschwendtner, A. Caldwell, and P. Muggli, Nucl. Instrum. Methods Phys. Res., Sect. A 909, 359 (2018).

The following publications report measurements that are complementary to this thesis and that partially cover content of this thesis:

- *Proton Bunch Self-Modulation in Plasma with Density Gradient*, in [60] F. Braunmüller et al. (AWAKE Collaboration), Phys. Rev. Lett. 125, 264801 (2020),
- *Simulation and Experimental Study of Proton Bunch Self-Modulation in Plasma with Linear Density Gradients*, in [58] P. I. Morales Guzmán, P. Muggli et al. (AWAKE Collaboration), Phys. Rev. Accel. Beams 24, 101301 (2021).

Before continuing, I also want to note that the main part of the text uses "we" instead of "I" because even though the thesis presents my results and work, it is never possible without teamwork.

Chapter 2

Theory and Concepts

In this chapter, we explain the main properties of plasma (following [61]) and plasma waves. We describe the plasma wakefields and derive the amplitude of the initial transverse wakefield which is needed for the studies of the phase reproducibility of the SM for various initial transverse wakefield amplitudes (see Chapter 6). We also discuss the difference between the phase velocity of the wakefields and the velocity of the proton bunch and how it can be influenced by linear plasma gradients (see Chapter 7). Last, we describe the discrete Fourier transform as it is part of the procedure that determines the modulation frequency and phase in this thesis.

2.1 Plasma and its Properties

A plasma is a partially or fully ionized gas with ions and free electrons. The ratio of plasma electrons and ions to the number of neutral atoms defines its degree of ionization α_I . For a gas with neutral particle density n_{n0} , plasma electron density n_{e0} and plasma ion density n_{i0} , α_I is given as [61]

$$\alpha_I = \frac{n_{i0}}{n_{n0} + n_{i0}} . \quad (2.1)$$

Its value ranges from 0% to 100%, where the latter corresponds to full ionization. The quasi-neutrality, i.e. $n_{e0} = n_{i0}$ is an important property of plasma, i.e. it is neutral when considered over a large volume.

Besides its ion and electron densities, a plasma is also characterized by its temperature T or corresponding energy $E = k_B T$, with $k_B = 1.3806 \times 10^{-23}$ J/K the Boltzmann constant¹. One calls a plasma ideal when the interaction process between particles is dominated by elastic scattering (from their large kinetic energy), and not by charge effects between single particles. The corresponding condition for plasma electron with a mean distance of $1/n_{n0}^{1/3}$ reads [61]

$$\frac{3}{2}k_B T \gg \frac{e^2}{4\pi\epsilon_0} n_{n0}^{1/3} . \quad (2.2)$$

¹Room temperature (20°C) corresponds to ≈ 25 meV.

The constant ε_0 denotes the vacuum permittivity. Plasmas are referred to as relativistic when their temperature is high enough such that particles reach relativistic velocities. Here, different definitions exist, e.g. that its energy must be larger than the energy-equivalent of the electron rest mass ($k_B T > 511 \text{ keV}$ [61]). Most plasmas are ideal (see [61], Fig. 1.1), including that of AWAKE.

The large number of free charges together with quasi-neutrality also cause that a plasma shields the electric field with respect to its outside. The Debye length λ_D describes the distance over which the electric potential of a plasma charge decreases by $1/e$. It is calculated as [61]

$$\lambda_D = \sqrt{\frac{\varepsilon_0 k_B T}{e^2 n_{e0}}} . \quad (2.3)$$

A general requirement of plasma is that its dimensions are larger than λ_D . Only then, collective effects can take place. For an ideal plasma, one therefore requires the number of particles within a sphere of radius λ_D (called Debye-sphere) to be $N_D = \frac{4}{3}\pi\lambda_D^3 n_{e0} \gg 1$.

In AWAKE, as mentioned in the introduction, the plasma is created out of Rb vapor through field-ionization with a high-intensity laser pulse. The created 10-m-long plasma channel is fully ionized ($\sim 100\%$, [51]) and n_{e0} is between 10^{14} cm^{-3} and 10^{15} cm^{-3} (see Chapter 3 for details). The baseline densities are $n_{e0} = 2 \times 10^{14} \text{ cm}^{-3}$ and $7 \times 10^{14} \text{ cm}^{-3}$. Its temperature corresponds to $\approx 4 \text{ eV}$ [62], giving $\lambda_D \approx 600 \text{ nm}$ and approximately $N_D = 630$ particles per Debye sphere.

2.2 Plasma Waves and Linear Wakefield Theory

Plasma waves in an undisturbed and unmagnetized plasma show a periodicity that corresponds to the plasma electron or ion frequency. The cold plasma approximation assumes that the ions are at rest due to their high mass and that the thermal velocity of the plasma electrons is also negligible, or in other words, that the thermal movements within a plasma period are much smaller than λ_{pe} . The waves in PWFA-based accelerators are electrostatic, i.e. so-called Langmuir waves. The electrons oscillate harmonically within the electric fields, i.e. plasma oscillations form with $\omega_{pe} = 2\pi f_{pe}$ their eigenfrequency. In AWAKE, the Rb ions are ≈ 5 orders of magnitude heavier than electrons and can thus be assumed to remain at rest over the time scales of interest. The plasma electron frequencies (Eq. 1.2) for the baseline densities are $f_{pe} = 127 \text{ GHz}$ and 238 GHz . With this simple case of an electrostatic wave without ion motion, the dispersion relation is $\omega = \omega_{pe}$. Plasma oscillations are dispersion-free, i.e. the group velocity for a wave with wavenumber k is $v_{gr} = \frac{\partial \omega_{pe}}{\partial k} = 0$ as they oscillate around a fixed position in the laboratory frame (see Figs.1 and 2). The

phase velocity is more important for electron injection and acceleration, with points of constant phase within the wakefields moving at v_{ph} , which is obtained through

$$v_{ph} = \frac{\omega_{pe}}{k} . \quad (2.4)$$

For electro-magnetic waves (such as light), dispersion occurs. The dispersion relation follows $\omega^2 = \omega_{pe}^2 + c^2k^2$. The group velocity is non-zero [61]:

$$v_{gr} = \frac{\partial\omega}{\partial k} = c\sqrt{1 - \frac{\omega_{pe}^2}{\omega^2}} = c\eta < c , \quad (2.5)$$

with η the index of refraction of the plasma. The phase velocity is calculated as

$$v_{ph} = \frac{\omega}{k} = c\sqrt{\frac{\omega^2}{\omega^2 - \omega_{pe}^2}} = \frac{c}{\eta} > c . \quad (2.6)$$

In this context, the plasma electron frequency is again an important parameter with regard to the response of the plasma to the electro-magnetic wave. Only waves with a frequency $\omega > \omega_{pe}$ can propagate in the plasma. Waves with $\omega < \omega_{pe}$ and incident on a sharp vacuum-plasma boundary are reflected within the distance of the plasma skin depth $k_{pe}^{-1} = c/\omega_{pe}$. In AWAKE-related literature [63], the plasma skin depth instead of the Debye length is used to describe distances within the plasma.

Linear Wakefield Theory

For the wakefields within and behind the proton bunch as it propagates through plasma, one usually uses a coordinate system with time t , z the position along the plasma, $\zeta = ct - z$ the position within the proton bunch and r or x the radial position with respect to the axis. The Gaussian proton bunch is usually described in cylindrical coordinates while assuming that its center at $\zeta = 0$ and $r = 0$, i.e. the normalized longitudinal and radial charge density distribution is described by

$$n_{b\parallel}(\zeta) = \frac{1}{\sqrt{2\pi}\sigma_z} \cdot \exp(-\zeta^2/2\sigma_z^2) \quad (2.7)$$

and

$$n_{b\perp}(r) = \frac{1}{\sqrt{2\pi}\sigma_r} \cdot \exp(-r^2/2\sigma_r^2) . \quad (2.8)$$

Here σ_z and σ_r denote the respective longitudinal and radial bunch length. The proton bunch density distribution is then

$$n_b(\zeta, r) = n_{b0} \cdot n_{b\parallel}(\zeta) \cdot n_{b\perp}(r) , \quad (2.9)$$

with n_{b0} the peak bunch density. However, as stated before, this thesis focuses on the timing of the micro-bunches and therefore uses $t = \zeta/c$ also to describe positions along the bunch. We set the center of the bunch as $t = 0$. The proton bunch number density becomes

$$n_b(t, r) = n_{b0} \cdot \exp\left(-t^2/2\sigma_t^2\right) \cdot n_{b\perp}(r) := \tilde{n}_b(t) \cdot n_{b\perp}(r) , \quad (2.10)$$

where $\tilde{n}_b(t)$ denotes the on-axis density as a function of time. With the AWAKE baseline parameters for the proton bunch of $\sigma_z = 7.4$ cm (equal to $\sigma_t = 250$ ps), $\sigma_r = 150$ μm (at waist position) and a population of $N_b = 3 \times 10^{11}$, the bunch density equals $n_{b0} = 1.1 \times 10^{13} \text{ cm}^{-3}$. As this is much smaller than the plasma density ($n_{e0} \approx 2$ to $7 \times 10^{14} \text{ cm}^{-3}$), we use two-dimensional linear theory to describe PWFA [25, 64]. The longitudinal and transverse wakefields $W_{\parallel}(t, r)$ and $W_{\perp}(t, r)$ can be expressed by [64]

$$W_{\parallel}(t, r) = \frac{ec}{\varepsilon_0} \int_{-\infty}^t \tilde{n}_b(t') \cos(\omega_{pe}(t - t')) dt' \cdot R(r) \quad (2.11)$$

and

$$W_{\perp}(t, r) = \frac{ec^2}{\varepsilon_0 \omega_{pe}} \int_{-\infty}^t \tilde{n}_b(t') \sin(\omega_{pe}(t - t')) dt' \cdot \frac{dR(r)}{dr} . \quad (2.12)$$

The expression for the radial dependency of the longitudinal wakefield $R(r)$ depends on the transverse profile of the bunch:

$$\begin{aligned} R(r) = & k_{pe}^2 K_0(k_{pe}r) \int_0^r r' n_{b\perp}(r') I_0(k_{pe}r') dr' \\ & + k_{pe}^2 I_0(k_{pe}r) \int_r^{\infty} r' n_{b\perp}(r') K_0(k_{pe}r') dr' \end{aligned} \quad (2.13)$$

Its derivative with respect to r is a measure for the radial dependency of W_{\perp} (Eq. 2.12) and calculated as

$$\begin{aligned} \frac{dR(r)}{dr} = & -k_{pe}^3 K_1(k_{pe}r) \int_0^r r' n_{b\perp}(r') I_0(k_{pe}r') dr' \\ & + k_{pe}^3 I_1(k_{pe}r) \int_r^{\infty} r' n_{b\perp}(r') K_0(k_{pe}r') dr' . \end{aligned} \quad (2.14)$$

The terms I_0 and I_1 denote the zeroth and first order modified Bessel functions of the first kind, K_0 and K_1 denote the zeroth and first order modified Bessel functions of the second kind. The longitudinal field has its maximum on axis, i.e. for $r = 0$. The transverse component $W_{\perp}(t, r)$, which is essential for the seeding of the SM has its maximum at $r = \sigma_r$.

As an example, Fig. 6(a) shows in red the corresponding longitudinal ($W_{\parallel}(t, r = 0)$, Eq. 2.11) and in blue the transverse wakefield ($W_{\perp}(t, r = \sigma_r)$, Eq. 2.12) for a plasma density of $n_{e0} = 2 \times 10^{14} \text{ cm}^{-3}$. The black line indicates the normalized bunch density for a Gaussian bunch with length $\sigma_z = 7.4 \text{ cm}$ and population $N_b = 3 \times 10^{11}$. In that example, a cut bunch is used, i.e. $n_b = 0$ for $t < 0$, as it is needed to seed the SM by the initial transverse wakefields driven by the sharp rise in charge density (see the following paragraph for the corresponding initial transverse wakefield amplitude). As explained in the introduction, in the experiment, cut bunches are not available and instead the plasma is created at the bunch center by the RIF, which is equivalent to that cut. The longitudinal fields are alternating accelerating and decelerating, while the transverse fields are first only mainly focusing for protons which is caused by the adiabatic response of the plasma. The enlarged view of the wakefields in Fig. 6(b) visualizes that the focusing or defocusing (W_{\perp}) and accelerating or decelerating wakefields (W_{\parallel}) are shifted in phase by a quarter period, as already discussed for Fig. 2 in Chapter 1.4.3.

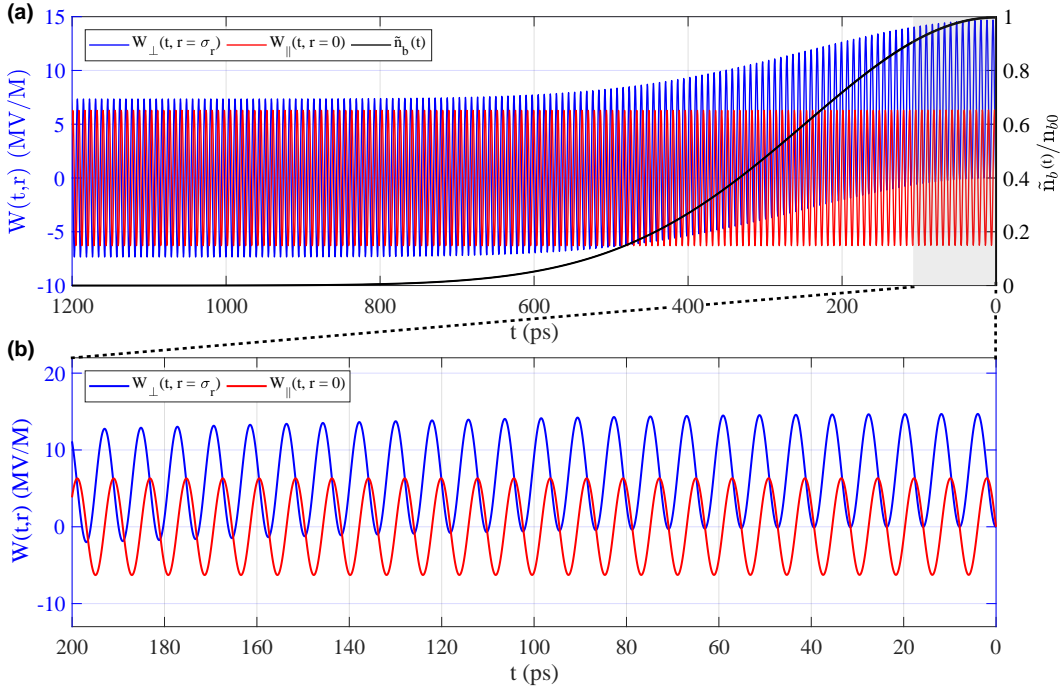


Figure 6: (a) Longitudinal ($W_{\parallel}(t, r = 0)$, red line) and transverse wakefield ($W_{\perp}(t, r = \sigma_r)$, blue line) for $\sigma_z = 7.4 \text{ cm}$, $N_b = 3 \times 10^{11}$ and $n_{e0} = 2 \times 10^{14} \text{ cm}^{-3}$ according to [65]. The black line represents the normalized, on-axis bunch density $\tilde{n}_b(t)/n_{b0}$. Propagation direction from left to right. The bunch is cut at its center, i.e. $n_b = 0$ for $t < 0$. (b) Enlarged view of the wakefields.

2.3 Initial Transverse Wakefield and Noise Amplitudes

The SM studies on seeding and its influence on the phase reproducibility compares the SMI and SSM regimes with respect to the respective amplitude of the initial transverse wakefield at the position of the RIF within the bunch. We call the time at which the RIF creates the plasma t_{RIF} . To obtain an expression for that amplitude, we evaluate Eq. 2.12 for $t = t_{RIF}$ and $r = \sigma_r$. Because the part of the proton bunch that propagates before the RIF in Rb vapor does not interact with the vapor nor the plasma, the bunch density is again equal to that of a cut bunch. Here, we assume that the bunch density is described by a step function that start at $t = t_{RIF}$ and remains constant from the RIF over one period of the wakefields: $n_b(t) \cong n_b(t_{RIF})$ for $t_{RIF} \leq t \leq t_{RIF} + 2\pi/\omega_{pe}$. Equation 2.12 therefore becomes

$$W_{\perp}(t, r = \sigma_{r0}) = \frac{ec^2}{\varepsilon_0\omega_{pe}} \tilde{n}_b(t_{RIF}) \cdot \int_{t_{RIF}}^t \sin(\omega_{pe}(t-t')) dt' \cdot \left. \frac{dR(r)}{dr} \right|_{r=\sigma_{r0}}. \quad (2.15)$$

Integrating this expression by substitution gives

$$W_{\perp}(t_{RIF} \leq t \leq \frac{2\pi}{\omega_{pe}}, r = \sigma_{r0}) = \frac{ec^2}{\varepsilon_0\omega_{pe}^2} \tilde{n}_b(t_{RIF}) (1 - \cos(\omega_{pe}(t - t_{RIF}))) \left. \frac{dR(r)}{dr} \right|_{r=\sigma_{r0}}. \quad (2.16)$$

The +1 term before the cosine term represents the adiabatic response of the plasma with a constant bunch density. The desired seed wakefield, or more precisely, the initial transverse wakefield amplitude at the position of the RIF, $W_{\perp,RIF}$, is the difference between the maximum and the minimum values:

$$W_{\perp,RIF} = 2 \frac{ec^2}{\varepsilon_0\omega_{pe}^2} \tilde{n}_b(t_{RIF}) \left. \frac{dR(r)}{dr} \right|_{r=\sigma_{r0}}. \quad (2.17)$$

Substituting ω_{pe} with Eq. 1.2 allows for writing $W_{\perp,RIF}$ as a function of the beam-to-plasma density ratio:

$$W_{\perp,RIF} = 2 \frac{m_e c^2}{e} \frac{\tilde{n}_b(t_{RIF})}{n_{e0}} \left. \frac{dR(r)}{dr} \right|_{r=\sigma_{r0}}. \quad (2.18)$$

After seeding, the SMI grows along the propagation path in plasma, i.e. along z . This process depends on n_b and z and can be obtained from literature ([66]) as

$$W_{\perp}(n_b, z) = W_{\perp,RIF} \cdot e^{\Gamma(n_b, z)z}. \quad (2.19)$$

Here, $\Gamma(n_b, z)$ denotes the growth rate, which is calculated for a long bunch as [66]

$$\Gamma(n_b, z) = \frac{3\sqrt{3}}{4} \omega_{pe} \left(\frac{ct}{z} \right)^{1/3} \left(\frac{n_b m_e}{2n_{e0} m_p \gamma_b} \right)^{1/3}. \quad (2.20)$$

The total growth of the wakefields corresponds to $\Gamma \cdot z \propto z^{2/3}$.

Amplitudes of Noise and Bunch Irregularities

In the measurement, we compare the value of $W_{\perp,RIF}$ against the amplitude of the wakefields driven by shot noise and bunch irregularities in the proton bunch distribution. The shot noise, originating from a "random" distribution of the electric field of the within the Gaussian bunch randomly distributed protons, was determined through calculations and simulation at the level of a few tens kV/m [55]. The bunch irregularities that might be imposed by the beam transport optics have no reliable estimate, but the initial wakefields driven by them follow the same scaling as that of the seed wakefields. An estimate of the combined noise level is obtained by the observation of the transition from SMI to SSM in this thesis (see Chapter 6.2).

2.4 The Phase Velocity of Wakefields

As it is shown in [65, 66], in a plasma with a constant density, the charge distribution of the proton bunch and the phase of wakefields move at different velocities until the SM reaches saturation [67]. This difference causes a phase shift between the two, which increases along the bunch (i.e., ζ) and the plasma (i.e., z). Accordingly, protons might transit from the focusing to the defocusing half of the wakefields and be lost. The phase velocity of the wakefield $v_{ph}(\zeta, z)$ or $v_{ph}(t, z)$, which is smaller than the velocity of the bunch v_b , is proportional to the growth rate Γ and is given by [66] as

$$v_{ph}(\zeta, z) = v_b \left[1 - \frac{1}{2} \left(\frac{\zeta}{z} \right)^{1/3} \left(\frac{n_b m_e}{n_{e0} m_p \gamma_b} \right)^{1/3} \right], \quad (2.21)$$

with m_p the proton rest mass and γ_b the relativistic Lorentz factor of the bunch. The difference between both velocities Δv_{ph} reads accordingly:

$$\Delta v_{ph}(\zeta, z) = \frac{1}{2} v_b \left(\frac{\zeta}{z} \right)^{1/3} \left(\frac{n_b m_e}{n_{e0} m_p \gamma_b} \right)^{1/3}. \quad (2.22)$$

The velocity of the wakefield can however be influenced by setting linear plasma density gradients g (units are %/m). These add a phase velocity of [60]

$$\Delta v_{ph,g}(z) = -\frac{1}{2} v_b \zeta \frac{(g/100)}{(1 + (g/100)z)^{1/2}}. \quad (2.23)$$

As shown by Eq. 2.23, negative gradients, defined as a density that decreases along the plasma, further increase the difference in phase velocities. By contrast, positive gradients, i.e. an increase in density along the plasma, can be used to compensate the difference in phase velocity between the drive bunch(es) and the wakefield. However, this effect also increases along the bunch and the plasma, i.e a compensation of the shift in wakefield phase can only be achieved for one position along the bunch and one z , which is the length of the plasma in this case.

2.5 The Discrete Fourier Transform of a Periodic Signal

The determination of the modulation frequency and the phase reproducibility of the micro-bunches from time-resolved images such as Fig. 5(c) uses a Fourier-based analysis procedure (see Chapter 4.4). The Fourier analysis allows a time-dependent signal to be transformed into a frequency-dependent function that represents the distribution of its frequency components. The continuous Fourier transform of an infinite signal $S(t)$ is obtained by

$$\hat{S}(f) = \frac{1}{\sqrt{2\pi}} \int_{-\infty}^{\infty} S(t) \exp(-i2\pi ft) dt . \quad (2.24)$$

The complex values of $\hat{S}(f)$ carry the information about the amplitude ($= |\hat{S}(f)|$) and phase (angle of the complex number with respect to the real axis $\arctan \text{Im}(\hat{S})/\text{Re}(\hat{S})$) of each frequency component in the spectrum. Its absolute value $|\hat{S}|$ is usually referred to as the power spectrum of the signal. Correspondingly, the inverse Fourier transform is used to compute a signal in the time domain from its power spectrum in the frequency domain. The inverse Fourier transform is defined as

$$S(t) = \frac{1}{\sqrt{2\pi}} \int_{-\infty}^{\infty} \hat{S}(f) \exp(+i2\pi ft) df . \quad (2.25)$$

The $1/\sqrt{2\pi}$ factors in Eq. 2.24 and 2.25 are required for normalization but may be found different in literature.

Data however is usually discrete and of finite length. To obtain the power spectrum of a discrete signal S_k consisting of N values with $k = \{0, \dots, N-1\}$ one uses the discrete Fourier transform (DFT). The transform as a function of frequency with N values \hat{S}_j , $j = 0, \dots, N-1$ is then calculated as

$$\hat{S}_j = \frac{1}{\sqrt{N}} \sum_{k=0}^{N-1} S_k \exp\left(-i2\pi \frac{jk}{N}\right) . \quad (2.26)$$

The inverse DFT is defined as

$$S_n = \frac{1}{\sqrt{N}} \sum_{m=0}^{N-1} \hat{S}_m \exp\left(+i2\pi \frac{jm}{N}\right) . \quad (2.27)$$

Here the normalization factors are $1/\sqrt{N}$. In the case of SC image profiles, S_k is a time-dependent signal of duration τ_s with N pixels on the temporal axis and a time step per pixel of $\Delta t = \tau_s/N$. The corresponding bin width in the frequency domain is $1/\tau_s$. The frequency resolution can in principle be increased by a longer duration

of the signal. In the case of a SC however where a signal of a certain duration is imaged on a sensor with a fixed number of pixels, a longer duration would increase the time step per pixel and thus decrease the temporal resolution. The time per pixel could be on the order of or exceed the duration of a plasma period, i.e. the modulation would then not be resolved anymore. Due to the limited duration, the power spectrum of a finite signal with only one frequency component does not show a δ -function, i.e. a single non-zero entry as expected for a signal of infinite length, but is convoluted with the Fourier transform of the square window function (the signal of finite duration can be regarded as an infinite signal multiplied by a square window function of duration τ_s). The Fourier transform of such a window function is a sinc function.

Zero padding, i.e. artificially increasing the length of the signal by adding an array of zero amplitudes to the original signal, is used to increase the sampling rate, i.e. to decrease the bin width in the power spectrum. This leads to a better resolution of the sinc function. Thereby, zero padding changes only the bin width with which the power spectrum is sampled, i.e. it allows for a more precise localization of a peak in the frequency spectrum, but does not increase the frequency resolution. The effect of zero padding is illustrated in Fig. 7. It shows the power spectrum of a cosine with frequency 120 GHz and a duration of $\tau_s = 73$ ps, the length of a SC window. The red points represents the unpadded case with a frequency bin size of $1/\tau_s = 13.7$ GHz. The frequency bin with highest amplitude is 123.3 GHz. Zero padding with an array

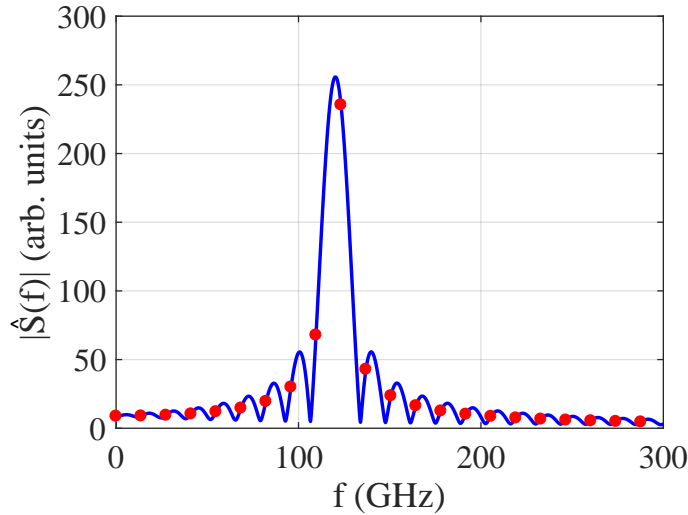


Figure 7: DFT of a sine function with length 73 ps and modulation frequency 120 GHz, once without zero padding (red symbols) and once zero-padded 50 times its length (blue line).

of zero amplitudes 50 times the length of the signal results in the power spectrum shown as a blue line, where $1/\tau_s = 0.3$ GHz. The sinc function is clearly resolved and the determination of the modulation frequency is significantly more accurate with a peak at 120.2 GHz. For the similar effect of zero padding on our data itself, we refer to Chapter 4.4.2.

Chapter 3

AWAKE and Experimental Setups

In this chapter, an overview over AWAKE's working principle, experimental area and its general components is given. We present in detail the components that are essential for the studies of this thesis, which include:

- the CERN accelerator complex and the AWAKE in particular¹.
- the laser system that supplies the pulses for the ionization of the Rb vapor and the laser reference signal (LRS),
- the Rb vapor source and its controls that are used to set the plasma densities and gradients for these studies,
- and the streak camera (SC) itself as the main diagnostic for the studies of the SM.

A separate part describes the diagnostics whose development, setup and operation are part this thesis. These are:

- the Rb vapor density diagnostic. We describe its extension to two independent interferometers and the integration into CERN's data infrastructure which is needed to make the values accessible for the event builder and to display the densities live in a control room for the operation of the experiment.
- the LRS that indicates the time-of-arrival of the ionizing laser pulse on the SC images, the key tool for the phase reproducibility studies.

At the end, we give an outlook of the future measurements of AWAKE Run 2.

3.1 General Description of the AWAKE Experiment

The AWAKE collaboration was founded in 2012. After the formal approval by CERN in 2013, the experiment was built in the former CERN Neutrinos to Gran

¹For additional information, a list of all AWAKE-related publications can be found online at [63].

Sasso (CNGS) facility at the SPS [68]. Its exact location within CERN's accelerator complex is shown in Fig. 8, Fig. 9 illustrates schematically the working principle of the experiment: One proton bunch from the SPS arrives and an intense laser pulse (intensity $\sim 450 \text{ TW/cm}^2$) is merged into its beam path. Both now co-propagating beams enter the 10m-long Rb vapor source. A white light interferometry diagnostic measures the real-time Rb vapor density inside at either end of it (see section 3.4.1). The RIF of the laser pulse forms the plasma by ionizing the Rb vapor. The position of the RIF with respect to the proton bunch is used to control the start point of the SM within the bunch. The part of the proton bunch that propagates in plasma self-modulates and turns into a train of micro-bunches (see Chapter 1.5). Electrons are externally injected from the electron gun into the wakefields that are resonantly driven by the micro-bunches, where they are accelerated. After the plasma, several transition radiation-based beam diagnostics measure the properties of the SM, like its longitudinal spatio-temporal structure or its transverse shape. These diagnostics include the optical transition radiation (OTR)/SC diagnostic used for this thesis, two imaging stations (IS) that display the transverse charge distribution and a coherent transition radiation (CTR) diagnostic. The SC time-resolves the incoming OTR light that has the same temporal profile than the modulated proton bunch on time windows between 73 ps and 50 ns. To indicate the relative position of the RIF with respect to the proton bunch on the images, a bleed-through of the laser pulse is guided to the SC and recorded together with the proton bunch images. This so-called laser reference signal is a key requisite for the analysis in this thesis and is described in detail in section 3.4.3. Downstream of the proton bunch diagnostics, an electron spectrometer measures the final energy and thus the energy gain of the electrons. Regarding the timeline, three years after the approval of the experiment, first protons reached AWAKE in 2016. At the end of that year, the Rb vapor source and proton beam diagnostics were fully assembled and first protons interacted with plasma for SM measurements. From that point on, several experimental beam times until the end of 2018 followed. The first achieved milestone was the first experimental proof of the SM of a long proton bunch in plasma and with this the confirmation that the modulation frequency matches the plasma frequency [51], as expected from theory [24]. These results also show that the start point of the SM within the proton bunch can be controlled. However, no conclusions about the reproducibility of the phase of the wakefields with respect to the RIF were made. Further, the growth of the transverse wakefields were studied [70]. At the end of 2017, the electron beam line was completed and first electrons were injected into the experiment. AWAKE successfully demonstrated the first acceleration of electrons in proton-driven plasma wakefields to up to 2 GeV [52]. With the effect of linear plasma density gradients on the SM being part of this thesis, we note that the highest observed electron energies were achieved by setting a positive linear density gradient on the order of a

3.1 General Description of the AWAKE Experiment

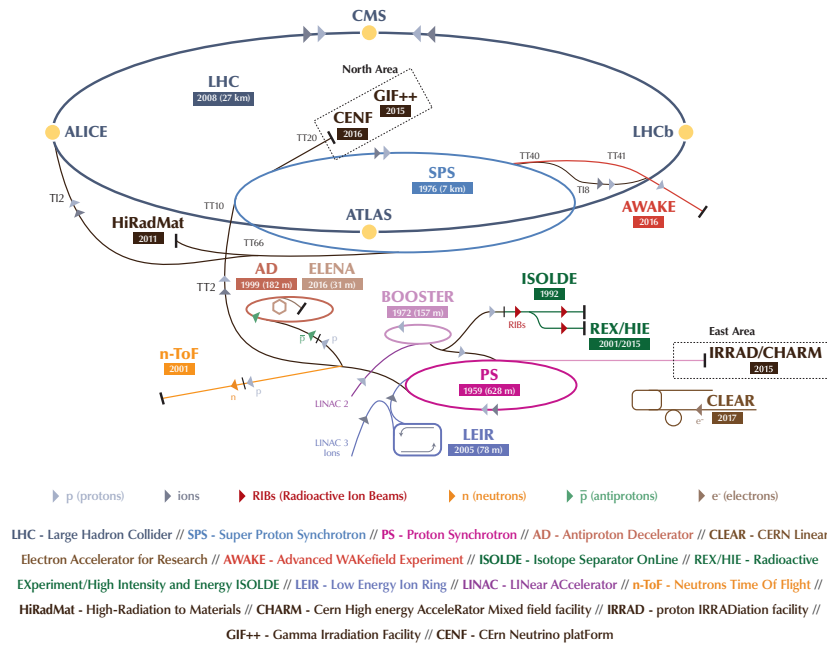


Figure 8: Overview over the CERN acceleration complex and the location of AWAKE. From: [69]

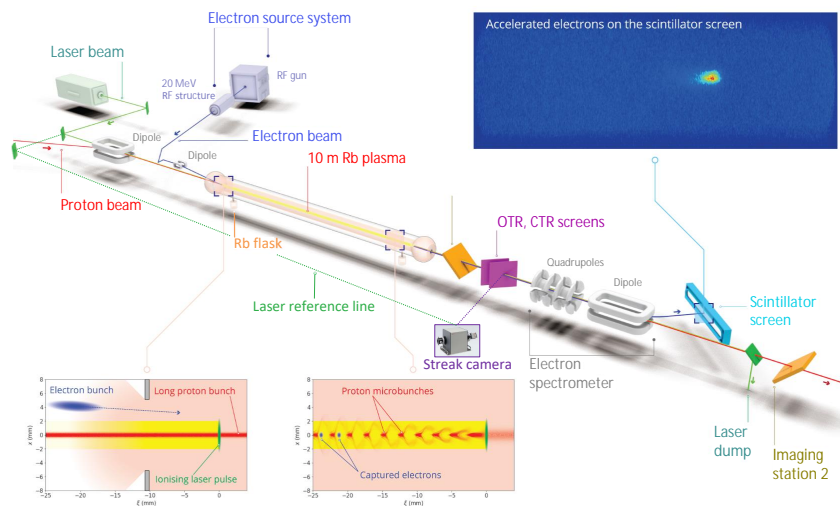


Figure 9: Schematic of the AWAKE experiment. The beams propagate from left to right. From: CERN.

few percent per 10 m along the acceleration path, even though electron acceleration results are not discussed here.

3.2 The Experimental Structure and Location of Components

The experiment is controlled and operated from a control room at the SPS access point 4, called ACC (AWAKE control center). There, a ≈ 800 m-long tunnel connects to the experimental area which is divided into several sectors, each hosting one or more of AWAKE's main components. An overview over the area and the location of these components is shown in Fig. 10. The laser room hosts the ionizing laser system and the beginning of the transfer line for the LRS. An optical transport line (under vacuum) connects the laser room and the electron bunker in sector TCV4. The bunker contains the electron gun and the electron transfer line from the bunker to the main beam line. Sector TT41 includes the main beam line, meaning

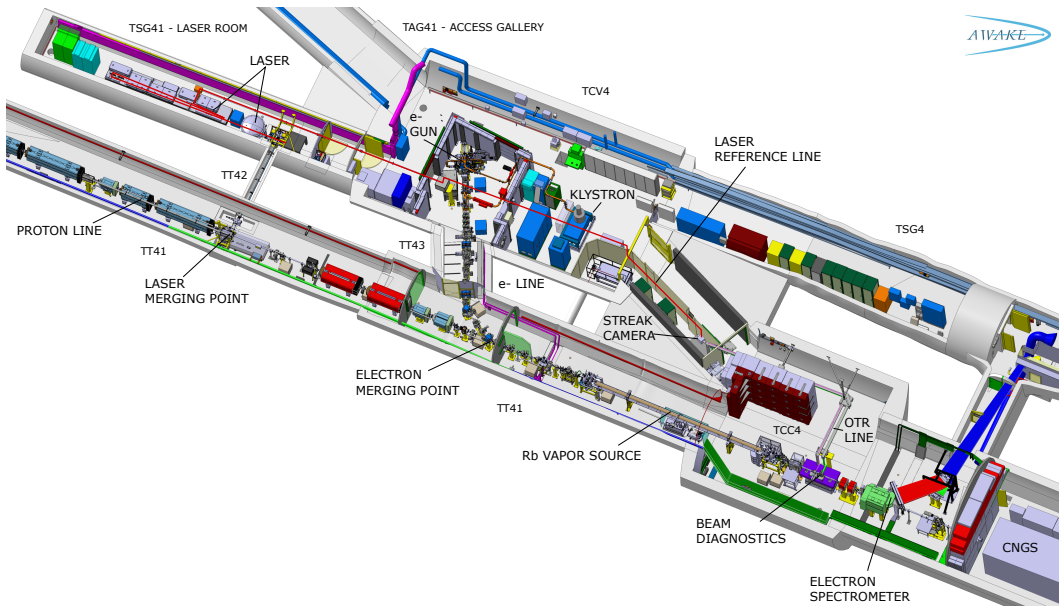


Figure 10: Overview over the AWAKE experimental area, its sections and the locations of its experimental components. From [71].

the proton transfer line from the SPS into which first the ionizing laser pulse and then the electron bunch are merged. The Rb vapor source, the downstream beam diagnostics and the electron spectrometer are located in TCC4. An optical transport line carries the OTR signal from this area to a darkroom hosting the SC. Sector TSG4

is considered a low radiation area, shielded from radiation from the main beam line and the still highly radioactive former CNGS target area. The signal of the electron spectrometer is propagated there, into another, separate darkroom that hosts the camera that records the images of the spectrometer’s scintillator screen. The sector also hosts the electronic racks for the control and operation of the experiment. The CNGS target area is downstream of the experiment and separated by a shielding wall from the AWAKE area and serves as evacuation path only. In the following, we explain these main components in detail.

3.3 The Experimental Components in Detail

3.3.1 The Proton Beam Line

The protons originate from the linear accelerator LINAC2 (energy 50 MeV) and are pre-accelerated by the Proton Synchrotron Booster and Proton Synchrotron (PS) to 25 GeV (see Fig. 8). The next accelerator is the SPS with a circumference of 7 km and a final energy of 450 GeV. Besides AWAKE, it also supplies several experiments like HiRadMat or experiments in CERN’s North Area and serves as the pre-accelerator for the LHC. For AWAKE, it accelerates one proton bunch with up to 3×10^{11} protons to a final energy of 400 GeV per proton [72]. An extraction kicker magnet sends the accelerated bunch via a 800 m long transfer line (TT41 in Fig. 8) to the experimental area. Their time-of-arrival at the experiment shows a 15 ps ($\sim 0.06 \sigma_t$) rms timing jitter. A photo of the transfer line is shown in Fig. 11. The repetition rate is approximately one event per 20 to 40 s and determined by the SPS operational cycle, called super cycle. One super cycles contains a sequence of one or two cycles for each experiment that receives protons from the SPS [73]. The cycles define the cycling of the extraction magnets and have a duration of multiples of the basic period of the PS-SPS complex of 1.2 s. The duration of the AWAKE cycle is 7.2 s [74].

Several diagnostics measure the proton bunch parameters in the SPS and the transfer line. A beam observation system, called BTV (for beam television) at CERN, measures the beam position, size and shape by inserting a scintillator screen into the beam path (see [75] for details). As a non-destructive method, beam position monitors (BPM) determine the position of the bunch in the beam pipe [76]. The emittance is measured in the SPS using the wire scan method. The bunches for AWAKE have on average a normalized emittance of 3.5 mm·mrad, a transverse focused beam size of $\sigma_r = 150 \mu\text{m}$ and 0.03% relative energy spread [77].

The SPS bunch length (σ_z) is 12 cm [77], but can be shortened by $\approx 25\%$ [78] using bunch rotation. We determine the bunch length in our data sets by fitting the proton distribution profile from SC images such as in Fig. 5(a). In the longitudinal

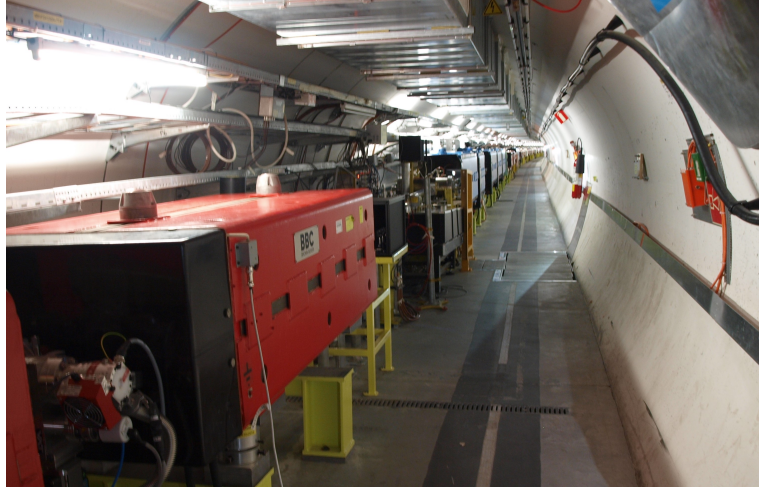


Figure 11: Photo of the proton transfer line from the SPS to AWAKE.

and transverse direction and under the assumption of a Gaussian proton distribution, the lengths $\sigma_{r,z}$ are given by Eqs. 2.7 and 2.8.

3.3.2 The Ionizing Laser System

The laser system serves for the ionization of the Rb vapor and thus the plasma creation, and supplies the light pulses for the LRS (IR) and the electron gun (UV). Further, its master oscillator and divider to which the laser is locked also provide the synchronization trigger signal for the various experimental components including the proton bunch extraction, the electron gun and the SC. To fulfill these various tasks, it consists of several optical beam lines which are illustrated in Fig. 12. The system is a CENTAURUS Titanium Sapphire (Ti:Sa) laser system [79, 80, 81] from Amplitude Technologies, customized to fulfill the AWAKE specifications. At the start of the laser path, a Menlo systems erbium-doped fiber oscillator emits a mode locked pulse train with a repetition rate of 88 MHz. The wavelength of 1560 nm is then frequency-doubled to meet the 780 nm required for the Rb ionization. The output power is increased using a chirped pulse amplification system [32] that includes a stretcher, a regenerative amplifier, a pre-amplifier, a main amplifier, and an in-vacuum compressor. Two Nd:YAG (neodymium-doped yttrium aluminum garnet) lasers pump the Ti:Sa crystals for the energy amplification. A photo of the laser room hosting these components is depicted in Fig. 13. The final pulse energy after compression is ≈ 450 mJ at a pulse duration of 120 fs, resulting in a peak power of around 4 TW. Table 3.1 summarizes the most relevant parameters for the ionizing laser pulses.

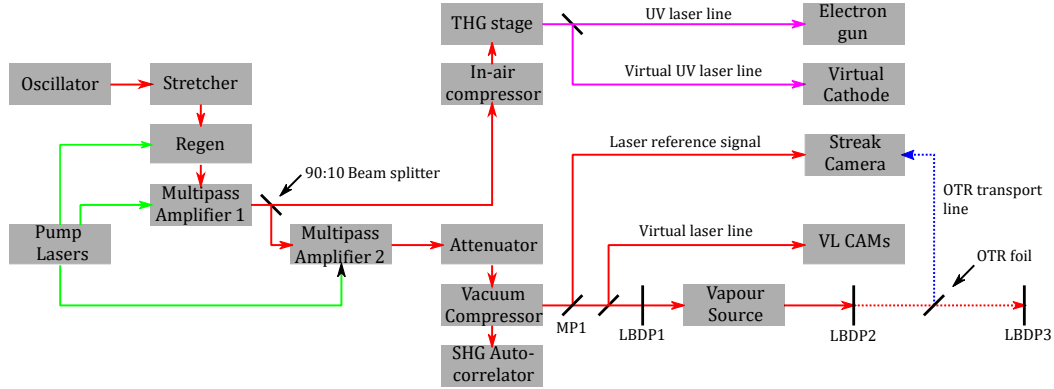


Figure 12: Schematic of the laser system showing its various components and beam lines. From: Mathias Hüther.

Parameter	Value
Central wavelength	Tunable from 780 nm to 785 nm
Bandwidth ($1/e^2$)	24 nm
Pulse duration	120 fs
Max. pulse energy after compression	450 mJ
Repetition rate	10 Hz
Energy stability	1.02%
Beam pointing stability	4.2 μm rad

Table 3.1: Technical parameter list of the ionizing laser pulse system [79, 82, 83].

After the in-vacuum compressor, the laser pulse is sent via the mirror MP1 into the main beam line. The optics focus the beam with an effective focal length of about 40 m to a waist size of 2.5 mm FWHM at the vapor source entrance. The RIF of the laser pulse fully ionizes the Rb atoms in its path, forming a plasma channel with ≈ 2 mm diameter over the entire length of the vapor source. Since Rb is an alkali metal, the energy of the RIF is only sufficient to remove the valence electron of every atom. As a result, the Rb vapor density equals the plasma density (i.e. $\sim 100\%$ ionization). This fact allows in the experiment to measure the Rb vapor density instead of the plasma density (see Chapter 3.4.1). Three laser beam dumps (LBDP1-3 in Fig. 12) protect the valves/diagnostic screens in the main beam line and the vacuum window at the downstream end of the beam line from the high power densities of up to 450 TW/cm². Depending on the type of the ongoing measurement, these laser beam dumps can be inserted into or retracted from the beam path. Using the OTR foil and in low power mode (i.e. not amplified), the laser pulses can also be



Figure 13: Photo from inside the laser room. The vacuum compressor is in the foreground, all other laser components are on the tables further back in the room. From: Ans Pardons, CERN.

sent to the SC to measure its timing with respect to the proton bunch and/or the LRS.

The LRS originates from mirror MP1 where it is formed out of the bleed-through of the ionizing laser pulse. Its optical transfer line from MP1 to the SC is described in Chapter 3.4.3.

To create the 260 nm UV pulses for the electron gun, a beam splitter couples out around 10% of the pulse. This part is then converted into the UV light using third harmonic generation [54]. Details about its optical transfer line labelled 'UV laser line' in Fig. 12 are available in [84].

The alignment of the different beam paths, except the laser reference line, is performed under the use of virtual laser lines and cameras that are placed at equal path lengths to the entrance, center and exit of the vapor source.

3.3.3 The Rb Vapor Source and Plasma Density Parameter Control

Rubidium is used as the plasma material because of its relatively low ionization energy of 4.177 eV, which allows for the plasma creation by field-ionization with an intense laser pulse. Further, the AWAKE baseline densities of $2 \times 10^{14} \text{ cm}^{-3}$ and $7 \times 10^{14} \text{ cm}^{-3}$ can be reached by heating it to comparably low¹ temperatures

¹The PWFA experiment E-164 at SLAC used a lithium heat pipe oven with temperatures up to 800°C [85] to reach similar densities.

of around 200°C. In addition to providing the baseline density values that fit to the proton bunch parameters (see Chapter 1.3), the Rb vapor source [86, 87] also has to provide the experimental conditions for an optimal growth of the SM and for deterministic electron acceleration, which brings strict prerequisites with it and which makes it the central part of the experiment. In order to maintain the desired amplitude of wakefields over the entire distance of 10 m, the source must provide a high vapor density uniformity and stability as the modulation frequency is linked to the plasma electron density. As stated before, the electron plasma density equals the Rb vapor density. From the ideal gas law, one can easily see that the requirement of a homogeneous density distribution translates into a homogeneous temperature distribution (for a constant volume and no flow in the system).

To achieve this homogeneity, the key component of the vapor source is a heat exchanger, consisting of two 10 m-long concentric tubes. Figure 14 shows a schematic and a photo of the vapor source where the heat exchanger is marked by #5. The inner tube has a diameter of 40 mm and contains the Rb vapor during the measurements, the outer one has a diameter of 75 mm. Between the inner and the outer tube, an inert heat transfer fluid (Galden HT270) circulates. The resulting temperature and thus density uniformity is $< 0.2\%$ [87]. According to [88], after a readout calibration, the temperature uniformity was measured to be 0.02%. On either side, an independently electrically heated reservoir (#3 in Fig. 14) contains Rb, which is solid at room temperature with its melting point at 39°C. The Rb evaporates and fills the vapor source until the saturation pressure is reached [86]. A valve on top of the reservoirs to open and close the flow path to the heat exchanger allows to remotely enabling or stopping the Rb vapor flow to the tube. To make a sharp transition between the vapor and vacuum while still providing a way for the different beams to pass through, each end is closed by an iris with 1 cm diameter that limits the Rb flow out of the vapor source, followed by an expansion chamber (#2 in Fig. 14). These expansion chambers have a large volume and are cooled to $\sim 10^\circ\text{C}$, which causes the Rb to condensate on its walls and form a density ramp with a length shorter than 10 cm [86]. A long density ramp would defocus the externally injected electrons and thus impede any acceleration experiment. Both ends of the vapor source are also equipped with viewports for optical diagnostics (#4 in Fig. 14). These viewports are used for the Rb vapor density measurement (see Chapter 3.4.1) and other plasma diagnostics, e.g. Schlieren imaging [89].

Plasma Density Parameter Control

The system is constantly monitored and fully remote-controlled by a CERN-provided programmable logic controller (PLC) with the Siemens SCADA software SIMATIC WinCC Open Architecture. For the operation of the system, 79 temperature probes control 15 heater sections [88]. To avoid Rb condensation inside the heat exchanger,

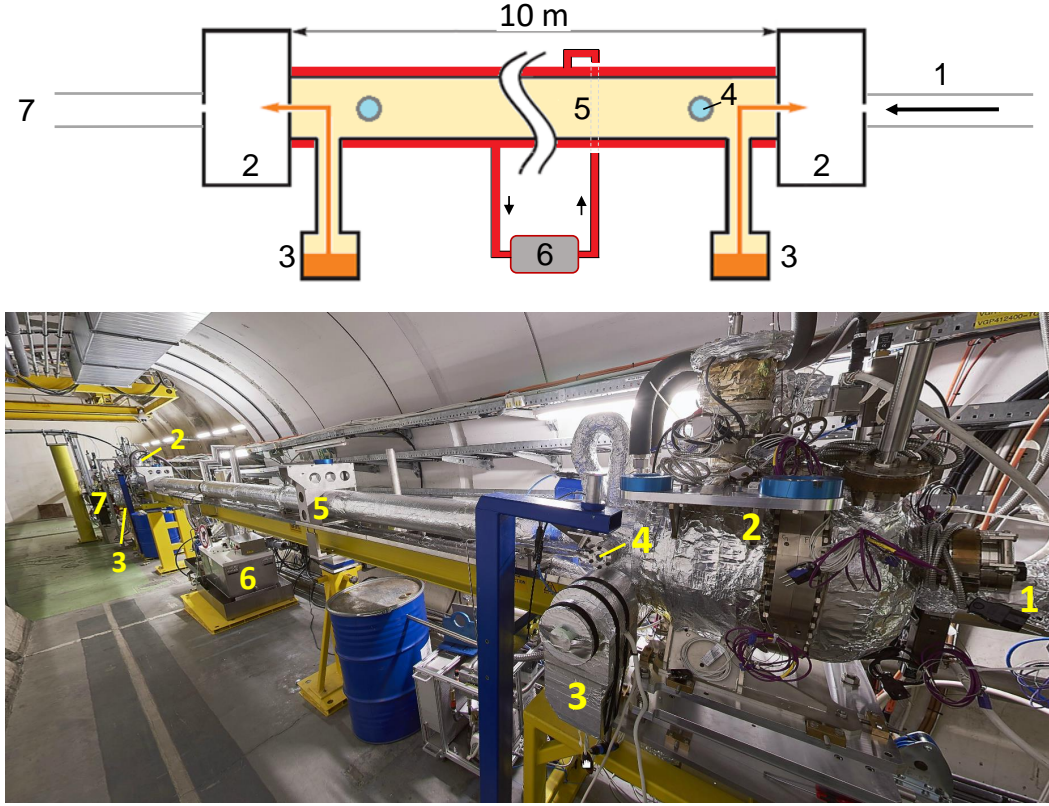


Figure 14: Schematic (top, not to scale) and photo (bottom, from: Maximilien Brice, CERN) of the Rb vapor source. 1) Main beam line for proton, laser and electron beam 2) Expansion chamber 3) Rb reservoir 4) Diagnostic window for the vapor density measurement 5) 10 m heat exchanger 6) Heating and pumping section 7) SM diagnostics.

we set its temperature to be always $\approx 15^\circ\text{C}$ above the temperature of the reservoirs. The relation between the Rb vapor temperature T and the Rb vapor density n_{Rb} is given by the ideal gas law and the vapor pressure curve of Rb [59]:

$$n_{Rb}(T) = \frac{1}{k_b T} \cdot 10^{(5.006 + A + B \cdot T^{-1} + C \cdot \log_{10}(T) + D \cdot T^{-3})}, \quad (3.1)$$

where A , B , C , D are Rb-specific constants [90]. In the experiment, n_{Rb} and thus the plasma electron density n_{e0} can be varied in the range of $0.5 \times 10^{14} \text{ cm}^{-3}$ to $1.1 \times 10^{15} \text{ cm}^{-3}$, corresponding to a temperature of 154°C to 215°C . Temperatures below 154°C cannot be reached because of the waste heat coming from the pump that circulates the heat transfer fluid, temperatures above 230°C must not be exceeded in

the heat exchanger to always stay 40°C below its boiling temperature. The AWAKE baseline parameter is having a constant density, i.e. a flat density profile inside the source. However, by setting different temperatures in the reservoirs, a linear density gradient on the percent level along the source and thus along the propagation axis of the particle bunches can be set [86]. Gradients of up to $\pm 2\%/m$ were tested in the experiments¹. In Chapter 7, we study the effect of a linear plasma gradient on the SM, Appendix A.2.4 shows the relation between the set temperature and the resulting density. Instructions on the valve handling and how to fill the source with Rb are summarized for future operators of the Rb vapor source in [91].

3.3.4 The SC/OTR Diagnostic

The SC [82, 92, 93] is the main diagnostic for the observation of the tempo-spatial structure of self-modulated proton bunches and thus also for the SM studies of this work. It uses transition radiation that is created when charged particles pass through matter in their beam path [94]. In our case, the self-modulated proton bunch passes through an aluminium-coated silicon wafer of 150 μm thickness. The thickness of its aluminium coating is 1 μm . When the protons enters the interface of the two media (vacuum and aluminum), the difference in the dielectric constant causes prompt emission of transition radiation in forward and backward direction. The part of the emitted radiation in the visible light spectrum, the optical transition radiation, shows the same spatio-temporal intensity modulation/profile than the proton bunch distribution and is therefore used in this diagnostic. Since the plasma electron frequency of the aluminium layer $\omega_{pe,Al}$ is higher than the optical light frequencies ($\sim 10^{16}$ Hz vs. $\sim 10^{15}$ Hz), the OTR emission is only backwards. The OTR is incoherent because the (micro-)bunch length is on the mm scale and thus much longer than the optical wavelengths. The opening angle of the emitted OTR scales as $\theta \sim 1/\gamma$ with γ the Lorentz factor of the protons. The total intensity of the transition radiation is directly proportional to γ [95] and follows:

$$I = \frac{N_b^2 e^2 \gamma \omega_{pe,Al}}{3c} . \quad (3.2)$$

Figure 15 illustrates the setup of the diagnostic by showing its location on the beam diagnostic table of the experiment (Fig. 10) and relative to the vapor source. The location of the silicon wafer, the so-called OTR foil, 3.5 m downstream of the vapor source is indicated by #6. The transport of the back-reflected OTR light from the foil to the SC is realized via a 15-m-long optical transfer line (#7 in Fig. 15, labelled OTR line in Fig. 10). The SC is placed in a dark room and thus protected from light and stray radiation from the main beam line [80]. Before the OTR reaches

¹I.e. 20% change over the entire length of the source.

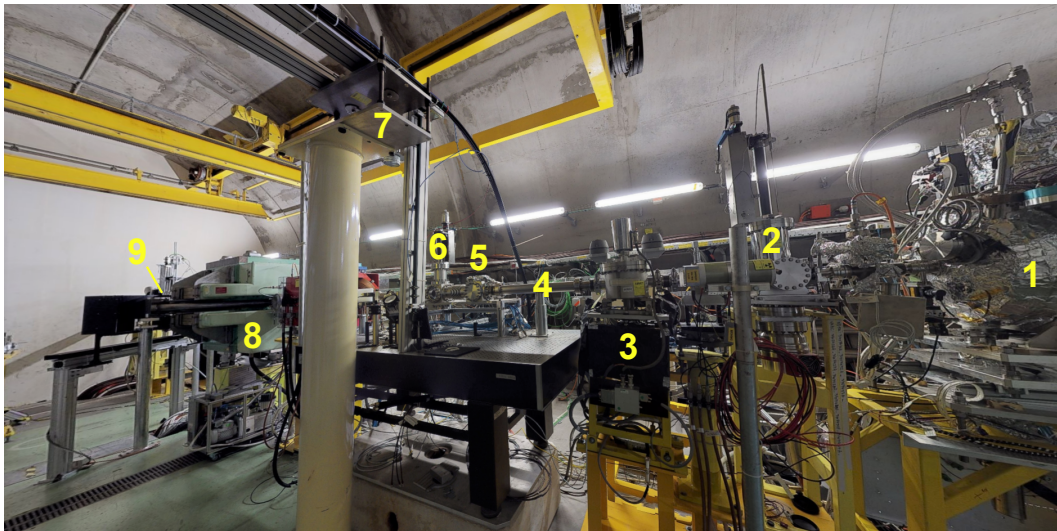


Figure 15: Photo of the beam diagnostics downstream of the vapor source 1) Expansion chamber 2) Laser beam dump LDBP2 3) Imaging Station 1 4) Main beam pipe 5) CTR foil 6) OTR foil 7) OTR transport line, laser and electron beams 8) Electron spectrometer 9) Imaging Station 2. From: [96].

the camera, different bandpass filters of several tens of nm thickness can be used to limit the spectral width of the incoming OTR and thus to improve the temporal resolution of the diagnostic. The SC model is C10910-05 from Hamamatsu Photonics, combined with a readout CCD camera [93]. Input optics image the SC slit on a photo-cathode that converts the photons into electrons, again with equal temporal intensity distribution and proportional to the incoming intensity. The electrons are accelerated by a mesh and propagate through a streak tube. Inside this tube, a time-dependent, high-voltage pulse sweeps the electrons transversely, which results in a time-dependent deflection of the axis. This rotates the train of electrons by 90° relative to the propagation axis. The temporal modulation of the incoming signal becomes a spatial modulation. After the streak tube, a micro-channel plate (mcp) multiplies the electrons in order to increase the signal strength before they hit a phosphor screen that turns them back into light. This light is recorded with an ORCA-Flash4.0 readout CCD camera. Binning the 2048×2048 pixel image in 2×2 and selecting a region-of-interest results in 512 pixels in the temporal direction and 672 pixels in the spatial direction for the final image to analyze [97]. Here we note that the SC images show the bunch charge density and not its charge because the entrance slit is narrower than the bunch radius at the screen location [98]. To set the time resolution and length of the signal under investigation, several time windows between 73 ps and 50 ns can be selected. For the window with the highest time

resolution (73 ps), one pixel corresponds to ~ 0.14 ps (see Chapter 4.1 for details) and the bin width in the frequency domain is 13.7 GHz. For this window, the temporal resolution was measured to 1.5 ps by sending an ultra-short pulse on the SC [99]. We note here that this is the time resolution obtained with the relatively high signal level we use in the experiment, The ultimate time resolution of the instrument is below 1 ps. The plasma density range used in AWAKE corresponds to a frequency range of 60 GHz to 300 GHz, i.e. periods of 16.7 ps to 3.3 ps. In the spatial direction, one pixel corresponds to 21.7 μm . During data taking, typical values were slit widths of 10 to 50 μm , a MCP gain of 40 to 50 and an exposure time of ~ 20 ms.

3.3.5 Other SM Diagnostics

In addition to the SC, AWAKE uses two additional transition radiation diagnostics for its studies of the SM. These are a Coherent Transition Radiation diagnostic and a system of two imaging stations which are described hereafter.

3.3.5.1 The CTR Diagnostic

The transition radiation of particles in a bunch add to each other coherently when the wavelength of the radiation is longer than the dimensions of the observed bunch. This CTR has its maximum spectral intensity at (and centered around) the modulation frequency of the incoming bunch and its harmonics [77, 100]. However, frequencies on the order of 100 GHz cannot be measured directly, for which a waveguide-based, heterodyne detector was developed as the CTR diagnostic [80, 82, 100]. It creates the CTR using a separate aluminium-coated screen in the beam line (see #5 in Fig. 15). A rectangular waveguide transports the CTR signal carrying the information about the modulation frequency to the mentioned waveguide-based heterodyne detectors. The diagnostic is based on heterodyne mixing [101, 102]. This technique brings the frequency of the signal f_{CTR} to a frequency range (< 25 GHz) that is accessible to measurements by coupling it with a RF reference signal of known frequency f_{ref} . The resulting intermediate beat frequency is $f_{IF} = |f_{CTR} - f_{ref}|$. This means that f_{ref} must be chosen such that the difference between f_{ref} and the expected modulation frequency¹ is in the mentioned measurable range. In the case of AWAKE, this frequency is measured with Schottky diodes and a fast oscilloscope. For more details, we refer to [100].

3.3.5.2 Imaging Stations

The OTR and CTR diagnostics aim to time-resolve the longitudinal charge distribution of the self-modulated proton bunch. As third diagnostic, two so-called imaging

¹With 100% ionization of the Rb vapor, the expected frequency is the plasma electron frequency given by Eq. 1.2.

stations [62] (Fig. 15, #3 and #9) were installed 2 m and 10 m downstream from the vapor source end to measure the transverse, time-integrated charge distribution. The protons traverse a scintillating Chromox¹ screen that emits light with the light yield being dependent on the energy deposited in the scintillating material. Since the emitted light intensity from the bunch core and the defocused protons differs by several orders of magnitude, the light is split and sent to two cameras in order to record both at the same time. One camera records the intense light created by the bunch core and one only the light from the defocused protons. To do so, the later one has a mask in front of it to block the light from the bunch core. For more details regarding the setup, see [62].

The main focus when using the diagnostic is thereby on the defocused protons. Experimental studies monitor the extent of transverse deflection from the axis (meaning the radius of the defocused charge distribution), the amount/fraction of defocused charge, its symmetry and, in case of asymmetries, the direction of the asymmetrically defocused charge distribution (e.g. in [54]).

3.3.6 The Electron Line

The electron source consists of a S-band RF photo injector with a caesium telluride (Cs₂Te) cathode and a booster structure [49, 77, 103, 104]. A klystron supplies the RF power for the gun and booster. Their location within the experiment is shown in Fig. 10. The electrons are created at the cathode and synchronized to the laser and proton beam by a UV pulse ($\lambda = 260$ nm) that is produced by third-harmonic generation [54] inside the ionizing laser pulse system and that propagates over the same distance as the ionizing laser pulses. The transport of the UV pulses from the laser room to the electron gun happens via the vacuum optical transfer line described in [84], and that is also used for the LRS (Chapter 3.4.3). The electron bunch typically has a duration of 4 ps (σ_t), a charge of 100 pC to 1 nC, a normalized emittance of 2 mm·mrad (rms) [49] and a final energy measured to 18.8 MeV [52]. An electron transport line carries the electron bunch to the main beam line where it merges with the proton bunch. In order to allow for different injection schemes (on-axis/off-axis [105, 106]), several quadrupole and steering magnets upstream of the vapor source are used to set the focal point and crossing angle between the electron and proton beam.

3.3.7 The Electron Spectrometer

A C-shaped horizontal dipole magnet with a quadrupole doublet in front forms the electron spectrometer [107]. Its position is 4.6 m downstream from the vapor source end (see Fig. 10 and #8 in Fig. 15). Inside the dipole magnet, a triangular vacuum

¹Al₂O₃:Cr₂O₃

chamber gives space to separate the electrons from the protons and disperse them in energy. Depending on their energy, they hit a scintillating screen on a different horizontal position. The measurable energy ranges up to 10 GeV. Details about the energy-horizontal position correlation or the spectrometer calibration can be found in [108].

3.4 Development of Experimental Diagnostics

Here, we describe the two diagnostics which were developed to facilitate the SM measurements of this thesis: the fully automated Rb vapor density measurement and the LRS for the relative and absolute measurement of timings on SC images.

3.4.1 The Rb Vapor Density Diagnostic

As mentioned before, the neutral Rb vapor density matches the plasma density because every Rb atom is only singly ionized. In the experiment, we therefore measure this vapor density instead of the plasma density using white light interferometry. To be able to measure a potential linear density gradient along the vapor source, we measure the density at either end of the source. The basic concept and development work of the diagnostic is described in detail in [59]. However, the diagnostic existed only as a prototype and the system was not integrated in AWAKE's/CERN's data acquisition system, nor was any density measured under the real experimental conditions. Therefore, the final implementation of the diagnostic with two interferometers into the experiment and the data acquisition system, the live display of these parameters in the ACC as well as the verification of the performance of the vapor source, are part of this thesis.

First, to obtain the two independent, but identically optical fiber-based Mach-Zehnder interferometers for the upstream and downstream end of the vapor source, we adapted the setup of [59] as depicted in Fig. 16 in the following way:

A supercontinuum white light laser (NKT SuperK COMPACT) supplies the intense and coherent broadband light for both interferometers. The light is coupled into a single mode optical fiber and split (into two) by a fiber-based 50:50 beam splitter. As the laser is located in the radiation-safe section of the experiment¹, two ≈ 120 m-long optical single mode fibers guide the light from this area to either end of the vapor source, where another 50:50 fiber splitter divides the light again to form the arms of the interferometers. In each interferometer arm, a fiber collimator couples the light out of the fiber and forms a parallel light beam. One of those beams passes through the Rb vapor and forms the so-called Rb arm. The other beam passes through air over the same distance, forming the reference arm. Sending the light through the Rb

¹TSG4, see Fig.10.

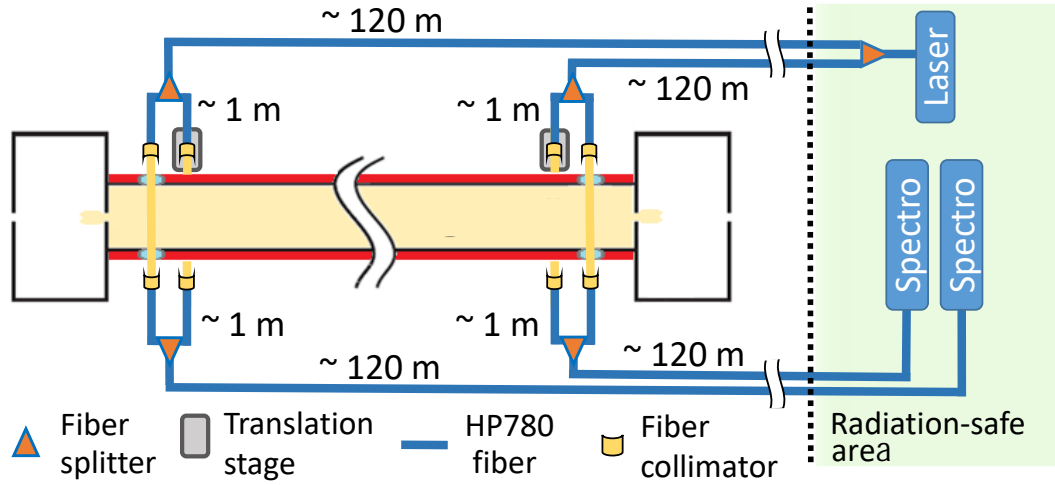


Figure 16: Schematic of the Rb vapor density measurement consisting of two independent white light interferometers.

vapor happens via two diagnostic viewports¹ made of sapphire glass at either end of the source. Figure 17 shows a photo of the downstream end of the vapor source with the diagnostic viewport (see also Inset 1) and the support structure for the optics. Inset 2 (same figure) shows the fiber coupler and the optical fiber in front of the diagnostic viewport. Identical fiber couplers at the other side of the vapor source re-couple the light into the fibers. To adjust the path length difference between both arms, one of the couplers in each interferometer is mounted on a linear translation stage. Then, a fiber splitter re-combines and thus interferes the light beams. Another pair of long optical fibers transports the light back to the radiation-safe area to two fiber spectrographs. These disperse the incoming light in wavelength and are set to simultaneously record spectrograms every 10 s (note that this value can be freely chosen but the density in the vapor source is assumed to be constant, meaning not changing on short, minute-like time scales, and protons arrive only every ~ 30 s; this value is therefore sufficient).

Examples for the resulting interference pattern for the cases of no Rb present in the source and with Rb ($n_{Rb} = 2.08 \times 10^{14} \text{ cm}^{-3}$) are shown in Fig. 18. While in the case of no Rb the observed intensity oscillation is at (almost) constant frequency, with Rb present in the source the frequency increases the closer the wavelength comes to the transition wavelength. This density-dependent change in the interference pattern can be explained by the fact that Rb has two optical transitions², at $\lambda_1 = 795 \text{ nm}$ (D1

¹The same viewports are used for other plasma-related measurements e.g. of the plasma light and plasma radius.

²Optical transition in the visible light spectrum is a characteristic of alkali metals.

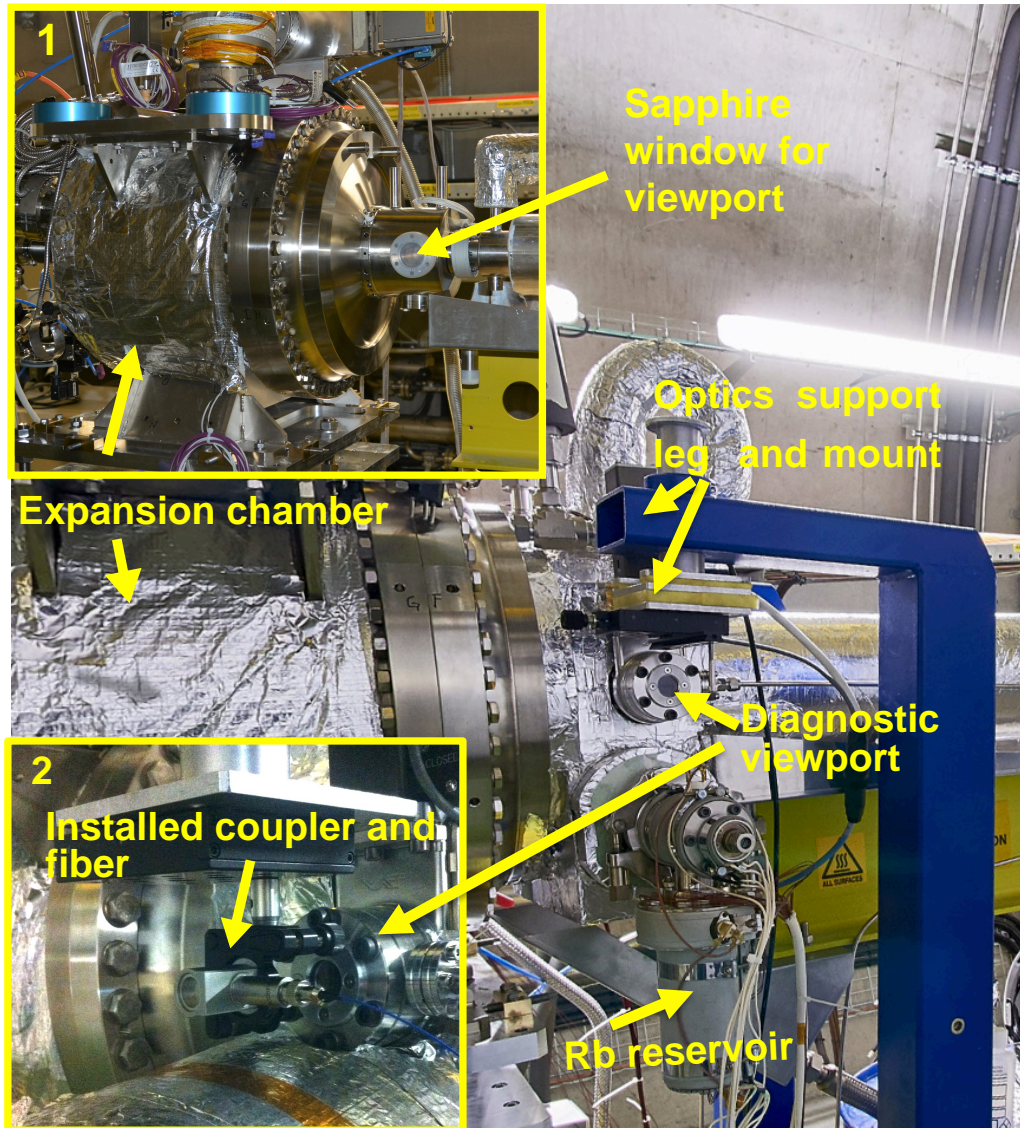


Figure 17: Photos showing the installations and the viewport for the Rb vapor density measurement at the downstream end of the vapor source. Inset 1: Photo of the downstream expansion chamber without insulation and without the Rb reservoirs mounted. Inset 2: The fiber coupler that forms the parallel light beam that traverses the Rb vapor is mounted in front of the diagnostic viewport. The optical fiber itself is also visible. Credits: modified drawing of Erdem Öz.

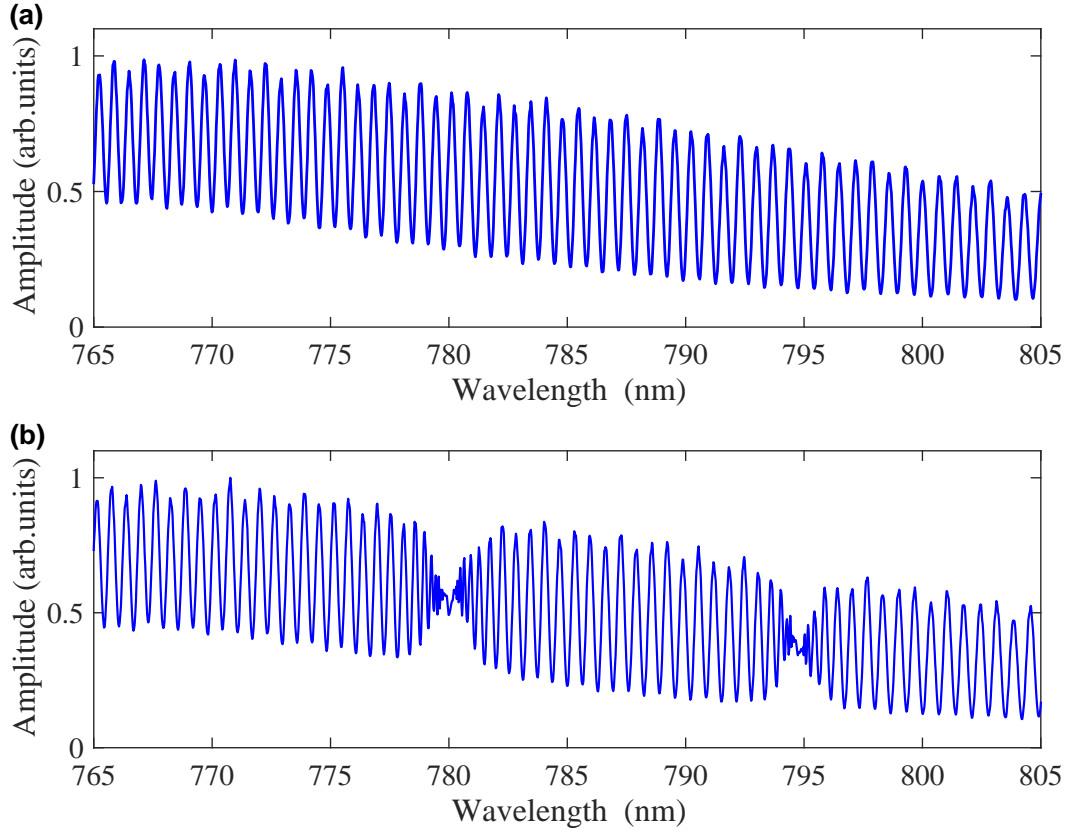


Figure 18: Exemplary interferograms of the Rb vapor density diagnostic with (a) no Rb in the vapor source and (b) $n_{Rb} = 2.08 \times 10^{14} \text{ cm}^{-3}$ showing the effect of the Rb vapor. The D1 line is at 795 nm, the D2 line at 780 nm.

line) and $\lambda_2 = 780 \text{ nm}$ (D2 line). When broadband light that covers these transitions traverses Rb vapor, the index of refraction for wavelengths close to these transitions changes due to optical dispersion. The strength of this effect increases with increasing n_{Rb} and with decreasing difference between the wavelengths of the light and the transition. The increase in index of refraction elongates or shortens the optical path length in the Rb arm, which changes the phase relation between the light in both arms. As a result, the interference pattern changes as seen in Fig. 18. The spectral intensity distribution $I_{tot}(\lambda)$ as observed with the spectrometers is given by

$$I_{tot}(\lambda) = I_1(\lambda) + I_2(\lambda) + 2\sqrt{I_1(\lambda)I_2(\lambda)} \cdot \cos(\Delta\phi(\lambda)) , \quad (3.3)$$

with $I_{1,2}$ the light intensities in each interferometer arm and $\Delta\phi$ the density-dependent, phase difference between them.

We calculate the vapor density value from this change in the interference pattern, i.e. $\Delta\phi$, in a fully automated way. An automatized Matlab script processes the spectrograms, calculates the plasma parameters (meaning the Rb vapor density and the resulting density gradient along the source) and publishes them by using the JAPC framework at CERN [109, 110]. The script sends the two spectrometer images (once available) to a server that runs a separate algorithm for the density calculation. The individual steps of the underlying fitting algorithm are explained in detail in Chapter 3.4.2. The final output consists of four variables: the timestamp of the spectrograms, the density values of the upstream and downstream measurements and the value for the density gradient. These values are then forwarded to a virtual variable reader [111] that is accessibly for CERN's data infrastructure such as the event builder of AWAKE or CERN's fixed display¹. The first ensures that for each event the data of all experimental diagnostics can be correlated to the plasma parameters existing around the moment the data was recorded, the later one is essential for the operation of AWAKE. As depicted in Fig. 19, one of the three fixed displays of AWAKE [112] in the ACC shows live (among other things) the state of the valves at the Rb reservoir, the temperature of the Rb, and the calculated Rb vapor density and gradient. For future users, we explain the actions required to operate the density diagnostic from the ACC step-by-step in [113].

3.4.2 Calculation of the Rb Vapor Density

In this paragraph we detail the fitting algorithm that computes the Rb vapor density values by the fully automated, interferometry-based diagnostic described in 3.4.1.

3.4.2.1 Fitting Algorithm

The Rb vapor density is calculated from a change in the interference pattern $I_{tot}(\lambda)$ (Eq. 3.3), meaning from the observed shift in phase $\Delta\phi(\lambda)$ each wavelength of the light in the interferometer experiences with $n_{Rb} \neq 0$ when compared to $n_{Rb} = 0$. To mathematically describe this effect of n_{Rb} on the periodicity of the interference pattern around the Rb transition lines and to calculate n_{Rb} , we use a Fourier-based fitting algorithm. We therefore change from the wavelength to the frequency domain, i.e. in Eq. 3.3 from wavelength to angular frequency ω :² $I_{tot}(\omega) = I_1(\omega) + I_2(\omega) + 2\sqrt{I_1(\omega)I_2(\omega)} \cdot \cos(\Delta\phi(\omega))$. The phase difference $\Delta\phi$ between the two interferometer

¹A screen in the control room permanently showing a selection of parameters that are essential for the operation of an experiment.

²The angular frequencies corresponding to $\lambda_{1,2}$ are $\omega_1/2\pi = 377$ THz and $\omega_2/2\pi = 384$ THz.

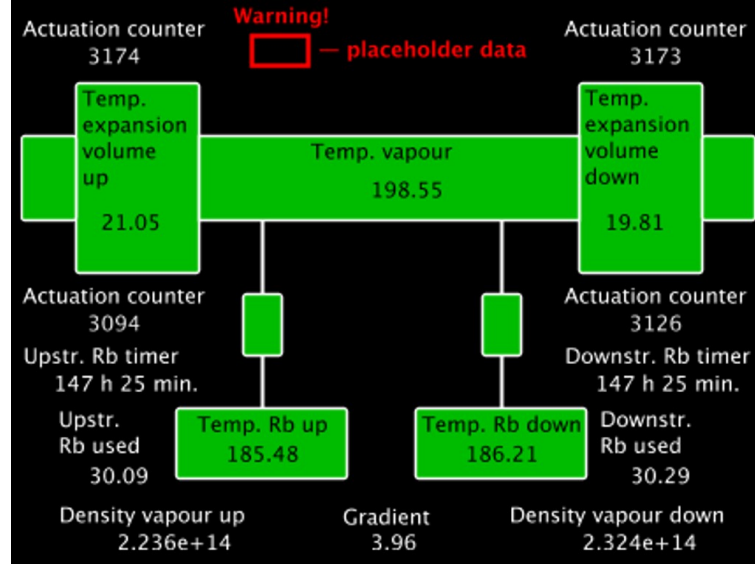


Figure 19: Experimental plasma and vapor source parameters as shown by the fixed display in the ACC at 22:23:00 on Dec 17, 2017. The density value is given in units of cm^{-3} , the gradient in $\%/10\text{m}$. From: [112].

arms that is important for the density determination is given by

$$\Delta\phi(\omega) = k\eta(\omega) \cdot (l_{F1} - l_{F2}) + k \cdot (l_1 - l_2) + kL(\eta_{Rb}(\omega) - 1) + (\phi_{01}(\omega) - \phi_{02}(\omega)) . \quad (3.4)$$

Herein, $\eta(\omega)$ denotes the index of refraction of the optical fiber, η_{Rb} the index of refraction of the Rb vapor and L the length of the Rb vapor column through which the light travels. For each interferometer arm, $l_{F1,2}$ represents the lengths over which light propagates inside the optical fiber, $l_{1,2}$ the path lengths in free space (outside any fiber) and $\phi_{01,2}$ the phase of the light. In order to split this term into a density-dependent and density-independent term, we Taylor-expand the term $\eta_{Rb}(\omega)$ around a center frequency ω_0 and obtain:

$$\Delta\phi(\omega) = \left[\frac{1}{2}\alpha\Delta\omega^2 + \beta\Delta\omega + \Delta l + \Delta\phi_0 \right] + \left[\frac{\omega}{c}L(\eta_{Rb}(\omega) - 1) \right] := [\text{I}] + [\text{II}] . \quad (3.5)$$

The constants α and β contain the frequency-independent contributions, Δl represents the path length difference $l_1 - l_2$ and $\Delta\phi_0 = \phi_{01} - \phi_{02}$. The first term in the equation, named [I], is independent of n_{Rb} , while [II] depends on n_{Rb} through the index of refraction of the Rb vapor. This index of refraction as a function of n_{Rb} , as shown

in [59], is calculated from the electric susceptibility χ_e as $\eta_{Rb} = \sqrt{1 + \chi_e}$. It can be written as

$$\eta_{Rb} = \sqrt{1 + \frac{e^2 n_{Rb}}{\epsilon_0 m_e} \sum_{i=1,2} \frac{f_i}{(\omega_i^2 - \omega^2)^2 - i\gamma_i^2 \omega^2}}, \quad (3.6)$$

with $\gamma_{1,2}$ the natural lifetime and $f_{1,2}$ the oscillator strength of the transition. By binomial expansion of the square root term for η_{Rb} , one sees that the effect on the interference pattern and thus on the phase shift is not proportional to the Rb vapor density but to the density-length product $n_{Rb}L$. However, we consider L as constant. A possible change in L caused by thermal expansion of the steal pipe can be considered a negligible contribution to the accuracy of measurement since its heat expansion factor is small ($\sim 10^{-5}$ m/(m K)), resulting in a systematic error on the order of $\sim 10^{-3}$. A thermal elongation of the vapor column would also effect both up- and downstream measurements equally, thus not having an impact on the gradient measurement. To reduce a possible systematic error on the density values, we measured the length of both vapor columns beforehand using a micrometer with 0.02% accuracy. To increase the accuracy of the density calculation, we take into account a potential Doppler broadening by computing the convolution of the expression for χ_e with a constant Doppler term equivalent to a line broadening at $T = 200^\circ\text{C}$. We also exclude a range of 1.5 THz width around the transitions from the calculation because Eq. 3.6 has two poles at $\omega = \omega_i$ and the spectrographs cannot resolve the high-frequency oscillations in the immediate vicinity of the optical transitions, as seen in Fig. 18 (b).

To determine n_{Rb} with Eqs. 3.3, 3.5 and 3.6, the general idea is to calculate term [I] from an interferogram that is recorded with $n_{Rb} = 0$ and thus [II] = 0, but otherwise under equal conditions (i.e. Δl and $\Delta\phi_0$ in term [I] remain unchanged). Because of these equal conditions, the density can then be determined from the observed shift in phase $\Delta\phi(\omega)$ which corresponds to the now non-zero term [II]. Before this calculation, we remove noise and the offset $I_1(\omega) + I_2(\omega)$ from the interference pattern and normalize them by applying a Fourier-based signal conditioning. The density calculation should be independent of the overall signal strength and the spectral light distribution in both interferometer arms. Furthermore, this step also allows for the determination of the envelope function of the interferograms which are required for the later density calculation.

As first step of the signal-conditioning, we calculate the fast Fourier transform (FFT) of both interferograms (with and without Rb). In Fig. 20, the absolute values, i.e. the power spectra of the FFTs, are shown for the cases of $n_{Rb} = 0$ and $n_{Rb} = 2.08 \times 10^{14} \text{ cm}^{-3}$ (see Fig. 18) in blue and red, respectively. Both spectra show a similar behavior at small oscillation times $\tau < 2$ ps. This part of each spectrum contains the information about high-frequency noise and the offset of the oscillation. By setting this part to zero, one removes both unwanted contributions from the

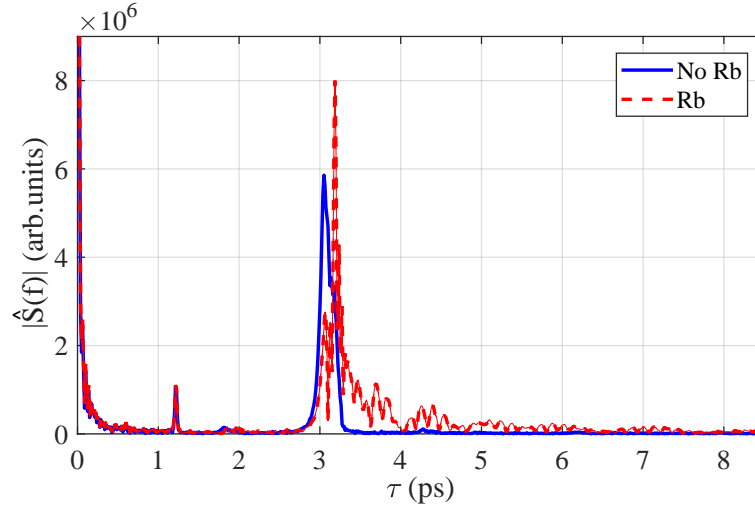


Figure 20: Power spectra (i.e. absolute value of the Fourier transform) of the interferograms in Fig. 18 for the cases of $n_{Rb} = 0$ (blue line) and $n_{Rb} = 2.08 \times 10^{14} \text{ cm}^{-3}$ (red-dotted line).

signal. Calculating the inverse Fourier transform of the remaining power spectrum centers the oscillation around the zero axis. For completeness, we mention that one obtains the offset ($I_1(\omega) + I_2(\omega)$) itself by calculating the inverse Fourier transform of the part that is set to zero, however it is not required for the density calculation. Before any further steps, we also zero the parts of the spectrum with large oscillation times ($\tau > \tau_{peak} + 10 \text{ ps}$) because they have no meaning that is significant for the density calculation but could disturb the analysis. In the remaining power spectra ($2 \text{ ps} < \tau < \tau_{peak} + 10 \text{ ps}$), distinct peaks are visible at oscillation times $\tau_{peak} \sim 3 \text{ ps}$. This part represents the intensity oscillations itself and contains the information about their envelope function. In the case of $n_{Rb} = 0$ (blue line), the peak represents the oscillation with (almost) constant period (see Fig. 18(a)) whose frequency is only defined by the path length difference Δl . By comparison, in the case of $n_{Rb} > 0$ (red-dotted line) the peak appears broader with several additional smaller peaks at oscillation times $3 < \tau < 7 \text{ ps}$ that originate from the change in oscillation frequency and from the envelope function changing around the transitions (see Fig. 18 (b)). The envelope function is obtained by shifting the peak to zero and calculate the absolute value of its inverse Fourier transform.

The same inverse Fourier transform is also used for the density calculation itself. By calculating its angle/phase with respect to a frequency ω_0 for both density cases, we obtain $\Delta\phi(\omega)|_{n_{Rb}=0} = [\text{I}]$ and $\Delta\phi(\omega)|_{n_{Rb}\neq 0}$, respectively. Since the phase at ω_0 has to be independent of the density and ω_0 must not be close to the transition

ω_1 or ω_2 , we set ω_0 to 390 THz, corresponding to 770 nm. Figure 21 shows $\Delta\phi(\omega)$ for the interferograms in Fig. 18, again for $n_{Rb} = 0$ in blue and $n_{Rb} = 2.08 \times 10^{14} \text{ cm}^{-3}$ in red. One clearly sees the shift in phase caused by the Rb vapor around the optical transition frequencies which are marked by the dashed black lines. The

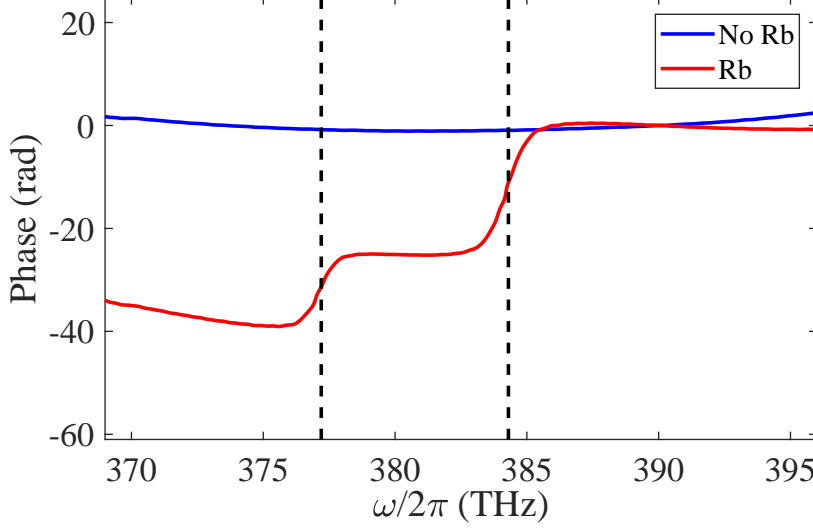


Figure 21: Measured phase difference $\Delta\phi(\omega)$ relative to $\phi(\omega_0)$ with $\Omega_0 = 390$ THz in case of no Rb vapor (blue line) and in case of Rb vapor present ($n_{Rb} = 2.08 \times 10^{14} \text{ cm}^{-3}$) (red line). The dashed lines represent the transition frequencies of the Rb atom.

offset between both lines corresponds to the density-dependent term [II] (see Eq. 3.5) $\Delta\phi(\omega)|_{n_{Rb} \neq 0}$ that is obtained from $\Delta\phi(\omega)|_{n_{Rb} \neq 0} - \Delta\phi(\omega)|_{n_{Rb} = 0}$.

This value for [II] gives a first estimate for the density which we use as the starting parameter for the final fit that determines the density. The final fit minimizes the difference between the zero-crossings of the conditioned signal and a function obtained by multiplying $\cos(\Delta\phi(\omega))$ with the envelope function determined in the signal conditioning process. This step requires to substitute Eq. 3.5 and Eq. 3.6 while using the just determined start value for n_{Rb} . The terms α , β , Δl and $\Delta\phi_0$ are kept as fitting parameters because external influences like small vibrations might change them on small scales which might cause a large error in this sensitive, interferometry-based diagnostic. We obtain their start values by fitting a second-order polynomial to $\Delta\phi(\omega)|_{n_{Rb} = 0}$.

The output of the entire procedure, i.e. the conditioned signal (blue line), the fit (red line) that determines the density and the identified zero crossings (red circles) are plotted in Fig. 22(a). The depicted frequency range covers only a 16 THz-wide

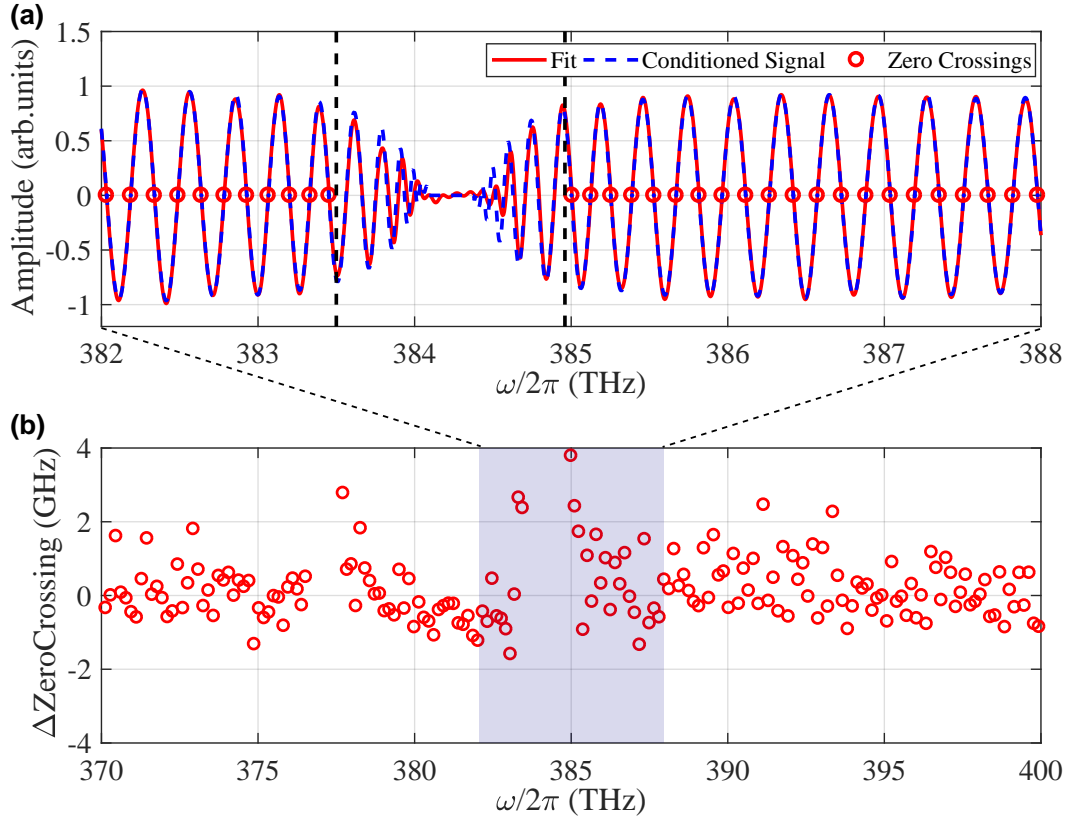


Figure 22: (a) Plot of the conditioned signal (blue), the zero crossings (red circles) and the fit (red line) vs. frequency ($\omega/2\pi$) for a 16-THz-wide part around the D2 line of the spectrum shown in Fig. 18(b). The dashed lines mark the spectrum around the transition that is excluded from the fit. (b) Plot of the difference between the zero-crossings of the signal and the fit vs. frequency for the entire recorded frequency range. The area marked in light blue represents the spectral part shown in (a).

region of the spectrum around the D2 transition for an enhanced visibility of the intensity oscillations. The dashed lines mark the part of the spectrum around the transition that is excluded from the analysis. The fit matches the signal in periodicity, location of the zero-crossings and shape (given by the envelope function). As an indicator for the goodness of the fit, we calculate the deviation of the zero-crossings of the fit from those of the signal. The outcome is shown in Fig. 22(b), where the shown frequency range covers again the entire frequency spectrum recorded (the range of (a) is marked in light blue). The observed deviations from the signal are with ± 4 GHz below the resolution of the spectrographs, i.e. the fit represents the data well.

The computing duration to perform this calculation is approximately 1 s. We apply the algorithm to the simultaneously recorded up- and downstream spectrograms to obtain the corresponding density values $n_{Rb,u}$ and $n_{Rb,d}$, respectively. From these we calculate the linear density gradient g along the 10 m-long vapor source as

$$g = (n_{Rb,d} - n_{Rb,u})/n_{Rb,u}/10 \text{ m} , \quad (3.7)$$

with units %/m. The fully automated script then sends the values for $n_{Rb,u}$, $n_{Rb,d}$, g and the time stamp of the spectrograms to the JAPC framework described in Chapter 3.4.1.

3.4.2.2 Measurement Accuracy

In order to confirm the measurement uncertainty recorded in [59], we record spectrograms over a short period (on the order of minutes), whereas the density changes happen on the order of hours. For a density of $7.7 \times 10^{14} \text{ cm}^{-3}$, close to one AWAKE baseline density, we measure $n_{Rb,u} = (7.719 \pm 0.006) \times 10^{14} \text{ cm}^{-3}$ and $n_{Rb,d} = (7.715 \pm 0.007) \times 10^{14} \text{ cm}^{-3}$. This corresponds to a statistical uncertainty of $\pm 0.08\%$ (standard deviation) upstream and $\pm 0.09\%$ downstream. For the entire density range ($0.5 - 11 \times 10^{14} \text{ cm}^{-3}$), we observe statistical uncertainties between $\pm 0.05\%$ at high densities and $\pm 0.30\%$ at low densities (see appendix A.2.1 for plots of the measured vapor density as a function of time at both baseline densities). Together with the systematic uncertainties of $\pm 0.10\%$ to $\pm 0.35\%$ from [59], the resulting total uncertainty is $\pm 0.11\%$ to $\pm 0.46\%$ (standard deviation, added in quadrature). This fulfills the AWAKE Run 1 requirement of measuring the vapor density gradient with sub-percent accuracy.

The accuracy of the diagnostic also plays a major role for the comparison of the modulation frequency and the expected plasma frequency one obtains from the Rb vapor density.

3.4.3 The Laser Reference Signal

3.4.3.1 Description

The SC triggering system has a jitter with respect to the proton bunch and ionizing laser pulse, meaning that the SC images do not show the exact same part of the proton bunch, but jump $\approx 5 \text{ ps}$ (rms, see Chapter 5.1.1) around a certain position from event to event. Further, the precision with which the timing/delay values of the SC window can be set is low when compared to the required sub-picosecond accuracy. This means that when delaying the window by a certain value in the software, e.g. 50 ps, the true value of the delay is observed to differ sometimes, with an uncertainty on the order of approximately $\pm 10 \text{ ps}$. For these reasons, there

was a demand for a timing signal that indicates with high, sub-ps accuracy the position/timing of the RIF within the proton bunch, or a point later in the bunch with known relative delay with respect to the RIF, on the SC images. In the following, we explain the design and setup of the hence developed LRS. Its characteristics such as its precision and possible timing jitters are described in Chapter 5.

The mentioned criteria translate into the requirement that the transfer line for the LRS must not promote a significant pulse length stretching due to optical dispersion. In addition, its optical path length must match that of the ionizing laser, meaning the 60 m-long path from MP1 via the laser-proton-merging point through the vapor source to the OTR foil and from there along the OTR transfer line to the SC. For a sub-picosecond accuracy, the difference in path length must be $< 300 \mu\text{m}$.

To account for these points, we transport a replica of the ionizing laser pulse in free space (i.e., in air) to the SC. This is allowed for by the fact that the pulse length stretching of the 780 nm pulse with 24 nm bandwidth over 60 m of air is only ~ 32 fs, making it a negligible contribution regarding the temporal resolution of the SC of 1.5 ps. The designed path of the LRS is shown in Fig. 23(a) in red/orange¹, the path to be matched of the laser light in blue. The LRS uses the bleed-through of the 120 fs-long ionizing laser pulse at the first mirror after the in-vacuum compressor (MP1, marked by #1 in Fig. 23, also shown in the schematic of the laser system in Fig. 12). We chose this location for the pickup because it is after all laser components that could possibly influence the timing of 120 fs-long ionizing laser pulse with respect to the LRS. From mirror MP1 on, their propagation times stay constant, even if the timing inside the laser changes. Further, this location provides the possibility to observe the LRS next to unmodulated proton bunches in no-plasma events where no ionizing pulse is sent along the vapor source. This can be achieved by closing beam dump LSBP1 or the laser shutter after MP1 (see Fig. 12).

From the pickup location, a sequence of 2-inch-diameter mirrors and 1-inch periscopes guides the LRS along the ceiling through the laser room and back to the optical table that hosts the other laser components in order to gain the required 60 m of path length. The path inside the laser room is shown in more detail in Fig. 23(b). On the table, a delay line (#2 in Fig. 23) allows for matching the path lengths. It consists of a 1.5 m linear translation stage that is used for a coarse adjusting of the length, a motorized translation stage (model Standa 8MT175-150 with stepper motor) with 15 cm travel range and $2.5 \mu\text{m}$ resolution (per full step) for the fine adjustment, and a roof-top mirror. The position of the motorized translation stage can be set in 100- μm steps. The delay line is depicted in Fig. 23(c). Its setup allows for moving the LRS in time by known time steps with respect to the ionizing laser pulse. This way, we are capable of observing the SM and studying its phase relative

¹Different shades of red were used to enhance the visibility of the different light path. No other meaning is intended.

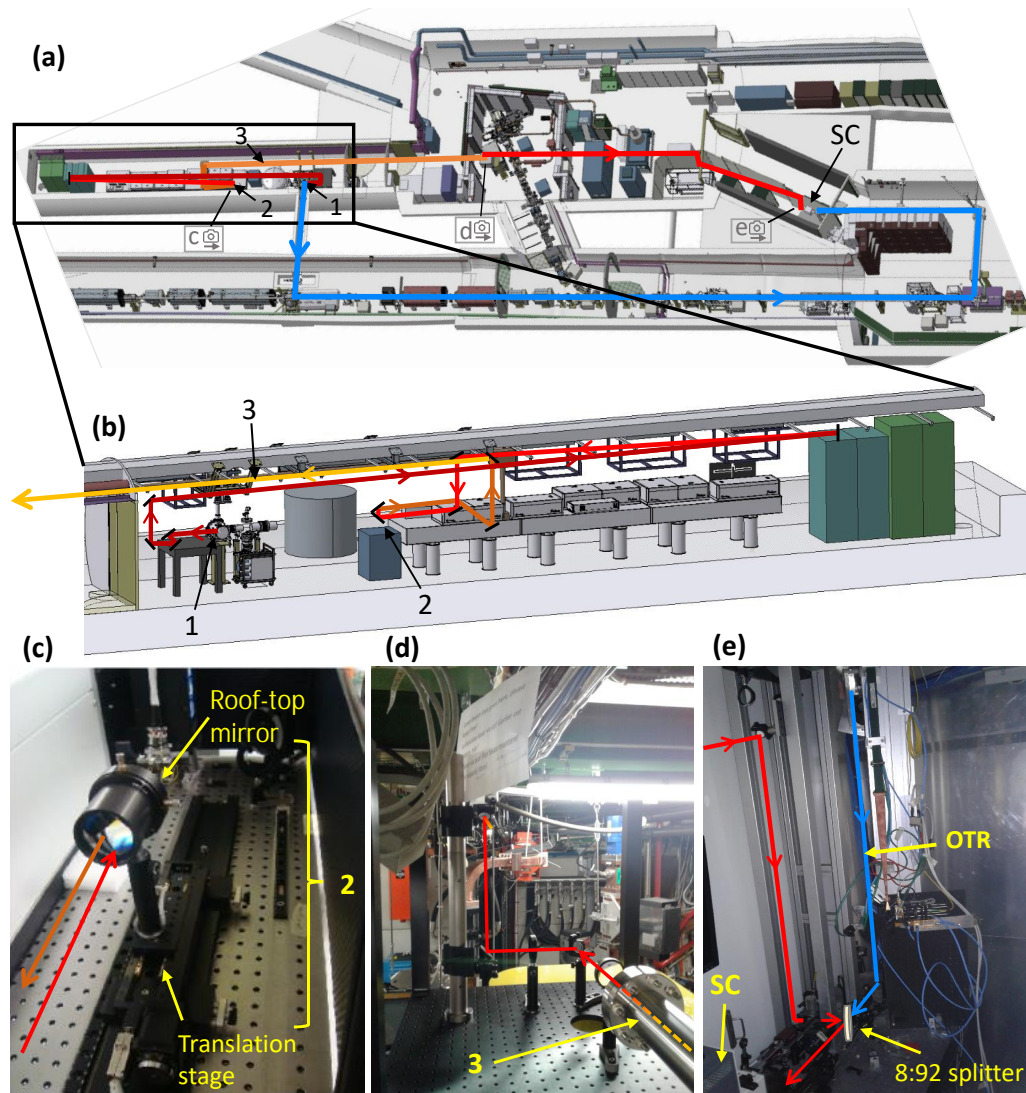


Figure 23: (a) Sketch of the experimental area showing the path of the LRS (red/orange) to the SC and the path of the laser through the main beam line and OTR line (blue). [71] (b) Enlarged detail of the optical paths of the LRS in the laser room. From: CERN (c) Photo of the delay stage (#2) with its translation stage and roof-top mirror. (d) Photo of the optical path inside the electron bunker. The LRS exits the transfer pipe, is lifted by ~ 40 cm and sent to the streak room. (e) The light path of the LRS (red) and the OTR (blue) close to the SC. All: Position #1 shows the location of mirror MP1, #2 the location of the delay stage and #3 the in-vacuum optical transfer pipe from the laser room to the electron bunker. The location of photos (c-e) is indicated in (a).

to the reference signal tens to hundreds of picoseconds behind the ionizing laser pulse. This feature is particularly important when the SM is not seeded (SMI), i.e. when the ionizing laser pulse is several 100 ps ahead of the SC window where the phase reproducibility is investigated.

Then, the LRS is sent through the in-vacuum optical transfer line (#3 in Fig. 23) that connects the laser room to the electron bunker and also transports the UV pulses to the electron gun [84]. In the electron bunker (Fig. 23(d)), another periscope brings the LRS close to the ceiling, from where it is sent across the experimental area to the streak room. Inside the streak room, the LRS is merged into the beam path of the OTR using a 8:92 beam splitter. From there, it is sent onto the SC (marked as SC in Fig. 23(d)). The last mirror before the splitter is motorized to ease the alignment of the LRS onto the SC slit and to remotely adjust the brightness and position of the LRS on the SC images. This is required because an excessive intensity of the LRS (but not high enough to cause damage) leads to a broadening of the LRS on the SC images of up to 10 ps because of space charge effects inside the streak tube. To not cover the OTR signal of the proton bunch on the SC images, the LRS is usually positioned on their left edge. The protection against harmful laser light intensities of the SC and people being present in the area is guaranteed by reducing the intensity of the LRS to non-harmful values using absorptive filters with an optical density between OD5 and OD6. These filters are placed directly after the pickup location at mirror MP1.

3.4.3.2 Time Matching

We match the times-of-arrival of the LRS and OTR by sending low-energy pulses from the ionizing laser via the main beam line and OTR foil onto the SC. This way, the LRS and ionizing laser pulse can be observed simultaneously and matched using the motorized delay line. Figure 24 shows such a SC image where both signals are visible, with the LRS 4.4 ps ahead the laser pulse. The timings of the LRS and laser pulse are synchronized by adjusting the delay line such that both signals overlap on the image. However, one has to take into account that the laser pulse used for the time matching and the OTR light used for the SM measurements possess different wavelength. While the central wavelength of the laser is ≈ 780 nm, the wavelength of the broadband OTR is filtered to ≈ 450 nm (set by the bandpass filter used to increase the temporal resolution, see Chapter 3.3.4). This difference in wavelength results in different propagation times/velocities and thus different times-of-arrival on the SC images, caused by dispersion in the glass-made optics in the OTR transfer line (e.g., the window that separates the beam line under vacuum and the free-space OTR line). By using different bandpass filters on the OTR line (450 nm and 775 nm) and observing the resulting temporal shift on the SC images, the propagation time difference was measured to 9.9 ps [114]. This delay must additionally be compensated

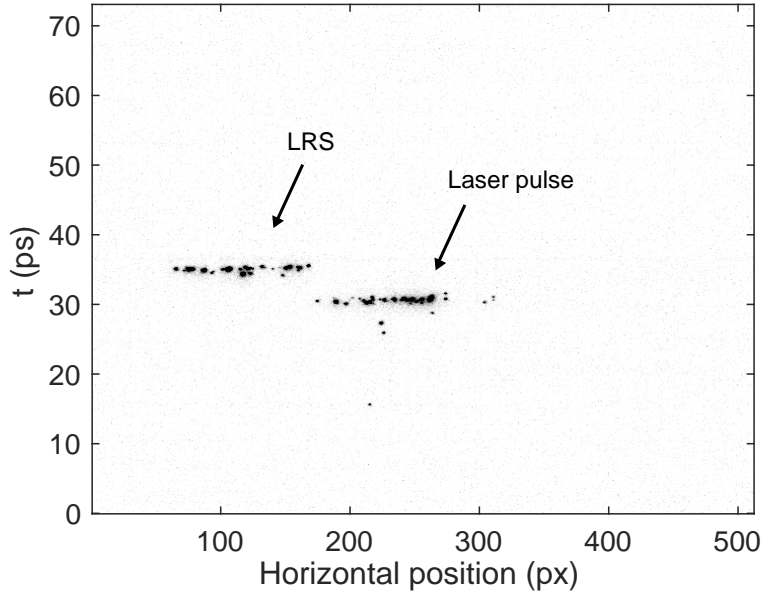


Figure 24: Streak camera image with the LRS (left signal) and the ionizing laser (in low-energy mode, right signal) simultaneously visible. The LRS is 4.4 ps ahead the laser pulse.

by adjusting the delay line accordingly (i.e. delaying the LRS with respect to the OTR by 9.9 ps). This way, the LRS indicates precisely the time-of-arrival of the ionization front within the proton bunch. Here, we want to note that any potential error on this delay matching would only impose a systematic error on the RIF time-of-arrival, but would not impact the intended measurements of the relative phases of the SM.

Phase studies at locations far behind the seed (100s of ps) are realized by delaying the translation stage together with the SC window, providing a relative timing signal on each image with known, constant delay with respect to the RIF. We call this temporal offset between the RIF and the LRS Δt_{LRS} . Displacing the translation stage by distance s will move the LRS by $\Delta t_{LRS} = 2s/c$ in time.

The procedure to locate the LRS on SC images and how to use it for the phase determination and "stitching" of several SC images to reconstruct an image of the entire proton bunch with ps-accuracy is explained in Chapter 4.2. For the determination of the precision, accuracy and further characteristics (e.g. potential jitters) of the LRS, we refer to Chapter 5. Detailed instructions for operators to use the LRS during the experimental beam times can be found in [115].

3.5 AWAKE Run 2

In this last paragraph of the chapter we describe the modifications of the AWAKE setup that are planned for the next scientific run period, called Run 2, to meet the long-term goals of the experiment [116, 117, 118]. After the successful demonstration of the SM and proof-of-concept of electron acceleration in a proton-driven, PWFA-based accelerator in Run 1, Run 2 aims to accelerate electron bunches with bunch qualities suited for applications. This means a sufficiently large final energy (multi-GeV), a high bunch charge, a small relative energy spread and a low emittance. The strategy to achieve this goal is to separate the processes of electron acceleration and of the growth of the SM where the phases of the wakefields change over the first few meters, hence being defocusing for electrons at some point. By splitting the two processes, one is able to provide the optimal conditions for each.

As shown in Fig. 25, the modified setup will therefore not have one, but two plasmas, i.e. two vapor sources. The first one will be used for the SM of the proton bunch with a focus on optimizing the micro-bunch formation. The vapor source will have eight independent electrical heating zones to set a temperature and thus plasma density step along the propagation path. This density step is supposed to stabilize the state of the micro-bunches [57] and thus to keep the wakefield amplitudes close to their saturation value [28, 119]. The density step is chosen instead of a linear gradient because gradients cannot be maintained over long distances and shaping the plasma profile is only effective until saturation of the SM is reached. As another difference from the current setup, the SM will not be seeded by the RIF of a laser pulse, but by an electron bunch propagating ahead of the proton bunch in

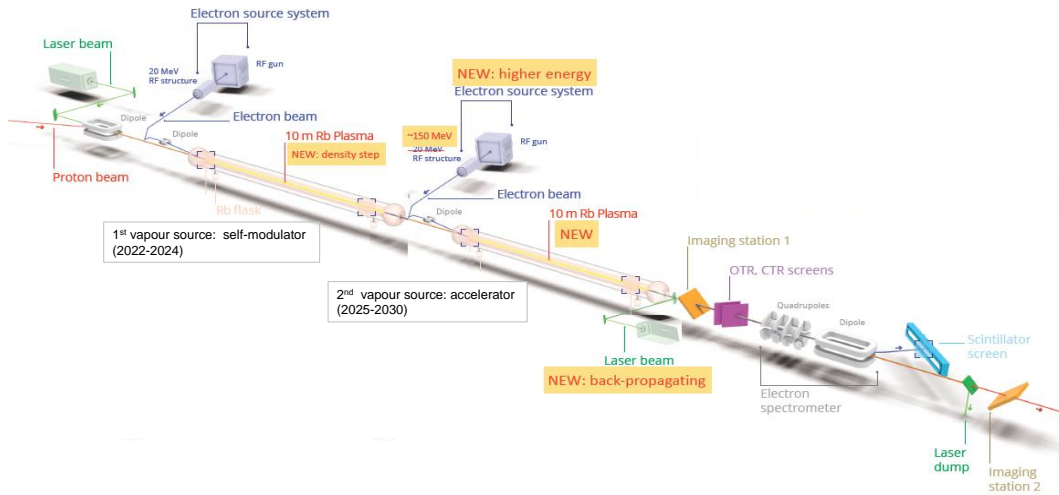


Figure 25: Planned layout for AWAKE Run 2c. From: [117].

a preformed plasma. The train of micro-bunches that formed in the first plasma propagates to the second vapor source, where it coherently drives wakefields in an also pre-formed plasma. The second source will have a heat exchanger similar to that of the Run 1 vapor source to guarantee a high plasma density uniformity. Electrons from a second electron gun can now be injected without having them to cross the defocusing wakefields of the SM evolution. In order to host the additional component like the second vapor source, the second electron gun and the larger laser system, the AWAKE area has to be expanded in the former CNGS target area (see Fig. 10), which is going to be dismantled for this purpose.

Schedule-wise, Run 2 will be split into four phases (2a-d) [116] in order to study the aforementioned physics objectives and because the scientific run periods of AWAKE are linked to the schedule of the CERN accelerator complex and its Long Shutdown periods that then interrupt all physic programs for around two years. In Run 2a, one will use the existing setup of Run 1 to study electron seeding of the SM. This gives time to prepare the modifications of the experimental area for the phases Run 2b-d. Measurements of the SM with electron bunch seeding, meaning studies of the resulting phase stability and the transition between instability and stability, similarly to the studies presented in this thesis, are foreseen for 2021/2022. The plans for Run 2b for 2023/24 include testing the new electrically heated vapor source and studying the effect of a density step on the SM and the stabilization of the micro-bunches. The main modifications of the experimental area for Run 2c and 2d are scheduled during CERN's Long Shutdown 3 from 2025 to 2027. This includes for example the expansion of the AWAKE experimental area and the installation of a new, 150 MeV electron source. After that shutdown, from 2027 on, Phase 2c is dedicated to electron acceleration experiments to validate the preservation of the electron bunch parameters, such as the emittance, after the acceleration. Last, one plans the demonstration of scalable plasma sources for Run 2d. A new helicon plasma source and a discharge source are under development for this reason [120].

Chapter 4

Analysis Tools and Procedures

In the following, we describe the analysis tools for the SM studies in this thesis. We explain the image processing required to prepare the raw SC images for the analysis of the SM. We describe the determination of the position and timing of the LRS on SC images. We show the procedure to measure the phase or timing of the micro-bunches using a DFT.

4.1 Image Processing

The raw SC data must be processed and filtered prior any SM analysis to mitigate the effects of noise present in the system. Possible sources of noise are background noise from the SC readout electronics, residual ambient light or stray radiation that causes hot or even single saturated pixels. A typical background image recorded during proton beam operation, but without signal from the proton or laser beam (MCP gain 40, entrance slit closed) is depicted in Fig. 26(a). Its histogram of the intensity distribution is shown in Fig. 26(b). The image shows a more or less continuous background with pixel counts of around 400 that appears on the entire image, overlaid with randomly appearing hot or saturated pixels (single occurrences of counts ≈ 5000 and larger). Since the noise, especially saturated pixels, might influence the intended analysis by distorting the determination of the LRS timing or the phase determination of the micro-bunches, the steps described in the following Chapters (4.1.1 and 4.1.2) aim to reduce the effect of the different noise contributions on the analysis outcome.

4.1.1 Background Subtraction

The part of the signal seen in Fig. 26 that is fairly continuous has two distributions. The first is an (almost) constant offset with respect to zero that is caused by the bias level of the CCD camera [121]. The bias level is an electric offset voltage that is applied to the analog-to-digital converter to avoid negative signal values. As shown in Figure 26(b), most of the pixel counts are < 1000 , with the highest number of occurrences at around 400 counts (see Inset). Counts below 340 are not observed.

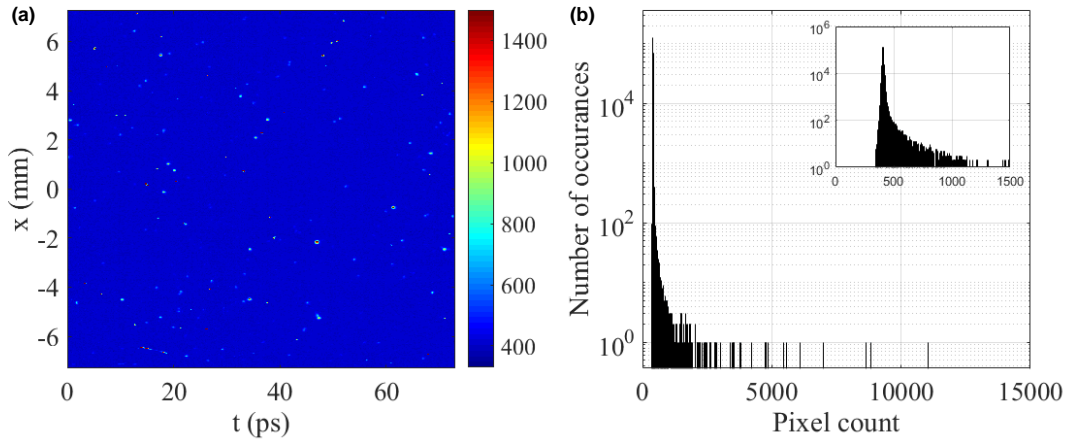


Figure 26: (a) Raw SC background image during proton injection with MCP gain 40 and slit closed. (b) Histogram of the intensity distribution in (a). Inset: Enlarged view of pixel counts <1500 showing the effect of the bias level.

This offset from zero corresponds to the bias level and has to be removed from the image to obtain the signal only. The second contribution is the readout noise and residual ambient light. Figure 27(a) shows a background image that was recorded without proton beam or laser operation, i.e. it shows only readout noise and ambient light, but almost no stray radiation. As seen from the corresponding histogram in

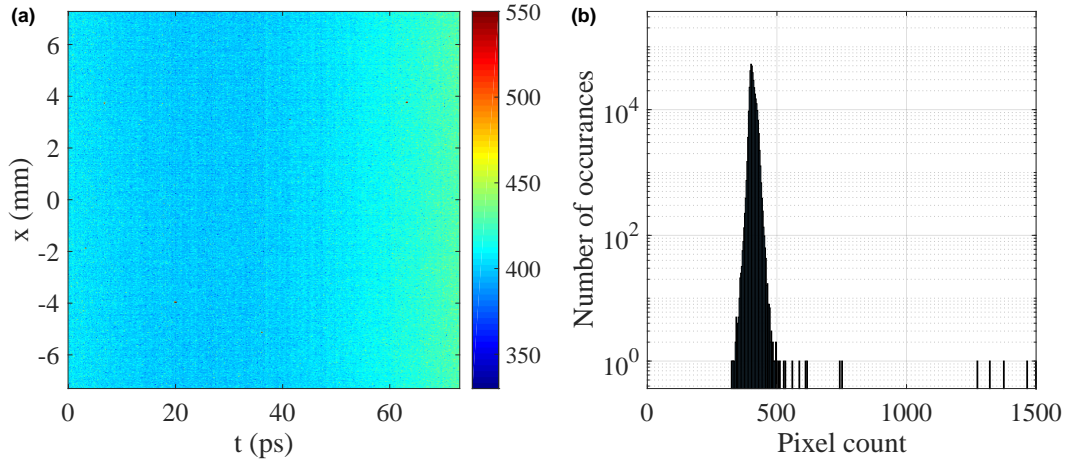


Figure 27: (a) 73 ps SC image recorded without any beams, i.e. no stray radiation. Only the bias level and readout noise are represented. (b) Histogram of the intensity distribution in (a).

Figure 27(b), the readout noise and ambient light causes small fluctuations around the bias level (broadened peak around pixel count 400). We remove these contributions from the signal by subtracting an averaged background image similar to that in Fig. 27(a) from the images to analyze. These background images are recorded with SC settings equal to those with which the data was taken, but without proton or laser beam operation causing stray radiation. After the background subtraction, the remaining background (without hot or saturated pixels) shows on average (2 ± 10) counts per pixel, which can be considered negligible.

4.1.2 Saturated Pixel Treatment

Saturated pixels as seen in Fig. 26 are mainly caused by stray radiation that is created when the proton bunch itself or single defocussed protons interact with matter, causing showers of secondary particles. The main interaction of the proton beam with matter appears when it passes through a vacuum separation window out of 200 μm -thick aluminium that separates the AWAKE vacuum system from the SPS. It is located ~ 4.5 m upstream of the laser merging point shown in Fig. 10. Protons that are defocussed in the SM process also cause stray radiation when they hit and interact with the walls of the vapor source.

By inducing a large, but false signal, these hot or saturated pixels can have a major impact on the phase analysis. Their large counts can lead to errors in the localization procedure of the LRS (described in the following Chapter 4.2) by possibly imposing a wrong position of the signal peak (see e.g. Figs. 24 and 30). As a result, observed phase variations could appear significantly larger than they actually are.

Filtering of saturated pixels is difficult due to their random distribution which prevents the definition of a representative background that could be subtracted from the original signal. However, since the main goal is to avoid that saturated pixels are falsely identified as a maximum of the LRS or in the proton bunch distribution, it is sufficient to filter them by setting an upper limit for single pixel counts in the SC images. For each data set, we define this limit by looking at a histogram of the intensity distribution of a SC image that is recorded under normal experimental conditions (i.e. with the LRS and self-modulated proton bunch shown), and with the SC background and the bias level already subtracted. An example for such a histogram is depicted in Fig. 28, where the image was recorded with MCP gain 50 and slit width 20 μm . The SC image that is used is shown in the Inset. The OTR signal leads to up to ~ 5000 counts per pixel. Single occurrences of higher pixel counts (up to a factor of ~ 3) represent hot or saturated pixels. We choose five occurrences of a pixel count as the limit (see red horizontal line in Fig. 28) and regard all pixels with higher counts (red vertical line) as hot or saturated pixels. Setting their readings to the count of the defined limit (in this example 5000) decreases their potential to distort or manipulate the analysis of the LRS and OTR signal.

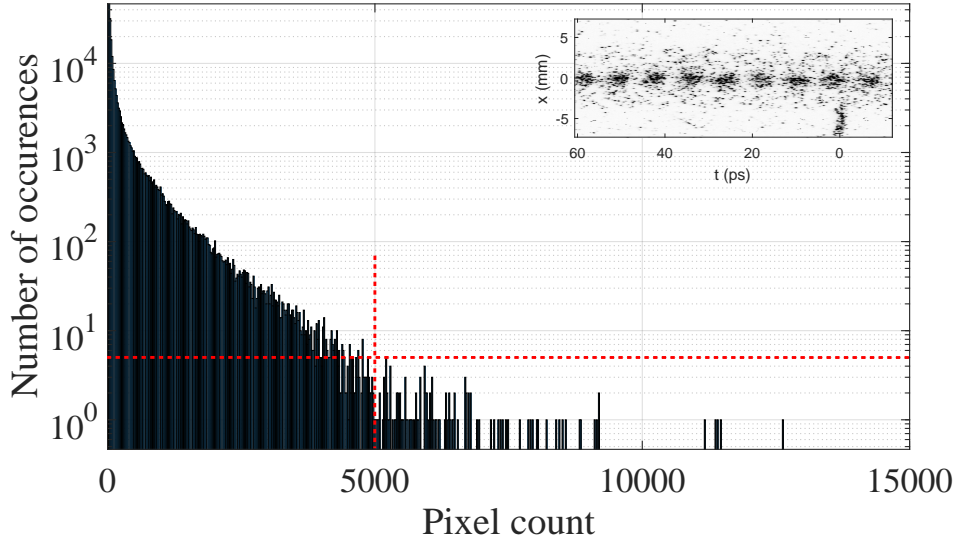


Figure 28: Histogram of the intensity distribution per pixel of a typical SC image (see Inset) of a self-modulated proton bunch. The continuous background is already removed. Dashed lines mark the limits that define hot or saturated pixels.

The background of other stray light cannot be filtered to due its lower intensity and randomness. However, they do not affect the analysis and average out when multiple images are stitched.

4.1.3 Linearization of the Temporal Axis

In addition to the background reduction, there is also a need to correct the temporal axis of the SC images that is provided by the SC itself. The sweep voltage in the streak tube of the SC (see Chapter 3.3.4 for its working principle) that deflects the electrons depending on their timing leads to a non-linear time axis, i.e. the time step per pixel on the SC image is not constant. This behavior is shown in Fig. 29 in blue for the two time window lengths used in this thesis of (a) 73 ps and (b) 211 ps. In both windows, the time per pixel is not constant but changes non-linearly along the temporal axis of the image. For the 73 ps time window, the change is small, $\approx 1\%$, but $\approx 10\%$ for the 211 ps window. This induces errors in the phase stability studies and the stitching procedure because the length with which a (constant) modulation period appears on the SC image changes with its position along the bunch. Further, a DFT as used for the determination of the modulation frequency and phase (see Chapter 2.5) assumes an equidistant sampling rate of the signal in the time and frequency domain.

Therefore, the time axis supplied by the SC software as well as the intensity

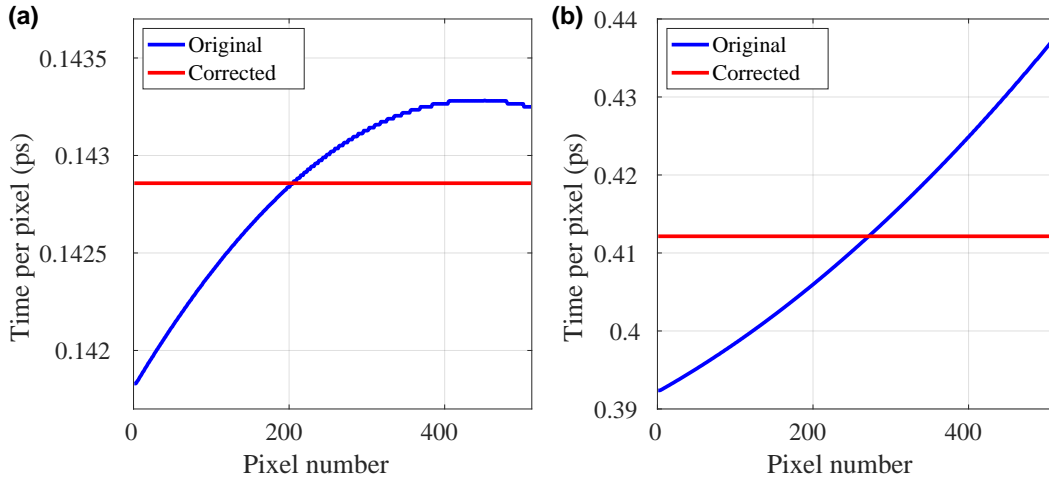


Figure 29: Original, non-linear (blue line) and corrected, linear (red line) SC time axis for the (a) 73 ps and (b) 211 ps time window.

distribution per pixel along the temporal axis must be corrected, i.e. linearized before proceeding with the analysis. This is implemented by an interpolation algorithm that re-distributes the original, nonlinear pixel counts onto a grid with uniform distribution in time, i.e. with a constant time step per pixel while preserving the total counts per image [56]. The outcome of this linearization procedure can be seen by the red curve in Fig. 29. For both windows, the time per pixel is now constant for every pixel along the temporal axis. For the 73 ps time window which is used for the phase analysis in this thesis, the required redistribution of pixel counts is on the order of $\approx 0.7\%$, for which its influence on the determination of the modulation phase can be neglected, especially since the LRS appears on approximately the same part of the image within one data set. For the 211 ps window, the pixel counts are adjusted by up to $\approx 7\%$. However, for this window, the correction of the pixel counts is strictly required for the stitching of SC images, which was for example used for studies of the influence of different plasma gradients on the micro-bunch train in Chapter 7. Without the corrections, micro-bunches would not align properly in time and the time profile (explained in Chapter 4.4.1) of the stitched images would show discontinuities.

4.2 Localization of the LRS

Almost all studies of this thesis rely on the use of the LRS as a relative timing signal for which we first describe its determination. The LRS is placed at the bottom of the SC images to not distort or superimpose the OTR signal. Figure 30(a) shows an

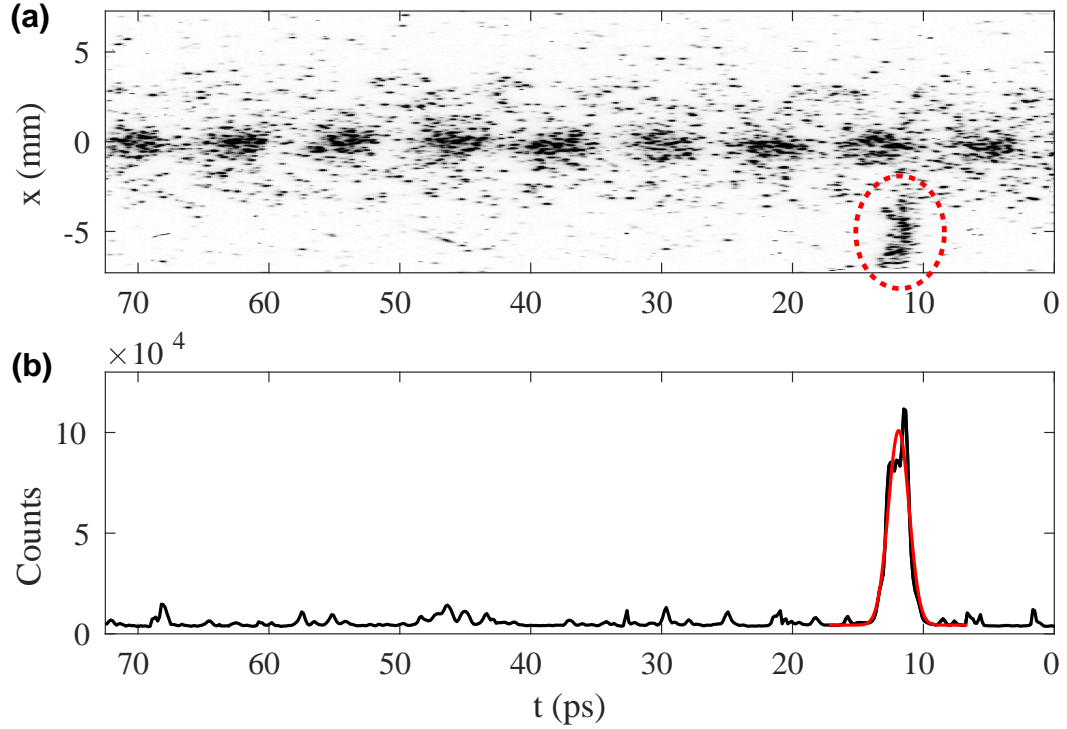


Figure 30: (a) Single 73 ps SC image of a self-modulated proton bunch recorded at density $n_{e0} = 1.81 \times 10^{14} \text{ cm}^{-3}$. The LRS is marked by the red circle. (b) Black line: Longitudinally summed counts for the region with $-6 \text{ mm} < x < -4 \text{ mm}$ containing only the LRS. Red dotted line: Gaussian fit to determine the position of the LRS.

exemplary SC image with the LRS visible at $11 \text{ ps} \leq t \leq 13 \text{ ps}$ and $x \leq -3 \text{ mm}$. To determine the temporal position of the LRS, we sum counts in a $\sim 2 \text{ mm}$ -wide region along the spatial axis at the bottom of the image. This region must only contain the LRS, but no OTR light. This is possible due to an aperture in the OTR optical transfer line to the SC that limits the OTR to $\pm 4 \text{ mm}$ on the SC images, which is faintly visible in Fig. 30(a).

The result of that sum is shown in black in Fig. 30(b). A prominent peak with an amplitude well above the noise level appears at $t \approx 12 \text{ ps}$. We determine its position and thus the timing of the LRS by applying a Gaussian fit to a $\pm 5 \text{ ps}$ wide region centered around the peak. The red line in Fig. 30(b) represents the fitted Gauss curve, with its peak at $t = 11.9 \text{ ps}$. As a reminder, this means that features at this time t have a temporal offset relative to the ionizing laser pulse equal to the Δt_{LRS} defined by the delay stage setting in the LRS line (see Chapter 3.4.3). In case the LRS is synchronized with the ionizing laser pulse (see Chapter 3.4.3.2 for details),

i.e. $\Delta t_{LRS} = 0$, the LRS indicates the position of the RIF within the bunch. The precision of the timing/position of the LRS is evaluated in Chapter 5.

4.3 Superposition and Stitching of SC Images

The LRS allows for a superposition and "stitching" of the SC images for a visual study of the SM. Regarding its temporal resolution, the SC works best with a low incoming light intensity, i.e. with a small signal amount, leading to rather granulated images as seen in Fig. 31(a). With larger signal strengths, smoother images would be achievable, but the features on the images then smear out due to space charge effects inside the streak tube of the SC, which decreases the time resolution. Assuming SM with reproducible timings/phases of the micro-bunches, a better signal-to-noise ratio and portrayal of the bunch charge density with the highest available resolution of ~ 1 ps over time scales much longer than the 73 ps window can be achieved by this superimposing and "stitching" of the SC images. We note that these procedures are only applicable for the SC images of the same data set recorded under equal experimental input parameters and settings, i.e. equal n_{Rb} , g , t_{RIF} and proton bunch parameters.

The superposition and thus an averaging of images such as in Fig. 31(a) with equal Δt_{LRS} is achieved by numerically adding their pixels counts such that the images are synchronized in time with respect to the LRS. Due to the jitter of the SC triggering system (see Chapter 5.1.1), a different number of images may contribute to each pixel in the final image. In order to avoid discontinuities, we normalize each pixel row in the final stitched image to the number of images that contributed to its count.

For the stitching of SC images showing different positions along the bunch,

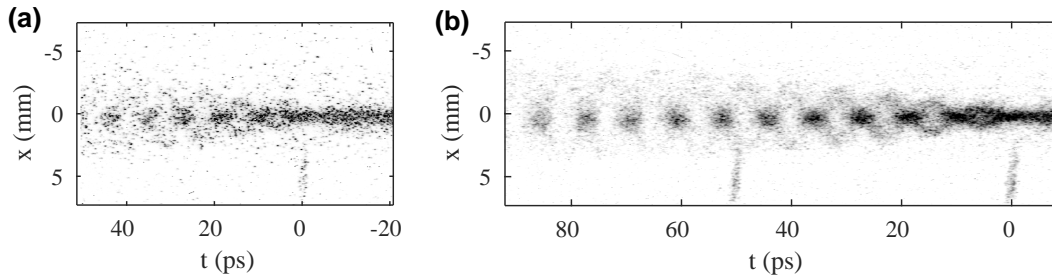


Figure 31: (a) Single, 73 ps SC image of a self-modulated proton bunch where the LRS is synchronized with the RIF ($\Delta t_{LRS} = 0$) and $n_{e0} = 1.81 \times 10^{14} \text{ cm}^{-3}$. The LRS and thus the RIF is at $t = 0$ ps. (b) A 100 ps long part of a reconstructed, "stitched" image of the modulated proton bunch using nine images like (a). The LRSs are separated by 50 ps ($\Delta t_{LRS} = 0$ and 50 ps).

i.e. recorded with different Δt_{LRS} , we place the images on the temporal axis according to their timing relative to the RIF that is defined by the LRS. Thereby, one must keep in mind that the pixel number that corresponds to the location of the LRS on the temporal axis must not be an integer number, but can be in between two pixels. In this case we round to the nearest integer as only full integer pixel numbers are suited for the stitching of SC images. This might impose an uncertainty or timing jitter of 0.5 px or its corresponding time value. We change Δt_{LRS} in 50 ps steps when recording with the 73 ps window and in 150 ps steps with the 211 ps window to portrait the entire modulated proton bunch and to guarantee a time overlap between the images with different delays. Since also the stitched images not necessarily obtain an equal number of images in each pixel row we normalize again each row of the final stitched image to the number of images that contributed.

The result of the averaging and stitching using the 73 ps window is exemplary illustrated in Fig. 31(b) for the first two delays of the LRS, i.e. $\Delta t_{LRS} = 0$ and 50 ps. For each Δt_{LRS} , we average nine events. The resulting image displays a ~ 100 ps long section of the micro-bunch train with the resolution of the 73 ps window (~ 1 ps). The image shows an improved signal-to-noise ratio, e.g. the structure of defocused protons becomes visible and the shape of the micro-bunches appears more distinct. By repeating this procedure of delaying the LRS together with the SC window multiple times, one obtains noise-averaged, high-resolution images along the entire modulated bunch, usually of several 100 ps length.

We want to mention that averaged SC images can provide a first, visual measure for the phase reproducibility for data sets where the behavior of the modulation phase is unknown. As already indicated, the peaks in the proton bunch charge density overlap in the case of SSM. By contrast, with randomly phased micro-bunches (SMI), the features of the individual images are expected to average/wash out.

4.4 Modulation Frequency and Phase Determination

We characterize the SM or micro-bunches with respect to their modulation frequency and phase or timing using a DFT-based analysis procedure as described in Chapter 2.5.

4.4.1 Determination of the Time Profile

We first obtain the time profile of the self-modulated proton bunch from the according to Chapter 4.1 processed images by summing the pixel counts within a region centered around the bunch axis, along the temporal axis. We define the width and center of this region by summing counts along the spatial coordinate of the SC image. We thereby limit the summing longitudinally to those parts of the temporal axis that only contain signal from the protons but not from the LRS. For the example SC image in Fig. 30(a), only signal with $t \leq 15$ ps is summed along x .

Figure 32 depicts the result of this sum. The counts for $-1 \text{ mm} \leq x \leq 1 \text{ mm}$ originate from the micro-bunches, signal within $-4 \text{ mm} < x < -1 \text{ mm}$ and $1 \text{ mm} < x < 4.5 \text{ mm}$ represents defocused protons. It can also be seen that outside $-4 \text{ mm} < x < 4.5 \text{ mm}$ no OTR signal reaches the CCD of the SC because transport optics in its optical transfer line limit the field of view. Since the incoming proton bunch distribution is approximately Gaussian [77], we fit a Gaussian profile to the peak ($\approx -1 \text{ mm} \leq x \leq 1 \text{ mm}$ on Fig. 32) to determine the transverse bunch center which defines $x = 0 \text{ mm}$ on the images and the transverse rms width σ_r of the micro-bunch charge distribution (measured at the OTR foil 3.5 m after the plasma). Based on these values, for the determination of the time profile of the self-modulated bunch, we set the width of the summed region along the temporal axis to be $\pm 1\sigma_r$ and centered around the peak of the distribution ($x = 0$). For the example in Fig. 32, $\sigma_r \cong 430 \mu\text{m}$.

Figure 30 is re-produced in Fig. 33 with supplementary information to emphasize the steps of frequency and phase determination from this time profile. The time profile one obtains when using the width of $430 \mu\text{m}$ is added in Fig. 33(b) in blue.

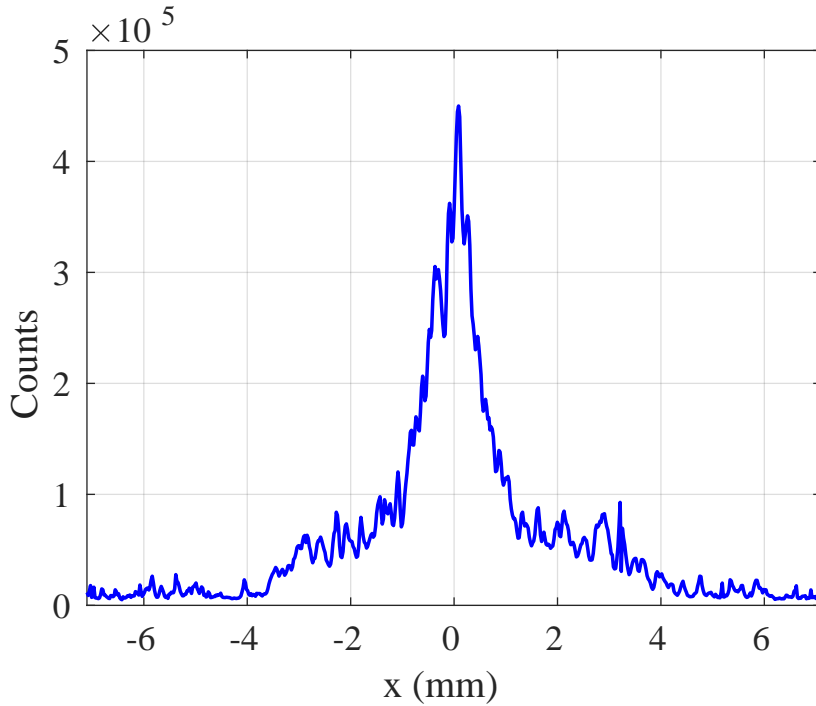


Figure 32: Spatial profile of Fig. 30(a) obtained by summing counts in a $\cong \pm 430 \mu\text{m}$ -wide region around the bunch axis.

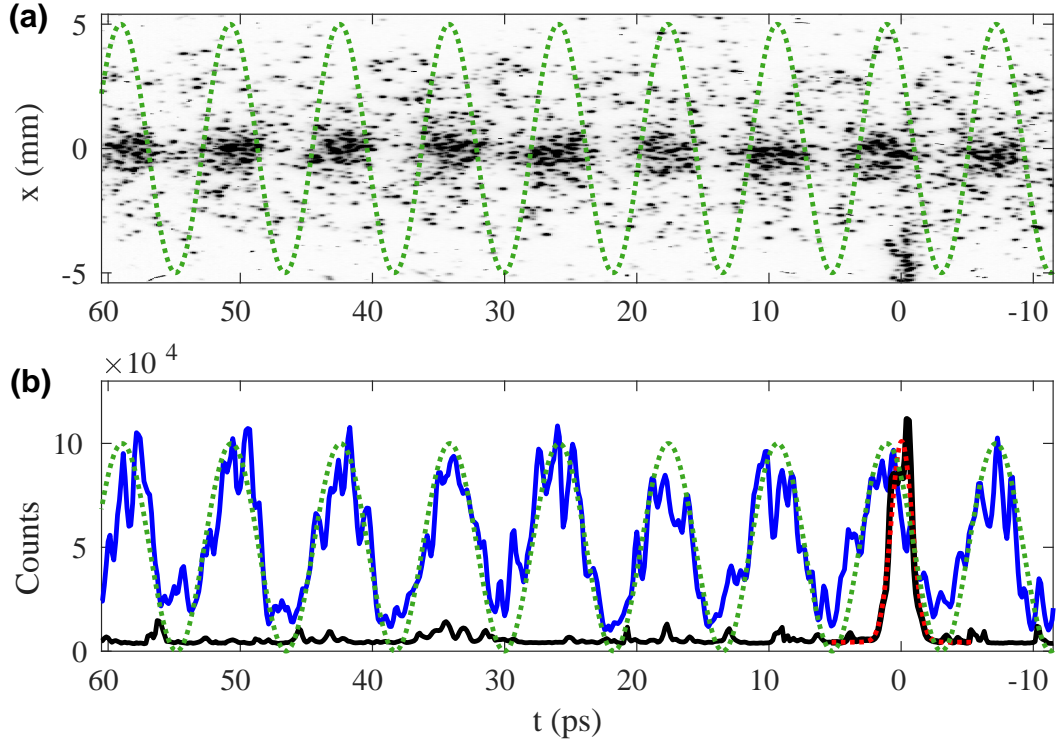


Figure 33: (a) Single 73 ps SC image of a self-modulated proton bunch recorded at density $n_{e0} = 1.81 \times 10^{14} \text{ cm}^{-3}$. (b) Blue line: Bunch modulation profile summing a $\cong \pm 430 \mu\text{m}$ -wide region around the bunch axis of (a). Other features equal to those in Fig. 30. Green line, both Figs: cosine of the average DFT frequency used for the analysis and the measured phase value.

4.4.2 The DFT of the Time Profile

Next, we calculate the DFT (Chapter 2.5) of this time profile to determine the modulation frequency and phase. The resulting frequency bin size is $\Delta f_{DFT} = 1/73 \text{ ps} \cong 13.7 \text{ GHz}$ for the 73 ps time window and $\cong 4.75 \text{ GHz}$ for the 211 ps time window. In order to increase the resolution of the frequency determination, we decrease the bin size by zero padding (see Chapter 2.5) the time profile with an one-dimensional array of 50 times its length, i.e., with 50×512 zero amplitudes. Similarly to Fig. 7, Fig. 34 depicts the power spectrum of the time profile of Fig. 33(a) (blue line in (b)). The red points represent the power spectrum of the unpadded signal with its 13.7-GHz-binning. The blue line shows the equivalent spectrum of the zero-padded signal. The zero padding reduces Δf_{DFT} to $13.7 \text{ GHz}/50 \cong 0.27 \text{ GHz}$, bringing it on the same order as the accuracy of the Rb vapor density diagnostic. The enhanced

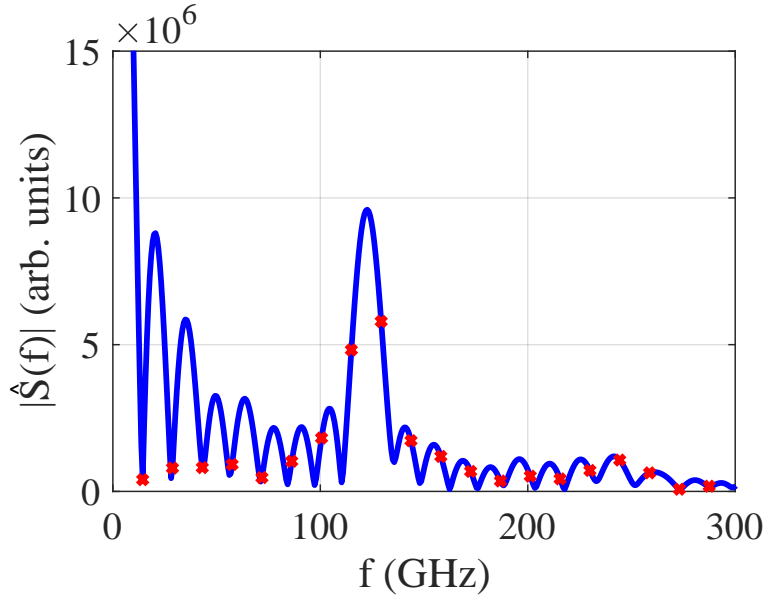


Figure 34: DFT of the modulation profile of Fig. 33 without zero padding (red symbols) and zero-padded 50 times its length (blue line).

resolution of the sinc function is clearly visible, leading to a much more accurate representation of the peak in the power spectrum that corresponds to the modulation frequency f_{mod} .

We want to note that specially tailored window functions that are multiplied to the signal are often used to reduce the convolution effect of the signal's square window function and thus to reduce the share of the sinc function in the power spectrum. These usually Gauss- or Hann-like window functions lower or remove the hard edges of the square window function that cause the sinc function to dominate the power spectrum. However, the window functions can never completely remove the convolution effect since the Fourier transform of any window function is always convoluted with that of the signal, independent of its shape. For the images used in this thesis that displays only six to nine micro-bunches on the 73 ps SC window depending on the Rb vapor density, these window functions do not improve the frequency and phase determinations. The resulting even small number of modulation periods per image leads to higher uncertainties in the analysis outcome. Further, we also do not characterize the power spectra according to the width or amplitude of the peaks. We therefore do not use window functions when determining the modulation frequency and phase.

4.4.3 Determination of the Modulation Frequency and Phase

The modulation frequency of the micro-bunch train seen in Fig. 33(a) is obtained from the power spectrum of the zero-padded signal by determining the frequency peaking with the largest amplitude. We limit the search to a range centered around the plasma frequency expected from the Rb vapor density measurement because their agreement is well proven [51]. For the example event in Fig. 33, we measure a frequency of 122.1 GHz. We refrain from defining a filter or numerical criteria to select or exclude events for mainly two reasons. First, the study of the SMI with possible large fluctuations in the modulation profile could be falsified by such a filter that excludes SMI events. The identification of events with a presumably significantly different phase or modulation depth has to be possible. Second, we are not only evaluating the SM near the bunch center with a high population density and thus a high signal strength of the OTR, but also at the back of the bunch, up to $2\sigma_t$ behind the bunch center where the signal-to-noise ratio is much smaller. In this case, a filter algorithm could falsify the results in a similar way. Instead of filtering, events are accepted if experimental input parameters with regard to the Rb vapor or plasma density, proton bunch and laser alignment are met. In addition, every event is visually inspected to verify that a beam-plasma interaction happened, which is possible due to the relatively low number of events (~ 100) per data set.

For data sets recorded under same experimental conditions (in this context, i.e. equal n_{Rb} , g , t_{RIF} , proton bunch parameters and SC settings), variations in f_{mod} up to 1.8 GHz (rms) from event to event are observed. These frequency variations caused by noise on the images appear in particular at low n_{Rb} where the number of micro-bunches on the SC is small. The implied variations in plasma density on the percent level are significantly higher than what is expected from the Rb vapor density measurement ($<0.3\%$, see also appendix A.2.1). These large variations also stands in contradiction to observations of the SM, for example presented in Chapter 6.3 of this thesis. A frequency variation of 1.8 GHz would translate into a phase variation of 81% (of 2π) for the micro-bunches $2\sigma_t$ behind the start point of the SM, which is not observed. However, the determination of the correct frequency bin is of utmost importance for the phase analysis. A correct interpretation of any observed phase behavior is only feasible for a constant f_{mod} . We therefore interpret the average of the measured modulation frequencies as the modulation frequency to be used in the entire phase determination of the respective data set. This conclusion is justified based on the Rb vapor density measurement, the full ionization of the Rb vapor within the plasma column ($>99.9\%$, [51]) and the proven correlation between plasma density n_{e0} and modulation frequency f_{mod} [51].

To study the phase reproducibility, we select the phase value of the frequency bin that corresponds to that average frequency for each event. With the position of the LRS known (see Chapter 4.2), the modulation phase of all events of a data set

can be referred to each other. The time difference between the LRS and the next micro-bunch is determined from this phase relative to the LRS using the average modulation frequency. For the SC image shown in Fig. 33, the phase with respect to the LRS is 0.8 rad for an average frequency of 120.8 GHz, corresponding to a time difference of 1.1 ps.

We characterize the phase variation $\Delta\Phi$ observed for a set of events recorded under equal experimental conditions in two ways. We calculate the full range of observed phases, given as the fraction of one plasma period, in % of 2π . This range is expected to cover almost the full 2π of a plasma period when the SMI dominates, but only a small fraction of it when the SM is seeded. Further, we determine the rms of the phase distribution, also in % of 2π . While we expect a small variation on the percent level for the case of SSM, the rms of a random phase distribution in the case of SMI is expected to be near the rms value of a random distribution of $100\%/\sqrt{12} = 29\%$. The beforehand mentioned uncertainty in the modulation frequency determination does not influence the phase analysis. The value of the phase variation depends only negligibly on the selected average frequency, as long as the variation in frequency is small when compared to the DFT bin width. This can be seen in Fig. 35, where the phase variation is plotted versus the average modulation frequency for an exemplary data set at $n_{e0} = 1.81 \times 10^{14} \text{ cm}^{-3}$, equivalent to 121.0 GHz. The phase variation remains within 2.8% and 3.1% of 2π for frequencies $\pm 4 \text{ GHz}$ around the average

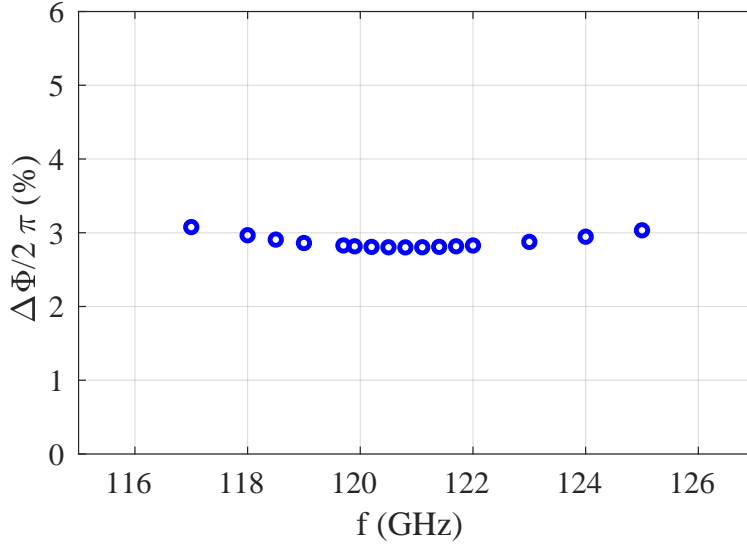


Figure 35: Observed phase variation $\Delta\Phi/2\pi$ versus chosen DFT frequency bin for a data set recorded at $n_{Rb} = 1.81 \times 10^{14} \text{ cm}^{-3}$, corresponding to a modulation frequency of $f_{mod} = 121.0 \text{ GHz}$.

modulation frequency measured to $f_{mod} = 120.8$ GHz, which justifies the use of the average modulation frequency for the phase determination.

Chapter 5

Characterization of the Laser Reference Signal

The quality of the phase reproducibility studies as well as of the stitching and averaging of the SC images strongly depends on the uncertainties that originate from the LRS (assuming a satisfying data quality), as the observed variation in phase or timing is convoluted with the measurement uncertainties of the LRS. This chapter aims to identify the sources that contribute to this uncertainty and to quantify them. Since the LRS can serve as a relative or absolute timing signal on the SC images, it is important to differentiate between uncertainties that affect the data analysis in both cases or that only come into play when the LRS is used as an absolute timing signal. The total uncertainty of this diagnostic is an essential requirement to understand which part of the results, e.g. the observed phase variations, have a physical origin and which can be attributed to the measurement errors.

5.1 The Identification and Determination of Uncertainties

The potential measurement uncertainties introduced by the LRS include a trigger system jitter between the LRS and the SC trigger system, a timing jitter between the ionizing laser pulse and the LRS, and uncertainties in the localization of the LRS on the image, i.e. also the determination of Δt_{LRS} . Further, the accuracy and precision of the translation stage in the delay line of the LRS's beam path (see Fig. 23(c)), i.e. the reproducibility and precision of its travel distance has to be considered. This last uncertainty only affects data sets in which the LRS is used for absolute timing measurements, i.e. where the translation stage is moved within the recording of a data set. This includes the stitching of SC images and the determination of the timing difference of micro-bunches with respect to the RIF. Data where the LRS is used only as a relative diagnostic is not affected by this. Examples for this are the phase determination or the averaging of SC images.

We determine the uncertainties mentioned first from SC images where the LRS and the ionizing laser pulse are simultaneously visible on the same 73 ps SC window. Figure 36 shows an example image with the LRS on the right and the ionizing laser

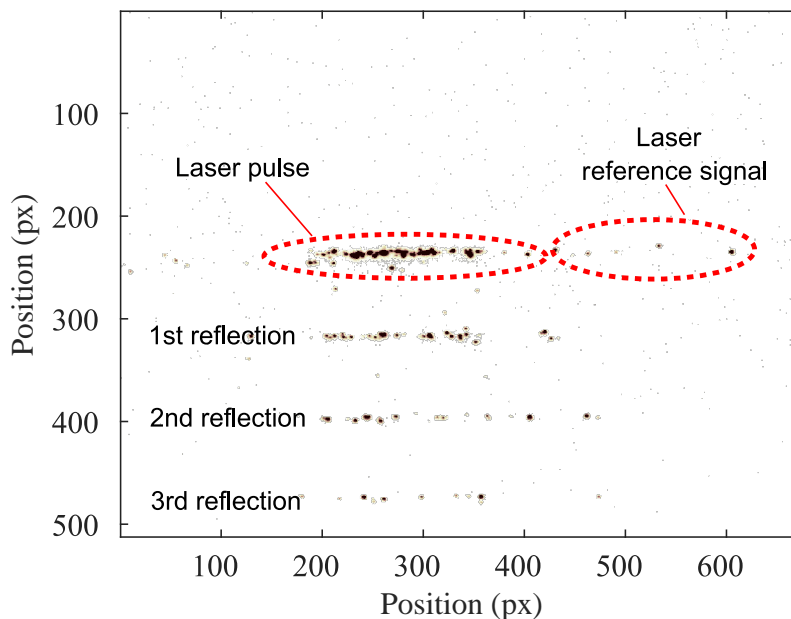


Figure 36: Raw SC image with the LRS (left signal) and the ionizing laser pulse (right signal) in low-energy mode visible, similarly to Fig. 24. Reflections of the laser pulse created by multi-surface reflection on glass are additionally visible.

pulse in low power mode on the left. Below the ionizing laser pulse, the image shows three reflections of the pulse caused by a 5-mm-thick piece of glass placed in the beam path. These reflections were created solely for these measurements to simulate the presence of several LRSs, needed in the following characterization of the LRS uncertainties.

5.1.1 Trigger System Jitter between Laser and SC

We start with the measurement of the trigger system jitter between the SC and the laser, which was the main reason to install the LRS into the experiment. As mentioned before, this jitter causes the proton micro-bunches to jitter around a certain position on the SC images. Because this jitter is much larger than the bunch train period, it makes it impossible to compare consecutive events to each other. To characterize this jitter, we determine the position of the LRS for 100 events that only show the LRS, following the procedure described in Chapter 4.2. A histogram of the detected positions on the temporal axis of the images in pixel is depicted in Fig. 37. The position of the LRS varies over a total range of 160 px or 22.8 ps. The standard deviation of this variation is 34 px or 4.8 ps. It is important to note that because

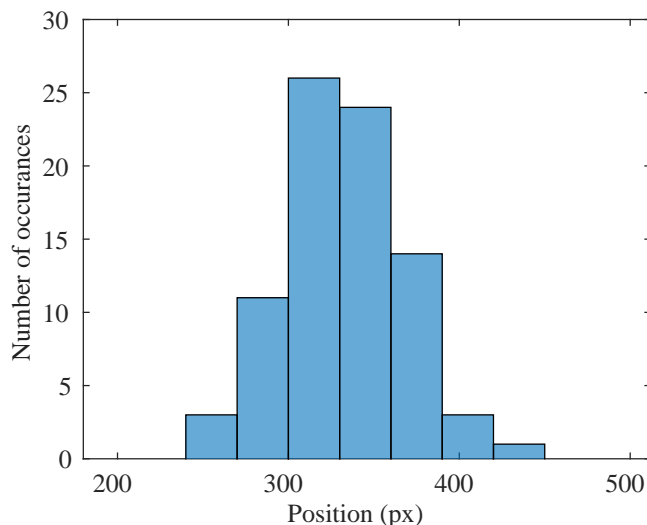


Figure 37: Histogram of the detected position of the LRS in pixel on the 73 ps window. The variation in position is due to the triggering system jitter.

we use the LRS, this jitter has no direct impact on the quantitative outcomes of the data analysis. However, in case the features of interest (e.g. the onset of the self-modulation or a certain micro-bunch within the bunch train, but also the LRS) are placed on the edge of the SC image, this jitter might cause that these features are not visible on the image for some events. This is avoided by placing them at times within approximately 15 ps from the ends of the time window.

5.1.2 Uncertainty on the Temporal Position of the LRS

The potentially largest contribution to the measurement uncertainty with which the LRS impacts the data analysis comes from the determination of the temporal position of the LRS on the image itself. To determine this uncertainty, we use the multi-layer reflections shown in Fig. 36. Since the LRS is a replica of the ionizing laser pulse, having these reflections is equivalent to having multiple LRSs in one image. The uncertainty in measuring the spacing of the reflections is therefore used to estimate the uncertainty in determining the timing of the LRS. Assuming that the beam path is unaltered, including that the thickness of the piece of glass in the beam path that causes the reflections does not change its relative angle and thus thickness, we regard the temporal spacing between two reflections as constant.

We use the laser pulse itself and the first reflection for this purpose. A histogram of the detected spacings for 1000 images is plotted in Fig. 38. The distribution is centered around 80.6 px with an rms width of 1.1 px, corresponding to 157 fs on the

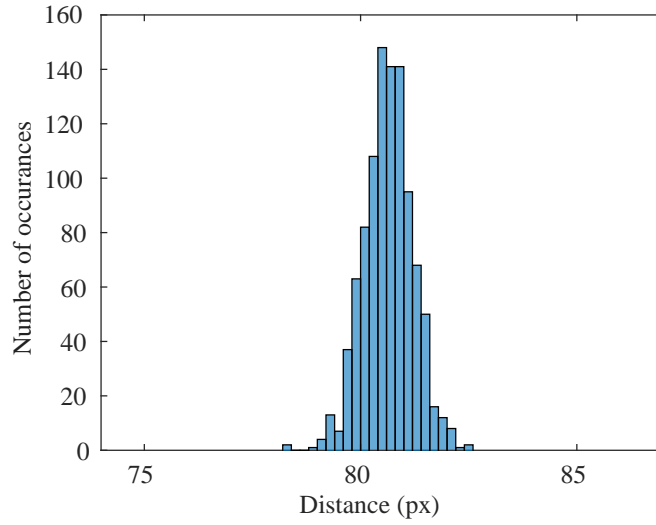


Figure 38: Histogram of the detected temporal spacing between the ionizing laser pulse and its first reflection for 1000 events, as observed with the SC. The measured mean value is (80.6 ± 0.6) px.

73 ps time window. This value represents twice the error of localizing one LRS (being added in quadrature). Accordingly, the uncertainty in determining the location of the LRS is $157 \text{ fs}/\sqrt{2} = 111 \text{ fs}$. We note here that this value represents the uncertainty in determining a for the SC well adjusted signal strength where a broadening of the signal due to space charge effects in the SC is avoided. With higher intensities, the LRS appears broader as mentioned in Chapter 3.4.3.1, which can influence the measurement uncertainty.

5.1.3 Timing Jitter between Laser Pulse and LRS

A timing jitter between the time-of-arrival of the ionizing laser pulse and the LRS might originate from vibrations, air drafts and pointing jitters in its in-air, 60-m-long optical transfer line (see Chapter 3.4.3 and Fig. 23). From 100 images with the ionizing laser pulse and the LRS displayed simultaneously on the 73 ps window (as in Fig. 24 and 36), we determine the position on the temporal axis of both signals and analyze the relative position to each other. The detected positions of both signals are plotted in Fig. 39(a). The figure clearly shows the large timing jitter due to the triggering system (4.8 ps rms, determined in Chapter 5.1.1) on the 73 ps time window. It also shows that the jitter between the two laser pulses is much smaller. This is confirmed by Fig. 39(b) which shows the relative position between the two laser pulses in pixels. The average measured relative position of both signals is 4.0 px

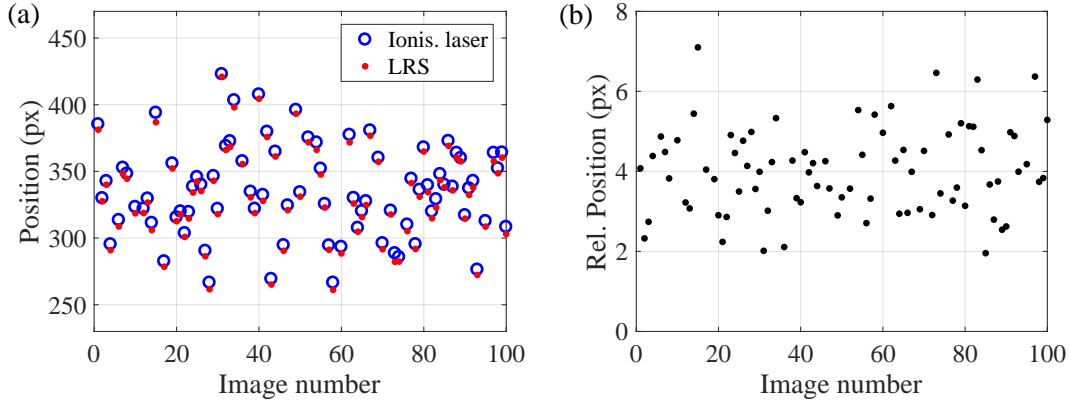


Figure 39: (a) Measured positions of the ionizing laser pulse and the LRS with both simultaneously visible on the same 73 ps SC window for 100 events. (b) Calculated relative position between both signals from (a). The mean is (4.0 ± 1.1) px.

with a standard deviation of 1.1 px. This uncertainty of 1.1 px or 157 fs is as large as the uncertainty in determining the position of the LRS found in Chapter 5.1.2 (also 157 fs). We therefore conclude that within the measurement uncertainty, no timing jitter between the ionizing laser pulse and the LRS is observed. As a side note, we add that a relative position to each other of 4.0 px on the 73 ps time window means that for this data set, the ionizing laser pulse and the LRS are synchronized within 0.6 ps (see Chapter 3.4.3.2 for the matching of both signals).

5.1.4 Uncertainty on Translation Stage Movements

For the study of micro-bunches in the back of the proton bunch as a function of their timing with respect to the RIF (and for delays larger than the length of the used SC window), the precision with which the delay between the RIF and the LRS is set gains importance as a potential uncertainty on the absolute timing and delay values. As mentioned, measurements where the LRS serves only as a relative timing signal (i.e. for example Fig. 39(a)) are not affected. We evaluate the precision and repeatability of the translation stage used to set this delay by moving it repeatedly over various travel distances and positions between 0 between 60 mm. The travel range of 60 mm, corresponding to a round trip delay of $\Delta t_{LRS} = 400$ ps, is approximately equal to the range used in the experiment. As a reminder, the delay induced on the LRS for a travel distance s of the translation stage is $\Delta t_{LRS} = 2s/c$ and the position of the stage is set in 0.1 mm steps (see Chapter 3.4.3.2). For 70 positions, we measure the actual displacement s_m using a caliper with 0.05 mm accuracy (equal to 0.08 % over 60 mm) and compare it to the set travel distance s_{set} .

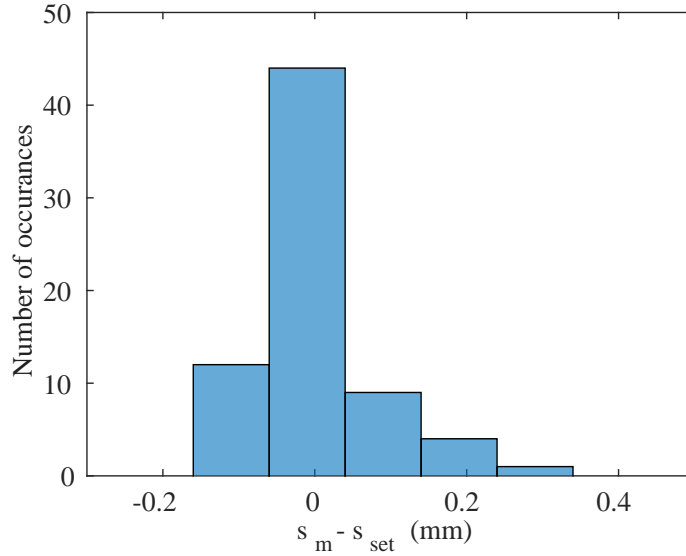


Figure 40: Histogram of the deviation between measured and set displacement of the translation stage $s_m - s_{set}$.

The result, given as $s_m - s_{set}$, is illustrated by the histogram in Fig. 40. The deviation from the set value is on average -0.01 mm, with an rms width of 0.16 mm. This corresponds to an uncertainty in setting the absolute value of the delay of 529 fs. This is thus the uncertainty on the delay between data sets acquired at various positions along the proton bunch (e.g. used in stitched images like Fig. 31, or Fig. 49(a) later in this thesis).

5.2 The Total Measurement Uncertainty

We determine the total measurement uncertainty implied by the LRS on the SM studies. As mentioned previously, the trigger system jitter between the SC and the laser does not influence the measurement uncertainties. In case the LRS is used as a relative timing signal, e.g. for the studies of the phase reproducibility at a constant position relative to the proton bunch center and to the RIF, only the uncertainties in determining the temporal position of the LRS on SC images (111 fs rms) and the jitter of the relative delay between both pulses (below measurement limit) have to be taken into account. When determining the delay between the LRS and the RIF with the same procedure, the uncertainty on the temporal position must be taken into account twice, adding (in quadrature) to 157 fs.

The total error when the LRS is also used as an absolute timing signal (i.e. for

studies as a function of the position along the proton bunch) is obtained by adding the uncertainty on the translation stage movement (529 fs), also in quadrature. The resulting value is 552 fs (rms), mainly dominated by the uncertainty implied by the translation stage.

The data presented in this thesis was mostly obtained with densities of $n_{Rb}=0.94\times 10^{14}\text{ cm}^{-3}$ and $1.81\times 10^{14}\text{ cm}^{-3}$. With these densities, the electron plasma frequencies are $\cong 87.1\text{ GHz}$ and $\cong 120.8\text{ GHz}$, corresponding to periods of 11.5 ps and 8.3 ps, respectively. Here, the total relative errors correspond to 1.9% of 2π and 1.4% of 2π . We also note that these values describe the uncertainty of the diagnostic itself. The additional error of 0.5 px or $\approx 0.6\%$ that originates from the analysis code by rounding the pixel number that corresponds to the location of the LRS (see Chapter 4.3) is thereby not included and must be added extra, if needed.

Chapter 6

Instability and Seeding of the Self-Modulation

The experimental results presented in this chapter characterize the different regimes of the SM expected for different initial wakefield amplitudes provided by the RIF of the ionizing laser pulse. In the non-seeded case, the plasma is created ahead of the proton bunch or at the very beginning of it and the SM grows as an instability from noise present in the system, which is the regime of the SMI. In [55], shot noise is calculated to be on the order of 10 kV/m. Another source of noise can be irregularities in the proton bunch distribution due to the beam transport of unknown extent. For simplicity, we refer to both (shot noise and bunch irregularities) as the noise in the system. When the RIF is placed within the proton bunch, i.e. when seeded, the sudden onset of the plasma triggers the start of the SM because of sufficiently high initial transverse wakefield amplitudes. The amplitude of the initial transverse wakefields is controlled through the timing of the RIF relative to the bunch center t_{RIF} , which changes the bunch density ($W_{\perp,RIF}(n_b(t_{RIF}))$), Chapter 2.3, Eq. 2.18). The characterization of these two different SM regimes is the goal of this chapter.

To begin, we compare consecutive SC images with respect to the appearance of the SM and the phase reproducibility of the micro-bunches for clear cases of SMI and SSM. By measuring the phase variation as a function of t_{RIF} , we determine the transition point between both regimes, i.e., which initial transverse wakefield amplitude is required to overcome the noise in the system. We give an explanation for the randomness of the phase of the micro-bunch train for the non-seeded case. Last, for the regime of SSM, we study the reproducibility of the phases or timing of the micro-bunches as a function of their position along the bunch (and with constant t_{RIF}). We also evaluate the evolution of the relative modulation phase along the bunch and compare the corresponding modulation frequencies to each other. The experimental results for these measurements were recorded during the beam time periods of AWAKE in May and November 2018.

6.1 Observation of Different SM Regimes

We demonstrate the existence of the two distinct SM regimes by placing the RIF once ahead of the proton bunch for SMI and once close to the bunch center where SSM was already experimentally observed during previous measurements (e.g., in [51]). For each case, we compare the timing or phase of the micro-bunch train between consecutive events in composite images. The Rb vapor and thus plasma density during the experiment was chosen to be $\approx 1 \times 10^{14} \text{ cm}^{-3}$ in order to have a longer plasma period for a more accurate determination of the phase reproducibility, but still a minimum of six micro-bunches visible per 73 ps SC window. The density profile is chosen to be flat, i.e. no linear density gradient along the source is set, $g = 0$. We use a bunch population of $N_b \approx 3 \times 10^{11}$ protons per bunch. The duration of the (unmodulated) proton bunch is measured from 1 ns SC images without plasma present in the source, giving $\sigma_t = 250$ ps.

6.1.1 The Self-Modulation Instability Regime

To study the behavior of the micro-bunch train when no seed is provided (SMI), we use the following SC and timing settings: the RIF is placed at $t_{RIF} = 600$ ps (or $2.4\sigma_t$) ahead the proton bunch center. The 73-ps-long SC window (slit width 20 μm , MCP gain 40) and the LRS are placed 150 ps ($0.6\sigma_t$) ahead of the bunch center, i.e., the timing difference between RIF and the LRS on the images $\Delta t_{LRS} = 450$ ps ($1.8\sigma_t$). In total, 18 events were recorded with these settings. The measured average modulation frequency is 87.1 GHz, equivalent to a modulation period of $\cong 11.5$ ps. The corresponding plasma (and Rb vapor) density¹ is $n_{e0} = 0.94 \times 10^{14} \text{ cm}^{-3}$.

An example of a SC image of this data set is shown in Fig. 41. The single image itself shows micro-bunches with no visible difference to images when the SM is seeded (see e.g. Fig. 31 or [51]). To obtain the composite image from the set of images, we align the center of ten consecutive images² in time using the LRS (see Chapters 3.4.3 and 4.2, visible at $t = 0$ ps in Fig. 41, not visible on the composite images) and normalize each image to its incoming bunch population. The aligned images are then displayed above each other.

The result of this procedure is shown in Fig. 42 for the ($-1 \text{ mm} < x < 1 \text{ mm}$) range, with the temporal axis of the SC on the horizontal axis and the image number on the vertical axis. The composite image clearly shows that even though all events have a constant offset with respect to the RIF as indicated by the LRS at $t = 0$ ps (LRS not

¹We note that during the recording of this data set, the Rb vapor density measurement was not operational due to a fault of the white light laser that supplies the light for the interferometer (see Chapter 3.4.1). Because of the well-proven agreement between the vapor, plasma and modulation frequency ([51]), we calculated the corresponding density value for this data set only.

²Only ten out of 18 events are shown for a better visibility of the single events.

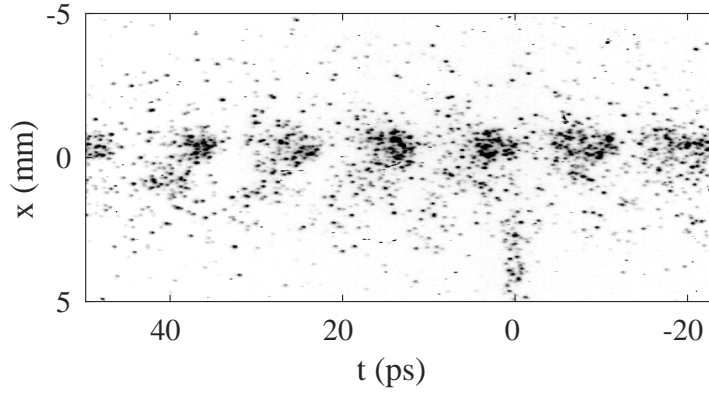


Figure 41: 73 ps SC image of the modulated bunch without seeding with the RIF 600 ps (or $2.4\sigma_t$) and the LRS 150 ps ($0.6\sigma_t$) ahead of the bunch center.

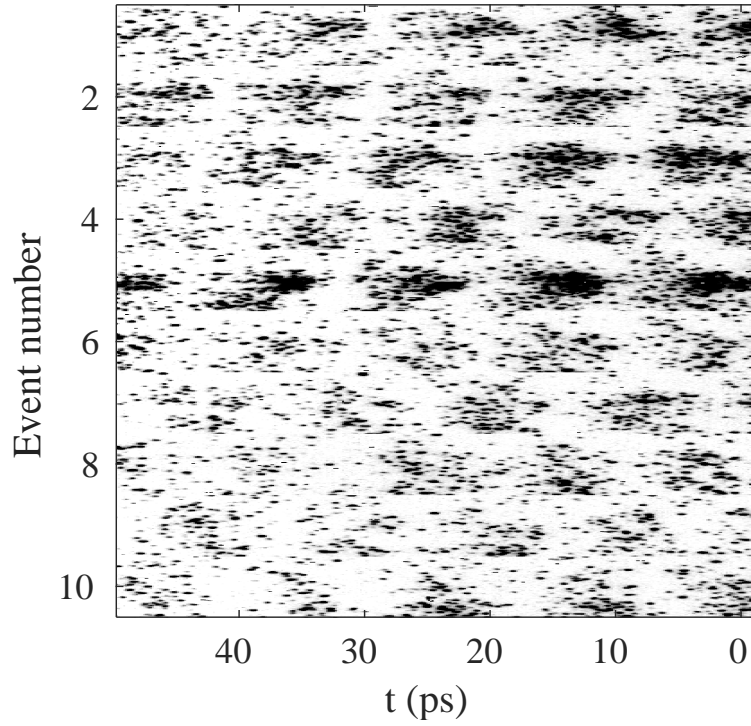


Figure 42: 73 ps composite image of ten events with the RIF 600 ps ($2.4\sigma_t$) and (b) RIF 350 ps ($1.4\sigma_t$) ahead of the bunch center. Front of the bunch on the right hand side. Events aligned w.r.t. LRS at $t = 0$, not shown), LRS 150 ps ($0.6\sigma_t$) ahead of bunch center, $n_{e0} = 0.94 \times 10^{14} \text{ cm}^{-3}$.

visible), the micro-bunches appear at no particular timing from event to event. The timing and phase of the micro-bunch train vary significantly (i.e., by one or more than one period). In addition, the bunch charge density also varies considerably from event to event. This can be assigned to amplitude variations of the focusing and defocusing fields as the electric fields might develop with different initial wakefield amplitudes and growth rates. These two observations, i.e., the timing and charge density variations, are typical for an instability-based process.

We determine the variation of the phase with respect to the LRS for each of the 18 events in the data set to quantify the observed variations. The phases of the bunch train are determined according to the procedure explained in Chapter 4.4 with 87.1 GHz as average modulation frequency. Already with this relatively small number of events, the measured phases cover 96% of 2π and the rms of the distribution is 30% of 2π . This is in good agreement with the variation of a uniform distribution of $1/\sqrt{12} = 0.289$, which confirms the observations in Fig. 42. When the SM process is not seeded, the SM grows as an instability.

The Cause of Random Phases

The variations in phase with SMI can in general be caused by changes in modulation frequency or by varying starting points of the SM. However, we consider the modulation frequency constant as it is demonstrated in [51] that the SM modulates the bunch with the plasma electron frequency and no significant deviations from this are observed so far. Also the Rb vapor density and thus the plasma electron frequency can be considered constant (within $< 0.3\%$) as seen from the Rb vapor density measurement (see Appendix A.2.1) and temperature readings [122]. Therefore, to determine the cause for the randomly distributed phases we create a composite image of 211-ps-long SC images that show parts of the proton bunch closer to the RIF where the SM grows. We have to note that the only recorded data that displays this part of the bunch while large phase variations are observed is recorded at different experimental parameters ($n_{e0} = 1.81 \times 10^{14} \text{ cm}^{-3}$, $g = 0$, $t_{RIF} = 650 \text{ ps}$ ($2.6\sigma_t$) and $\Delta t_{LRS} = 350 \text{ ps}$ ($1.4\sigma_t$), i.e., the LRS and SC window are 300 ps ($1.2\sigma_t$) ahead the bunch center). However, we expect the conclusions to be the same at all densities.

The composite image of ten consecutive events with these parameters and aligned with the LRS at $t = 0$ (again not shown) is presented in Fig. 43. For a better visibility of the modulation profile, this image uses a different color map. In general, the parts of the proton bunch visible on the right side of the image ($t < -60 \text{ ps}$) show no sign of modulation. The SM seems to evolve from different times, between -50 ps and 0 ps on the image, i.e. 300 ps and 350 ps after the RIF. Also the the time difference from the point where a first change to the proton bunch density is visible to the first distinct micro-bunch is different from event to event and stretches over up to $\sim 100 \text{ ps}$ (see e.g. event number seven and ten). Also the identification of the first

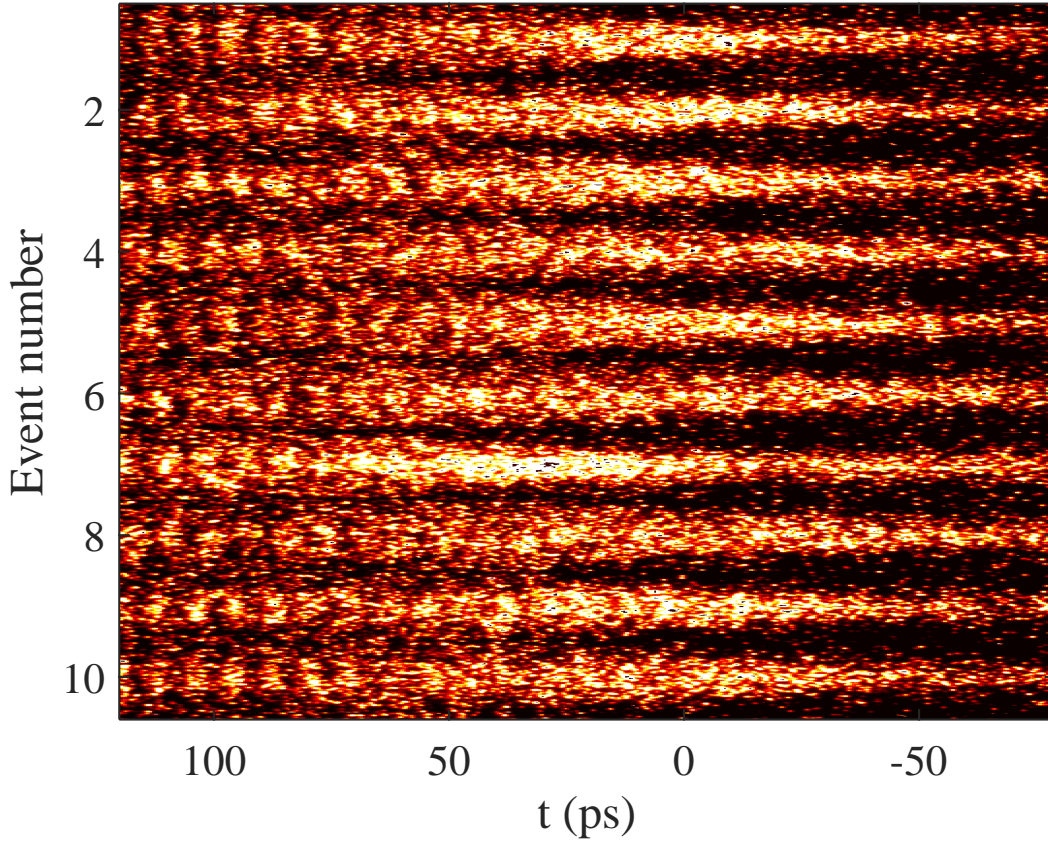


Figure 43: 211 ps composite image of ten events with the RIF 650 ps ($2.6\sigma_t$) ahead of the bunch center and 350 ps ($1.2\sigma_t$) ahead of the SC window and LRS (at $t = 0$, not visible). Front of the bunch on the right hand side. Events aligned w.r.t. LRS, $n_{e0} = 1.81 \times 10^{14} \text{ cm}^{-3}$.

micro-bunch is difficult due to a different evolution of the modulation from event to event. The modulation frequency (obtained from SC images that do not show the onset of the SM but only micro-bunches) agrees within the uncertainties with the expected frequency of 120.8 GHz calculated from the Rb vapor density measurement.

To better distinguish the unmodulated part of the bunch from the onset of the SM, Fig. 44 compares a 73 ps SC image without plasma to two SMI events with $n_{e0} = 1.81 \times 10^{14} \text{ cm}^{-3}$, $g = 0$ and $t_{RIF} = 550 \text{ ps}$ ($2.2\sigma_t$) (same other experimental parameters). The corresponding time profiles (obtained according to Chapter 4.4.1) are shown on their right. The LRS indicates here the delay between the image/LRS with respect to the RIF of 200 ps. Accordingly, the LRS sets $t = 200 \text{ ps}$ on each

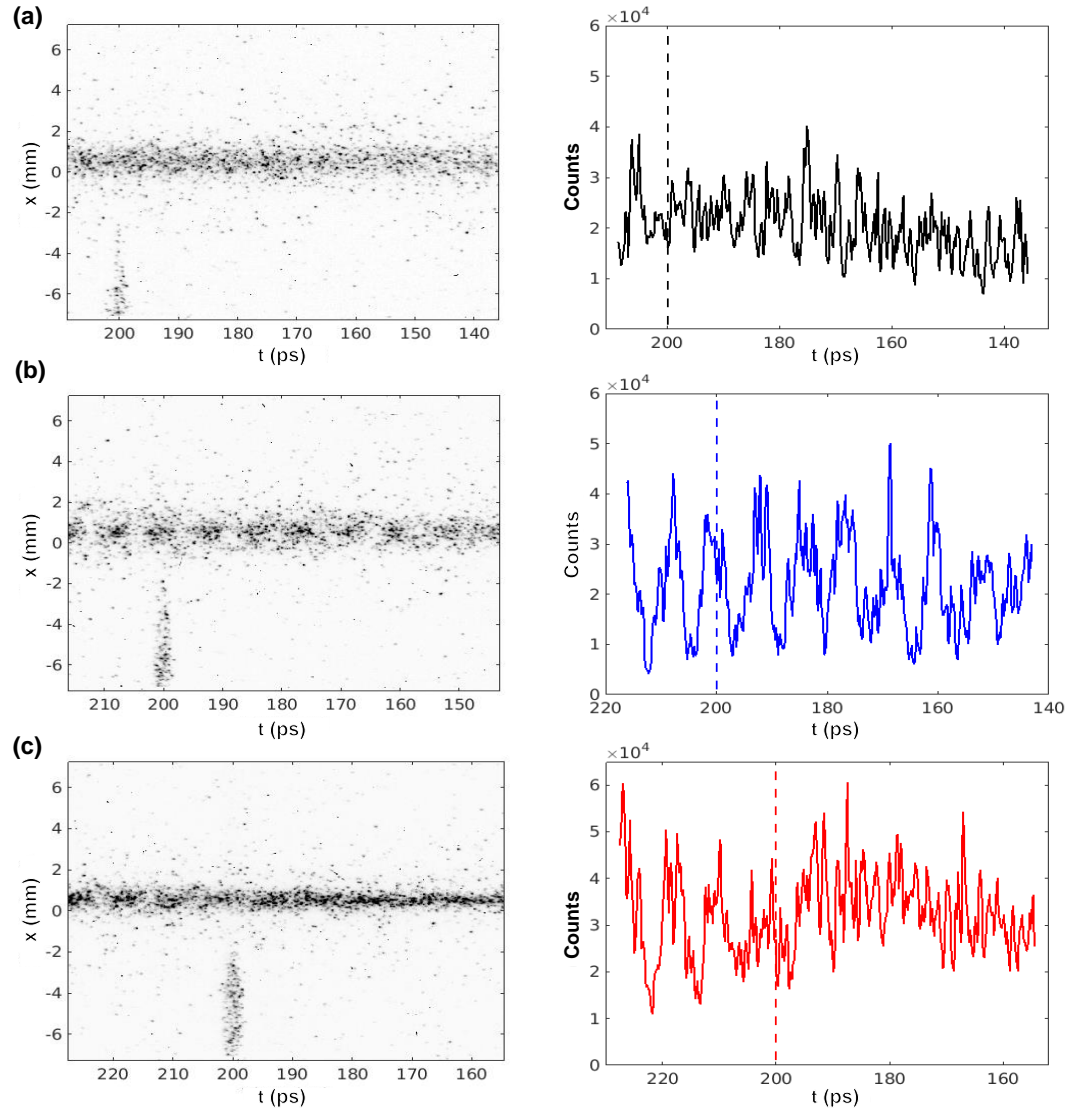


Figure 44: Left column: 73 ps SC images with RIF 200 ps ahead of the window and LRS for the cases of no plasma in (a) and for $n_{e0} = 1.81 \times 10^{14} \text{ cm}^{-3}$ in (b) and (c). Right column: corresponding time profiles of the bunch charge density. Dashed lines mark the position with 200 ps delay with respect to the RIF, as indicated by the LRS on the images.

image¹, the RIF is set at $t = 0$ on the same scale. The image with the laser off and thus without plasma (Fig. 44(a)) shows the unmodulated proton bunch, its time profile only exhibits noise from the SC image itself. In Fig. 44(b), micro-bunches are visible along the entire image, which is also confirmed by the equivalent time profile. The SM starts at a time before the window that is shown on the image. In Fig. 44(c), the SM becomes visible for $t > 195$ ps, both in the image and in the time profile. Before that, the image shows a profile similar to that of the no-plasma case of Fig. 44(a). Here, the bunch appears unmodulated but focused due to adiabatic focusing which starts at the location of the RIF. This can also be seen from the fact that even though the images are normalized to the incoming bunch charge, the counts of the time profile are higher in Fig. 44(c) than in (a).

The comparison of Fig. 44(b) and (c) in combination with the observations in Figs. 42 and 43 therefore proves that when no seeding is provided, the SM grows as an instability from a location or time along the bunch after the RIF that changes from event to event. The start of SM (< 150 ps on (b) and > 195 ps on (c)) can vary by at least 45 ps $\gg 1/f_{mod} = 8.26$ ps, thus explaining the phase variation observed e.g. on Fig. 42.

6.1.2 The Seeded Self-Modulation Regime

In order to obtain a composite image similar to Fig. 42 for the seeded case at otherwise equal parameters, we set $t_{RIF} = 350$ ps ($1.4\sigma_t$) to provide larger initial transverse wakefields at the location of the RIF. To observe the same part of the proton bunch, the position of the SC window and LRS with respect to the bunch center remain unchanged at 150 ps ($0.6\sigma_t$) ahead of the bunch center. Also all other parameters are kept unchanged. Figure 45 shows the resulting composite image, again displaying the center region of ten consecutive events aligned with the LRS (at $t = 0$ ps, not visible).

Clear differences with respect to Fig. 42 are visible. The micro-bunches of the different events line up in time (i.e., in the vertical direction on the image), meaning that timing of the micro-bunches and the phase of the modulation are essentially constant with respect to the RIF from event to event. The bunch charge density in the modulated bunch appears much more consistent than in the non-seeded case. The determination of the phase variation for this data set (16 events, average modulation frequency 87.1 GHz) confirms the observations by giving an rms variation of 6% of 2π and a total range of $< 30\%$ of 2π . These observations match the expectations of a seeded process such as the SSM. They imply that seeding the SM does not only trigger the SM at the RIF, but also cause the SM to evolve from the exactly same point in a reproducible way (and with constant modulation frequency as already known).

¹The LRS can be sent to the SC without sending ionizing laser pulses along the vapor source by closing the shutters in the laser room, as described in Chapter 3.4.3.1.

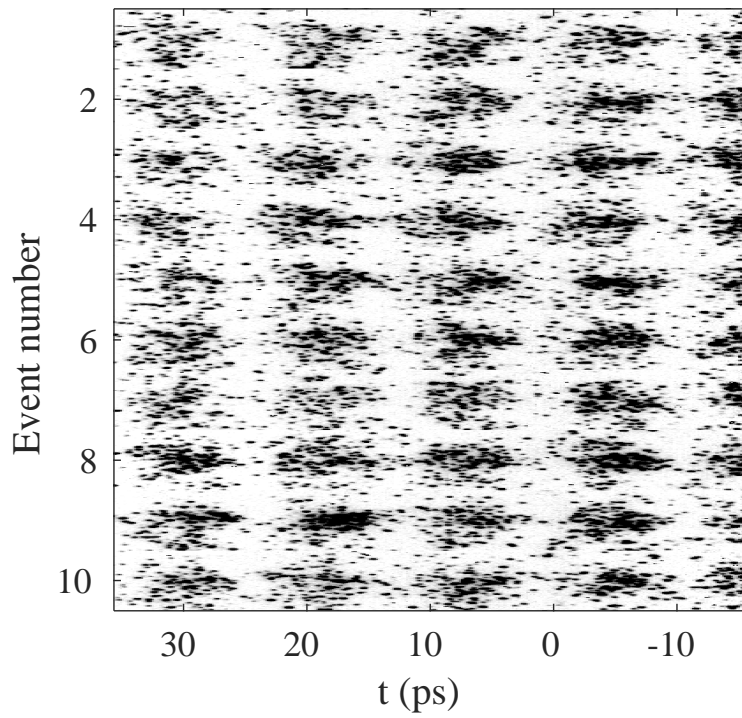


Figure 45: Composite image of ten events with the RIF 350 ps ($1.4\sigma_t$) ahead of the bunch center. Front of the bunch on the right hand side. Events aligned w.r.t. LRS, at $t = 0$, not shown), LRS 150 ps ($0.6\sigma_t$) ahead of bunch center, $n_{e0} = 0.94 \times 10^{14} \text{ cm}^{-3}$.

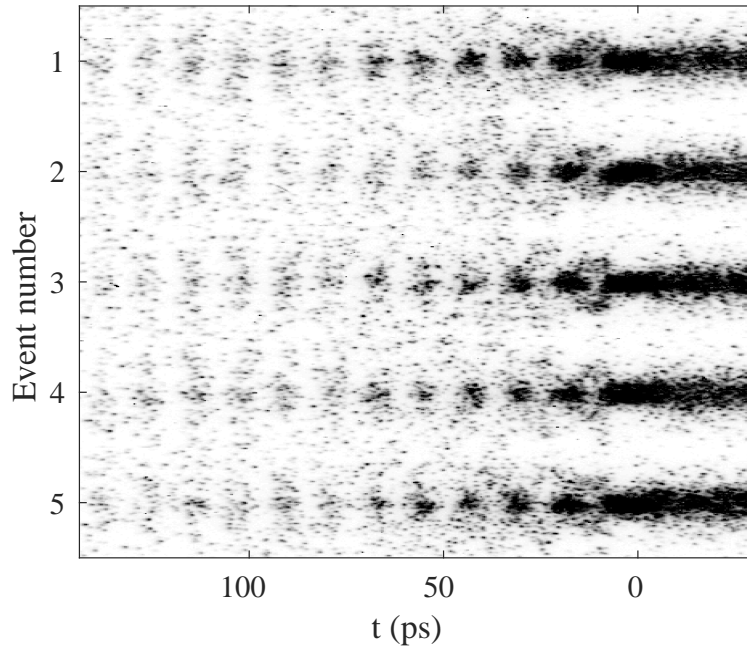


Figure 46: Composite image of five events with the RIF at the bunch center ($t_{RIF} = 0$) and the LRS (at $t = 0$, not shown) synchronized with the RIF. Front of the bunch on the right hand side. $n_{e0} = 0.94 \times 10^{14} \text{ cm}^{-3}$.

This is confirmed by the composite image in Fig. 46. It shows five SSM events on the 211 ps time window where the LRS (at $t = 0$, not shown) is synchronized with the RIF at the proton bunch center, i.e., $t_{RIF} = \Delta t_{LRS} = 0$. Accordingly, parts of the images with $t < 0$ show the unmodulated proton bunch that does not travel in plasma but in Rb vapor. For all events, the modulation starts by focusing the bunch at $t \sim 0$ where the initial transverse wakefield at the RIF seeds the SM. The SM evolves equally from event to event and all micro-bunches behind the RIF show the same timing or phase relative to the RIF.

In summary, we conclude that when an insufficient initial transverse wakefield amplitude is provided by the RIF, i.e. smaller than the noise in the system, then the SM starts at random points along the bunch and grows as an instability, leading to a distribution of the phase of the micro-bunch train that varies by more than a modulation period relative to the RIF. This is the regime of the SMI. By contrast, when the RIF is placed closer to the bunch center to provide larger initial wakefield amplitudes, the SM is triggered instantaneously, i.e. starts at the time of the RIF. The entire process of SSM, especially the phase or timing of the micro-bunches, is reproducible from event to event. Assuming that wakefields driven in the plasma are tied to the RIF and the modulation profile of the proton bunch after saturation of the SM process [67], the phase of wakefield is also reproducible from event to event. The results presented here therefore show that by seeding the process one can control the phase of the (accelerating and focusing) wakefields driven by the micro-bunches as it is required for deterministic acceleration of externally injected electrons in a possible wakefield accelerator.

6.2 Transition between SMI and SSM

The results in paragraphs 6.1.1 and 6.1.2 show the existence of the two clearly distinguishable SM regimes of SMI and SSM. As a longer train of micro-bunches translates into more micro-bunches that then coherently drive large wakefields, there is a strong motivation to place the RIF as early as possible within the bunch without being in the regime of SMI. To determine this transition between both regimes and to further quantify the observations from paragraph 6.1.1 and 6.1.2, we measure the phase variation $\Delta\Phi$ as a function of t_{RIF} . We vary t_{RIF} in 50 ps ($0.2\sigma_t$) steps between the two observed cases of $t_{RIF} = 350$ ps ($1.4\sigma_t$, Fig. 42) and $t_{RIF} = 600$ ps ($2.4\sigma_t$, Fig. 45), with approximately 18 events per step (including the events of Figs. 42 and 45). As before, the LRS and SC window are kept stationary to observe the same position within the bunch of 150 ps ($0.6\sigma_t$) ahead of the bunch center. The density is $n_{Rb} = 0.94 \times 10^{14} \text{ cm}^{-3}$, with the corresponding average modulation frequency of 87.1 GHz used for the phase determination for all RIF timings. This is

justified as shown in Fig. 47 because within the error bars, the modulation frequency is independent of t_{RIF} and is also well within the range of ± 4 GHz from Fig. 35 over which no effect on $\Delta\Phi$ is observed.

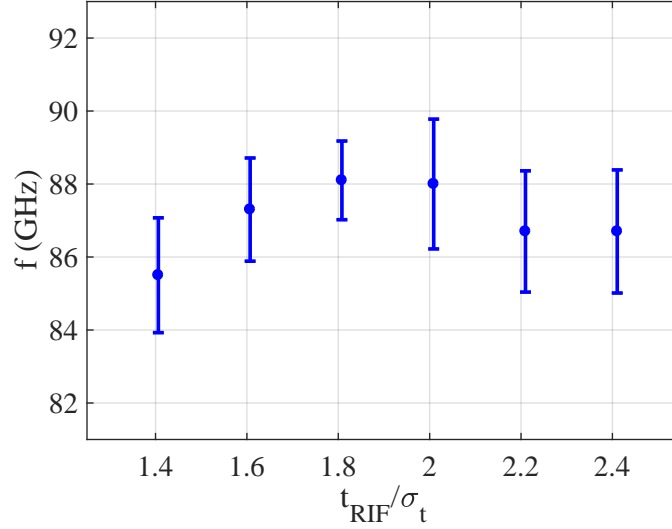


Figure 47: Measured mean DFT frequency per subset vs. t_{RIF} normalized to σ_t . The error bars indicate the rms variation in frequency.

The findings for the phase variation are summarized in Fig. 48. The plot shows the phase variation $\Delta\Phi/2\pi$ in %, once as the range of the measured phase distribution $\Delta\Phi/2\pi$, i.e. the fraction of 2π of a plasma period that is covered (blue diamonds), and once its rms (blue circles), both versus t_{RIF} normalized to σ_t . One observes that for $t_{RIF} \geq 2.0\sigma_t$, the phase distributions cover a range close to 100% of 2π . Since the start point of the SM varies within the proton bunch in the case of SMI (see Fig. 43 and 44), the micro-bunches visible on the SC images might belong to a different plasma period, i.e. the total change in phase is possibly larger than 2π and these values must be considered as modulo 2π . Their rms variation approaches 30% which is close to the value of 28.9% expected for randomly and uniformly distributed values. This shows that for all $t_{RIF} \geq 2.0\sigma_t$ (and under these experimental conditions), the SM grows from noise (shot noise or bunch irregularities) with random timing and thus phase.

For $t_{RIF} \leq 1.8\sigma_t$, in contrast, the ranges cover only a part $\ll 2\pi$ of a period. The RIF provides sufficiently large initial transverse wakefield amplitudes to overcome the noise present in the system. The comparison of the timing of events relative to each other looks similar to those in Fig. 45. The rms variations are around 6% of 2π , showing the phase reproducibility from event to event due to that seeding.

Besides the intrinsic phase variation whose determination is the goal of these

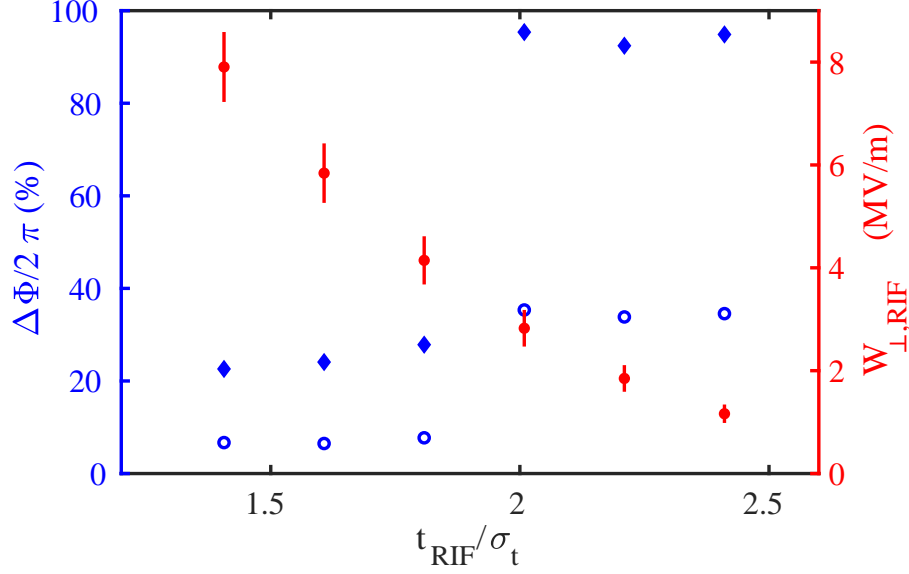


Figure 48: Measured rms (blue circles) and full phase variation (blue diamond), and initial linear transverse wakefield amplitude (filled red circles) as a function of t_{RIF} normalized to σ_t . The error bars indicate the statistical uncertainty of 10.1% (see text). Error bars representing the uncertainty in t_{RIF} due to the 15 ps ($0.06\sigma_t$) rms proton timing jitter are not plotted. Same LRS timing and n_{e0} as in Figs. 42 and 45.

studies, this value of $\sim 6\%$ of 2π is the outcome of the convolution with two other, main contributions. The first is variations in the experimental input parameters such as the proton bunch and plasma density parameters that might lead to a change in modulation phase. For the data sets of this study, we observe an rms variation in incoming bunch population of $\approx 5\%$, in bunch length of $\approx 1.6\%$ and in plasma density of $<0.3\%$. Other possible sources of uncertainty such as the bunch parameters (emittance, transverse bunch size, beam waist size and location) might contribute as well, but are not monitored on an event-to-event basis. The influence of these parameters on the phase is the topic of (ongoing) numerical simulation studies, e.g. by M. Moreira et al. [123]. However, it is difficult to reach an accuracy at the percent level in the relative phase determination. The second contribution to the measured phase variation is the uncertainty in the phase determination itself. This includes signal noise on the SC images (e.g., see Fig. 30), a limited number of only six to nine micro-bunches per 73 ps time window and uncertainties in determining the timing of the LRS from the images (0.16 ps, see Chapter 5.1.2). Rounding of the location of the LRS (see Chapter 4.3) might add up to 0.7 ps or 0.6% of 2π in addition. The observed values for the variation in phase have therefore to be seen as an upper limit only and

the true value is lower. For a further investigation of this topic we refer to Chapter 6.3.

The jump in phase variation when changing t_{RIF} from $2.0\sigma_t$ to $1.8\sigma_t$ shown in Fig. 48 represents the transition from SMI to phase-reproducible SSM when the increasing initial transverse wakefield amplitude exceeds the shot noise and irregularities in the bunch distribution. To determine the wakefield amplitude that corresponds to this transition point and that is minimal required to seed the SM, we calculate the corresponding initial transverse wakefield amplitude for each t_{RIF} according to two-dimensional linear plasma wakefield theory (Chapter 2.2, Eq. 2.18). The corresponding values are plotted in Fig. 48 by the red filled circles. The error bars represent the measurement uncertainty on the field calculation of maximal 10.1% that includes the input parameter variations described above and the 15 ps ($0.06\sigma_t$) rms timing jitter of the proton bunch with respect to the laser system, all added in quadrature. The SMI is observed for wakefield amplitudes $W_{\perp,RIF} \leq (2.8 \pm 0.3) \text{ MV/m}$. Minimum $(4.1 \pm 0.4) \text{ MV/m}$ are required to overcome any noise and to be in the phase-reproducible regime of SSM. This threshold value is substantially larger than the level of shot noise of $\sim 10 \text{ kV/m}$ that is expected according to [55], implying that irregularities in the proton bunch distribution represent a significant contribution to the noise in the system. The observed values in required initial wakefield amplitude correspond to bunch charge irregularities of $\exp(-2.0^2/2) \approx 14\%$ to $\exp(-1.8^2/2) \approx 20\%$, respectively.

Even though these results were obtained from one specific parameter set, the initial transverse wakefield amplitude driven by either the RIF or by bunch irregularities show the same dependencies on those ($W_{\perp}(t) \propto \tilde{n}_b(t)/n_{e0}$), meaning that a change in e.g. the plasma density or the bunch charge density affect both quantities in an equal way. We therefore expect the transition between both SM regimes to happen at the same temporal position within the bunch for other plasma densities. In theory, the same is also expected for changes in the proton bunch population, which changes n_{b0} and thus $\tilde{n}_b(t)$. However, in practice, changing the bunch population usually also implies changes in the bunch size. Bunches of different length might be transported in a slightly different way, i.e. the bunch irregularities originating from the beam transport might be smaller or larger. In that case, the transition point might be observed at a different position or timing with respect to the bunch center.

6.3 Phase Variation along the Modulated Bunch with Seeding

The previous results demonstrate the phase reproducibility for SSM at one fixed position of the SC window within the proton bunch for different values of t_{RIF} . The injection of electron bunches in the wakefields at varying position in the back

of the modulated bunch (as done in [67]), however, requires phase reproducibility along the entire bunch. We therefore evaluate the variation in phase of the first micro-bunch appearing after the LRS for a fixed seed and various delays of the SC window and LRS relative to the bunch center, i.e. with t_{RIF} constant and changing Δt_{LRS} . With a density of $n_{e0} = 1.81 \times 10^{14} \text{ cm}^{-3}$, a flat plasma density profile (i.e., $g = 0$) and $t_{RIF} = 125 \text{ ps}$ ($0.5 \sigma_t$), subsets of ≈ 10 images were recorded while increasing Δt_{LRS} in 50 ps ($0.2 \sigma_t$) increments from 0 to 500 ps ($2.0 \sigma_t$). For these parameters, $W_{\perp, RIF} = 17.3 \text{ MV/m}$. As the RIF is placed much closer to the bunch center than the determined SMI/SSM transition point of $\sim 1.9 \sigma_t$ (Fig. 48), $W_{\perp, RIF}$ is approximately four times larger than the observed threshold value and we expect the SM to be in the SSM regime.

For a first visual inspection, the images are stitched according to the procedure described in Chapter 4.3. The result, in Fig. 49(a), shows that the modulation of the proton bunch starts at the position of the RIF at $t = 0$ as already observed in previous SSM events (e.g. Fig. 46). Micro-bunches are visible over the entire length of more than $2.0 \sigma_t$. This already proves the seeding for each event and phase reproducibility along the entire bunch because the micro-bunches from all events align themselves in time. As mentioned in Chapter 4.3, features would wash out through the stitching process if the timing of the micro-bunches would be randomly distributed.

We quantify this observation by calculating the phase variation for each delay point of the LRS where $\Delta t_{LRS} \geq 50 \text{ ps}$. We ignore the subset with the LRS at t_{RIF} (i.e. $t = 0$) for the phase determination because images include the part of the

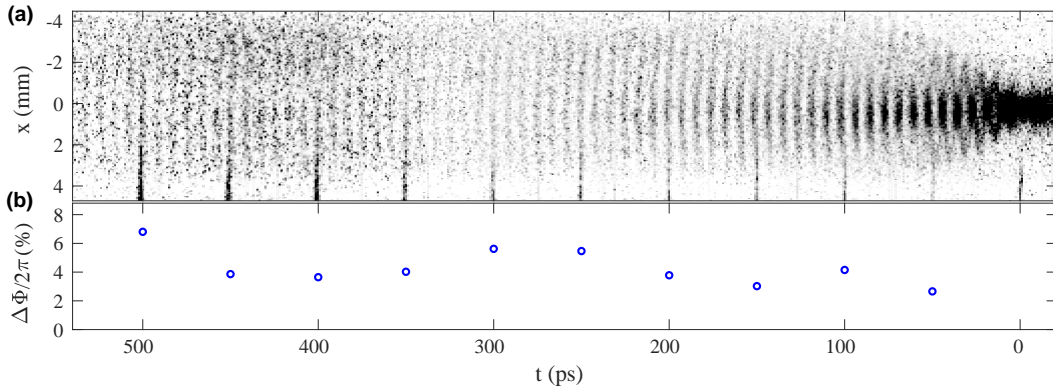


Figure 49: (a) Time-resolved, stitched image of the self-modulated proton bunch with $t_{RIF} = 125 \text{ ps}$ ($0.5 \sigma_t$), $n_{e0} = 1.81 \times 10^{14} \text{ cm}^{-3}$. The RIF is at $t=0$ on the image (not visible). The LRS is visible every 50 ps at the bottom of the image. (b) Modulation rms phase variation for each subset with equal LRS timing.

bunch not in plasma ($t < 0$ ps) as well as the onset of the SM. The length of the first micro-bunch is different from that of following ones [56], for which the DFT frequency and phase determinations might not be accurate. The calculation of the modulation phase uses the average DFT modulation frequency of the data set, as described in Chapter 4.4.3. We determine this average frequency using all events with $\Delta t_{LRS} \geq 50$ ps and use the result of 120.8 GHz for the phase determination of each subset. Using only one frequency value for all events is again justified as the uncertainty on the average frequency of ± 1.3 GHz is small, i.e. does not influence significantly the determination of the phase variation (see Chapter 4.4.3 and Fig. 35). Further, this average DFT frequency agrees well with the frequency expected from the Rb vapor density measurement. The measured vapor density of $n_{e0} = (1.808 \pm 0.004) \times 10^{14} \text{ cm}^{-3}$ corresponds to a plasma electron frequencies of $f_{pe} = (120.73 \pm 0.27) \text{ GHz}$.

Figure 49 (b) shows the rms of $\Delta\Phi/2\pi$ obtained for each Δt_{LRS} increment. Error bars indicating the uncertainty on the LRS position with respect to the RIF of 529 fs are not shown as they do not influence the determination of $\Delta\Phi$. The relative phase variation in each subset is between 3% and 7% of 2π , thus confirming phase reproducibility along the full measurement range of up to $2\sigma_t$ after the RIF. This marks an important result as external injection of electrons is planned $\sim 1\sigma_t$ behind the seed point and thus deterministic acceleration of these electrons is possible independently of the delay between the seed and injection point (as long as injection happens in the focusing and accelerating part of the wakefields).

These values for $\Delta\Phi$ represent again a convolution of the true phase variation with uncertainties originating from input parameter variations and from the phase determination, as discussed previously in paragraph 6.2. Some of the observed variations in $\Delta\Phi$ along the bunch are probably caused by variations in signal strength as visible in Fig. 49(a) and on single images. We consider them the dominant contribution. On one hand, given that the SM grows along the bunch, one would expect the accumulation of timing/phase variations along the bunch. However, this is not observed. On the other hand, a 7% of 2π rms variation in the last window at micro-bunch number 62 ($t = 500$ ps), if interpolated to micro-bunch number seven ($t = 50$ ps), would correspond to a phase variation $< 0.1\%$ of 2π when assuming the accumulation of phases. We therefore conclude that the observed values are dominated by the analysis procedure of images with significant noise, and the real variations are much smaller than those observed, possibly at the sub-percent level.

6.4 Relative Modulation Phase and Frequency along the Bunch

The observed phase reproducibility along the bunch in case of SSM allows for a study of the mean relative phase evolution of the modulation along the bunch. Figure 50(a) compares the mean relative phases or timings of the first micro-bunch appearing after each LRS obtained in the phase variation analysis of the data presented in the previous paragraph 6.3 (i.e., again for a fixed, mean DFT frequency of 120.8 GHz for all subsets). The error bars represent the rms variation of Fig. 49 together with the uncertainty in determining the position of the LRS of 157 fs from Chapter 5.1.2, both added in quadrature. The relative phase increases monotonically from subset to subset as expected. The cause for this is that the number of modulation periods per 50 ps increment between each LRS is not a full integer, i.e. the relative phase or timing of the first micro-bunch after the LRS increases or decreases from one LRS to the next. When assuming a constant modulation frequency equal to the plasma

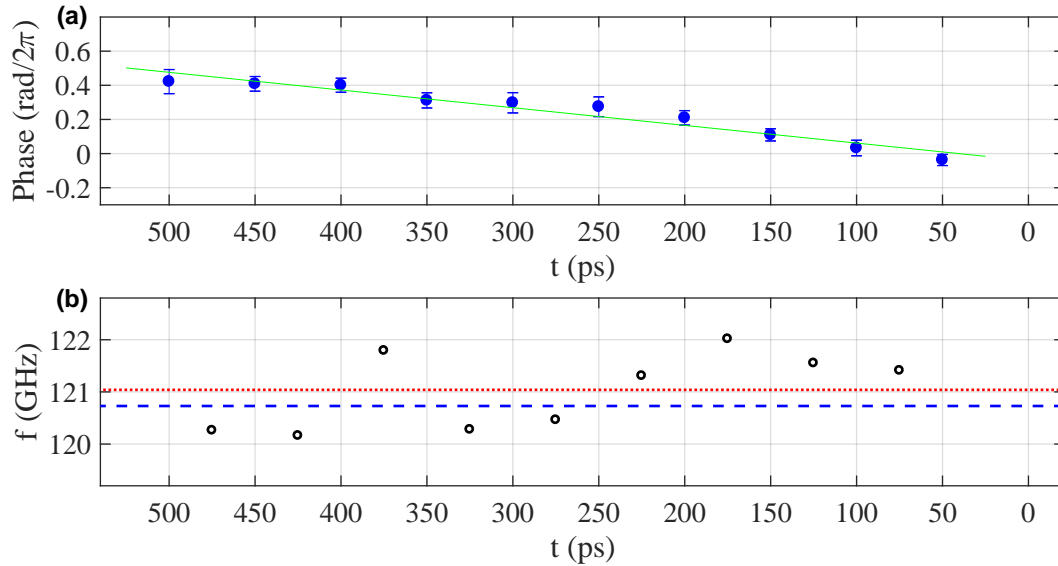


Figure 50: (a) Relative phase of the first micro-bunch after the LRS with respect to the LRS for each subset of images shown in Fig. 49(a). The green line represents a linear fit over the data points, the error bars the rms phase variation together with the uncertainty in the position determination for the LRS. (b) Modulation frequency calculated from the change in relative phase from one subset to the next. The red dotted line indicates their mean, the blue dashed line the frequency expected from the density measurement.

electron frequency, one expects this change in relative phase from subset to subset to be constant, i.e the evolution to be linear. This is confirmed by a linear fit over the data points of Fig. 50(a). The fit, shown by the green line, gives a slope for the change in relative phase between subsets of $0.0518 \text{ rad}/2\pi$ per subset or per 50 ps delay. This can be calculated back to the modulation frequency f_{mod} using that slope which is simply given as $\Delta t/\tau_{mod} - N_m$. Here $\Delta t=50 \text{ ps}$ is the time delay between two subsets, $\tau_{mod} = 1/f_{mod}$ is the period of the bunch modulation, and $N_m=6$ is the integer number of modulation periods within Δt . The result of $\tau_{mod} = 8.26 \text{ ps} \hat{=} f_{mod} = 121.04 \text{ GHz}$ matches the frequency obtained from the Rb vapor density measurement of 120.81 GHz) within 0.19%, showing that the phase variation follows the expected dependency.

The small deviations from the linear fit in this plot that might guide the eye to see more than one slope which is however caused by the high sensitivity of the phase analysis in this specific case. With almost a full integer (≈ 6.05) of periods per 50 ps increment, the measurement uncertainties or possible small changes in experimental parameters become enhanced when only showing the relative change in phase ($\approx 0.05 \text{ rad}/2\pi$ per 50 ps) instead of the full number of periods (6.05). The through a change in slope implied possibility of changes in modulation frequency can be excluded by calculating the modulation frequencies that corresponds to that changes in relative phase from one subset to the next. The outcome is displayed in Fig. 50(b) where the frequency values are positioned on the temporal axis in between the subsets, e.g. the frequency value at $t = 75 \text{ ps}$ corresponds to the change in relative phase from subsets $t = 50 \text{ ps}$ to $t = 100 \text{ ps}$. The modulation frequencies per subset shows no trend, but are scattered within $\pm 1\%$ around their mean value¹ of 121.04 GHz indicated by the red, dotted line. The frequency expected from the density measurement (120.73 GHz) is also shown for reference by the blue, dashed line. Therefore we attribute the cause of the small deviations from the expected linear trend in Fig. 50(a) to the measurement uncertainties.

Remarks on the Modulation Frequency

We want to note that retroactively, the findings in Figure 50(b) further validate the choice to use only one fixed value for the phase determination of all subsets. The arguments based on Fig. 35 and on all observations from the Rb density, temperature or SM measurements so far were strictly speaking only valid for the determination of $\Delta\Phi$, but not completely sufficient for the relative phases themselves (even though there are no reasons known to us that suggest a different approach, especially when having a flat plasma density profile along the 10 m of the vapor source). Nevertheless, this can be additionally justified by applying the DFT frequency analysis to the

¹Note that this mean frequency is identical to the average f_{mod} determined from the fit (Fig. 50(a)).

stitched SC image of Fig. 49(a). To obtain the time profile, we sum counts over a $\cong \pm 430 \mu\text{m}$ -wide area around the bunch axis. We limit the DFT again to parts of the bunch with $t > 50 \text{ ps}$ to avoid contributions of the unmodulated part of the bunch ($t < 0 \text{ ps}$) or the onset of the SM. The power spectrum is plotted in Fig. 51. Due to the much longer signal length of the stitched image of almost 500 ps and

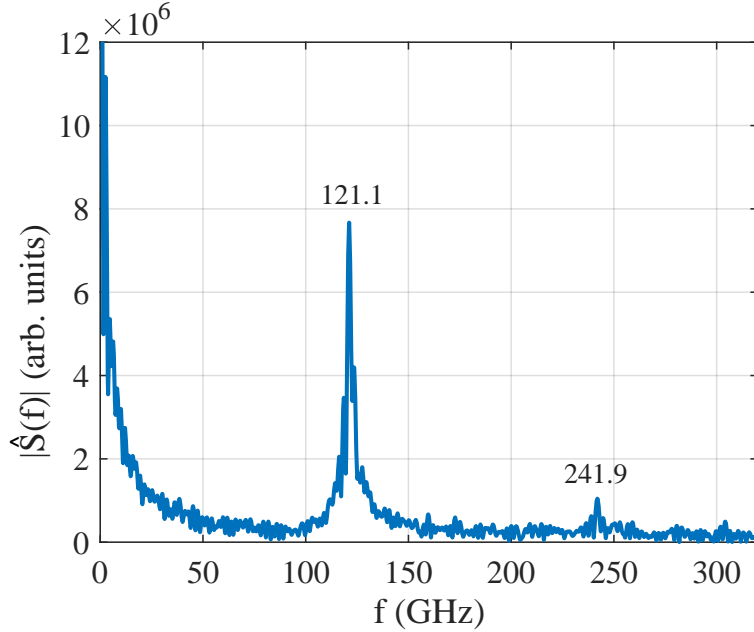


Figure 51: Power spectrum of the stitched SC image in Fig. 49(a). The frequency value of the first and second harmonic of the modulation frequency are also displayed.

a lower signal-to-noise ratio when compared to single, 73-ps-long SC window, the frequency resolution is improved by a factor of ≈ 7 (from a bin width of 13.7 GHz to 2.1 GHz) and the share of the sinc function in the power spectrum becomes significantly reduced. Zero padding the time profile (see Chapter 4.4.2 for details) is therefore not needed here. A distinct peak is visible at $\approx 121.1 \text{ GHz}$, as well as its second harmonic at $\approx 241.9 \text{ GHz}$, indicating a periodic signal with deep modulation. These frequencies (121.1 GHz and $241.9 \text{ GHz}/2 = 120.95 \text{ GHz}$) agree within the respective uncertainties with all other frequency values obtained from averaging the DFT frequency from all images (120.8 GHz), from the Rb vapor density measurement ($(120.73 \pm 0.27) \text{ GHz}$) and from the calculations of f_{mod} from the change in relative phase in Figure 50, both in (a) and (b). The assumption of a constant f_{mod} along the bunch and the use of one frequency for all subsets is therefore justified.

In total, both the modulation phase and frequency follow the expected trends

along the bunch, meaning that no change in either quantity is observed along the bunch for this data set of SSM where no gradient along the vapor source was set. The effect of linear gradients up to the percent level on SSM is investigated in the following Chapter 7.

6.5 Summary

The findings in this chapter demonstrate the existence of two clearly distinct SM regimes, depending on the initial transverse wakefield amplitude provided by a RIF. We found that when placing the RIF $2.0\sigma_t$ or more ahead of the bunch, the SM grows from shot noise or bunch irregularities from a point (in space or time) after the RIF that is different from event to event. As a result, the phase of the micro-bunch train with respect to the RIF varies over the full range of the (modulo) 2π plasma period. Moving the RIF closer to the bunch center, i.e. $t_{RIF} \leq 1.8\sigma_t$ for which $W_{\perp,RIF} \geq (4.1 \pm 0.4)$ MV/m, one crosses the transition point from SMI to SSM from where on the initial wakefield overcomes the noise present in the system and triggers the SM process. In the SSM regime, the phase is reproducible from event to event and its variation much smaller than a plasma period, measured to be between 3% to 7% of 2π all along the bunch. Taking into account that these values are convoluted with the various measurement uncertainties and that the phase variation does not accumulate along the bunch, we conclude that the true value is even smaller, at the sub-percent level.

The SSM regime together with its demonstrated phase reproducibility is an essential prerequisite for deterministic electron acceleration of electron bunches shorter than the plasma period as it is planned for AWAKE Run 2 [118]. Based on these results, the phase of the wakefields into which the electron will be externally injected can be controlled by setting a fixed delay between the RIF or the seed electron bunch (see Chapter 3.5). This is possible with ≈ 670 fs precision, or $\approx 7\%$ in phase [124]. Scanning this delay over the duration of one plasma period will allow to determine the delay that optimally synchronizes the electron bunch with the accelerating and focusing part of the wakefields. Beyond the aspect of phase reproducibility, the finding that phases are reproducible as long as a sufficient seed is provided also means that the electron bunch seeding in Run 2 can be performed at the very head of the proton bunch in a preformed plasma. This way, no unmodulated front of the proton bunch can interfere with the electron acceleration in the second plasma (see [117]).

Chapter 7

Experimental Studies of SM with Linear Density Gradients

The results so far were recorded with a constant density profile, i.e., gradient $g = 0$. In this case however, the charge distribution of the modulated proton bunch and that of the wakefields eventually dephase due to the phase velocity of the wakefields being smaller than the velocity of the proton bunch [65, 66] (see Chapter 2.4). As a consequence, towards the end of the plasma, the micro-bunches originally propagating in the focusing half of the wakefield might end up in the defocusing half which reduces the number of micro-bunches in the bunch train. Positive plasma density gradients along the beam path promise to increase the phase velocity (Eq. 2.23) and therefore may allow for an (at least partial) compensation of the shift in phase [65, 66], leading to more micro-bunches in the train and to more charge per micro-bunch, thus to potentially larger wakefield amplitudes along the plasma. The electron acceleration experiments at small positive gradients ($\approx 0.5\%/m$) in [52] support this prediction by yielding higher final electron energies when compared to the no-gradient case. Negative gradients are accordingly expected to lead to a faster dephasing and thus a stronger defocusing of the protons, contrary to the requirements of the acceleration experiments.

In this chapter, we study the effect of positive and negative, linear plasma density gradients on the micro-bunch formation in the regime of SSM from stitched images (see Chapter 4.3) that display the whole modulated bunch. Since for $g \neq 0$ the plasma density changes along the beam path, we also investigate the modulation frequency f_{mod} of the proton bunch charge distribution after the 10 m of plasma as function of g , the radial position and the position along the bunch. We compare these results to simulation work by P.I. Morales Guzmán in [58] that uses the 2D particle-in-cell code OSIRIS [125] and to the heterodyne frequency measurements using CTR by F. Braunmüller et al. [60]. At the end, we determine the phase variation and relative phase along the bunches to prove that seeding provides phase reproducibility also with plasma gradients.

7.1 Observation of the Micro-Bunch Train as a Function of the Density Gradient

From stitched images similar to that in Fig. 49(a), we study the trains of micro-bunches that form under the influence of various plasma density gradients within $\pm 2\%/m$. As a reminder, g is defined as the difference between the two Rb vapor densities measured with high ($< 0.5\%$) accuracy at either end of the vapor source and divided by its length of 10 m (Eq. 3.7, see Chapters 3.4.1 and 3.4.2 for details). The mentioned range in gradient of $\pm 2\%/m$ therefore corresponds to a change in density of $\pm 20\%$ over the 10 m of propagation length in plasma. Positive gradients indicate that the density is higher at the exit of the vapor source. We set the gradients by keeping the Rb vapor density at the vapor source entrance (and thus the density at the beginning of the plasma) constant at $n_{Rb,u} = 1.804 \times 10^{14} \text{ cm}^{-3}$ while only varying the density at the vapor source exit between $n_{Rb,d} = 1.46 \times 10^{14} \text{ cm}^{-3}$ and $2.17 \times 10^{14} \text{ cm}^{-3}$. Thus, the vapor and plasma density at position z along the bunch is given as $n_e(z) = n_{e0} (1 + (g/100)z)$. We set eight different gradients: $g = [-1.93, -0.93, -0.52, +0.03, +0.43, +0.87, +1.30, g = +2.00] \%/m$. A plot of the measured Rb vapor densities at vapor source entrance and exit and the corresponding gradients can be found in Fig. A6 of Appendix A.2.3.

The proton bunch population for the measurements is $N_b = (2.98 \pm 0.16) \times 10^{11}$, its duration is measured as $\sigma_t = 230 \text{ ps}$. To be in the SSM regime, the RIF is placed at $t_{RIF} = 128 \text{ ps}$ ahead the bunch center, i.e. a time very similar to the setting in Chapter 6.3 where phase reproducibility is observed. The corresponding initial transverse wakefield amplitude (from Eq. 2.18) is 18.2 MV/m , which is approximately four times larger than the values for which SSM is observed in Chapter 6.2 for a plasma density only approximately two times larger. The SC images are recorded on the 211 ps window (temporal resolution $\approx 3 \text{ ps}$) with a slit width of $20 \mu\text{m}$ and a MCP gain of 30. We move the LRS (and the SC window) in 150 ps steps from $\Delta t_{LRS} = 0$ to 450 ps along the bunch to guarantee an overlap in time between images and record ≈ 17 images per LRS delay. These images are stitched together according to the procedure in Chapter 4.3, resulting in ≈ 670 -ps-long images of the bunch charge distribution. To characterize the on-axis micro-bunch train, we obtain the corresponding time profiles by summing the images over $\pm 0.75\sigma_r = \pm 330 \mu\text{m}$ in the transverse direction along the bunch axis (see Chapter 4.4.2).

Figure 52 shows the stitched images with identical color scales for all eight gradients, from the most positive one in (a) to the most negative in (h). The equivalent time profiles are plotted below each image. The LRSs used for the stitching are visible on the bottom of each image¹ at $t = [0, 150, 300, 450] \text{ ps}$. The RIF is located at $t = 0$

¹Except for (a), where $t = [0, 50, 150, 300, 400, 500] \text{ ps}$ are used due to wrong settings during the data taking.

7.1 Observation of the Micro-Bunch Train as a Function of the Density Gradient

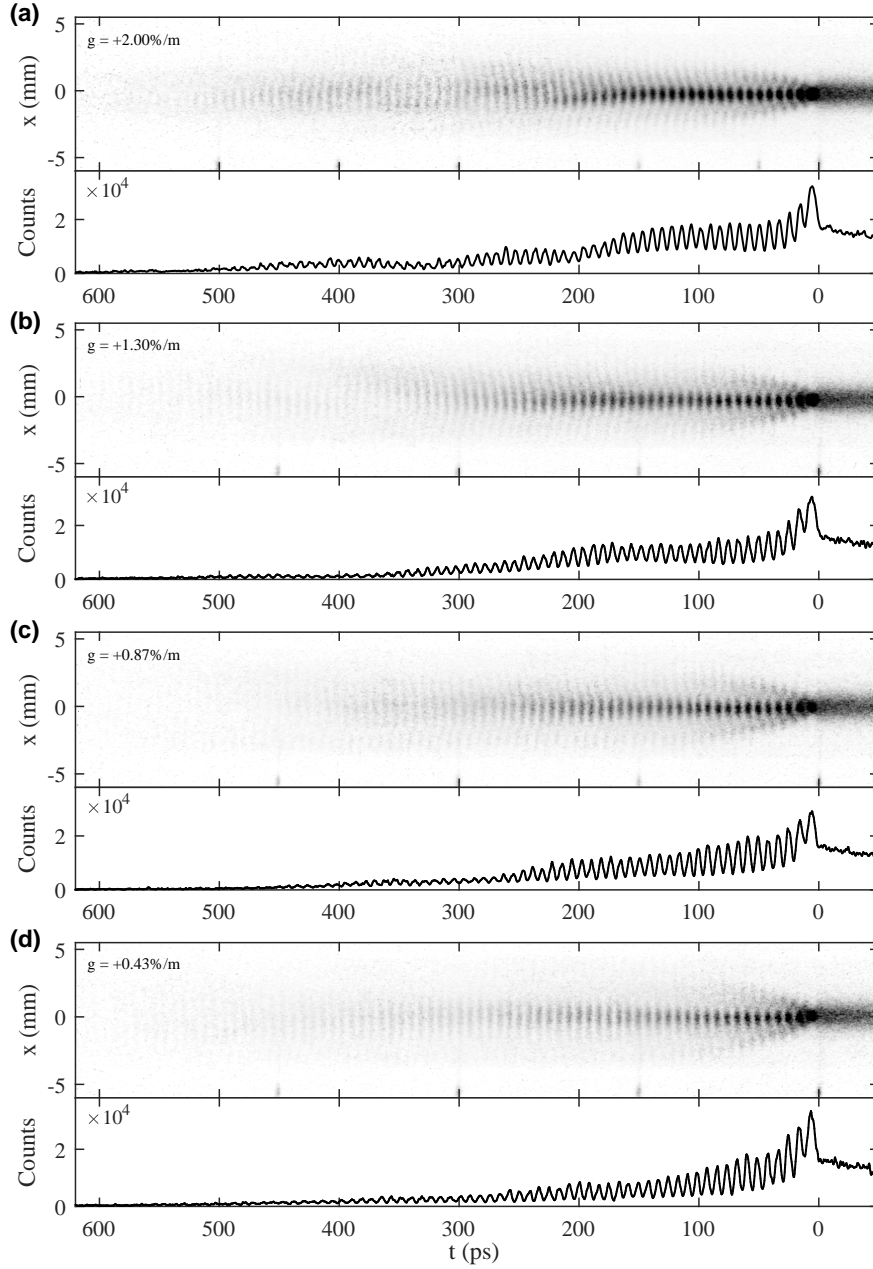


Figure 52: Stacked 211-ps-long SC images and corresponding time profile below for $n_{Rb,u} = 1.804 \times 10^{14} \text{ cm}^{-3}$ constant and a linear plasma gradient of (a) $g = +2.00$, (b) $+1.30$, (c) $+0.87$, (d) $+0.43\%/m$. The RIF is at $t = 0$ on the images, the LRSs used for the stitching are visible at the bottom every 150 ps. Front of the bunch on the right hand side, identical color scale for all images. Time profiles are obtained by transversely summing counts within $\pm 0.75\sigma_r = \pm 330 \mu\text{m}$ (red dashed line in (e) on following page) along the bunch axis (used in Chapter 7.3).

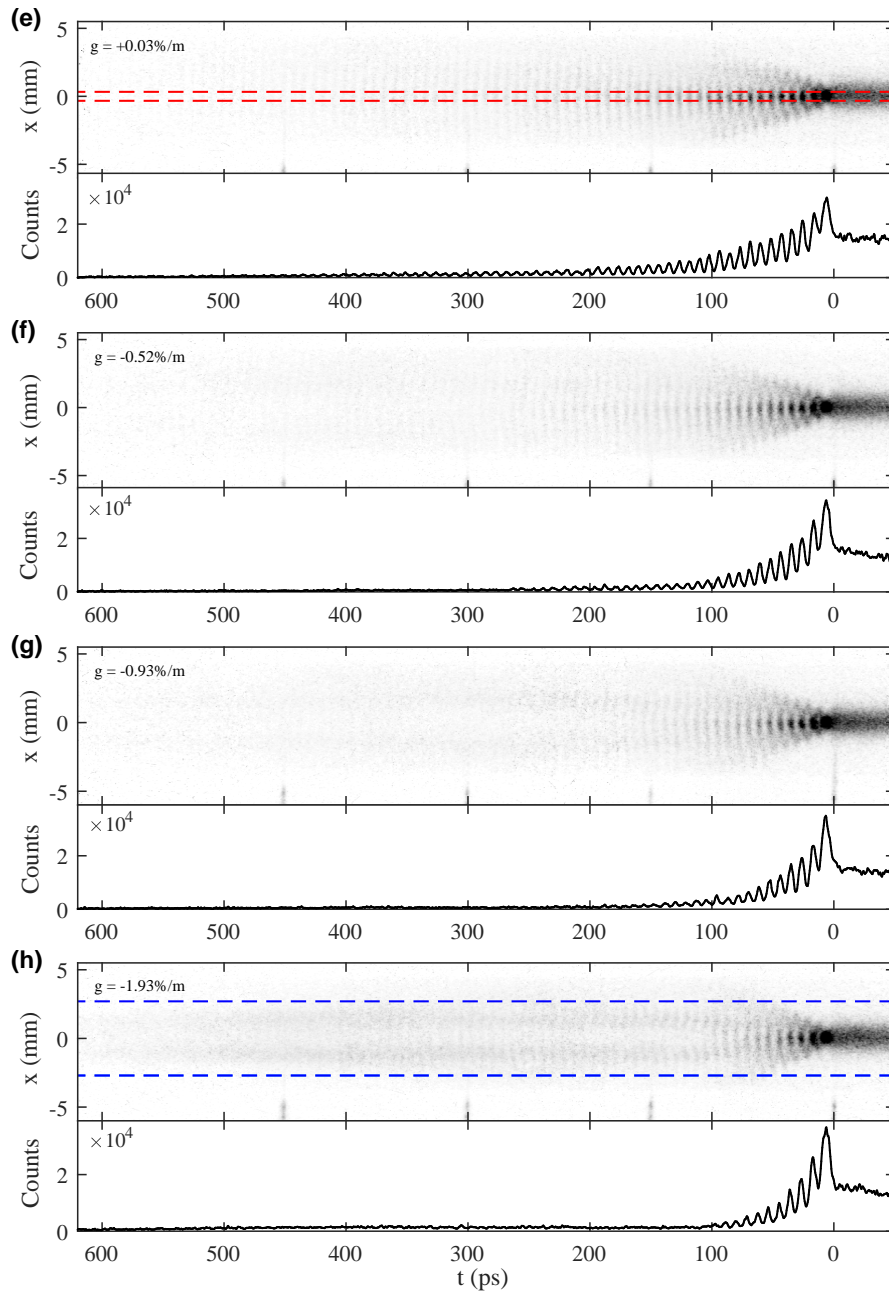


Figure 52: Continuation of the previous figure for the plasma gradients of (e) $+0.03$, (f) -0.52 , (g) -0.93 and (h) $g = -1.93\%/m$. The red dashed line in (e) represents the width of $\pm 0.75\sigma_r = \pm 330 \mu\text{m}$ used to determine the time profiles. The blue dashed line in (h) indicates a width of $\pm 6.3\sigma_r = \pm 2.7 \text{ mm}$ (used in Chapter 7.3).

on every image, i.e., parts with $t < 0$ show the unmodulated head of the bunch that travels in Rb vapor only. In all cases, the SM starts right at the location of the RIF, and trains of micro-bunches form, as already seen for SSM (e.g. in Fig. 46). Again, micro-bunches on the stitched images show an increased contrast (i.e. signal-to-noise ratio) when compared to single images, meaning that features overlap in time. As explained in Chapter 6.3, this indicates phase reproducibility and thus the SSM regime, independently of the gradient (the phase reproducibility for various gradients will be studied in detail in paragraph 7.4).

However, the length and appearance of the micro-bunch train differs depending on g . For the most positive case of $g = +2.00\%/m$ in Fig. 52(a), micro-bunches are visible up to $t \approx 520$ ps ($2.17 \sigma_t$). Compared to the no-gradient case (Fig. 52(e)), more micro-bunches form. The micro-bunches within the first 180 ps ($0.78 \sigma_t$) after the RIF seem to be more focused and with a higher charge per micro-bunch, which can be seen from the increase in counts when comparing time profiles at the time of a certain micro-bunch. We note that this increase in charge per micro-bunch is also documented in [60] where F. Braunmüller et al. applied the procedure from [98] to calculate the charge per micro-bunch from the charge density (studies of charge per micro-bunch are not part of this thesis). This procedure considers that the SC displays the charge density and not the charge, i.e. the signal on the SC image decreases with increasing micro-bunch size due to the SC slit [98]. Up to $t = 180$ ps, the charge density within $\pm 0.75 \sigma_r$ remains approximately constant, whereas a constant decrease is observed with $g = 0$ in Fig. 52(e). For $t > 180$ ps, asymmetries and irregularities in the charge distribution with respect to the propagation axis appear. For $g = +1.30\%/m$ (Fig. 52(b)), the micro-bunch train appears shorter on the image and from the time profile. An on-axis modulation structure is visible up to $t = 400$ ps ($1.74 \sigma_t$ after the RIF), also with (less strong) irregularities from $t \approx 300$ ps ($1.30 \sigma_t$) on. From $t \approx 350$ ps ($1.52 \sigma_t$) on, the charge density on axis is significantly lower as shown by the time profile, which seems to be caused by the irregularities just mentioned. Figure 52(c) with $g = +0.87\%/m$ is comparable to (b) in the sense that micro-bunches are visible until $t \approx 400$ ps and that their time profile are alike but the charge distribution is much more symmetric with respect to the propagation axis, in particular for $t > 300$ ps. The irregularities disappear. For $g = +0.43\%/m$ (Fig. 52(d)), the bunch distribution is fully axisymmetric. The part with (almost) constant charge density within $\pm 0.75 \sigma_r$ for $t < 180$ ps is less pronounced and micro-bunches show a slightly lower charge density after that point (but still more than with $g = 0$). On the image, micro-bunches are again visible up to $t = 500$ ps. With $g = +0.03\%/m$ (Fig. 52(e)), a modulation in charge density is still visible up to minimum 400 ps, as already observed before (see Fig. 49), but the charge density in the micro-bunches decreases continuously along the bunch.

With $g < 0$, an opposite behavior is observed. With $g = -0.52\%/m$, shown in Fig. 52(f), less micro-bunches leave the plasma than with no or a positive gradient.

The train of micro-bunches is shorter, only ≈ 270 ps long, and the charge per micro-bunch also decreases. With even more negative gradients, this effect is enhanced. A gradient of $g = -0.93\%/m$ (Fig. 52(g)) causes the micro-bunches to defocus earlier along the bunch, from 180 ps or $0.78 \sigma_t$ after the RIF. From 250 ps ($1.09 \sigma_t$) on, the proton bunch distribution leaves the axis. For $g = -1.93\%/m$, the most negative gradient at which we measured (Fig. 52(h)), only approximately 10 to 12 micro-bunches stay on-axis, no charge is left there for $t > 100$ ps. All the charge after that point appears defocused, away from the axis. However, a modulation pattern is also observed for the defocused charge.

In general, these observations match the expectations from the phase shift mentioned at the beginning of this chapter. Indeed, in a uniform plasma without gradient ($g = 0$, Fig. 52(e)), the phase velocity of the wakefields is different to that of the protons which can be seen from the fact that micro-bunches in the far back of the bunch become defocused at some position within the plasma. Negative gradients increase the phase shift as even more parts of the bunch experience defocusing fields when compared to the case of $g = 0$. Also the charge per micro-bunch decreases (see time profiles). For large negative gradients ($g \leq -0.9\%/m$), this effect is even strong enough to let the protons leave the wakefields close to the beginning of the plasma as shown later by Fig. 55(a). By contrast, positive gradients clearly lead to a larger number of micro-bunches in the train and to higher charges close to the bunch center as the micro-bunches stay longer in the focusing part of the wakefields. Our findings suggests that an optimum concerning the compensation of the phase shift due the density gradient along the propagation path is achieved for around $g = +0.43\%/m$, because the largest number of micro-bunches without irregularities are visible here when comparing all $g > 0$ cases. Together with the higher charge per micro-bunch when compared to $g = 0$, this may cause the accelerating wakefields to be stronger further along the bunch. Note that depending on the (fixed) delay between the electron bunch and the RIF, the increase in charge might be the dominant contribution. For $g > +0.9\%/m$, based on the appearance of the irregularities, the increase in phase velocity seems to over-compensate the phase shift between the charge distribution and the wakefields.

These observations are confirmed by the simulation work of P.I. Morales Guzmán [58] where nine values of g between $-2\%/m$ and $+2\%/m$ were studied. Other simulation input parameters were set to match those of our data set. The simulations reproduce the observed features and demonstrate good agreement with respect to the charge distribution in the stitched images for all values of g . As an example, Fig. 53 shows the corresponding images, with the stitched image for $g = -0.93\%/m$ from Fig. 52(g) in (a) and the simulation result for $g = -1\%/m$ from [58], Fig. 1(a) in (b). The corresponding time profiles are shown below each image. Both images and time profiles match each other with respect to the development of the SM, i.e. to

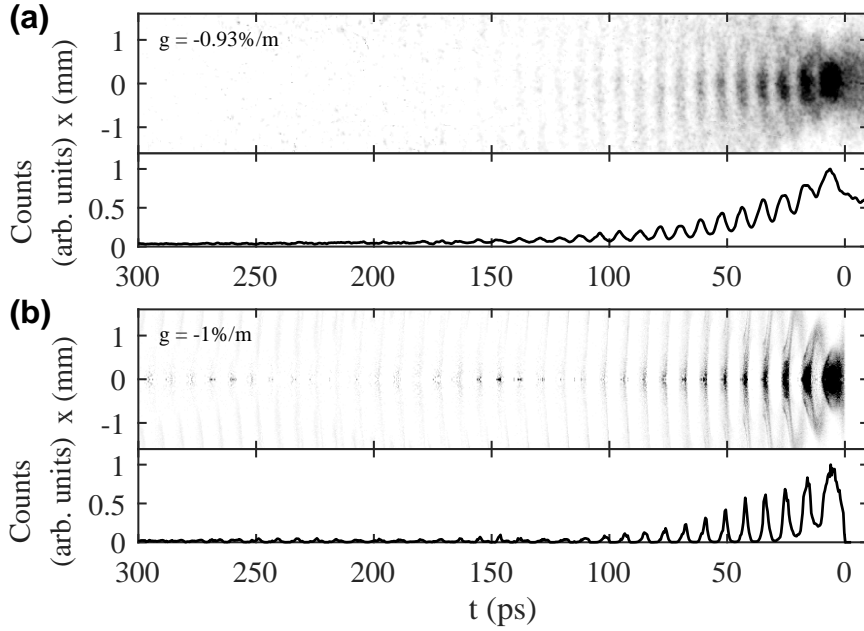


Figure 53: Comparison of (a) the stitched SC image of Fig. 52(g) with $g = -0.93\%/m$ to (b) a 2D simulation from [58] with $g = -1\%/m$ and similar input parameters. The corresponding time profiles are shown below the images.

the focusing and defocusing of the protons, and to the decrease in on-axis charge. For a comparison of our experimental data to simulation results for also a positive and no gradient, we refer to [58].

The simulations also support our statement that an optimum for the compensation of the phase shift is reached for a gradient around $g = +0.43\%/m$. In the simulations, the largest wakefield amplitude and the highest remaining on-axis charge are obtained for a comparable value of $g = +0.5\%/m$. This is additionally validated by the experimental electron acceleration results of AWAKE [52], where higher final electron energies were achieved when the gradient along the vapor source was $\approx +0.5\%/m$ instead of zero (and keeping all other parameters constant).

7.2 Modulation Frequency as a Function of Plasma Gradient

The results in Chapter 6.4 and [51] prove that the proton bunch self-modulates at the plasma electron frequency for a density constant along the propagation path. The studies in the previous paragraph show the influence of linear plasma density gradients on the number of micro-bunches in the bunch train, but not how these gradients affect f_{mod} . With linear density gradients, the local density and thus plasma

electron frequency changes monotonically ($\propto \sqrt{n_{e0}}$) along the propagation path. The modulation frequency could be expected to match the local plasma frequency at the entrance of the vapor source, that at its exit, or to take a value in between those two. We therefore study the modulation frequency of the micro-bunch train after 10 m of plasma as a function of g in the following. To determine f_{mod} , we apply the DFT-based procedure of Chapter 4.4 to the time profiles of the longitudinal charge distributions of the stitched images that we obtain by summing counts within $\pm 0.75\sigma_r = \pm 330 \mu\text{m}$ and that are shown in Fig. 52 below each image. Similarly to the previous chapters, we exclude the unmodulated part of the bunch, the onset of the SM and the first micro-bunch that has a length different to that of the other bunches. The f_{mod} values are plotted versus g in Fig. 54 (black diamonds). The dashed lines indicate the expected plasma frequencies at the vapor source entrance ($f_{entrance}$) and exit (f_{exit}). For $g = 0$, $f_{mod} = 120.0 \text{ GHz}$ is similar to the expected plasma frequency of 120.6 GHz , as seen before. With decreasing negative gradients, f_{mod} decreases linearly. It thereby shows great agreement with the respectively expected plasma frequency at the vapor source exit. For the most negative gradient $g = -1.93\%/m$, we measure $f_{mod} = 108.3 \text{ GHz}$, while expecting 108.2 GHz from the density measurement. With positive gradients, f_{mod} also increases, but saturates at large values of g ($f_{mod} \approx 123 \text{ GHz}$ for $g = +1.30\%/m$ and $+2.00\%/m$). The values are larger than $f_{entrance}$, but smaller than f_{exit} .

We compare those to the results of the heterodyne frequency measurement based on CTR by F. Braunmüller that are published in [60] (its setup is briefly described in Chapter 3.3.5.1 of this thesis). Figure 54 shows these frequencies as red circles, the error bars represent the standard deviation of the measurement. For positive gradients, both measurements agree within the uncertainties as the frequencies also increase and saturate for $g \geq +1.30\%/m$. For negative ones, the values do not match each other as the curve of the CTR frequencies flatten out for large negative gradients, comparable to the large positive gradients.

The reason for this difference is the fact that time profiles used for the DFT analysis represent a relatively narrow analysis window in transverse direction ($\pm 0.75\sigma_r = \pm 330 \mu\text{m}$), only containing the on-axis charge distribution of the micro-bunches, but no information from the defocused charge. In contrast, the CTR diagnostic receives the signal of the whole bunch charge distribution that passes through, including the defocused protons. Both diagnostics can be brought to an agreement by increasing the width of the DFT analysis window to also include the whole OTR signal that reaches the SC, i.e. including that of the defocused protons. The new analysis window to determine f_{mod} therefore includes all charge within $\pm 6.3\sigma_r = \pm 2.7 \text{ mm}$ as indicated by the dashed line in Fig. 52(h). In the following, we refer to this as the wide window. The increase in window width leads to good agreement between the independent OTR and CTR diagnostics as shown by the blue squares in Fig. 54. For $g < 0$, the frequencies now match the trend of the CTR measurement (red circles)

where frequencies flatten out for large absolute gradients. For positive gradients, all three measurements, i.e. with the narrow and wide window, and the CTR show a very similar behaviour.

We also compare these results to the simulation work in [58]. Its Fig. 6 shows the same differences in behavior for narrow and wide analysis windows. A DFT with a narrow window of ± 0.3 mm width yields frequencies that follow the plasma frequency at the vapor source exit for $g < 0$ but saturate at a frequency between

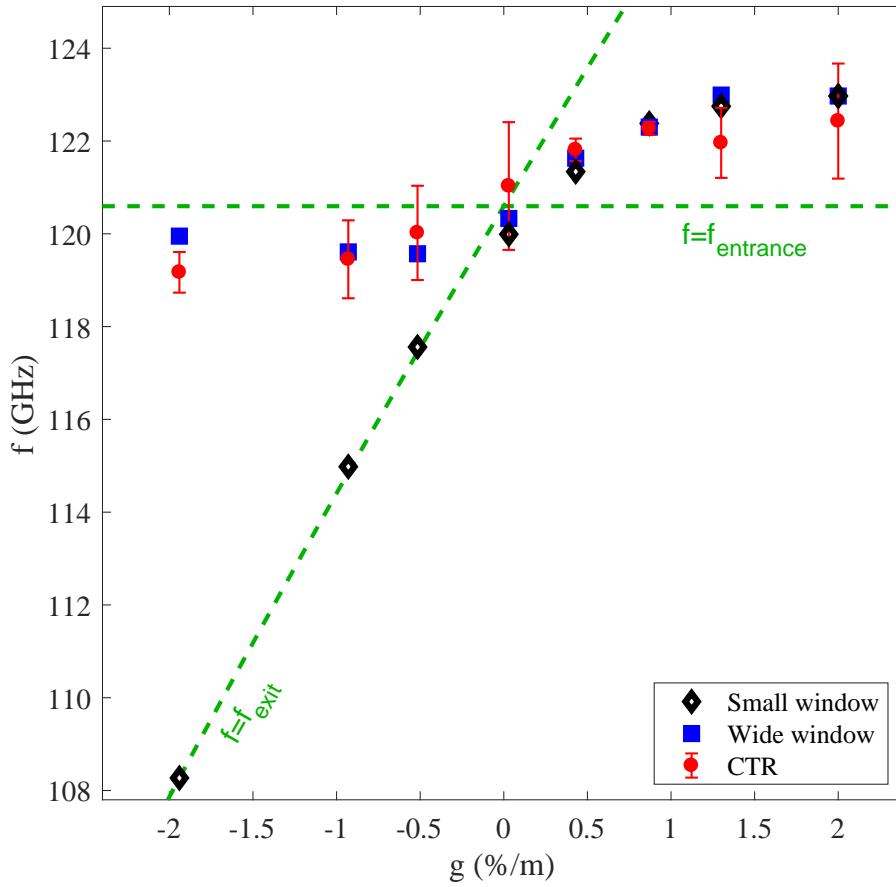


Figure 54: DFT frequency as a function of g for a narrow ($\pm 0.75\sigma_r = \pm 330$ μm wide, black diamonds) and wide analysis window ($\pm 6.3\sigma_r = \pm 2.7$ mm wide, blue squares) and compared to the CTR-based frequency measurement of [60] (red, filled circles). The error bars represent the standard deviation of each data point. Green, dashed lines indicate the plasma frequencies expected at the vapor source entrance and exit (f_{entrance} and f_{exit}).

those of the entrance and exit for $g > 0$. With a wide window, the curve flattens out for large negative and positive values as also seen for our data. In total, good agreement between experiment and simulation is demonstrated.

We therefore conclude that the defocused protons contribute with different frequency components to the DFT than the on-axis micro-bunches. Figure 54 suggests a higher frequency for the distribution of the defocused protons, i.e., a frequency that is close to f_{entrance} . With positive gradients, on-axis and defocused charge seem to carry a similar f_{mod} . We confirm this by evaluating the modulation frequency as function of the radial position of the charge distribution in the following paragraph.

7.3 Frequency Dependency on Transverse Position

We determine f_{mod} for 200 μm -wide longitudinal slices of the images at different transverse center positions from $x = -2.1$ mm to $+2.1$ mm ($\approx \pm 5 \sigma_r$) for $g = 0$ and the two largest gradients $g = -1.93\%/m$ and $+2.00\%/m$. The corresponding stitched images are depicted in Fig. 52(a),(e) and (h). Figure 55 shows the results of the DFT analysis, with f_{entrance} indicated by the blue, dashed lines and f_{exit} by the green ones.

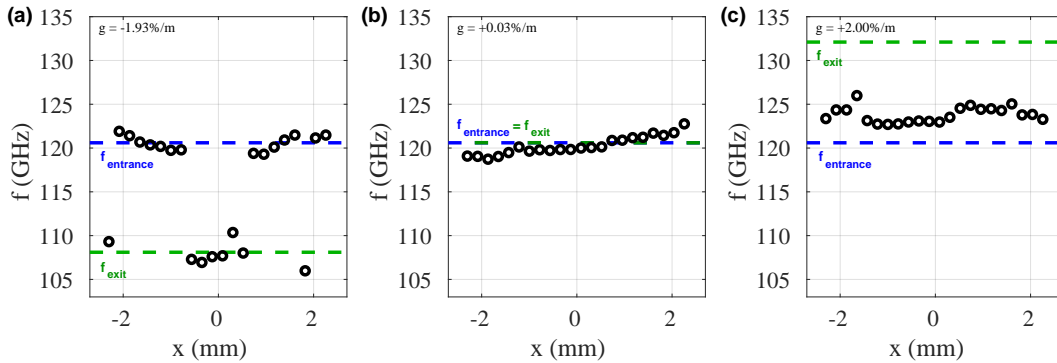


Figure 55: DFT frequency as a function of transverse position x for 200- μm -wide slices as analysis window and gradients (a) $g = -1.93\%/m$, (b) $g = +0.03\%/m$ and (c) $g = -2.00\%/m$. Blue, dashed lines indicate f_{entrance} , green lines f_{exit} .

For $g = -1.93\%/m$ (Fig. 55(a)) and slices within $-550 \text{ mm} \leq x \leq +550 \mu\text{m}$, the DFT frequencies match f_{exit} , which means that the micro-bunches carry the local plasma frequency of the end of the plasma. Outside that range in x , i.e. where the defocused protons are visible on Fig. 52(h), the frequency values correspond to f_{entrance} . Consequently, the defocused protons left the axis and the wakefields early, towards its beginning. This agrees with observations for the corresponding stitched image in Fig. 52(h) where a much stronger and earlier defocusing of the protons is

observed when compared to images with $g \geq 0$ since the difference in phase velocity of the wakefields with respect to the proton distribution is enhanced due to the large negative gradient (Eq. 2.23). The presence of these two frequency regions between the micro-bunches and charge further away from the axis also explains the difference outcomes for a narrow and a wide analysis window for $g < 0$ seen in Fig. 54.

With a constant plasma density ($g = 0$, Fig. 55(b)), the DFT frequencies are equal to the plasma frequency for all transverse positions x . The micro-bunches and the defocused protons show the same modulation frequency. Because $f_{\text{entrance}} = f_{\text{exit}}$ for $g = 0$, this is also expected.

Also for $g = +2.00\%/m$ (Fig. 55(c)), the frequency shows no dependency with respect to the position of the slice along x . The micro-bunches on axis and the defocused protons show approximately the same modulation frequencies. However, their values are consistently larger (≈ 123 GHz) than those of Fig. 55(b) (and (a)), hence larger than f_{entrance} (120.6 GHz) but smaller than f_{exit} (132.1 GHz). The value of ≈ 123 GHz agrees with the results of Fig. 54 for $g > 0$ that also shows that frequency for both windows sizes. As a result, we conclude that the micro-bunches stay longer and in higher numbers in the focusing wakefields and thus on the propagation axis, as also seen on Fig. 52(a) (and for all other smaller positive gradients on Fig. 52(b) to (d)). This is due to the (at least partial) compensation of the phase shift between the wakefields and the protons (Eq. 2.23). The defocused protons leave the plasma wakefields much later when compared to negative gradients, toward the exit of the vapor source, supposedly where the SM saturates. A local plasma frequency of 123 GHz corresponds to a position 6 m into the plasma. A saturation before the end of the 10 m of plasma is also suggested by experimental studies of the longitudinal and transverse wakefields published in [67].

In summary, the studies of the radial dependency of the modulation frequency of the charge distribution reproduce the observations of the previous paragraph 7.3, i.e. the findings of Figs. 54 and 55 are consistent with each other. This is another direct proof of the change in phase velocity of the wakefields based on a plasma gradients postulated through Eqs. 2.22 and 2.23. For negative gradients, two frequency components are found in the charge distribution after the plasma (Fig. 55(a)) because the decreased phase velocity of the wakefields further enhances the phase shift with respect to the charge distribution, causing the protons to be defocused early along the plasma. With positive gradients, protons stay longer in the focusing fields as the phase velocity of the wakefields increases.

7.4 Phase Reproducibility with Plasma Gradients

For a constant density profile, the results of Chapter 6 with SSM demonstrate phase variations at the percent level even though the wakefields propagate with a phase

velocity different to that of the protons until the SM saturates. Gradients $g \neq 0$ influence the phase velocity of the wakefields beyond that saturation point all along the plasma, as shown in paragraph 7.1. For this reason, we investigate the phase reproducibility of the micro-bunch train with plasma gradients in this paragraph.

Similarly to the argumentation in the analysis of the stitched SSM image of Fig. 49, the images in Fig. 52 give a direct visual proof of phase reproducibility for all values of g . After stitching, the micro-bunch structures do not wash out, but overlap and are clearly visible along the whole train. For negative gradients, as mentioned before in Chapter 7.1, the charge away from the axis also appears modulated (e.g. see Fig. 52(h)). One can therefore conclude that the defocusing wakefields far back in the bunch are also phase reproducible.

We quantify these observations by determining the phase variation $\Delta\Phi/2\pi$ for every position of the LRS using the DFT-based analysis of Chapter 4.4.3, as it is also done for Fig. 49(a). We compare these variations by plotting the mean of all subsets along the bunch (i.e. of four LRS positions) for each gradient in Fig. 56. The error bars representing the standard deviation of the measurements (for $g = -1.93\%/m$, no error bar is shown as it only contains the phase variation of the first subset with the LRS at $t = 0$). The plot shows that independently of g , the phase variation is small, i.e. much smaller than a plasma period. Their range of $\approx 4\%$ to 9% of 2π is comparable to that seen in Fig. 49(b) (3% to 7% of 2π there). The phase variation of the individual subsets along the bunch also show rather constant values and all below 12% of 2π , as indicated by the error bars. Thus, plasma gradients (within

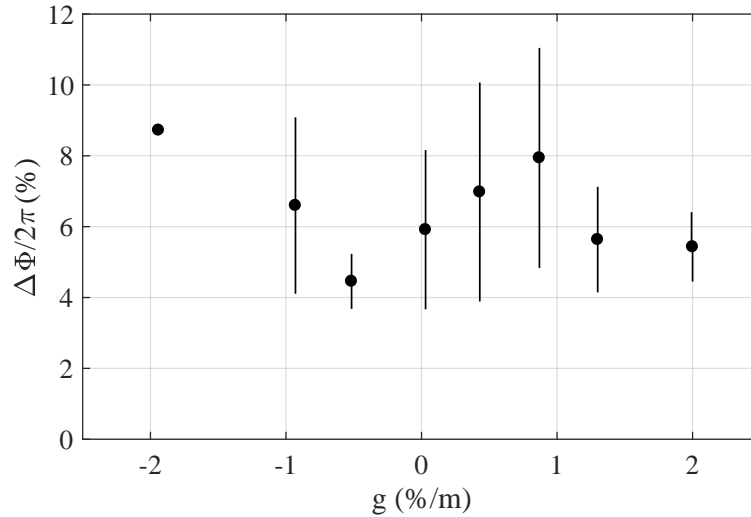


Figure 56: Mean phase variation along the bunch in percent of 2π versus plasma density gradient. Error bars represent the standard deviation of each measurement.

the observed range) do not influence the phase reproducibility in the SSM regime and seeding also works for $g \neq 0$. Only for the most negative gradient, the phase variation seems to be slightly higher (but still well below a plasma period). This is however caused by the strong defocusing of the protons from the axis, which decrease the number of micro-bunches on the axis (see the time profile of Fig. 52(h) which is used in the DFT), causing the measurement uncertainties to increase. In addition, acceleration measurements at this density gradient are not foreseen due to their negative impact on the micro-bunch train.

7.5 Relative Modulation Phase and Frequency with Plasma Gradients

With the phase reproducibility demonstrated for all values of g , we study the relative phase of the micro-bunches directly after each LRS along the bunch. For the first subset, we exclude the first ≈ 15 ps that display the unmodulated part of the proton bunch, the onset of the SM and the first micro-bunch that has a length different to the following ones [56], similarly to other phase analysis before. We set the modulation phase of the first considered micro-bunch (after $t = 15$ ps) in the first subset¹ (LRS at $t = 0$) as reference, i.e. zero. For $g = -1.93\%/m$, the early defocusing of the protons for $t > 100$ ps prevents a determination of the modulation phase beyond the position of the first LRS.

The mean relative phases for the gradients $g = +2.00$ to $g = -0.93\%/m$ (stitched images Fig. 52(a) to (e)) are plotted in Fig. 57(a). Error bars representing the rms variation of the mean relative phases are not shown for a better visibility of the individual values as they are already plotted in Fig. 56. The relative phase along the bunch changes monotonically from one subset to next and follows a linear trend for all gradients. Similarly to Chapter 6.4, this implies a constant modulation frequency along the bunch. The delay between two LRSs of 150 ps is not a full integer of the plasma period (≈ 8.26 ps for a density of $n_{Rb,u} = 1.804 \times 10^{14} \text{ cm}^{-3}$), causing that the residual parts of a plasma period add up from subset to subset. As f_{mod} increases with g (see Fig. 54), the slope of that linear trend also changes, as observed on Fig. 57(a). For increasingly positive gradients, the relative phase with respect to the LRS increases monotonically along the bunch, while it decreases for more negative g . The change in slope is quantified by linear fits to the respective data points and their results are shown in Fig. 57(a) by lines in the same color as the data points. We obtain slopes between $-0.66 \text{ rad}/2\pi$ and $+0.53 \text{ rad}/2\pi$ per 150 ps delay

¹Be reminded that for the $g = +2.00\%/m$ data set, the LRSs are placed at different positions than for the others due to wrong settings during the data taking. However, this does not influence the results.

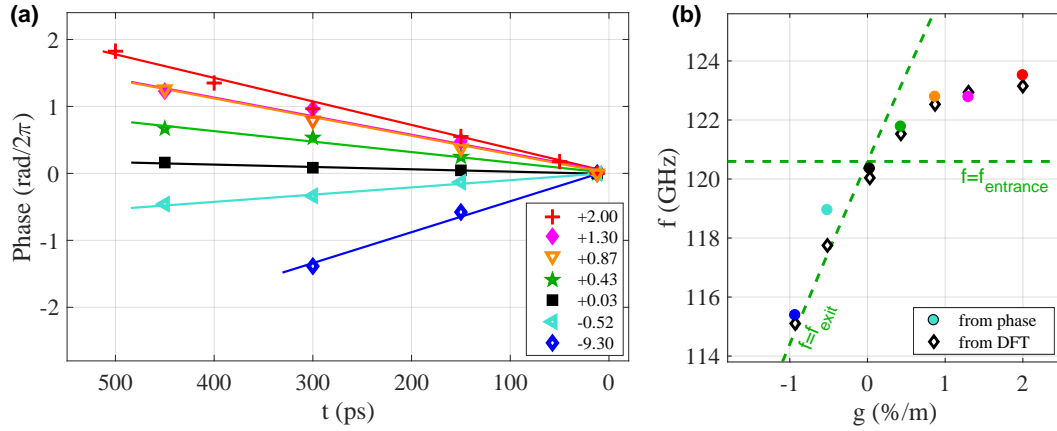


Figure 57: (a) Relative phase of the first micro-bunch after the LRS for each subset and g from $-1.93\%/m$ to $+2.00\%/m$. The phases for the first subsets are set zero for a better comparison. Lines represent linear fits over the respective data points. Legend: plasma density gradients in $\%/m$. (b) Modulation frequency that corresponds to the slope of the change in relative phase given by the fit in (a).

step of the LRS. For $g = +0.03\%/m$, we measure a value equal to that of Fig. 50 ($0.05 \text{ rad}/2\pi$).

Each of these slopes represents a different modulation frequency. We calculate that f_{mod} for a comparison with Fig. 54 using the relation of Chapter 6.4 where, as a reminder, the slope per delay step is given by $\Delta t/\tau_{\text{mod}} - N_m$. With $N_m = 18$ used for all values of g and $\Delta t = 150$ ps, we obtain the frequencies shown in Fig. 57(b) (filled circles, the color indicates the corresponding gradient by using the same scheme as Fig. 57(a)). We replot the DFT frequencies for the narrow analysis window of Fig. 54 (black diamonds) and the lines that indicate f_{entrance} and f_{exit} for comparison. The f_{mod} obtained from the slope of the fits follows the corresponding curve of Fig. 54. For $g < 0$, the frequency corresponds to f_{exit} , and for $g > 0$, f_{mod} saturates at ≈ 123 GHz. Together with the fact that the change in relative phase along the bunch is linear, this indicates that the micro-bunch trains are modulated with those frequencies all along the bunch.

7.6 Summary

This chapter demonstrates the effect of linear plasma density gradients on the SSM and its formation of the micro-bunch train. Stitched images recorded with a constant plasma density at the vapor source entrance and linear density gradients between $\pm 2\%/m$ along the plasma give direct proof that the phase velocity of wakefields can

be influenced along the propagation path in order to match that of the protons using these density gradients. Positive gradients increase the phase velocity of wakefields, leading to a higher number of micro-bunches and charge per micro-bunch when compared to the no-gradient case due to a better matching of the phase velocities of the wakefields and protons. The modulation frequency of the micro-bunches and of the protons that left the axis increases thereby with g and saturates at a frequency in between that of the vapor source entrance and exit for the largest positive gradients. Best results in terms of compensating the phase shift between the protons and the wakefields seem to be achieved for plasma gradients around $+0.43\%/m$, which is confirmed by simulations [58] and acceleration experiments [52]. In contrast, negative gradients cause a further decrease in phase velocity of the wakefields, leading to a much earlier defocusing of the protons, i.e. to significantly shorter micro-bunch trains. Also the charge per micro-bunch decreases. The defocused protons carry the plasma frequency of the vapor source entrance where they left the plasma, whereas the bunch train is modulated with f_{exit} . The determination of the phase reproducibility along the bunch shows small variations, $< 9\%/2\pi$, for all gradients, i.e. seeding is not affected by gradients. The relative phase of the micro-bunches with respect to the LRSs changes thereby linearly along the bunch, meaning that f_{mod} is constant along the bunch. The frequency that corresponds to the respective change in relative phase follows again that of the vapor source exit, i.e. all results of this chapter show great consistency to each other.

Chapter 8

Conclusion and Outlook

As a proton-driven plasma wakefield accelerator, AWAKE relies on the self-modulation (SM) of a proton bunch in order to match the drive bunch with the plasma wavelength in terms of longitudinal and transverse size. The control of the phase or timing of the resulting micro-bunches with respect to the relativistic ionization front (RIF) that creates the plasma and to the electron bunch is thereby essential for a successful, external injection of the electrons into the accelerating and focusing phase of the wakefield. It is a key requirement for deterministic acceleration to high energies while maintaining bunch quality in terms of population, energy spread and emittance.

In this context, in **the first part of this thesis**, I proved the existence of two clearly distinct SM regimes. When the RIF is placed ahead of the bunch or at its very front, the initial transverse wakefield it excites is low in amplitude and the SM grows as an instability from transverse wakefields originating from shot noise or bunch irregularities. I showed that as a consequence, the SM starts from a random position along the bunch, after the RIF. This is demonstrated by streak camera images that are aligned in time using the laser reference signal I developed for this purpose. On the images, due to this variation in the start point of the SM, the micro-bunches appear with no particular timing from event to event. Their phase varies randomly over the entire (modulo) 2π of plasma period, which is the regime of the self-modulation instability (SMI).

By contrast, moving the RIF close to the bunch center allows for providing seed wakefield amplitudes that are larger than those from the noise or bunch irregularities. I demonstrated for the first time that the resulting sudden onset of the SM at the location of the RIF leads to the required phase reproducibility of the micro-bunch train from event to event. On streak camera images, the micro-bunches of every event appear with essentially the same timing with respect to the RIF. This represents the regime of seeded SM (SSM) where one clearly controls the phase and timing of the micro-bunches. Determining the variation in phase of the micro-bunch train using a DFT-based analysis procedure results in variations much smaller than a plasma period, between 3% and 7% of 2π , all along the bunch. Due to measurement uncertainties and small variations in the experimental parameter, this value for the

phase variation has to be regarded as an upper limit, meaning that the true variation is even lower, on the sub-percent level. In addition, this phase analysis for the SSM revealed that the relative phase of the micro-bunches follows a trend which corresponds to a constant modulation frequency along the bunch. This frequency matches with the plasma electron frequency expected from the density measurement, thus confirming the results of the modulation frequency analysis in [51].

I determined the transition point between the SM regimes in terms of RIF timing and corresponding wakefield amplitude by moving the RIF in steps of 0.2 times the proton bunch duration σ_t along the bunch. The closer the RIF is to the bunch center, the larger the initial transverse wakefield amplitude. The SMI is thereby observed for timings of the RIF $\geq 2.0\sigma_t$ ahead of the bunch center, i.e. for initial transverse wakefield amplitudes $\leq (2.8 \pm 0.3) \text{ MV/m}$. By changing the timing of the RIF to $1.8\sigma_t$ and smaller, i.e. for wakefield amplitudes $\geq (4.1 \pm 0.4) \text{ MV/m}$, phases become reproducible. The direct measurement of this transition from SMI to phase-controlled and reproducible SSM is an important result for the future planing of AWAKE. For Run 2, the SM will be seeded by a short electron bunch ahead of the bunch in a preformed plasma. In this thesis it is demonstrated that also in that case one is capable of controlling the phase of the micro-bunches and thus of the wakefields, as long as one provides a sufficiently large initial transverse wakefield to overcome those driven by bunch irregularities or noise in the system. Future plans, mainly that of Run 2a in 2021/22, therefore include studies of the phase reproducibility with electron seeding similar to that in this work. The proton bunch will enter a pre-formed plasma and the variation in phase measured as a function of the seed electron bunch timing. As an outlook and based on this thesis, other possible measurements with RIF-based seeding for Run 2a include:

- A repetition of the phase reproducibility studies with varying plasma density and/or proton bunch population. The results of Chapter 6.2 on the transition point between SMI and SSM have been obtained at one plasma density and for one fixed bunch population, i.e. one initial bunch charge density. Measurements to evaluate that the transition point is indeed independent of these parameters would be beneficial. As stated in Chapter 6.2, changes in the bunch charge density might also change the size and thus the extend of irregularities in the bunch profile, which would influence the location of the transition point. It is therefore not trivial to predict to outcome of these suggested measurements.
- A more detailed study of start point of the SM, as we characterized the different SM regimes by mainly observing a fixed window within the modulated bunch. A future focus could be on the location where the SM starts to evolve while transiting from SMI to SSM to better reveal the evolution of the SM as function of the initial transverse wakefield amplitude.

-
- The effect of seeding on the transverse proton distribution. This was not part of this work, but imaging stations 1 and 2 provide the possibility to study possible differences in symmetry of the transverse charge distributions as a function of transverse wakefield amplitude and thus of the SM regime.

Shaping the plasma profile along the propagation path is foreseen for AWAKE Run 2b to mitigate the phase shift between wakefields and the proton distribution that appears due to a difference in their phase velocities. This way, the micro-bunches can stay over longer distances in the focusing parts of the wakefields and higher saturation amplitudes of the wakefields are reached.

In the second part of this thesis, I therefore study the effect of linear plasma density gradients on the SSM. The phase reproducibility with SSM allows for a stitching of individual streak camera images to reconstruct a high-resolution image of the entire modulated bunch. These stitched images were used to characterize the micro-bunch train for gradients in the range of $\pm 2\%/m$ over the 10 m of plasma. Negative gradients result in a smaller number of micro-bunches and smaller charge per micro-bunch when compared to the no-gradient case. The more negative the gradient, the more micro-bunches propagate to the defocusing part of the wakefields. A frequency analysis of the proton bunch modulation as a function of their radial position showed for the largest negative gradient that the protons further away from the axis carry a frequency equal to the local plasma frequency of the beginning of the plasma. Accordingly, the protons must have left the plasma at this location. By contrast, the micro-bunch train on axis carries the local frequency of the end of the plasma. These observations prove that negative gradients further decrease the phase velocity of the wakefields, i.e. are not suitable for acceleration experiments.

Positive gradients increase the number of micro-bunches that remain on axis. On stitched images, they appear more focused, i.e. show an increased charge per micro-bunch. The frequency analysis showed that micro-bunches and defocused protons are modulated with the same frequency that lies within that of the beginning and end of the plasma. The fact that protons stay longer in the focusing part of the wakefields gives direct evidence that positive gradients increase the phase velocity of the wakefields and therefore reduce the phase shift, as it is required for the physics plans for AWAKE Run 2 [118]. The images suggest an optimum with respect to the number of micro-bunches and on-axis charge at a gradient around $0.43\%/m$, which is also supported by simulations [58]. Interestingly, gradients close to this value also led to the highest final electron energies during acceleration experiments [52].

These findings represent another key result for the upcoming AWAKE Run 2 and the design of future, up to hundreds of meters long proton-driven plasma wakefield accelerators. The fact that adjusting the plasma density gradient is a well-suited tool to control and optimize the phase velocity of wakefields in beam-

driven plasma wakefield experiments strongly supports the plans of Run 2b. There, based on the simulation results of [57], a density step will be tested to preserve the micro-bunch train and to maintain large wakefield amplitudes over long distances.

To summarize, this thesis produced two of the main results of AWAKE Run 1: the proof that phase reproducibility (and thus control over the wakefields) can be achieved by seeding the self-modulation, and the demonstration of the effect of linear plasma density gradients on the evolution of the self-modulation of the proton bunch. The future measurements in AWAKE will build on the work presented here, as well as the AWAKE physics program in general.

Acknowledgments

It is probably fair to say that no PhD Thesis would be possible without the help and support of many people. This is also true for this thesis, as it was made possible through the collaboration and cohesion of the Max-Planck-Institute for Physics (MPP) with its IMPRS graduate school, CERN and the Wolfgang-Gentner Programme (sponsored by the German Federal Ministry of Education and Research (BMBF), grant no. 05E18CHA). Therefore, I first want to express with my sincerest gratitude to:

- My PhD supervisor Prof. Dr. Allen Caldwell, who strongly supported my research topic and always helped to coordinate the interplay between all parties involved.
- My daily supervisor Dr. Patric Muggli, without whom the physics of this thesis would not be at this level, for teaching me all the scientific tools and tricks I needed, and for not resting until our work was the best we could do. Also thank you for trusting me with the vapor source, it was an honor to have the responsibility for it.
- My supervisor at CERN, Dr. Edda Gschwendtner, where I always knew that I have her full support, and who always ensured that her "kids at AWAKE" are doing fine, where ever it was, either in the control room or at the team outings.

A big thank you also goes to all my colleagues at AWAKE and other groups at CERN I worked with, below and on the surface. I probably cannot list all people I would have to mention after 4.5 years, nevertheless I try and want to say thank you to:

- Karl Rieger, who helped me in many technical and physics aspects, specially during my first weeks at CERN, and without whom the streak camera and thus also other theses would not exist.
- Dr. Erdem Öz and Dr. Falk Braunmüller, who taught me almost all my knowledge, tricks and techniques around the vapor source, and Dr. Michele Bergamaschi, who took over from me.
- The post-docs Dr. John Farmer, Dr. Spencer Gessner, Dr. Mikhail Martyanov, Dr. Joshua T. Moody and Dr. Giovanni Zevi della Porta, who helped with

the laser, the LRS or some administrative problems and who always offered a sympathetic ear, including some after-work beers and insides into American politics.

- Jan Pucek, my office mate, not only for together coordinating and carrying out the tunnel- and WDL related work, but also for all the nonsense around.
- Daniel Easton, Justin Pisani and Jim Uncle from WDL for the great collaboration.
- Oliver Boettcher, Jarmo Kortesmaa, Ans Pardons, Roberto Speroni, Dr. Marlene Turner and Dr. Michael Hauschild from CERN.
- Dieter Fischer, Pablo I. M. Guzmán, Vasyl Hafych, Dr. Frank Steffen and Ina Wacker from MPP.

and of course

- Gian Luigi d'Alessandro, James Chappel, Florence Friebel, Fiona Harden, Kook-Jin Moon, Barney Williamson and other my colleagues in building 530 and 112, who were always up for a coffee break, an ice cream, a hike or for Junction and whoever listened to my stories about work.
- Anna-Maria Bachmann and Mathias Hüther (now both also Dr.). Thank you for the always guaranteed support, both at work and in our flat.

Then, big thank you to all my friends in Landshut, Munich and Brazil, for keeping the links so strong. I was relatively far away, but still part of everything.

Special thanks go to Kevin Buffet and Lukas Felsberger, it is just an endless list of fun travels, cycling trips, nights out and parties, etc. Also, thank you a lot for the moral support.

Last, of a big thank you to my parents, sister and entire family, where no words can describe it.

Appendices

Appendix A

Supplemental Material

A first part presents complementary observations of micro-bunches at high plasma densities. I show that stitched images can be used to better resolve the micro-bunch train at densities where the modulation period is small when compared to the streak camera resolution. In a second part, I give supplementary information about the Rb vapor density diagnostic, the setting of linear vapor density gradients and the correlation between the Rb reservoir temperature and the measured density of the neutral Rb vapor.

A.1 Stitched Images of SSM at High Plasma Density

During AWAKE Run 1, the baseline density $n_{e0} = 2 \times 10^{14} \text{ cm}^{-3}$ is used because the corresponding modulation period $\tau_{mod} \approx 8 \text{ ps}$ is sufficiently larger than the resolution of the SC of 1.5 ps, meaning that micro-bunches with a duration $\leq \tau_{mod}/4$ can be well observed for the proof-of-principle experiments of Run 1. At the second baseline density of $n_{e0} = 7 \times 10^{14} \text{ cm}^{-3}$, the corresponding frequency is $f_{pe} = 237.6 \text{ GHz}$ and $\tau_{mod} \approx 4 \text{ ps}$. Micro-bunches are thus shorter than the SC resolution and their observation using single SC images is not trivial. Usually, no structure or modulation can be observed on these single images.

However, stitched and thus averaged images (see Chapter 4.3) helps to resolve the micro-bunch train with SSM also at these high densities. Figure A1(a) shows the stitched image for $n_{e0} = 5.35 \times 10^{14} \text{ cm}^{-3}$, $N_b = 3 \times 10^{11}$ and seeding at the bunch center ($t_{RIF} = 0$). The LRS (at $t = 0$ on the image) is placed 50 ps behind the RIF. The temporal profile for a $\cong \pm 430 \mu\text{m}$ -wide region around the

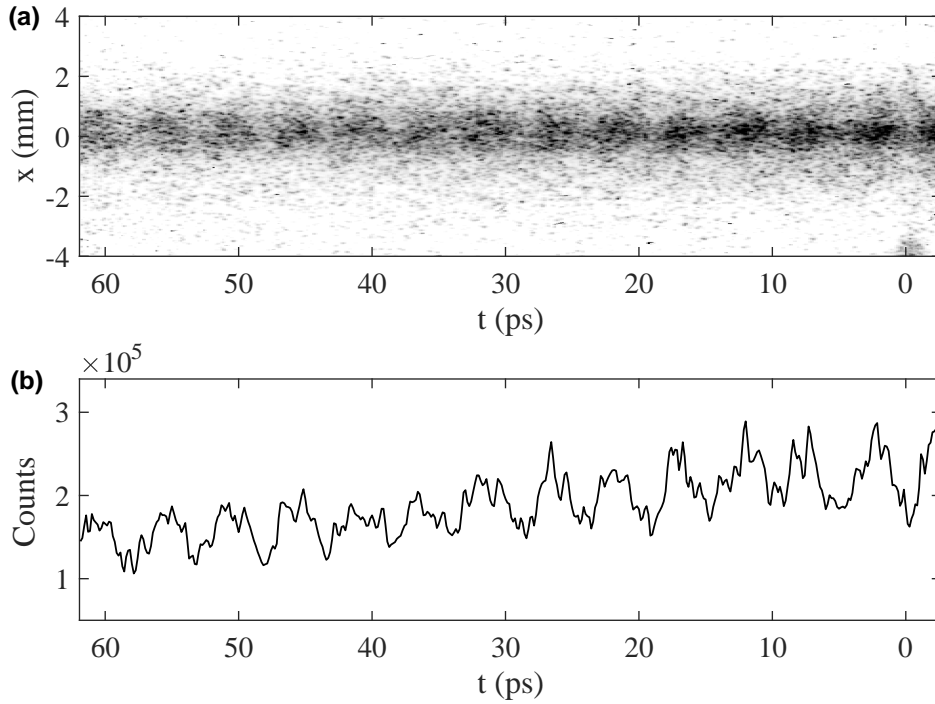


Figure A1: (a) Result of stitching eight 73 ps SC images for $n_{e0} = 5.35 \times 10^{14} \text{ cm}^{-3}$, $N_b \approx 3 \times 10^{11}$ and $t_{RIF} = 0$. Front of the bunch on the right hand side. (b) Temporal profile obtained by summing over a $\cong \pm 430 \mu\text{m}$ -wide region around the bunch axis ($x = 0$).

propagation axis is shown in Fig. A1(b). As seen for measurements at lower density ($n_{e0} = 0.94 \times 10^{14} \text{ cm}^{-3}$ for Chapter 6, $n_{e0} = 1.81 \times 10^{14} \text{ cm}^{-3}$ for Chapter 7), the stitched image shows a periodic micro-bunch train. The only difference from stitched images at lower densities is that regions of focused and defocused protons are harder to differentiate, i.e. the modulation profile appears less distinct due to the insufficient SC resolution. This can also be seen from the temporal profile (Fig. A1(b)). The profile shows a periodic modulation with a smaller modulation amplitude than e.g. that of Fig. 33. Nevertheless, the modulation frequency of the bunch train $f_{mod} = 208.5 \text{ GHz}$ (determined with the DFT-based procedure of Chapter 4.4) agrees within the uncertainties of the DFT with the expected plasma electron frequency of $f_{pe} = 207.7 \text{ GHz}$ (see also [51]).

At a density of $n_{e0} = 7.68 \times 10^{14} \text{ cm}^{-3}$, close to the second baseline density, it is even more challenging to observe micro-bunches on stitched images. An example of thirteen 73 ps SC images stitched together is displayed in Fig. A2. For this data set, the exact position of the LRS with respect to the RIF is unknown, but appears to

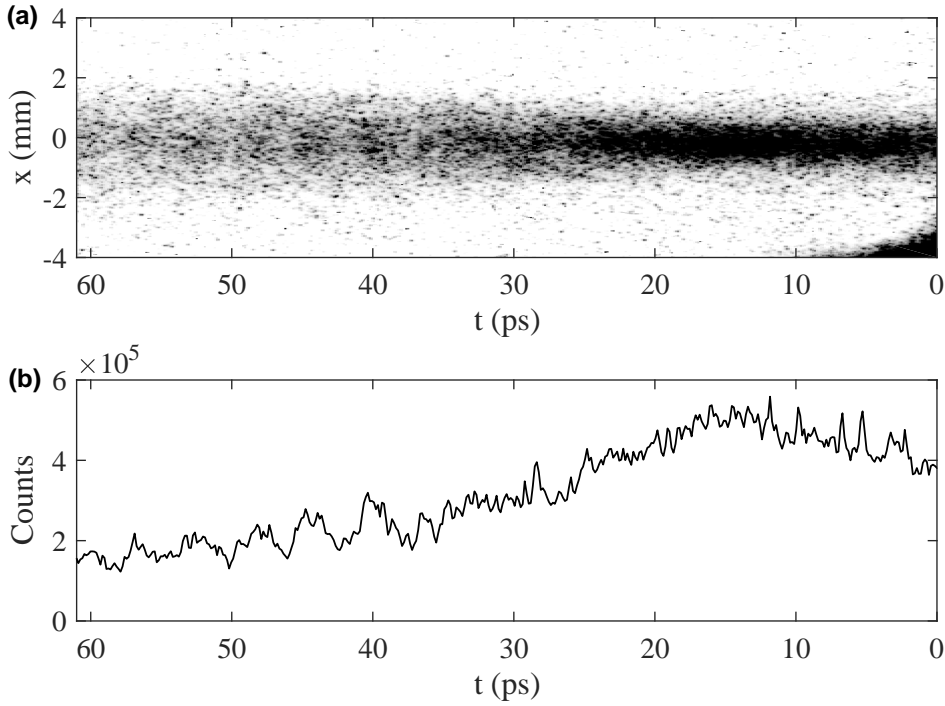


Figure A2: (a) Result of stitching thirteen 73 ps SC images for $n_{e0} = 7.68 \times 10^{14} \text{ cm}^{-3}$, $N_b \approx 3 \times 10^{11}$ and the RIF $t_{RIF} = 125 \text{ ps}$ ahead the center. Front of the bunch on the right hand side. (b) Temporal profile obtained by summing over a $\cong \pm 430 \text{ }\mu\text{m}$ -wide region around the bunch axis ($x = 0$).

be near the seed point. From the image in (a) and the temporal profile in (b), the modulation appears to start at $t \approx 35$ ps, the first micro-bunch is faintly visible at $t = 40$ ps. For $t > 40$ ps, micro-bunches can be identified every $\tau_{mod} \approx 4$ ps. Even though a DFT analysis produced no reliable results due to an insufficient resolution of the modulation, this value matches the expected modulation period of $1/f_{pe} = 4.0$ ps ($f_{pe} = 248.8$ GHz).

A.2 Evaluation of the Rb Vapor Density Measurement

Here, we provide complementary information about the Rb vapor density diagnostic presented in Chapter 3.4.1 and its accuracy discussed in Chapter 3.4.2.2.

A.2.1 Measurement Accuracy and Density Uniformity

The accuracy of the diagnostic is determined as the standard deviation of density measurements with in the vapor source constant temperature T and thus constant n_{e0} , and no gradient ($g = 0$). To determine the accuracy around both AWAKE baseline densities, spectrograms (see Fig. 18 in Chapter 3.4.1) are recorded every 10 s, i.e. the data set is taken over a time range much shorter than that over which changes in the vapor density might appear (\sim hours). Figure A3(a) shows the measured up- and downstream densities $n_{Rb,u}$ and $n_{Rb,d}$ for a Rb reservoir temperature of $T = 182.26^\circ\text{C}$, which provides a density of $n_{Rb} = 1.96 \times 10^{14} \text{ cm}^{-3}$. The gradient values g calculated from the density measurement are plotted in Fig. A3(b). Both densities and the gradient remain constant over time. For the duration of the measurement of ≈ 3 h, the measured values are $n_{Rb,u} = (1.962 \pm 0.005) \times 10^{14} \text{ cm}^{-3}$ and $n_{Rb,d} = (1.967 \pm 0.003) \times 10^{14} \text{ cm}^{-3}$. The standard deviations correspond to statistical uncertainties of 0.25% and 0.15%, respectively. The gradient $g = (0.23 \pm 0.29)\%/m$ (Eq. 3.7).

We repeat the same analysis for the second, higher baseline density, and also $g = 0$. The measured densities and gradient for a reservoir temperature of $T = 208.73^\circ\text{C}$ and $n_{Rb} = 7.68 \times 10^{14} \text{ cm}^{-3}$ is shown in Fig. A4.¹ Similar to Fig. A3, the measured Rb vapor densities $n_{Rb,u}$ and $n_{Rb,d}$ (Fig. A4(a)) and g (Fig. A4(b)) are constant over time. Over 1.5 h, we measure $n_{Rb,u} = (7.682 \pm 0.007) \times 10^{14} \text{ cm}^{-3}$, $n_{Rb,d} = (7.685 \pm 0.005) \times 10^{14} \text{ cm}^{-3}$ and $g = (0.04 \pm 0.10)\%/m$. The respective statistical uncertainty is 0.09% upstream and 0.07% downstream. As stated in the main text in Chapter 3.4.2.2, adding in quadrature the systematic errors from [59] leads to a total uncertainty of $\pm 0.11\%$ to $\pm 0.46\%$, depending on the density. The

¹Note that the absolute density values are slightly different to those cited in Chapter 3.4.2.2 because different data sets with a 0.02°C lower reservoir temperature were used here. However, the results for the accuracy are equivalent.

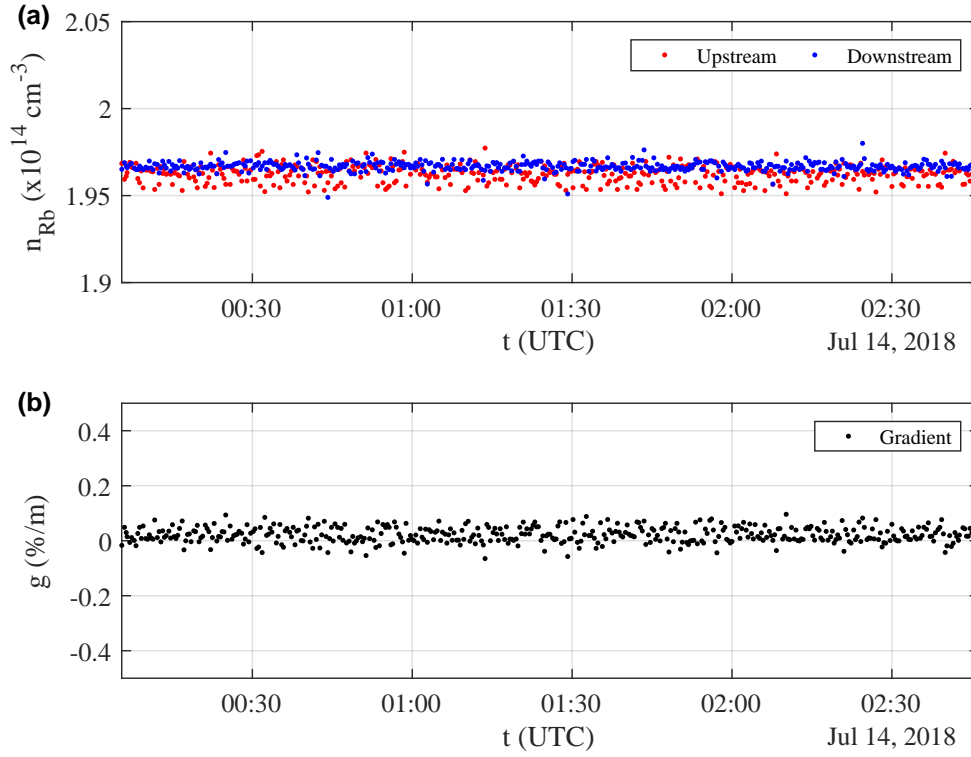


Figure A3: (a) Upstream (red dots) and downstream (blue dots) Rb vapor density vs. time (UTC) for a constant density profile and equal values up- and downstream of $n_{\text{Rb}} = 1.96 \times 10^{14} \text{ cm}^{-3}$. (b) Corresponding density gradient over 10 m along the vapor source vs. time (UTC). Positive gradients indicate that the density is higher downstream.

accuracy of the measurement improves with higher density as the effect of the phase shift on the interference pattern (Fig. 18) enhances.

In summary, these results do not only confirm the high accuracy of the density diagnostic, but also outline the ability of the vapor source to provide the required Rb vapor and thus plasma density uniformity.

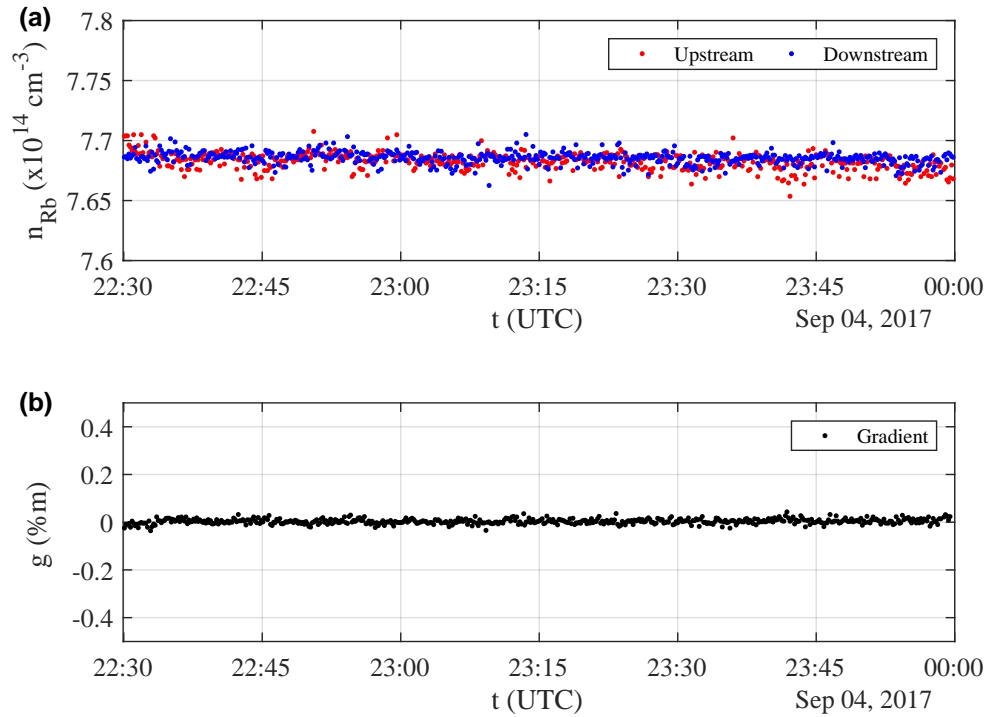


Figure A4: (a) Upstream (red dots) and downstream (blue dots) Rb vapor density vs. time (UTC) for a constant density profile and equal values up- and downstream of $n_{Rb} = 7.68 \times 10^{14} \text{ cm}^{-3}$. (b) Corresponding density gradient over 10 m along the vapor source vs. time (UTC). Positive gradients indicate that the density is higher downstream.

A.2.2 Setting Rb Vapor Density Gradients

In the experiment, linear Rb vapor density and thus plasma gradients along the vapor source are obtained by setting different temperatures in the up- and downstream reservoir (see Chapter 3.3.3). The density at the upstream end of the vapor source is usually kept constant (e.g. as it was also done for the studies of the SM with plasma gradients in this thesis, see the following paragraph A.2.3 for details). Keeping the Rb vapor density constant upstream while increasing the density downstream thereby not only requires changing the temperature of the downstream Rb reservoir, but also adjusting that of the upstream one in the opposite direction. The reason for the necessity of these adjustments is the Rb flow inside the vapor source, which is calculated in [86]. With $g \neq 0$, there is a constant Rb mass flow along the source from the higher-density end to the one with lower density. This means that e.g. increasing the downstream density also increases the flow towards the upstream end and the flow out of the upstream Rb reservoir has to be reduced by lowering its temperature in order to keep $n_{Rb,u}$ constant (and vice versa).

This effect is depicted in Fig. A5 which shows an example measurement where the up- and downstream temperatures and thus densities are adjusted in a way such that a constant increase of $n_{Rb,d}$ and thus g is obtained while keeping $n_{Rb,u}$ constant (the correlation between temperature T in the Rb reservoir and n_{Rb} is presented in Chapter A.2.4 of this appendix). At time $\approx 14:10$, $n_{Rb,d}$ is increased to obtain a positive density gradient along the source. It is clearly visible that also $n_{Rb,u}$ begins to rise and the upstream reservoir temperature had to be adjusted to keep $n_{Rb,u}$ constant. This becomes visible another time at $\approx 15:45$ when a gradient of $\approx +2.0\%/m$ was reached and the downstream density was adjusted to obtain a new, constant gradient of $\approx 0.7\%/m$. With a rapidly decreasing $n_{Rb,d}$, $n_{Rb,u}$ drops as well as long as the upstream reservoir temperature was unchanged. Another adjustment of $n_{Rb,u}$ was necessary. This increase in $n_{Rb,u}$ acted back on $n_{Rb,d}$ which can be seen from the fact that the decrease in density was less step during the time $n_{Rb,u}$ increased (at $\approx 16:50$). After that, the densities and the gradient stabilized within ≈ 30 min.

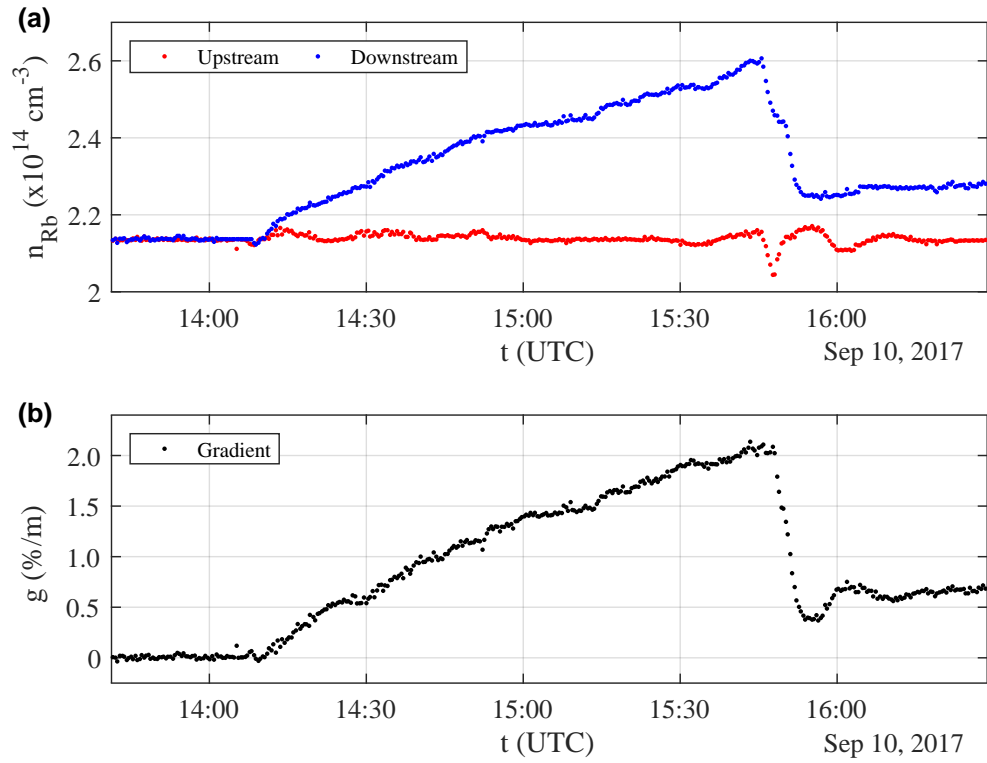


Figure A5: (a) Rb vapor density vs. time (UTC) during a gradient scan. The downstream density (blue) increases and is then lowered again while the density upstream (red) is kept constant. (b) Corresponding density gradient over 10 m along the vapor source vs. time (UTC). Positive gradients indicate that the density is higher downstream.

A.2.3 Vapor Density Measurements for the SM Studies with Plasma Gradients

Here we present the Rb vapor densities and gradients used during the studies of SM with linear plasma gradients in Chapter 7. Figure A6 shows the values of the Rb vapor density, measured at the up- and downstream end of the vapor source ($n_{Rb,u}$ and $n_{Rb,d}$). To maintain a constant plasma density at the vapor source entrance, $n_{Rb,u}$ is kept constant at $1.80 \times 10^{14} \text{ cm}^{-3}$. The density at the downstream and is varied between $2.17 \times 10^{14} \text{ cm}^{-3}$ and $1.46 \times 10^{14} \text{ cm}^{-3}$ to obtain the linear density gradients between $+2\%/m$ and $-2\%/m$. The gaps visible represent times when the Rb valves were closed, i.e. when $n_{Rb} = 0$.

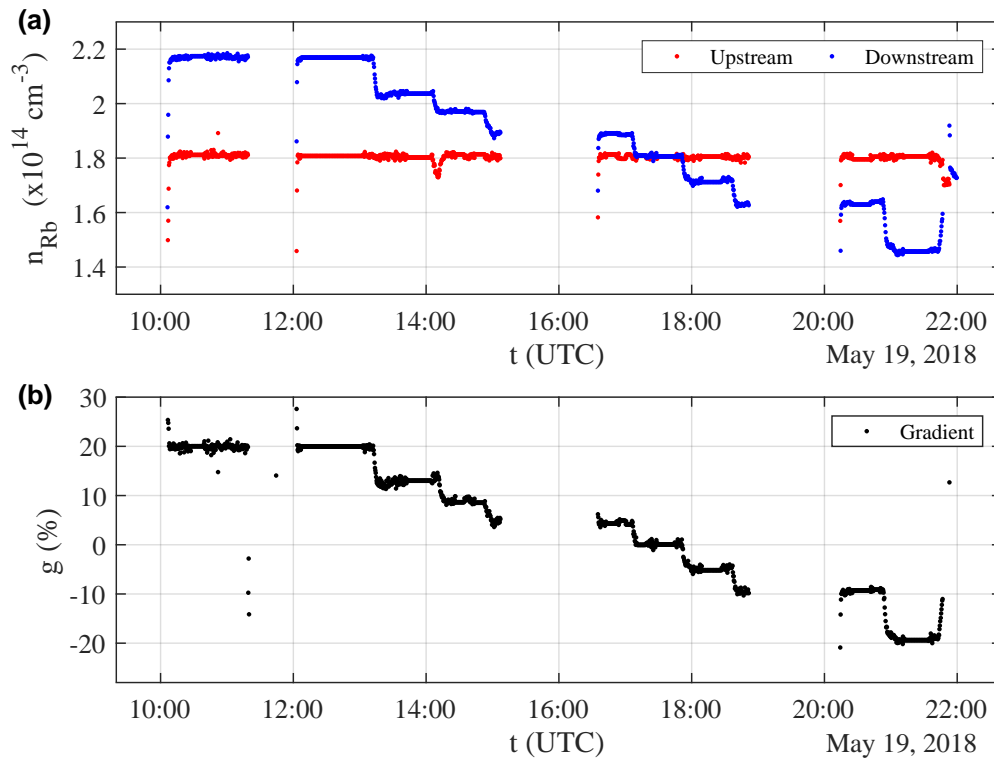


Figure A6: (a) Plot of Rb vapor density vs. time (UTC) on May 19, 2018 for the data presented in Chapter 7. The density at the vapor source entrance (red) is kept constant while the density at its exit (blue) changes. (b) Corresponding density gradient along the vapor source vs. time (UTC). Positive gradients indicate that the density is higher downstream.

A.2.4 Temperature-Density Correlation

Last, we present the correlation between the temperature T in the Rb reservoir and the measured Rb vapor density n_{Rb} inside the vapor source with $g = 0$, i.e. equal densities up- and downstream (see Chapter 3.3.3). The values for n_{Rb} are compared to the values one expects from the vapor pressure curve (Eq. 3.1 in Chapter 3.3.3). As shown in Fig. A7(a), temperatures of 154°C to 215°C lead to vapor densities between $n_{Rb} = 0.5 \times 10^{14} \text{ cm}^{-3}$ to $1.1 \times 10^{15} \text{ cm}^{-3}$. From the vapor pressure curve, one expects

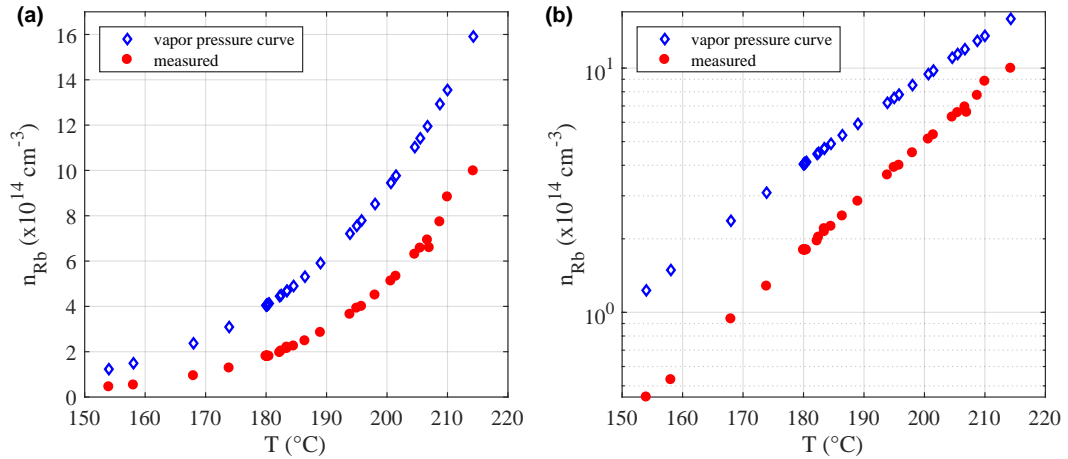


Figure A7: Measured Rb vapor density (red, filled circles) and from the vapor pressure curve (Eq. 3.1) expected density (blue diamonds) versus Rb reservoir temperature on a (a) linear and (b) logarithmic scale.

consistently higher densities, between $1.2 \times 10^{14} \text{ cm}^{-3}$ and $1.6 \times 10^{15} \text{ cm}^{-3}$ for the same range in T . The same plot on a logarithmic scale (Fig. A7(b)) shows that the density follows nevertheless an exponential behavior (as expected from Eq. 3.1). The measured densities are between 2.73 times (at low density) and 1.59 times (at high density) lower than those from the vapor pressure curve. This is explained by the fact that the vapor pressure curve assumes a closed volume without any flow. However, this is not the case for the vapor source of AWAKE (see Fig. 14, Chapter 3.3.3). The Rb flows from the reservoir into the 10 m long heat exchanger. From there, Rb flows through an iris into the expansion chamber to provide a sharp transition between Rb vapor (or plasma) and vacuum. The lower densities therefore agree with the expectation on the general behavior of the vapor source. A detailed analysis of the Rb flow and the dependency of the Rb vapor density in the heat exchanger of the vapor source are not part of this thesis, but are foreseen to be covered in a separate publication of the AWAKE collaboration.

Appendix B

Publications

Transition between Instability and Seeded Self-Modulation of a Relativistic Particle Bunch in Plasma

F. Batsch¹, P. Muggli¹, R. Agnello², C. C. Ahdida³, M. C. Amoedo Goncalves³, Y. Andrebe², O. Apsimon^{4,5}, R. Apsimon^{4,6}, A.-M. Bachmann¹, M. A. Bastrukov^{7,8}, P. Blanchard², F. Braunmüller¹, P. N. Burrows⁹, B. Buttenschön¹⁰, A. Caldwell¹, J. Chappell¹¹, E. Chevally³, M. Chung¹², D. A. Cooke¹¹, H. Damerau³, C. Davut^{4,13}, G. Demeter¹⁴, H. L. Deubner¹⁵, S. Doebert³, J. Farmer^{1,3}, A. Fasoli², V. N. Fedosseev³, R. Fiorito^{4,5}, R. A. Fonseca^{16,17}, F. Friebel³, I. Furno², L. Garolfi¹⁸, S. Gessner^{3,19}, I. Gorgisyan³, A. A. Gorn^{7,8}, E. Granados³, M. Granetzny²⁰, T. Graubner¹⁵, O. Grulke^{10,21}, E. Gschwendtner³, V. Hafych¹, A. Helm¹⁷, J. R. Henderson^{4,22}, M. Hüther¹, I. Yu. Kargapolov^{7,8}, S.-Y. Kim¹², F. Kraus¹⁵, M. Krupa³, T. Lefevre³, L. Liang^{4,13}, S. Liu¹⁸, N. Lopes¹⁷, K. V. Lotov^{7,8}, M. Martyanov¹, S. Mazzoni³, D. Medina Godoy³, V. A. Minakov^{7,8}, J. T. Moody¹, K. Moon¹², P. I. Morales Guzmán¹, M. Moreira^{3,17}, T. Nechaeva¹, E. Nowak³, C. Pakuza⁹, H. Panuganti³, A. Pardons³, A. Perera^{4,5}, J. Pucek¹, A. Pukhov²³, R. L. Ramjiawan^{3,9}, S. Rey³, K. Rieger¹, O. Schmitz²⁰, E. Senes^{3,9}, L. O. Silva¹⁷, R. Speroni³, R. I. Spitsyn^{7,8}, C. Stollberg², A. Sublet³, A. Topaloudis³, N. Torrado¹⁷, P. V. Tuv, ^{7,8} M. Turner^{3,24}, F. Velotti³, L. Verra^{1,3,25}, V. A. Verzilov¹⁸, J. Vieira¹⁷, H. Vincke³, C. P. Welsch^{4,5}, M. Wendt³, M. Wing¹¹, P. Wiwattananon³, J. Wolfenden^{4,5}, B. Woolley³, G. Xia^{4,13}, M. Zepp²⁰ and G. Zevi Della Porta³

(AWAKE Collaboration)

¹Max Planck Institute for Physics, Munich, Germany

²Ecole Polytechnique Federale de Lausanne (EPFL), Swiss Plasma Center (SPC), Lausanne, Switzerland

³CERN, Geneva, Switzerland

⁴Cockcroft Institute, Daresbury, United Kingdom

⁵University of Liverpool, Liverpool, United Kingdom

⁶Lancaster University, Lancaster, United Kingdom

⁷Novosibirsk State University, Novosibirsk, Russia

⁸Budker Institute of Nuclear Physics SB RAS, Novosibirsk, Russia

⁹John Adams Institute, Oxford University, Oxford, United Kingdom

¹⁰Max Planck Institute for Plasma Physics, Greifswald, Germany

¹¹University College London, London, United Kingdom

¹²Ulsan National Institute of Science and Technology, Ulsan, Republic of Korea

¹³University of Manchester, Manchester, United Kingdom

¹⁴Wigner Research Center for Physics, Budapest, Hungary

¹⁵Philipps-Universität Marburg, Marburg, Germany

¹⁶ISCTE–Instituto Universitário de Lisboa, Portugal

¹⁷GoLP/Instituto de Plasmas e Fusão Nuclear, Instituto Superior Técnico, Universidade de Lisboa, Lisbon, Portugal

¹⁸TRIUMF, Vancouver, Canada

¹⁹SLAC National Accelerator Laboratory, Menlo Park, California, USA

²⁰University of Wisconsin, Madison, Wisconsin, USA

²¹Technical University of Denmark, Lyngby, Denmark

²²Accelerator Science and Technology Centre, ASTeC, STFC Daresbury Laboratory, Warrington, United Kingdom

²³Heinrich-Heine-Universität Düsseldorf, Düsseldorf, Germany

²⁴Lawrence Berkeley National Laboratory, Berkeley, California, USA

²⁵Technical University Munich, Munich, Germany



(Received 18 December 2020; revised 18 February 2021; accepted 9 March 2021; published 20 April 2021)

We use a relativistic ionization front to provide various initial transverse wakefield amplitudes for the self-modulation of a long proton bunch in plasma. We show experimentally that, with sufficient initial amplitude [$\geq (4.1 \pm 0.4)$ MV/m], the phase of the modulation along the bunch is reproducible from event to event, with 3%–7% (of 2π) rms variations all along the bunch. The phase is not reproducible for lower

initial amplitudes. We observe the transition between these two regimes. Phase reproducibility is essential for deterministic external injection of particles to be accelerated.

DOI: 10.1103/PhysRevLett.126.164802

Introduction.—Accelerators rely on precise control of parameters to produce high-quality, high-energy particle bunches for numerous applications. A class of novel accelerators using plasma as a medium to sustain large accelerating [1,2] and focusing [3] fields has emerged and has made remarkable experimental progress over the past two decades [4–6].

Most of these accelerators use a very short (< 1 ps), intense laser pulse [1] or a dense, relativistic particle bunch [2] to drive wakefields in plasma. The amplitude of the accelerating field that can be sustained with a plasma of electron density n_{e0} is on the order of the wave breaking field [7]: $E_{\text{WB}} = (m_e c/e)\omega_{pe}$. Here $\omega_{pe} = (n_{e0}e^2/\epsilon_0 m_e)^{1/2}$ is the plasma electron angular frequency [8]. Assuming the driver of rms duration σ_t fits within the structure, i.e., $\sigma_t \cong 1/\omega_{pe}$, one can rewrite: $E_{\text{WB}} = (m_e c/e)(1/\sigma_t)$. Therefore, operating at high accelerating field (> 1 GV/m) requires high plasma density and short (< 2 ps) pulses or bunches with similarly small radii ($\sigma_{r0} \leq c/\omega_{pe} \leq 600 \mu\text{m}$) [9].

The system extracts energy from the driver and transfers it to a witness bunch, through the plasma. The total energy gain of the witness bunch is limited to the energy carried by the driver. Short laser pulses and particle bunches available today and suitable to drive > 1 GV/m amplitude wakefields carry less than ~ 100 J of energy. Laser pulses and particle bunches carrying much more energy are too long, typically > 100 ps, to drive large amplitude wakefields when following the above $E_{\text{WB}} \propto 1/\sigma_t$ scaling. However, long laser pulses [10] and long, relativistic particle bunches [11] propagating in dense plasma, i.e., $\sigma_t \gg 1/\omega_{pe}$, are subject to self-modulation (SM) instabilities. These instabilities can transform them into a train of pulses or bunches shorter than, and with a periodicity of $2\pi/\omega_{pe}$. The train can then resonantly excite large amplitude wakefields. Control of the SM process, in particular of the relative phase of the wakefields, is necessary to deterministically inject a witness bunch shorter than $1/\omega_{pe}$ into the accelerating and focusing phase of the wakefields.

As the first proton-driven plasma wakefield acceleration experiment, AWAKE [12,13] recently demonstrated that the SM process does indeed transform a long proton bunch ($\sigma_t > 200$ ps) into a train of microbunches with period $2\pi/\omega_{pe}$ (< 10 ps) [14]. We also demonstrated that the process grows along the bunch and along the plasma, from the initial wakefield amplitude, to saturate at much larger values [15,16]. Electrons were externally injected in the wakefields, though without phase control (electron bunch duration on the order of $2\pi/\omega_{pe}$) and accelerated from ~ 19 MeV to ~ 2 GeV [17]. For this scheme to become an

accelerator that can produce not only sufficiently high-energy particles, but also sufficiently high-quality bunches in terms of high population, low energy spread, and low emittance [18], one needs to show that the SM process can be controlled.

Seeding of SM in the sense of triggering the start of its growth has been demonstrated experimentally with a relativistic ionization front (RIF) in a long pulse, laser-driven plasma wakefield accelerator [19], and with the sharp density front of a long electron bunch in a particle-driven plasma wakefield accelerator [20]. However, measurements on the effect of that seeding on the phase of growing wakefields have not been reported. As demonstrated below, triggering the SM is not sufficient to ensure the reproducibility of the phase of the wakefields from event to event.

In this Letter, we demonstrate experimentally for the first time that the phase of the SM of a long, relativistic particle bunch can be controlled by seeding the process with a RIF. This means that we define seeding as the conditions leading to a reproducible timing or phase of the SM along the bunch with respect to the RIF from event to event. From time-resolved images of the bunch obtained at two plasma densities, we analyze the relative timing or phase of the microbunches along the proton bunch, after the plasma. We control the initial wakefield amplitude through the timing of the RIF along the bunch. When the process is not seeded, we observe randomly distributed phases and thus the SM instability (SMI) [11]. With sufficiently strong initial amplitude, the phase of the wakefields varies by only a small fraction of 2π from event to event, the characteristic of seeded SM (SSM) [13]. This is despite natural variations of the incoming bunch parameters [21]. We thus observe the transition from SMI to SSM. We also observe phase reproducibility over more than $2\sigma_t$ along the bunch. Phase reproducibility is essential for future experiments [13] with deterministic, external injection of particles to be accelerated (e^- or e^+) at a precise phase within the accelerating and focusing region of the wakefields [18].

Experimental results presented here show that the phase of the self-modulation instability, a fundamental beam-plasma interaction mechanism [11], can be controlled. It is also a requirement for future acceleration experiments.

Experimental setup.—The CERN Super Proton Synchrotron (SPS) provides a Gaussian bunch with 400 GeV energy per proton, 3×10^{11} particles, and a rms duration $\sigma_t = 250$ ps. The bunch enters a 10-m-long vapor source [22,23], as shown in Fig. 1, with rms waist size $\sigma_{r0} = 150 \mu\text{m}$. The source contains rubidium (Rb) vapor

with density n_{Rb} adjustable in the $(0.5\text{--}10) \times 10^{14} \text{ cm}^{-3}$ range and with uniform temperature and thus density distributions ($\Delta n_{\text{Rb}}/n_{\text{Rb}} = \Delta T/T < 0.2\%$ [23]). The vapor density is measured to better than 0.5% [24] at both ends of the source. A Ti:sapphire laser system provides a 120 fs, ≤ 450 mJ laser pulse that can serve two purposes. First, when propagating along the vapor column it creates the plasma at the RIF. The RIF transforms the Rb vapor into a ~ 2 mm diameter plasma with density and uniformity equal to those of the vapor [14]. Therefore, hereafter we quote the corresponding plasma density instead of the measured Rb vapor density ($n_{e0} = n_{\text{Rb}}$). Second, when propagating within the proton bunch, the RIF triggers the sudden ($\ll 1/\omega_{pe}$) onset of beam plasma interaction that can seed the SM process. Seeding can occur because this onset corresponds to the driving of initial plasma wakefields starting at the RIF and with amplitudes depending on the local bunch density [14,15].

The train of microbunches resulting from the SM process leaves the plasma after 10 m and passes through an aluminum-coated screen where protons emit optical transition radiation (OTR), 3.5 m from the plasma exit. The OTR has the same spatiotemporal structure as the modulated proton bunch. A streak camera resolves the incoming OTR light imaged onto its entrance slit in space and in time with resolutions of $80 \mu\text{m}$ and ~ 1 ps, respectively, over a 73 ps time window. Since the entrance slit is narrower than the bunch radius at the screen location, images display the bunch charge density and not its charge [25]. A transfer line (dashed blue line in Fig. 1 [26]) guides a mirror bleed-through of the laser pulse to the streak camera. This signal (in red circle in inset 2 of Fig. 1) indicates on each image the relative timing of the RIF within the proton bunch with 0.53 ps (rms) accuracy and 0.16 ps precision. It can be delayed together with the camera trigger signal to appear on the image at times later than that of the RIF, as seen every 50 ps at the bottom of Fig. 4(a). This signal is necessary to refer images in time with respect to the RIFs and with respect to each other's timing, because the streak camera triggering system has a time jitter of 4.8 ps (rms), equivalent to approximately half a period of the wakefields.

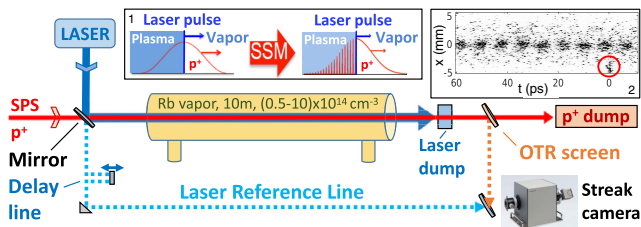


FIG. 1. Schematic of the experimental setup showing the main components used for measurements presented here. Inset 1: RIF in the middle of the proton bunch ($t_{\text{RIF}} = 0$ ps). Inset 2: streak camera image of a modulated proton bunch, laser reference signal at $t = 0$ ps (red circle).

In the following, we refer to this signal as the laser reference signal (LRS).

Results.—We observe that when we use the RIF for plasma creation only, placing it nano- to microseconds ahead of the proton bunch, SM occurs [27]. In this case SM can grow from noise present in the system. The wakefield amplitude driven by shot noise in the proton bunch distribution was estimated at the tens of kV/m level [28]. The laser pulse drives wakefields at the < 100 kV/m level at the plasma densities of these experiments [29]. Figure 2(a) shows a composite image of the time structure of the center part of the modulated proton bunch (compare Fig. 1, inset 2) for ten events in the 73 ps window, placed 150 ps ($0.6\sigma_t$) ahead of the bunch peak. These events are aligned in time with respect to the LRS. The LRS alignment procedure yields a ~ 50 -ps-long common window between images. The LRS (not shown) is placed at $t = 0$ ps on each image. The RIF is 600 ps ($2.4\sigma_t$) ahead of the bunch peak (i.e., 450 ps, $1.8\sigma_t$ between RIF and $t = 0$ on the image). Each image is normalized to its incoming bunch population. The figure clearly shows that from event to event microbunches appear at no particular times with respect to the RIF. It also shows that the measured microbunch charge density varies considerably. Variations in bunch density on these images can be attributed to amplitude variations of focusing and defocusing fields [25]. Variations in timing or phase and amplitude of the modulation are expected for the occurrence of a (nonseeded) instability such as SMI [11].

Figure 2(b) shows a similar plot to that of Fig. 2(a), but with the RIF placed closer, 350 ps ($1.4\sigma_t$) ahead of the bunch peak and thus with larger wakefield amplitude at the RIF, with all other parameters unchanged. It is clear that in this case the microbunches appear essentially at the same time with respect to the RIF and with much more consistent charge density than in the previous case. These data show the behavior expected from a seeded process such as SSM. From these two plots we conclude that in the first case the

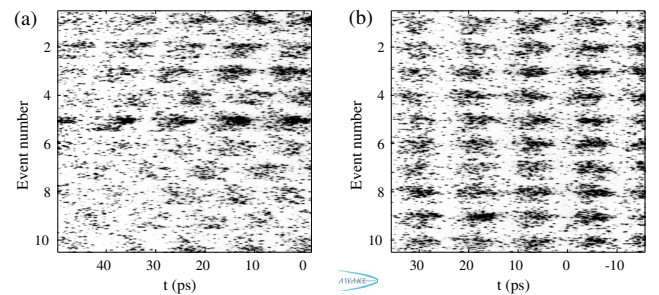


FIG. 2. Composite images of the center part of the streak camera image (see Fig. 1, inset 2) for ten events with (a) RIF 600 ps ($2.4\sigma_t$) and (b) RIF 350 ps ($1.4\sigma_t$) ahead of the proton bunch center. Front of the bunch on the right-hand side. Events aligned with respect to LRS ([26], at $t = 0$, not visible). Both cases: LRS 150 ps ($0.6\sigma_t$) ahead of bunch center, $n_{e0} = 0.94 \times 10^{14} \text{ cm}^{-3}$.

phase of the modulation is not reproducible from event to event (SMI), whereas it is in the second case (SSM).

In order to quantify the observed effect, we determine the phase or timing (using the modulation frequency or period) of the bunch modulation with respect to the RIF. For this purpose we sum counts of the bunch image in a $\cong \pm 430\text{-}\mu\text{m}$ -wide region around the axis of the bunch at the OTR screen to obtain a time profile of the bunch SM. At this location the incoming bunch transverse rms size is $\cong 574\ \mu\text{m}$ [see Fig. 4(a), $t < 0$ ps]. For each event, we determine the time of the LRS in the 73 ps window. We calculate the relative phase or timing of the microbunch appearing after the LRS as explained in the Supplemental Material [30]. For the dataset analyzed here ($n_{e0} = 0.94 \times 10^{14}\ \text{cm}^{-3}$), the modulation frequency is 87.1 GHz.

Figure 3 shows the variation in relative phase for six series (including the events of Fig. 2) of approximately 18 events each, measured with the analysis window (and LRS) 150 ps ahead of the bunch peak, as a function of the RIF timing t_{RIF} along the bunch normalized to the rms bunch duration. The phase distributions for $t_{\text{RIF}} \geq 2.0\sigma_t$ cover a range (blue diamonds) close to 2π and their rms (blue circles) approaches the value expected for a uniform distribution, 29%. This corresponds to a phase randomly distributed from event to event, possibly varying over more than 2π . On the contrary, for $t_{\text{RIF}} \leq 1.8\sigma_t$, the ranges are $\ll 2\pi$ and their rms is small, $\sim 6\%$, which shows that the phase of the SM is reproducible from event to event (within the rms range). This is the transition from SMI, with the modulation phase not reproducible [Fig. 2(a)], to SSM, with the modulation phase reproducible within a small range of 2π [Fig. 2(b)], when the initial wakefield amplitude increases. We show later, by delaying the observation window timing for a fixed t_{RIF} , that when reached in one

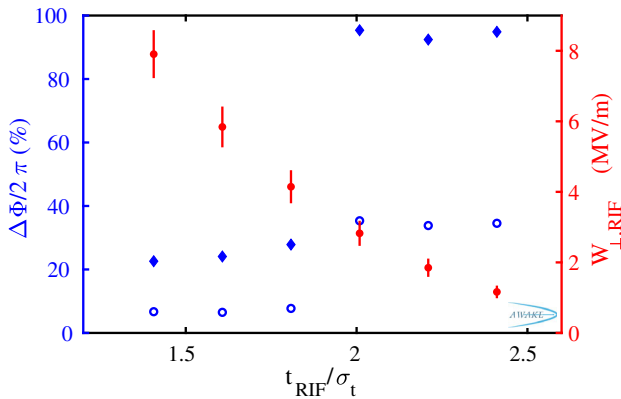


FIG. 3. Measured rms (blue circles) and full phase variation (blue diamond), and initial linear transverse wakefield amplitude (filled red circles) as a function of t_{RIF} normalized to σ_t . The error bars indicate the statistical uncertainty of 10.1% (see text). Error bars representing the uncertainty in t_{RIF} due to the 15 ps ($0.06\sigma_t$) rms proton timing jitter are not plotted. Same LRS timing and n_{e0} as in Fig. 2.

window, the timing or phase reproducibility occurs all along the bunch, as expected. In the SMI regime, time-resolved images (not presented here) of the SM near the seed point show that full SM starts at different times along the bunch, unlike in the seeded cases, where it starts at the RIF [14]. This explains the $\sim 2\pi$ (modulo) phase variations observed with SMI. In the SSM regime, the observed phase rms variations of $\sim 6\%$ (of 2π) results from at least three main contributions. First, the intrinsic phase variations that are the goal of the measurement. Second, variations of initial parameters from event to event originating from the bunch or the plasma. We measure rms variations in bunch length, $\approx 1.6\%$, population, $\approx 5\%$, and plasma density, $< 0.2\%$. There may be additional variations in bunch waist size and location and emittance that we do not monitor for each event. The influence of these variations on the phase can in principle be obtained from numerical simulations [21], though reaching percent level precision is very challenging. Third, variations due to the measurement accuracy influenced by the streak camera resolution of the modulation, the limited number of microbunches per image, signal noise, and uncertainties in determining the position of the LRS (0.16 ps). As a consequence, the measured variations can only be seen as an upper limit for the real phase variations. They are probably dominated by the last two contributions mentioned, mainly by uncertainties originating from the noisy measured modulation profile (see Supplemental Material [30]).

The initial transverse wakefield amplitude (at the plasma entrance) can be calculated as a function of the RIF timings of Fig. 3: $W_{\perp,\text{RIF}}(t = t_{\text{RIF}})$ (see Supplemental Material [30]). The initial proton bunch density [$n_b(t) = n_{b0}e^{-t^2/2\sigma_t^2}$, with $n_{b0} = 1.1 \times 10^{13}\ \text{cm}^{-3}$] is smaller than the plasma density ($n_{e0} = 0.94 \times 10^{14}\ \text{cm}^{-3}$). We thus use two-dimensional linear plasma wakefield theory [31] to evaluate this amplitude. The modulation period ($\cong 11.5$ ps) is much shorter than the rms bunch duration ($\sigma_t = 250$ ps). We therefore consider the Gaussian bunch density $n_b(t = t_{\text{RIF}})$ constant over one period behind the RIF and thus $W_{\perp,\text{RIF}} = 2(m_e c^2/e)[n_b(t_{\text{RIF}})/n_{e0}]dR/dr|_{r=\sigma_{r0}}$. The radial dependence of wakefields through the $R(r)$ coefficient [31] is a function of the transverse bunch profile, considered as Gaussian, and is evaluated at $r = \sigma_{r0}$, independent of t .

We plot the amplitude of $W_{\perp,\text{RIF}}$ for each data point in Fig. 3 (filled red circles). The input parameter variations mentioned above cause a maximum statistical uncertainty of 10.1% on the field calculation, which includes a 15 ps ($0.06\sigma_t$) rms timing jitter between the proton bunch and the laser pulses (RIF and LRS), all added in quadrature. This uncertainty is indicated by the error bars. The plot shows that for the parameters of these experiments, the transition between SMI and SSM occurs between (2.8 ± 0.3) and (4.1 ± 0.4) MV/m. The fact that initial wakefield amplitudes of (2.8 ± 0.3) MV/m do not seed the SM process may indicate that the bunch has density irregularities

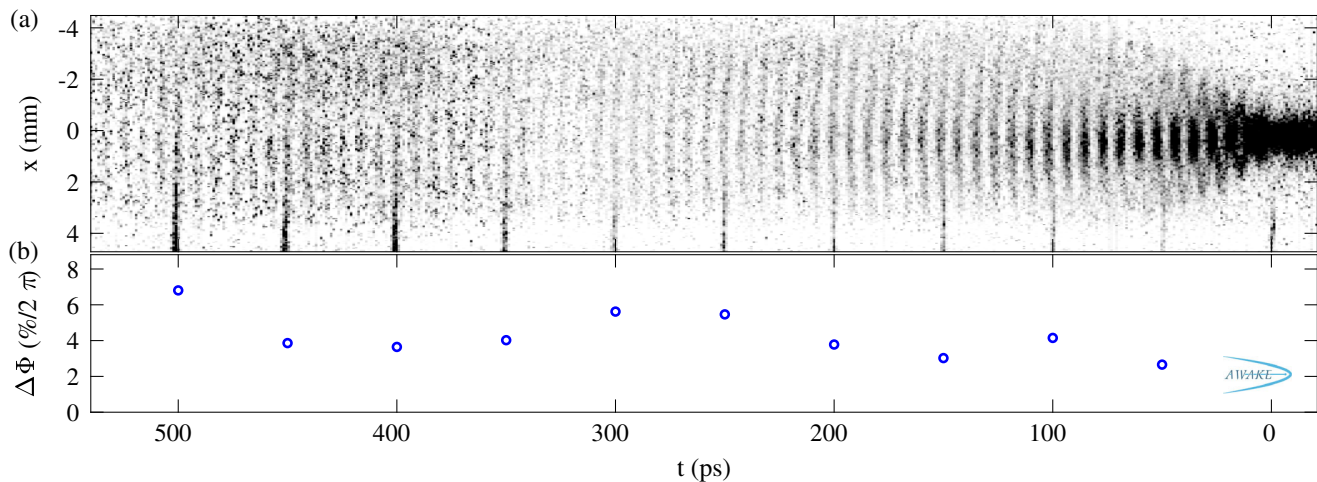


FIG. 4. (a) Time-resolved, “stitched” image of the self-modulated proton bunch with $t_{\text{RIF}} = 125$ ps ($0.5\sigma_t$), $n_{e0} = 1.81 \times 10^{14}$ cm $^{-3}$. The RIF is at $t = 0$ on the image (not visible). The LRS is visible every 50 ps at the bottom of the image. (b) Modulation rms phase variation for each set of images with equal LRS timing.

driving initial wakefields with amplitude [between (2.8 ± 0.3) and (4.1 ± 0.4) MV/m] much larger than those of the shot noise assumed in [28] driving < 100 kV/m fields. These irregularities correspond to 14%–20% of the bunch peak density maintained over at least one period of the wakefields. Since the amplitude of the initial wakefields at the RIF and that of wakefields driven by incoming bunch irregularities follow essentially the same scaling [$W_{\perp}(t) \propto n_b(t)/n_{e0}$], we expect the transition from SSM to SMI to occur at the same time along the bunch, independently of the bunch and plasma densities. We also note here that we interpret the reproducibility of the bunch modulation as also that of the wakefields driven toward the end of the plasma, after saturation of the SM process [16]. The wakefield structure is intrinsically linked to the distribution of the self-modulated proton bunch.

The phase reproducibility can be further confirmed by similar phase variation measurements at various delays behind the RIF. Sets of approximately ten images with delay increments of 50 ps between each set were acquired at a higher plasma density $n_{e0} = 1.81 \times 10^{14}$ cm $^{-3}$ and a fixed RIF timing of 125 ps ($0.5\sigma_t$). Since for these measurements, the RIF is placed much closer to the bunch center ($0.5\sigma_t$) than the SSM-SMI transition point determined from the lower plasma density measurements ($\sim 1.9\sigma_t$), we expect the SM process to be in the SSM regime. This is confirmed by Fig. 4. Because of the time overlap between sets, all images can be “stitched” together using the LRS as described in Ref. [26] [see Fig. 4(a)]. It is immediately clear from the figure that microbunches of all events align themselves in time or phase and form a coherent modulation of the bunch density over $\sim 2\sigma_t$ behind the RIF. This is only possible when proper seeding is provided (SSM) for each event, relative phase variations between events are small [i.e., all sequences look similar to

that of Fig. 2(b)], and the modulation phase is reproducible all along the bunch. All features visible in Fig. 4(a) would wash out if phases were randomly distributed as in Fig. 2(a).

Figure 4(b) shows the result of the phase analysis applied to these events. Over the $\sim 2\sigma_t$ measurement range, larger than the delay from the RIF of $\sim 1\sigma_t$ typically foreseen for external electron injection, the phase variations remain small and in a similar range to those obtained at lower plasma density. Variations along the bunch are most likely due to changes in signal that can be seen in Fig. 4(a) and on individual images, which affects the accuracy of the phase determination. The measured variations remain approximately constant and between 3% and 7% (of 2π) all along the bunch.

Summary.—We presented the results of experimental studies of the SM phase for different timings of the RIF with respect to the proton bunch, measured after the 10-m-long plasma. These results demonstrate that the SM process can be seeded; i.e., the phase of the modulation can be defined by the RIF and reproducible from event to event. We observe the transition from phase nonreproducibility and instability (SMI) to seeding and phase reproducibility (SSM) when the transverse wakefield at the RIF exceeds a threshold amplitude, between (2.8 ± 0.3) and (4.1 ± 0.4) MV/m for $n_{e0} = 0.94 \times 10^{14}$ cm $^{-3}$. This value is much larger than that calculated from the bunch shot noise assumed in [28] driving < 100 kV/m fields. We show that in the SSM regime variations of the modulation phase along the bunch ($\sim 2\sigma_t$) are small, measured at $\leq 7\%$. We attribute most of these small variations to the measurement accuracy of the modulation phase within single, 73 ps time windows including only 6–9 modulation periods. The phase reproducibility also observed at higher plasma density allows for detailed observation of

the SM process along the whole bunch with \sim ps time resolution [Fig. 4(a)].

Based on these results, one can thus expect that for the studies of electron acceleration during AWAKE Run II [29], the wakefields driven by the bunch train in the second plasma will have a timing or phase also reproducible from event to event since they will be driven by the bunch emerging from the first plasma. Phase reproducibility is required for deterministic acceleration of electrons externally injected into the wakefields, with a fixed delay with respect to the seed.

This work was supported by the Wolfgang Gentner Programme of the German Federal Ministry of Education and Research (Grant No. 05E15CHA); in parts by a Leverhulme Trust Research Project Grant No. RPG-2017-143 and by STFC (AWAKE-UK, Cockcroft Institute core and UCL consolidated grants), UK; a Deutsche Forschungsgemeinschaft Project Grant No. PU 213-6/1 “Three-dimensional quasi-static simulations of beam self-modulation for plasma wakefield acceleration”; the National Research Foundation of Korea (No. NRF-2016R1A5A1013277 and No. NRF-2020R1A2C1010835); the Portuguese FCT—Foundation for Science and Technology, through Grants No. CERN/FIS-TEC/0032/2017, No. PTDC-FIS-PLA-2940-2014, No. UID/FIS/50010/2013, and No. SFRH/IF/01635/2015; NSERC and CNRC for TRIUMF’s contribution; the U.S. National Science Foundation under Grant No. PHY-1903316; and the Research Council of Norway. M. Wing acknowledges the support of DESY, Hamburg. Support of the Wigner Datacenter Cloud facility through the “Awakelaser” project is acknowledged. The work of V. H. has been supported by the European Union’s Framework Programme for Research and Innovation Horizon 2020 (2014–2020) under the Marie Skłodowska-Curie Grant Agreement No. 765710. The AWAKE Collaboration acknowledge the SPS team for their excellent proton delivery.

-
- [1] T. Tajima and J. M. Dawson, *Phys. Rev. Lett.* **43**, 267 (1979).
 - [2] P. Chen, J. M. Dawson, R. W. Huff, and T. Katsouleas, *Phys. Rev. Lett.* **54**, 693 (1985).
 - [3] P. Chen, J. J. Su, T. Katsouleas, S. Wilks, and J. M. Dawson, *IEEE Trans. Plasma Sci.* **15**, 218 (1987); P. Chen, S. Rajagopalan, and J. Rosenzweig, *Phys. Rev. D* **40**, 923 (1989).
 - [4] I. Blumenfeld *et al.*, *Nature (London)* **445**, 741 (2007).
 - [5] M. Litos *et al.*, *Nature (London)* **515**, 92 (2014).

- [6] A. J. Gonsalves *et al.*, *Phys. Rev. Lett.* **122**, 084801 (2019).
- [7] J. M. Dawson, *Phys. Rev.* **113**, 383 (1959).
- [8] Constants have usual meaning: e electron charge, ϵ_0 vacuum permittivity, m_e electron mass, c speed of light in vacuum.
- [9] J. J. Su, T. Katsouleas, J. M. Dawson, P. Chen, M. Jones, and R. Keinigs, *IEEE Trans. Plasma Sci.* **15**, 192 (1987).
- [10] C. J. McKinstrie, *Phys. Fluids B* **4**, 2626 (1992).
- [11] N. Kumar, A. Pukhov, and K. Lotov, *Phys. Rev. Lett.* **104**, 255003 (2010).
- [12] E. Gschwendtner *et al.*, *Nucl. Instrum. Methods Phys. Res., Sect. A* **829**, 76 (2016).
- [13] P. Muggli *et al.* (AWAKE Collaboration), *Plasma Phys. Controlled Fusion* **60**, 014046 (2018).
- [14] AWAKE Collaboration, *Phys. Rev. Lett.* **122**, 054802 (2019).
- [15] M. Turner *et al.* (AWAKE Collaboration), *Phys. Rev. Lett.* **122**, 054801 (2019).
- [16] M. Turner *et al.* (AWAKE Collaboration), *Phys. Rev. Accel. Beams* **23**, 081302 (2020).
- [17] AWAKE Collaboration, *Nature (London)* **561**, 363 (2018); AWAKE Collaboration, *Phil. Trans. R. Soc. A* **377**, 20180418 (2019).
- [18] Veronica K. Berglyd Olsen, E. Adli, and P. Muggli, *Phys. Rev. Accel. Beams* **21**, 011301 (2018).
- [19] S. P. Le Blanc, M. C. Downer, R. Wagner, S.-Y. Chen, A. Maksimchuk, G. Mourou, and D. Umstadter, *Phys. Rev. Lett.* **77**, 5381 (1996).
- [20] Y. Fang, V. E. Yakimenko, M. Babzien, M. Fedurin, K. P. Kusche, R. Malone, J. Vieira, W. B. Mori, and P. Muggli, *Phys. Rev. Lett.* **112**, 045001 (2014).
- [21] M. Moreira, J. Vieira, and P. Muggli, *Phys. Rev. Accel. Beams* **22**, 031301 (2019).
- [22] G. Plyushchev, R. Kersevan, A. Petrenko, and P. Muggli, *J. Phys. D* **51**, 025203 (2018).
- [23] E. Öz, and P. Muggli, *Nucl. Instrum. Methods Phys. Res., Sect. A* **740**, 197 (2014).
- [24] F. Batsch, M. Martyanov, E. Oez, J. Moody, E. Gschwendtner, A. Caldwell, and P. Muggli, *Nucl. Instrum. Methods Phys. Res., Sect. A* **909**, 359 (2018).
- [25] A.-M. Bachmann and P. Muggli, *J. Phys. Conf. Ser.* **1596**, 012005 (2020).
- [26] F. Batsch, *J. Phys. Conf. Ser.* **1596**, 012006 (2020).
- [27] S. Gessner *et al.* (AWAKE Collaboration), arXiv:2006.09991.
- [28] K. V. Lotov, G. Z. Lotova, V. I. Lotov, A. Upadhyay, T. Tückmantel, A. Pukhov, and A. Caldwell, *Phys. Rev. ST Accel. Beams* **16**, 041301 (2013).
- [29] P. Muggli *et al.*, *J. Phys. Conf. Ser.* **1596**, 012008 (2020).
- [30] See Supplemental Material at <http://link.aps.org/supplemental/10.1103/PhysRevLett.126.164802> for a description of the analysis that yields the timing or phase of the microbunch train and for the calculation of the initial transverse wakefield amplitude.
- [31] R. Keinigs and M. E. Jones, *Phys. Fluids* **30**, 252 (1987).

Setup and Characteristics of a Timing Reference Signal with sub-ps Accuracy for AWAKE

Fabian Batsch for the AWAKE Collaboration

CERN, CH-1211 Geneva 23, Switzerland

E-mail: fabian.batsch@cern.ch

Abstract. We describe a method to overcome the triggering jitter of a streak camera to obtain less noisy images of a self-modulated proton bunch over long time scales (~ 400 ps to ns) with the time resolution (~ 1 ps) of the short time scale images (73 ps). We also determine that this method, using a reference laser pulse with a variable delay, leads to the determination of the time delay between the ionizing laser pulse and the reference pulse with an error of 0.6 ps (rms).

1. Introduction

The AWAKE experiment is a proof-of-principle experiment at CERN demonstrating electron acceleration in a proton-driven plasma wakefield accelerator [1, 2]. A 10 m-long vapor source provides rubidium (Rb) vapor with homogeneous temperature and density uniformity (better 0.2 % [3]) (see Fig. 1). A Ti:Sapphire laser system ionizes the vapor (first e^- of each Rb atom)

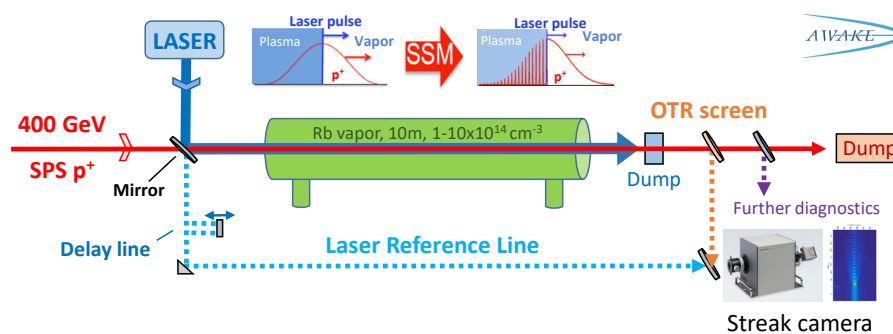


Figure 1. Schematic of the AWAKE experiment showing the different beam and diagnostic components, in particular the beam path of the laser timing reference signal.

which forms a plasma with ~ 1 mm radius along the source. A co-propagating proton bunch from the CERN SPS (energy 400 GeV, bunch length $\sigma_z = 6 - 12$ cm) self-modulates into micro-bunches [4] (see sketch in Fig. 1). These micro-bunches resonantly drive wakefields, in which electrons from a 19 MeV electron source are captured and accelerated. The self-modulation (SM) process can start from noise (so-called self-modulation instability, SMI) or can be seeded by placing the ionizing laser pulse within the proton bunch (seeded self-modulation, SSM) [4, 5]. In AWAKE, the sharp ionization front serves as the seed.

Downstream of the vapor source, diverse beam diagnostics and the electron spectrometer are located. A thin metallic dump directly after the plasma blocks the ionizing laser pulse to protect these. The diagnostic to image the modulated proton bunch uses optical transition radiation (OTR) and a streak camera [4]. The micro-bunches pass through a metallic foil, emitting OTR. This light propagates over a 15-m-long transport line to a streak camera.

The streak camera triggering system exhibits a ≈ 5 ps jitter (rms) with respect to the ionizing laser pulse (see chapter 3.1). For best time resolution (~ 1 ps), the streak camera window is 73 ps and the modulation period is in the 3 to 10 ps range. Comparison of the relative modulation timing between events and over the long timescale of the proton bunch (~ 1 ns) is therefore not possible. We thus developed and implemented a laser timing reference signal indicating the laser time-of-arrival on the streak camera images with sub-ps accuracy, as described in the following.

2. Experimental implementation

2.1. Setup and working principle

The chirp-pulse amplification Ti:Sapphire laser system produces pulses with an energy up to 450 mJ and a duration of 120 fs. For the timing reference signal, we pick up the bleed-through of the ionizing laser pulse from the first mirror after the laser system [2]. This ensures that changes in the laser timing, originating from the amplifiers and the compressor in the laser chain, do not affect the synchronization between the reference signal and the ionizing laser pulse. An optical transfer line with in total 18 partially motorized, 2-inch-diameter mirrors and 1-inch periscopes guides the reference signal in free-space to the streak camera. It uses a separate, 60 m-long path parallel to the proton beam line (partially using the vacuum transport pipe described in [6]). Neutral density filters reduce the light intensity to protect the streak camera. The simplified path of the reference signal is sketched in Fig. 1 as the dashed blue line. It includes a delay line, consisting of a motorized translation stage with 15 cm travel range and a retro reflector. It allows for remotely adjusting the time-of-arrival of the reference signal on the streak camera over the range of 1 ns. The free-space propagation of the reference signal provides a dispersion-minimized transport and a pulse length comparable to thus of the ionizing laser pulse.

The streak camera (512×672 pixel) time-resolves the spatial structure of the incoming OTR light with time windows from 50 ns to 73 ps. Figure 2(a) shows a single streak camera image of a self-modulated proton bunch behind the ionization point, as recorded on the 73 ps window.

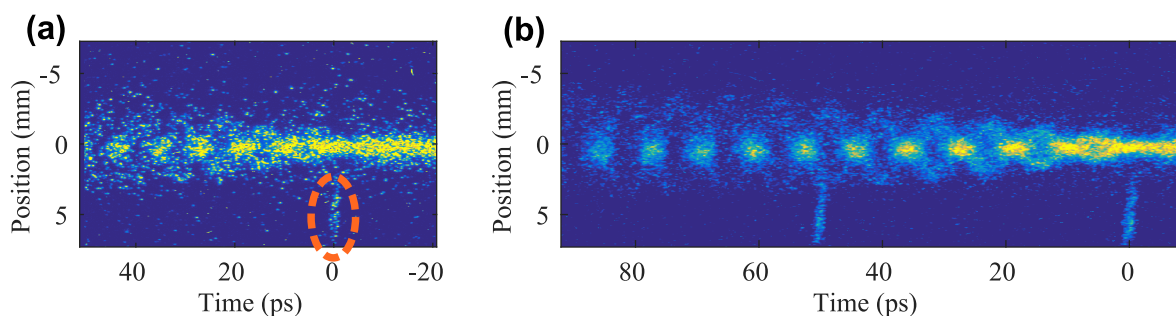


Figure 2. (a) Streak camera image showing the self-modulation behind the ionization laser pulse and the laser reference signal, marked by the orange circle. The head of the bunch is at negative time values. The event was recorded using the 73 ps streak camera window and with a Rb vapor density of $1.8 \times 10^{14} \text{ cm}^{-3}$. (b) Reconstructed image of the self-modulated proton bunch. We delayed the reference signal by 50 ps with respect to the zero timing and averaged over nine events for each delay position of the reference signal.

The reference signal, visible at the bottom of the image at $t = 0$ ps (marked by a circle), shows the time-of-arrival of the ionization front. Its timing is used as the zero point for most SM analysis, including the studies on seeding processes, the phase reproducibility of the SM and on the influence of a plasma gradient on the SM, all described in separate publications and to be published soon. For image processing, series of images with similar experimental parameters can be synchronized in time with respect to the reference signal timing and numerically added together or averaged, despite the triggering system jitter. The resulting image of the proton bunch is an average of the events with improved signal-to-noise ratio and reveals more details of the SM process.

To obtain an averaged image of the entire proton bunch using the highest time resolution window (73 ps) and thus analyse the micro-bunches 10s to 100s of ps behind the seed point, we introduce a delay between the reference signal and the ionization front using the translation stage (see Fig.1). We delay the trigger of the streak camera by the same amount. Then, we stitch together these superimposed events according to the delay of the reference signal. Figure 2(b) shows an example for the resulting procedure of superimposing and stitching events. Nine consecutive events are superimposed for each of the two delay steps. The reference signal was delayed once by 50 ps. Repeating this procedure several times allows for imaging the entire self-modulated proton bunch with the highest resolution of 1 ps and the improved signal-to-noise ratio.

2.2. Time matching

To indicate the time-of-arrival of the ionizing laser with sub-ps accuracy, the path length of the reference signal line and of the ionizing laser beam line (≈ 60 m) must be matched with an accuracy better $300 \mu\text{m}$ (or 1 ps). To verify this, we send the ionizing laser pulse in low energy mode along the beam path onto the OTR foil and observe both pulses simultaneously on the streak camera. In high laser energy mode, the ionizing laser pulse is blocked by an aluminium foil placed between the plasma and the OTR foil and is not visible on streak camera images (e.g. Fig.2(a)). We use the delay line to match the reference signal and ionizing laser time-of-arrival and thus their path lengths. For the matching, one has to take into account the different propagation times through optics material for the low-energy laser beam at 780 nm and the broadband OTR light (filtered to (450 ± 10) nm to maximize the time resolution of the streak camera [4]). The optical dispersion induced by optical elements in the beam path between the OTR light and the laser light was measured to be 9.9 ps [7]. It can be compensated for with the delay line to obtain a reference signal effectively synchronized with OTR light and thus with the SM. Any error on this delay would correspond to a systematic error in timing and would not influence measurements between events.

3. Characteristics

The purpose of the laser timing reference signal is to be used as a timing reference with respect to the ionizing laser pulse, with a variable delay. During experiments, the measured variation in relative time is a convolution of the real time variation and the measurement uncertainties from the timing reference signal. These main uncertainties originate from a timing jitter between the ionizing laser pulse and the reference signal (caused by pointing jitter, mechanical vibrations and air draft), from the uncertainty in determining the time-of-arrival of the reference signal and from the error on the translation stage moving distance. To characterize these uncertainties, we set the reference line delay so that it is visible together with the laser in low energy mode on the same streak camera image with a 73 ps window. For this test measurement, we also introduce a 5 mm-thick piece of glass in the beam path to obtain multiple surface reflections. Figure 3 shows a streak camera image with the reference signal as well as the low power ionizing laser pulse including its reflections.

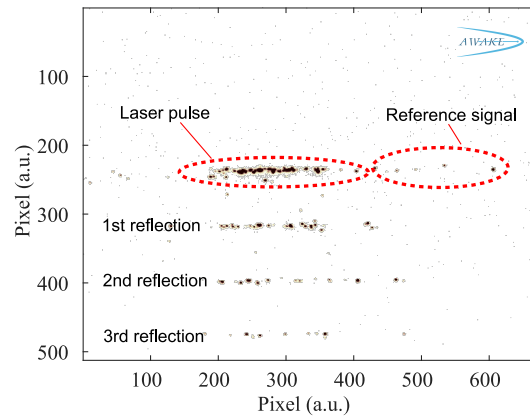


Figure 3. Streak camera image showing the laser pulse and its three reflections.

3.1. Trigger system jitter between streak camera and laser

Before characterizing the measurement errors, we quantify the trigger system jitter of the streak camera time window relative to the laser reference signal by measuring the pixel (time) at which the reference signal appears on the streak camera image for fixed settings. Figure 4 shows the distribution of the signal. The laser reference signal jitter covers a total range of 160 pixel or 22.8 ps, with a standard deviation of 34 pixel = 4.8 ps. This jitter does not impact directly the data analysis thanks to the use of the reference signal, but might cause the signal and region of interest on the streak camera image to jitter off the screen.

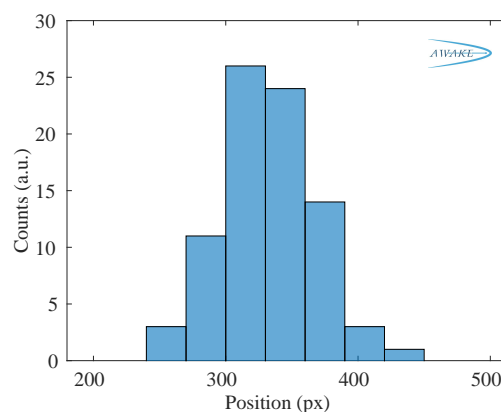


Figure 4. Histogram of the detected reference signal position in pixel on the 73 ps window. The variations are due to the triggering system jitter.

3.2. Uncertainty on the temporal position of the reference signal

The most likely contribution to the measurement error is the determination of the temporal position of the reference signal on the streak camera images. From these images, we determine the timing by fitting a Gaussian profile to a line-out obtained by summing the signal over 50 pixel (vertical direction in Fig.2(a)) that only contains the reference signal. For the test here (Fig.3), having the multiple laser pulse reflections is similar to having several reference signals. It allows for determining the uncertainty of the algorithm by measuring the spacing between two reflections. Hereby we assume that for different events, the temporal spacing between two

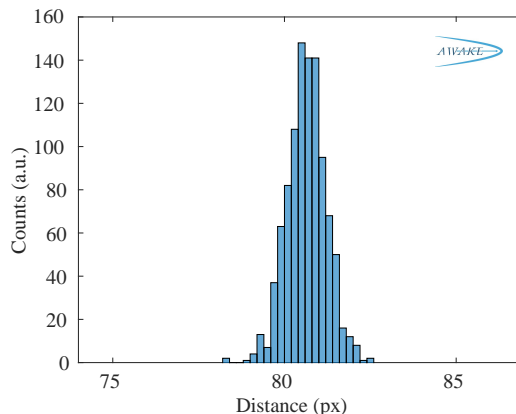


Figure 5. Detected temporal spacing between the laser light and its reflection, observed with the streak camera. The measured mean value is (80.6 ± 0.6) pixel.

reflections does not change since the propagation distances of the reflected light is unaltered. From the uncertainty of this difference, we can then estimate the uncertainty in determining the position in time of the reference signal. Figure 5 shows the distribution of the detected distance between the main signal and the first reflection, measured in pixels. The histogram has a rms width (equal to two standard deviations) of 1.1 pixel. On the 73 ps streak window, this corresponds to an uncertainty in measuring their spacing of 157 fs. The uncertainty for the determination of a single reference pulse is accordingly $157/\sqrt{2} = 111$ fs. However, this value is only relevant for events with well adjusted intensity of the reference signal as in this test measurement. When a stronger signal is recorded, the signal broadens in time inside the streak camera due to space charge effects and thus increases the uncertainty. We avoid this by increasing the strength of the filters that attenuate the intensity of the reference signal (described in chapter 2.1).

3.3. Timing jitter between laser pulse and reference signal

The pointing jitter of the ionizing laser pulse, mechanical vibrations or air drafts inside the transport line of the reference signal might cause a relative timing jitter between the ionizing laser pulse and the reference signal. To quantify this timing jitter, we determine and compare their relative positions from 200 streak camera images as shown in Fig.3. The difference in their positions shows a standard deviation of 1 pixel, equal to 143 fs on the streak camera window. Since this value is convoluted with and smaller than the uncertainty in determining the timing of both pulses of 157 fs (see chapter 3.2), we conclude that no measurable jitter is observed.

3.4. Precision of the reference signal delay setting

For the analysis of the SM in the back of the proton bunch (i.e. with delays with respect to the ionizing laser pulse larger than the streak camera window), the precision and reproducibility with which the timing reference signal delay is set gains importance. The displacement of the translation stage in the delay line is set in units of mm. The corresponding temporal offset is twice the travel distance divided by the speed of light. To test the reliability of the translation stage settings and thus of the reference signal delay, we move the stage step-wise over a total travel range of 60.0 mm (the range we use in the measurements) and measure repeatably the actual displacement x_m versus the set distance x_{set} using a caliper with an accuracy of 0.05 mm (corresponds to 0.08 % over 60 mm). The histogram in Fig.6 shows the deviation of the measured

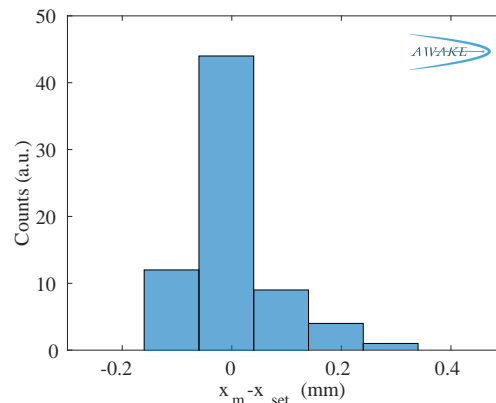


Figure 6. Histogram of the deviation between measured and set displacement of the translation stage.

from the set distance. The distribution has a rms width of 0.16 mm. Thus, the corresponding error in setting the delay of the reference signal is 529 fs (rms).

3.5. Total uncertainty

We measured the three main uncertainties that the laser timing reference signal impose on the analysis of the self-modulation of a proton bunch: the uncertainty in determining the temporal position of the reference signal on streak camera images (111 fs rms), the jitter of the relative delay between both beams (below measurement limit) and an error introduced by the uncertainty in the translation stage position when changing the delay of the reference signal with respect to the laser pulse (529 fs). To combine these uncertainties, one has to take into account that the uncertainty on the temporal position on the streak camera must be considered twice when determining the delay between the reference signal and laser pulse with the same procedure. The resulting total error (added in quadrature) is 552 fs (rms), with the largest contribution from setting the delay with the translation stage.

4. Summary

We describe the implementation of a laser timing reference signal into the AWAKE experiment by propagating a replica of the ionizing laser pulse in a free-space transfer line to the streak camera diagnostic. We show the procedure to determine and adjust the delay between this reference signal and the ionizing laser pulse. This allows for denoised, high-resolution (~ 1 ps) images of self-modulated proton bunches over time scales much longer (100s of ps) than the streak camera window (73 ps width) despite a triggering system jitter between the streak camera and the ionizing laser pulse. We measure this jitter using the reference signal to be 4.8 ps (rms). We characterize the error this reference signal implies on data analysis. The uncertainties that originate from determining the timing of the reference signal on the streak camera images, from the jitter between main and reference signal and from setting the delay with respect to the ionizing laser pulse add up to a total uncertainty of 0.6 ps (rms).

Acknowledgment

This work is sponsored by the Wolfgang Gentner Program of the German Federal Ministry of Education and Research (05E15CHA).

References

- [1] AWAKE Collaboration, *Nature* **561** 363, 2018
- [2] AWAKE Collaboration, CERN-SPSC-2018-030. SPSC-SR-240, CERN, Geneva, 2018
- [3] E. Öz, and P. Muggli, *Nucl. Instr. Meth. A* **740** 197, 2014
- [4] AWAKE Collaboration, *Phys. Rev. Lett.* **122** 054802, 2019
- [5] N. Kumar, A. Pukhov, K. Lotov, *Phys. Rev. Lett.* **104** 255003, 2010.
- [6] V. Fedosseev et.al., *IPAC2019 Proceedings* THPGW054, 2019
- [7] M. Martyanov, private communication



Contents lists available at ScienceDirect

Nuclear Inst. and Methods in Physics Research, A

journal homepage: www.elsevier.com/locate/nima

Interferometer-based high-accuracy white light measurement of neutral rubidium density and gradient at AWAKE

F. Batsch^{a,b,c,*}, M. Martyanov^b, E. Oez^b, J. Moody^b, E. Gschwendtner^a, A. Caldwell^b, P. Muggli^{a,b}^a CERN, Geneva, Switzerland^b Max Planck Institute for Physics, Munich, Germany^c Technical University Munich, Munich, Germany

ARTICLE INFO

Keywords:

Proton driven plasma wakefield
AWAKE
Accurate density and gradient measurement
Rubidium vapor source
Mach-Zehnder interferometer
Fourier-based signal conditioning

ABSTRACT

The AWAKE experiment requires an automated online rubidium (Rb) plasma density and gradient diagnostic for densities between 1 and $10 \cdot 10^{14} \text{ cm}^{-3}$. A linear density gradient along the plasma source at the percent level may be useful to improve the electron acceleration process. Because of full laser ionization of Rb vapor to Rb^+ within a radius of 1 mm, the plasma density equals the vapor density. We measure the Rb vapor densities at both ends of the source, with high precision using, white light interferometry. At either source end, broadband laser light passes a remotely controlled Mach-Zehnder interferometer built out of single mode fibers. The resulting interference signal, influenced by dispersion in the vicinity of the Rb D1 and D2 transitions, is dispersed in wavelength by a spectrograph. Fully automated Fourier-based signal conditioning and a fit algorithm yield the density with an uncertainty between the measurements at both ends of 0.11 to 0.46% over the entire density range. These densities used to operate the plasma source are displayed live in the control room.

1. Introduction

The AWAKE project at CERN is a proof-of-concept experiment that uses a proton bunch for particle beam driven plasma wakefield acceleration of electrons [1–3]. The goal is to reach energies on the scale of several GeV using coherently driven plasma waves with acceleration gradients $>1 \text{ GeV/m}$ [4]. The entire process, i.e. modulating the 12 cm long (σ_z), 400 GeV proton bunch [3] by seeded self-modulation (SSM) [4,5] into micro bunches, wakefield creation and electron acceleration, happens in a 10 m long, 4 cm diameter rubidium (Rb) vapor source [6–8], depicted in Fig. 1. At each end, a flask with separately controlled electrical heaters is filled with Rb, providing Rb vapor densities up to $1 \cdot 10^{15} \text{ cm}^{-3}$. The baseline density is $n_{\text{Rb}} = 7 \cdot 10^{14} \text{ cm}^{-3}$ [7]. A fluid heat exchanger with temperature-stabilization surrounds the source and ensures a high temperature and vapor density uniformity ($<0.2\%$, [6]). An intense laser pulse ionizes the Rb vapor (first e^- of each Rb atom), forming a 2 mm diameter plasma along the source with equal density and uniformity. By setting different temperatures in the downstream and upstream flasks, a linear vapor/plasma density gradient along the source can be set. Beside the density uniformity, the absolute vapor density and a possible gradient along the source influence the acceleration process [9]. The absolute

density determines the proton bunch modulation frequency. Density gradients on the order of +1 to +10% (i.e. the density increases along the 10 m pipe in direction of the beam) can affect the e^- acceleration in a positive way [9].

We determine the plasma density and gradient by measuring the Rb vapor density through diagnostic windows located at each of the source ends (see Fig. 1) using a Mach-Zehnder interferometer and white light interferometry [10,11]. To ensure a sufficiently high accuracy in gradient determination, we aim for an uncertainty in measuring the densities at both source ends to better than 1%. To operate the vapor source remotely, from the control room, while ensuring the required densities and gradients, the diagnostic must allow for a fully automated and remote-controlled operation and provide online density values. The analysis to determine the densities is based on Fourier signal conditioning and on a fitting algorithm analyzing zero-crossings. The diagnostic and the signal analysis are described hereafter.

2. The diagnostic

The technique exploits the fact that alkali metals, such as Rb, have atomic transitions from the ground state to the first excited state in the

* Corresponding author at: CERN, Geneva, Switzerland.
E-mail address: fabian.batsch@cern.ch (F. Batsch).

<https://doi.org/10.1016/j.nima.2018.02.067>

Received 30 November 2017; Received in revised form 8 February 2018; Accepted 14 February 2018

Available online 24 February 2018

0168-9002/© 2018 The Authors. Published by Elsevier B.V. This is an open access article under the CC BY-NC-ND license (<http://creativecommons.org/licenses/by-nc-nd/4.0/>).

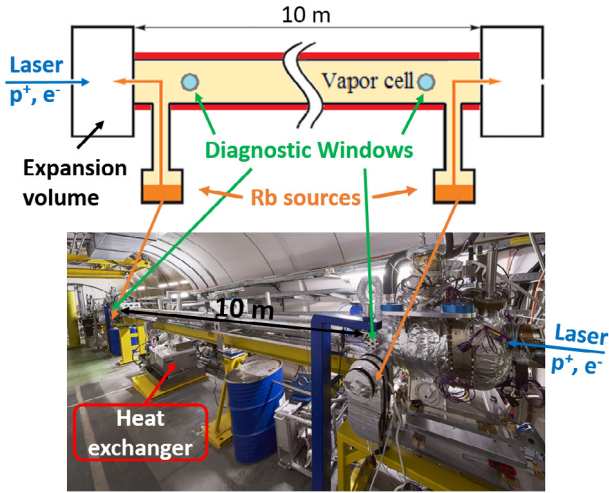


Fig. 1. Top: Schematic of the Rb vapor source showing the 10 m long pipe surrounded by the heat exchanger (red), two Rb reservoirs (orange) providing the Rb vapor and 2 diagnostic viewports near the source ends. Bottom: Photo of the AWAKE vapor source. The blue posts at each end are supports for the interferometer optics. (For interpretation of the references to color in this figure legend, the reader is referred to the web version of this article.)

optical wavelength range. Rubidium has two such lines, at 780.03 nm (D2) and 794.76 nm (D1) [12,13]. In the vicinity of these transitions, its optical properties change with wavelength (dispersion) and Rb density. This density-dependent change in the index of refraction for each wavelength results in an interference pattern that changes with density. We measure it by sending coherent white light in a fiber-based Mach-Zehnder interferometer and through the Rb vapor.

This setup, depicted in Fig. 2, includes a white light laser (NKT SuperK COMPACT, 240–2000 nm spectrum) as light source, located in a radiation-safe area. Wavelengths between 700–900 nm are then coupled into two single-mode optical fibers. These ≈ 120 m long fibers lead to each vapor source end. A fiber splitter forms the two arms of the Mach-Zehnder interferometer. One is called Rb arm in the following and guides the light to the diagnostic window. At the fiber end, a fiber collimator forms a parallel light beam that passes the Rb vapor transversely. A second fiber collimator re-couples the light into the fiber. The second arm, called reference arm, is a replica of the Rb arm and is located below the vapor source. Its free-space section (length equal to that of the Rb arm) contains a translation stage to adjust the path length difference between the two arms. Another fiber splitter recombines the light from both arms. The interfered signals from both interferometers propagate over a second pair of ≈ 120 m fibers (equal length), back to the radiation-safe area. There, two Ocean Optics HR4000 fiber spectrographs disperse the signals in wavelength with a resolution of 0.063 nm [11]. Fig. 3 shows the resulting interference patterns for the cases of no Rb and Rb vapor with a density of $1.365 \cdot 10^{14} \text{ cm}^{-3}$ in the source.

3. Density calculation

In interferograms such as those of Fig. 3, the interference pattern is given by

$$I_{\text{tot}}(\lambda) = I_1(\lambda) + I_2(\lambda) + 2\sqrt{I_1(\lambda)I_2(\lambda)} \cdot \cos(\Delta\Phi(\lambda)), \quad (1)$$

where $I_{1,2}(\lambda)$ are the light intensities in each interferometer arm at wavelength λ , $I_1(\lambda) + I_2(\lambda)$ is the oscillation offset (see red line in Fig. 3) and $\Delta\Phi(\lambda)$ the phase difference between the arms. Changing from wavelength λ to frequency ω , this phase difference is described by

$$\Delta\Phi(\omega) = k\eta(\omega) \cdot (l_{F1} - l_{F2}) + k \cdot (l_1 - l_2) + (\Phi_{01}(\omega) - \Phi_{02}(\omega))kL(\eta_{\text{Rb}}(\omega) - 1). \quad (2)$$

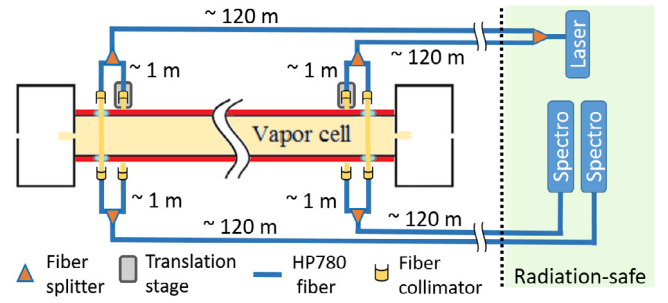


Fig. 2. Top view schematic of the fiber-based Mach-Zehnder interferometer assembly. From the light source, located in a radiation-safe area, 120 m fibers transport the light to the source ends, where the interferometers are formed by fiber splitters. The light traverses the source through the diagnostic windows, each reference arm is equipped with a translation stage to adjust its length. Equal length fibers transport the interfered light signal back to two fiber spectrographs.

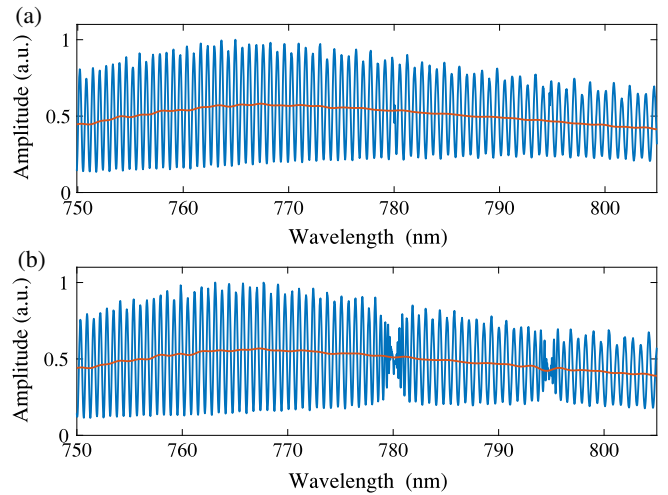


Fig. 3. (a) Interference pattern without Rb in the Rb vapor source. The oscillation shows nearly constant period. (b) Interference pattern with $n_{\text{Rb}} = 1.365 \cdot 10^{14} \text{ cm}^{-3}$ in the source. Around the transition lines (D1 at 795 nm and D2 at 780 nm), the period changes in a density-dependent way. The red lines represent the offset of the oscillation (see later). (For interpretation of the references to color in this figure legend, the reader is referred to the web version of this article.)

Here, $k = \omega/c$ is the wavenumber in vacuum, $\eta(\omega)$ the fiber's index of refraction, $l_{F1,2}$ the fiber lengths of each arm, $l_{1,2}$ the path lengths in free space outside the source or fibers, $\Phi_{01,2}$ the phase of the light in each arm, L the length of the Rb vapor column through which the light propagates and η_{Rb} the index of refraction of the Rb vapor. Taylor-expanding the fiber's index of refraction around center frequency ω_0 , one can rewrite the phase difference as

$$\Delta\Phi(\omega) = \left[\frac{1}{2}\alpha\Delta\omega^2 + \beta\Delta\omega + \Delta l + \Delta\Phi_0 \right] + \left[\frac{\omega}{c} L(\eta_{\text{Rb}}(\omega) - 1) \right] := [A] + [B]. \quad (3)$$

Here, the path length difference $\Delta l = l_1 - l_2$, $\Delta\Phi_0 = \Phi_{01} - \Phi_{02}$ and α, β include all frequency-independent terms. The first bracket contains the phase terms that are density-independent and we call it [A]. The second term ([B]) contains the terms that depend on the Rb vapor density n_{Rb} through $\eta_{\text{Rb}} = \sqrt{1 + \chi_e}$ and

$$\chi_e = \frac{e^2 n_{\text{Rb}}}{\epsilon_0 m_e} \sum_{i=1,2} \frac{f_i}{(\omega_i^2 - \omega^2)^2 - i\gamma_i^2 \omega^2}. \quad (4)$$

Here, χ_e is the electric susceptibility, i the index of the transitions (D1 and D2), $\omega_i = (2\pi c)/\lambda_i$ the transition frequencies, e the electron charge, ϵ_0 the vacuum permittivity, m_e the electron mass, f_i the transitions oscillator strength and γ_i its natural lifetime [11,13,14]. Doppler broadening is taken into account by correcting χ_e accordingly using a Rb temperature of 200 °C for all densities. However, we exclude a frequency range of width 0.15 THz around each transition line from the analysis because this range includes, in addition to the absorption lines, the not resolvable short-period oscillations (see Fig. 3(b)).

As described by these formulas, the effect of the Rb vapor on the phase difference is proportional to the density-length product $n_{\text{Rb}}L$ (which appears after a binomial expansion of $\sqrt{1 + \chi_e}$ to first order). However, we treat L as constant. The heat expansion factor of steel is negligible ($\sim 10^{-5}$ m/m K) and equal for both vapor column lengths, meaning that it does not affect the gradient measurement. To ensure low systematic error in density measurement, L was measured with 0.02% accuracy using a micrometer.

Before calculating the density from the phase shift induced by the Rb vapor ([B] in Eq. (3)) using a fitting algorithm, the spectra must be normalized and the offset ($I_1(\lambda) + I_2(\lambda)$) must be removed for the fitting algorithm (since the vapor density length product is contained only in the argument of the cosine in Eq. (1)). In addition, we extract the signal's envelope function which is required for the fit. For these steps, we use Fourier-based signal conditioning. Fig. 4 shows the absolute value of the fast Fourier transform (FFT) of the spectra shown in Fig. 3. The small oscillation times τ (< 2 ps) represent the oscillation offset and high-frequency noise. Setting this part of the Fourier spectrum to zero and applying an inverse Fourier transform of the remaining spectrum removes the offset (and noise), i.e. centers the oscillation around the horizontal axis. Further, the FFT spectrum shows a prominent peak (here at $\tau_{\text{peak}} \approx 3$ ps). In case of no Rb vapor in the source (blue line), it represents the oscillation with constant period, determined by Δl (for Fig. 3, $\Delta l \approx 9$ mm). Shifting this peak to zero and taking the absolute value of its inverse Fourier transform gives the oscillation's envelope function. Determining the phase of this inverse Fourier transform with respect to ω_0 (set to 390 THz $\hat{=}$ 770 nm) gives the phase difference $\Delta\Phi(\omega)$. Note that large τ values (i.e. $\tau > \tau_{\text{peak}} + 10$ ps) are zeroed before these steps as well, in order to remove the non-physical τ values which could possibly lead to an incorrect centering of the oscillation. We call this entire process signal conditioning. With Rb, the curve (red dashed line) looks similar, except around the prominent peak. The changing period around the Rb transition wavelength in the interferogram leads to a broader peak and a different $\Delta\Phi(\omega)$.

After the conditioning, one determines the density using a spectrum where $n_{\text{Rb}} = 0$ (i.e. [B] = 0) to obtain [A] and calculates $\Delta\Phi(\omega)$ for both cases (called $\Delta\Phi_{\text{NoRb}}$ and $\Delta\Phi_{\text{Rb}}$; note that all other parameter such as Δl must be equal). Measured examples for these phase terms are depicted in Fig. 5.

The comparison of $\Delta\Phi_{\text{Rb}} - \Delta\Phi_{\text{NoRb}}$ with the expression for [B] gives a first estimate for the density that is used as a starting value for the final fit. This final fit in the next step minimizes the distance between the zero-crossings of the conditioned signal and the curve given by the formula one obtains by multiplying $\cos(\Delta\Phi)$ with the envelope function calculated in the conditioning process. The cosine term is obtained by substituting Eq. (4) and the Rb density start value in Eq. (3). The terms α , β and $(\Delta l + \Delta\Phi_0)$ are kept as fitting parameters since the lengths, i.e. also the initial phases change slightly due to vibrations. To obtain their starting values, one fits $\Delta\Phi_{\text{NoRb}}$ with a second-order polynomial. Fig. 6(a) shows the conditioned signal (in blue), the zero-positions (red circles) and the fit (red line) for the case of Rb vapor in the source with $n_{\text{Rb}} = 1.365 \cdot 10^{14} \text{ cm}^{-3}$. The plotted frequency range covers only one side of the D2 line ($\omega_2/2\pi = 384$ THz) for a better visibility of the oscillations. The fit matches the data in shape (envelope) and zero-crossing position. The difference between the zero-crossings of the conditioned signal and the fit is a measure for the goodness of the fit. It is plotted in Fig. 6(b) for a wider frequency range covering both transition

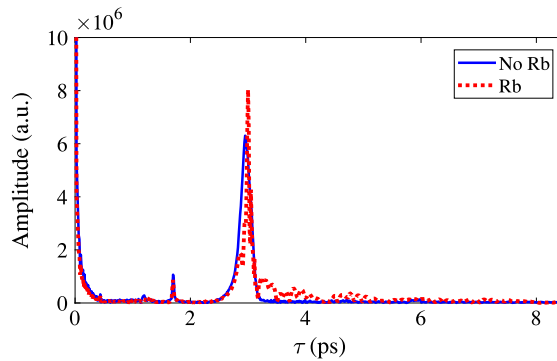


Fig. 4. Power spectra (i.e. absolute value of the Fourier transform) of interference spectra in case of no Rb vapor in the source (blue line) and in case of Rb vapor present ($n_{\text{Rb}} = 1.365 \cdot 10^{14} \text{ cm}^{-3}$) (red). (For interpretation of the references to color in this figure legend, the reader is referred to the web version of this article.)

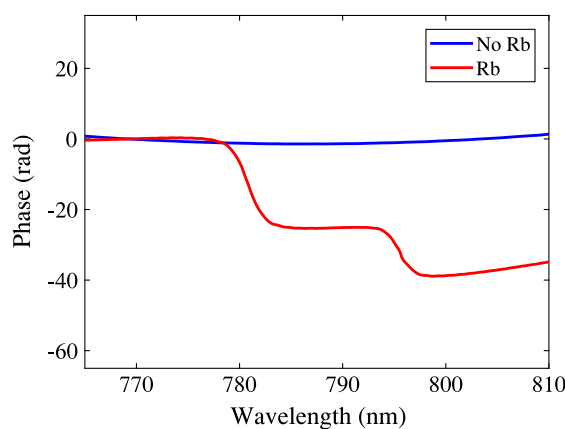


Fig. 5. Measured phase difference in case of no Rb vapor (blue line) and in case of Rb vapor present ($n_{\text{Rb}} = 2.092 \cdot 10^{14} \text{ cm}^{-3}$) (red). The difference between both lines corresponds to $\Delta\Phi$. (For interpretation of the references to color in this figure legend, the reader is referred to the web version of this article.)

frequencies ($\omega_1/2\pi = 377$ THz). The differences are within ± 4 GHz, which is below the spectrograph resolution, meaning that the fit matches the data.

During the experiment, this algorithm calculates in a fully automated way (every 10 s) the densities (duration of the calculation: ≈ 1 s) for each source end. Using these density values, one calculates the gradient over 10 m $\Delta n_{\text{Rb}} = (n_{\text{Rb},2} - n_{\text{Rb},1})/n_{\text{Rb},1}$, where $n_{\text{Rb},1}$ is the upstream value and $n_{\text{Rb},2}$ the downstream value. These density and gradient values are then displayed live in the control room.

4. Diagnostic operation and accuracy

The diagnostic has three main tasks for the Rb vapor source operation. First, it is used to characterize the correlation between the temperature set in the Rb reservoirs and the Rb vapor density in the source. Due to the fact that it is an open system (see Fig. 1), a calculation of the density from temperature/a vapor pressure curve [15] and the determination of the systematic uncertainty of one density measurement are not possible [8]. Temperatures between 146.0 °C and 215.0 °C in the Rb flasks lead to densities between $n_{\text{Rb}} = 3.09 \cdot 10^{13}$ and $n_{\text{Rb}} = 10.70 \cdot 10^{14} \text{ cm}^{-3}$. The systematic uncertainty of one diagnostic was checked previously [11], where the same setup and a comparable analysis algorithm was used. A closed metallic cube with two viewports that was immersed in an oil bath with temperature stabilization (0.1 °C

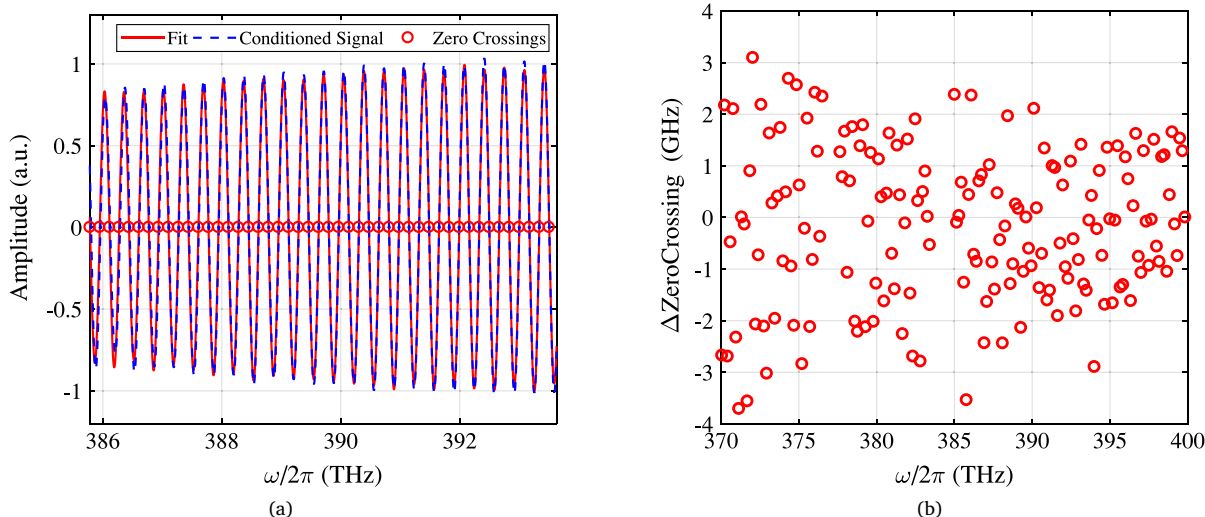


Fig. 6. (a) Plot of the conditioned signal (blue), the zero crossings (red circles) and the fit (red line) vs. frequency ($\omega/2\pi$) for the same spectrum as shown in Fig. 3(b) in the vicinity of the D2 transition. (b) Plot of the difference between the zero-crossings of the signal and the fit vs. frequency (range now covering both transitions). (For interpretation of the references to color in this figure legend, the reader is referred to the web version of this article.)

uncertainty) and calibrated temperature probes ($\pm 0.05^\circ\text{C}$ uncertainty) served as a test Rb vapor source providing known density values. For the densities used during the experiments (1 to $10 \cdot 10^{14} \text{ cm}^{-3}$), the systematic uncertainty is 0.3% to 2%.

The two remaining tasks are online monitoring and controlling the experiment key parameters: the Rb vapor density and gradient. Here the important observable is the statistical uncertainty in density measurement and the systematic uncertainty between both diagnostics for equal densities. We determine it from data taken within a short amount of time (e.g. 5 min), knowing that the temperature in the source changes on much longer timescales (\sim hours). This proves as well the ability of the analysis procedure to predict n_{Rb} against variations in the other fitting parameter on short time scales (e.g. in Δl due to vibrations).

Fig. 7 shows the Rb densities vs time at the AWAKE baseline density when the valves on top of the Rb reservoirs open and the 10 m pipe fills with Rb vapor. The density stabilized after ≈ 6 min. After stabilization, one measures at the upstream end $n_{\text{Rb},1} = (7.719 \pm 0.006) \cdot 10^{14} \text{ cm}^{-3}$ ($\pm 0.08\%$ standard deviation) and downstream $n_{\text{Rb},2} = (7.715 \pm 0.007) \cdot 10^{14} \text{ cm}^{-3}$ ($\pm 0.09\%$ standard deviation), in both cases averaged over measurements taken over 5 min. The gradient over 10 m along the source is $(+0.05 \pm 0.12)\%$. For the entire density range, the density values at constant temperature show statistical uncertainties between $\pm 0.05\%$ at high densities and $\pm 0.30\%$ at low densities. Combining this statistical uncertainties with the systematic error of $\pm 0.10\%$ to $\pm 0.35\%$ (checked in [11]) found in measuring the same Rb vapor density at different locations with two independent diagnostics leads to a total uncertainty between both measurements of $\pm 0.11\%$ to $\pm 0.46\%$ (added in quadrature).

To study the effect of a density gradient on the SSM, we change the temperature of the downstream reservoir, but keep the density constant upstream. These temperature adjustments require live monitoring of the densities. Fig. 8(a) shows an example of a such density scan, where the change in density was controlled and adjusted based on the density values provided online by this diagnostic. Figure (b) shows the resulting change in the gradient. It was increased from 0% to $\approx +20\%$ over 10 m and then decreased to 6.70% over 10 m (stable).

5. Conclusion

In conclusion, a method to measure Rb vapor densities in a fully automated way allowing for an online analysis is described. We use white

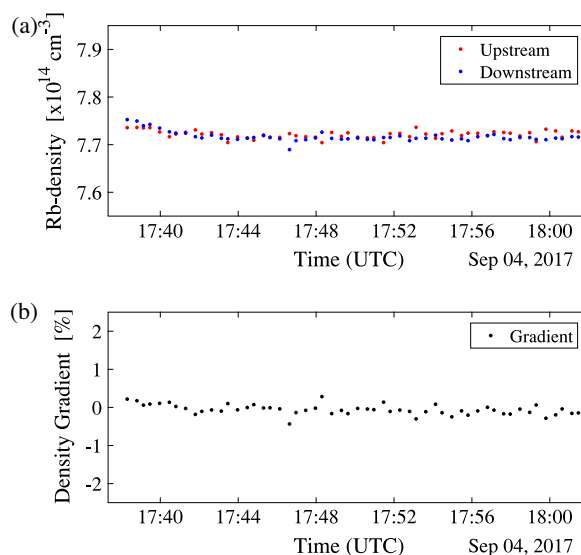


Fig. 7. Plot of (a) Rb vapor density vs. time (UTC) and (b) resulting gradient vs. time (UTC) for both source ends (upstream in red, downstream in blue). (For interpretation of the references to color in this figure legend, the reader is referred to the web version of this article.)

light interferometry where two independent, fiber-based Mach-Zehnder interferometers measure the Rb vapor density at each end of the vapor source. Fourier-based signal conditioning and a fit algorithm retrieve the density values with an uncertainty between both measurements of $\pm 0.11\%$ to $\pm 0.46\%$. This precision fulfills the requirements to determine the density gradient over 10 m within 1%. This is the main diagnostic to monitor and control the plasma density and is crucial for an effective wakefield formation and electron acceleration.

Acknowledgment

This work is sponsored by the Wolfgang Gentner Program of the German Federal Ministry of Education and Research (05E15CHA).

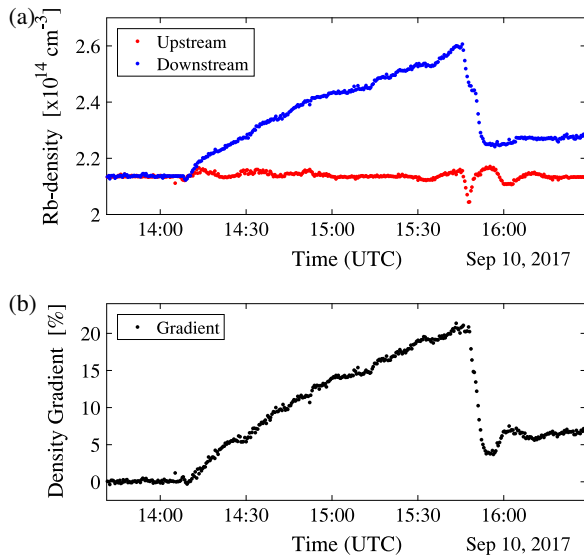


Fig. 8. (a) Plot of Rb vapor density vs. time (UTC) during a gradient scan. The downstream density (blue) is increased and then lowered again while the density upstream (red) is kept constant. (b) The resulting density gradient over 10 m along the vapor source vs. time (UTC). Positive gradients indicate that the density is higher downstream. (For interpretation of the references to color in this figure legend, the reader is referred to the web version of this article.)

References

- [1] (AWAKE-Collaboration), R. Assmann, et al., Proton-driven plasma wakefield acceleration: A path to the future of high-energy particle physics, *Plasma Phys. Control. Fusion* 56 (8) (2014) 084013. <http://stacks.iop.org/0741-3335/56/i=8/a=084013>.
- [2] E. Gschwendtner, et al., AWAKE, the advanced proton driven plasma wakefield acceleration experiment at CERN, *Nucl. Instrum. Methods Phys. Res. A* 829 (Suppl. C) (2016) 76–82. <http://dx.doi.org/10.1016/j.nima.2016.02.026>. 2nd European Advanced Accelerator Concepts Workshop - EAAC 2015. <http://www.sciencedirect.com/science/article/pii/S0168900216001881>.
- [3] A. Caldwell, et al., Path to AWAKE: Evolution of the concept, *Nucl. Instrum. Methods Phys. Res. A* 829 (Suppl. C) (2016) 3–16. <http://dx.doi.org/10.1016/j.nima.2015.12.050>. 2nd European Advanced Accelerator Concepts Workshop - EAAC 2015. <http://www.sciencedirect.com/science/article/pii/S0168900215016307>.
- [4] P. Muggli, et al., AWAKE readiness for the study of the seeded self-modulation of a 400 GeV proton bunch, *Plasma Phys. Control. Fusion* (2017). <http://iopscience.iop.org/article/10.1088/1361-6587/aa941c>.
- [5] N. Kumar, A. Pukhov, K. Lotov, Self-modulation instability of a long proton bunch in plasmas, *Phys. Rev. Lett.* 104 (2010) 255003. <http://dx.doi.org/10.1103/PhysRevLett.104.255003>.
- [6] E. Öz, F. Batsch, P. Muggli, A novel laser ionized rb plasma source for plasma wakefield accelerators, in: TUPME073, IPAC 2014 Proceedings.
- [7] A. Caldwell, (AWAKE-Collaboration), AWAKE Status Report, CERN-SPSC-2016-033. SPSC-SR-194, CERN, Geneva, 2016. <https://cds.cern.ch/record/2221183>.
- [8] G. Plyushchev, R. Kersevan, A. Petrenko, P. Muggli, A rubidium vapor source for a plasma source for AWAKE, 2017. [arXiv:1708.08280](https://arxiv.org/pdf/1708.08280). <https://arxiv.org/pdf/1708.08280.pdf>.
- [9] A. Petrenko, K. Lotov, A. Sosedkin, Numerical studies of electron acceleration behind self-modulating proton beam in plasma with a density gradient, *Nucl. Instrum. Methods Phys. Res.* 829 (2015) 63–66. [arXiv:1511.04360](https://cds.cern.ch/record/2102337). <https://cds.cern.ch/record/2102337>.
- [10] W.T. Hill, Column-density meter: A high precision technique for measuring line-of-sight vapor densities, *Appl. Opt.* 25 (23) (1986) 4476–4482. <http://dx.doi.org/10.1364/AO.25.004476>. <http://ao.osa.org/abstract.cfm?URI=ao-25-23-4476>.
- [11] F. Batsch, Interferometer-Based White Light Measurement of Neutral Rubidium Density and Gradient for the AWAKE Experiment at CERN (Master's thesis), Technical University Munich, 2016. https://www.mpp.mpg.de/~muggli/PDFs/MPPTtheses/MastersThesis_Batsch.pdf.
- [12] J.E. Sansonetti, Wavelengths, transition probabilities, and energy levels for the spectra of rubidium (Rb I through Rb XXXVII), *J. Phys. Chem. Ref. Data* 35 (1) (2006) 301–421. <http://dx.doi.org/10.1063/1.2035727>. <http://scitation.aip.org/content/aip/journal/jpcrd/35/1/10.1063/1.2035727>.
- [13] D.A. Steck, Rubidium 87 D Line Data, 2008. <http://steck.us/alkalidata/rubidium87numbers.pdf>.
- [14] A. Kramida, Y. Ralchenko, J. Reader, NIST ASD Team, NIST Atomic Spectra Database (version 5.4), 2016. <http://physics.nist.gov/asd>.
- [15] C.B. Alcock, V.P. Itkin, M.K. Horrigan, Vapour pressure equations for the metallic elements: 298–2500 K, *Can. Metall. Q.* 23 (3) (1984) 309–313. <http://dx.doi.org/10.1179/cm.1984.23.3.309>.

Glossary

α_I	degree of ionization of a plasma	in %
AC	alternating current	
ACC	AWAKE Control Center	
AWAKE	Advanced Wakefield Experiment	
BPM	Beam Position Monitor	
BTv	Beam Television (CERN-intern term)	
c	speed of light in vacuum	$c = 2.9979 \cdot 10^8$ m/s
CERN	Conseil européen pour la recherche nucléaire	
CLIC	Compact Linear Collider	
CNGS	CERN Neutrinos to Gran Sasso	
CPA	chirped pulse amplification	
CTR	coherent transition radiation	
$\Delta\Phi$	phase variation of the periodic bunch train	in $\%/2\pi$
$\Delta\phi$	phase difference between interferometer arms	
Δv_{ph}	difference in phase velocity	
Δt_{LRS}	temporal offset between LRS and RIF	
DFT	discrete Fourier transform	
ϵ_0	vacuum permittivity	$\epsilon_0 = 8.8542 \cdot 10^{-12}$ As/Vm
η	index of refraction	
η_{Rb}	index of refraction of Rb vapor	
e	elementary charge	$e = 1.6022 \cdot 10^{-19}$ C
E	energy	
E_{WB}	non-relativistic cold wave-braking field	
$\Phi_{01,02}$	phase of light in interferometer	
f	frequency	
$f_{1,2}$	oscillator strength of an optical transition	
f_{CTR}	modulation frequency obtained the CTR diagnostic	
$f_{entrance}$	local plasma frequency at vapor source entrance	

f_{exit}	local plasma frequency at vapor source exit	
f_{CTR}	intermediate frequency measured by the CTR diagnostic	
f_{mod}	frequency of the proton bunch modulation	
f_{pe}	plasma electron frequency	
f_{ref}	reference frequency for the CTR diagnostic	
FCC	Future Circular Collider	
FFT	fast Fourier transform	
Γ	Wakefield growth rate	
γ	relativistic Lorentz factor	
$\gamma_{1,2}$	natural lifetime of an optical transition	
g	rubidium vapor density gradient along vapor source	in %/m
I_0	zeroth-order modified Bessel function of the first kind	
I_1	first-order modified Bessel function of the first kind	
ILC	International Linear Collider	
IR	infrared	
IS	imaging station	
k	wavenumber	
K_0	zeroth-order modified Bessel function of the second kind	
K_1	first-order modified Bessel function of the second kind	
k_B	Boltzmann constant	$k_B = 1.3806 \cdot 10^{-23} \text{ J/K}$
k_{pe}	plasma electron wavenumber	
λ	wavelength	
λ_{pe}	wavelength of plasma electron oscillation	
L	length of the Rb vapor column	
$l_{F1,1,2}$	length of interferometer components	
LEP	Large Electron-Positron Collider	
LRS	laser reference signal	
LWFA	laser wakefield acceleration	
m	mass	
m_0	rest mass	
m_e	electron rest mass	$m_e = 9.1094 \cdot 10^{-31} \text{ kg}$
m_p	proton rest mass	$m_p = 1.6726 \cdot 10^{-27} \text{ kg}$
MCP	micro-channel plate	

N_b	bunch population	
n_b	bunch charge density	in m^{-3}
n_{b0}	peak bunch charge density	in m^{-3}
$n_{b\parallel}(\zeta)$	normalized longitudinal bunch charge density	
$n_{b\perp}(r)$	normalized radial bunch charge density	
$\tilde{n}_b(t)$	longitudinal, on-axis bunch charge density as a function of time	in m^{-3}
n_{e0}	plasma electron density	in cm^{-3}
n_{i0}	plasma ion density	in cm^{-3}
N_m	integer number of modulation periods	
n_{n0}	neutral gas density	in cm^{-3}
n_{Rb}	rubidium vapor density	in cm^{-3}
$n_{Rb,d}$	downstream rubidium vapor density	in cm^{-3}
$n_{Rb,u}$	upstream rubidium vapor density	in cm^{-3}
ω_{pe}	angular plasma electron frequency	
OTR	optical transition radiation	
PS	Proton Synchrotron	
PWFA	plasma wakefield acceleration	
q	electric charge	
r	radius or radial coordinate	
Rb	rubidium	
RF	radio frequency	
RIF	relativistic ionization front	
σ_0	transverse focused beam size of the proton bunch	
σ_r	bunch length in radial direction	
σ_t	bunch duration in longitudinal direction	
σ_z	bunch length in longitudinal direction	
$S(t)$	time-dependent signal	
$\hat{S}(f)$	Fourier transform of a time-dependent signal	
s	travel distance of a translation stage	
s_m	measured travel distance of a translation stage	
s_{set}	set travel distance of a translation stage	
SC	streak camera	
SLAC	Stanford Linear Accelerator Center	
SM	self-modulation	

SMI	self-modulation instability	
SPS	Super Proton Synchrotron	
SSM	seeded self-modulation	
τ_{mod}	modulation period $1/f_{mod}$	
τ_s	signal duration	
T	temperature	
t	time	
TNSA	target normal sheath acceleration	
UV	ultraviolet	
v_b	velocity of the drive bunch	
v_{gr}	group velocity	
v_{ph}	phase velocity	
$W_{\parallel}(t, r)$	longitudinal wakefield	
$W_{\perp}(t, r)$	transverse wakefield	
$W_{\perp, RIF}$	initial transverse wakefield amplitude at the position of the RIF	
x	radial position on streak camera images	
ζ	spatial coordinate in co-moving bunch frame	$\zeta = ct - z$
z	longitudinal coordinate in laboratory frame	

List of Figures

1	Schematic of plasma-based wakefield acceleration	6
2	Schematic of proton-driven plasma wakefield acceleration	7
3	Schematic of the self-modulation instability	11
4	Seeding of the self-modulation	12
5	Comparison of time-resolved images of the proton bunch without plasma and with creation of the plasma close to the bunch center . .	13
6	Plot of transverse and longitudinal wakefields	21
7	Unpadded and zero-padded DFT of the bunch modulation profile of sine function of limited duration.	25
8	Overview over the CERN acceleration complex.	29
9	Schematic of the AWAKE experiment.	29
10	Overview over the AWAKE experimental area.	30
11	Photo of the proton transfer line.	32
12	Schematic of the laser system.	33
13	Photo of the laser room.	34
14	Schematic and photo of the Rb vapor source.	36
15	Photo of the beam diagnostic section.	38
16	Schematic of the interferometer for the Rb vapor density measurement. .	42
17	Photos of the optical components of the Rb vapor density measurement. .	43
18	Exemplary interferograms of the Rb vapor density measurement . .	44
19	Plasma parameters shown by the fixed display in the control room of AWAKE	46
20	Power spectra of interferograms with and without Rb	48
21	Measured phase difference in case of no Rb vapor and of Rb vapor present	49
22	Conditioned interferogram together with the density-determining fit, and difference between the zero-crossings of the signal and the fit. .	50
23	Schematics and photos of the setup for the LRS	53
24	Streak camera image with the LRS and the ionizing laser pulse in low-energy mode shown simultaneously.	55
25	Planned layout for AWAKE Run 2c	56

26	SC image and histogram of typical background noise during proton operation.	60
27	SC image and histogram of a SC background image without any beams	60
28	Histogram of the intensity distribution of a typical SC image. . . .	62
29	Linearization of the SC time axis	63
30	Example SC image with micro-bunches and the LRS	64
31	Single and stitched SC image to illustrate the process of SC image stitching	65
32	Spatial profile of the charge density in Fig. 30(a).	67
33	Duplicate of Fig. 30 with supplementary information about the phase determination added.	68
34	Original and zero-padded DFT of the bunch modulation profile of Fig. 30(a).	69
35	Phase variation versus frequency chosen for the phase analysis . . .	71
36	Streak camera image with the LRS and the ionizing laser in low-energy mode, including its reflections, visible.	74
37	Histogram of the position of the LRS in pixel on the 73 ps SC window to determine the triggering system jitter.	75
38	Histogram of the detected temporal spacing between the ionizing laser pulse and its first reflection.	76
39	Measured positions of the ionizing laser pulse and the LRS to determine the timing jitter between both.	77
40	Histogram of the deviation between measured and set displacement of the translation stage.	78
41	73 ps SC image of the modulated bunch without seeding	83
42	73 ps composite image of ten SMI events	83
43	211 ps composite image of ten SMI events	85
44	Comparison of SC images showing different start point of the SM when not seeded	86
45	Composite image of ten SSM events	88
46	Composite image of five SSM events showing the begin of the modulation	88
47	Mean DFT frequency as a function of t_{RIF}	90
48	Phase variation and initial linear transverse wakefield amplitude as a function of the t_{RIF}	91
49	Stitched image of modulated proton bunch and phase variation measured along the bunch for constant t_{RIF}	93
50	Relative phase evolution and corresponding modulation frequency along a modulated bunch for SSM	95
51	Power spectrum of the stitched SC image in Fig. 49(a)	97

52	Stitched SC images and corresponding time profile for various linear plasma gradients	101
53	Comparison of a stitched SC image in Fig. 52(g) to a 2D simulation from [58]	105
54	DFT frequency as a function of g for two widths of the analysis window and compared to the CTR measurements of [60]	107
55	DFT frequency as a function of transverse position for 200- μm -wide slices as analysis window	108
56	Mean phase variation $\Delta\Phi$ along the bunch versus plasma density gradient	110
57	Relative modulation phase and corresponding modulation frequency along modulated bunch for SSM with gradients	112
A1	Stitched image at a higher density of $n_{e0} = 5.35 \times 10^{14} \text{ cm}^{-3}$	124
A2	Stitched image at a higher density of $n_{e0} = 7.68 \times 10^{14} \text{ cm}^{-3}$	125
A3	Rb vapor density vs. time (UTC) for a constant density of $1.96 \times 10^{14} \text{ cm}^{-3}$	127
A4	Rb vapor density vs. time (UTC) for a constant density of $7.68 \times 10^{14} \text{ cm}^{-3}$	128
A5	Rb vapor density vs. time (UTC) during a gradient scan	130
A6	Rb vapor densities and gradient for the data presented in Chapter 7	131
A7	Measured Rb vapor density and expected density versus Rb reservoir temperature	132

Bibliography

- [1] H. Wiedemann. *Particle Accelerator Physics*, volume 151. Springer Nature, 2015.
- [2] O. S. Brüning et al. *LHC Design Report*. CERN Yellow Reports: Monographs. CERN, 2004.
- [3] R. Van de Graaff. A 1,5000,000 Volt Electrostatic Generator. *Phys. Rev.*, 38:1919, 1931.
- [4] J. Cockcroft and E. Walton. Disintegration of Lithium by Swift Protons. *Nature*, 129:649, 1932.
- [5] E. O. Lawrence and M. S. Livingston. The Production of High Speed Light Ions Without the Use of High Voltages. *Phys. Rev.*, 40:19–35, 1932.
- [6] CERN Public Information Office. *Synchro-cyclotron of 600 MeV*. Technical notebook. CERN, Geneva, 1971.
- [7] G. Aad et al. Observation of a new particle in the search for the Standard Model Higgs boson with the ATLAS detector at the LHC. *Physics Letters B*, 716(1):1–29, 2012.
- [8] G. Arduini et al. Electron-positron collisions at 209 GeV in LEP. In *Proceedings of the 2001 Particle Accelerator Conference*, volume 1, pages 356 – 358 vol.1, 2001.
- [9] C. Sutton. *SLAC*. Encyclopedia Britannica, 2008. Accessed: 2021-06-01.
- [10] P. Lebrun et al. The CLIC programme: Towards a staged e^+e^- linear collider exploring the terascale: CLIC conceptual design report, 2012.
- [11] T. Behnke et al. The International Linear Collider Technical Design Report - Volume 1: Executive Summary, 2013.
- [12] M. Benedikt et al. Future Circular Collider - European Strategy Update Documents. Technical Report CERN-ACC-2019-0007, CERN, Geneva, 2019.
- [13] M. Benedikt et al. Future Circular Collider - European Strategy Update Documents. Technical Report CERN-ACC-2019-0005, CERN, Geneva, 2019.

- [14] M. Benedikt et al. Future Circular Collider - European Strategy Update Documents. Technical Report CERN-ACC-2019-0003, CERN, Geneva, 2019.
- [15] M. Gallinaro. Top quark physics: A tool for discoveries. *Journal of Physics: Conference Series*, 447:012012, 2013.
- [16] D. Castelvecchi. Next-generation LHC: CERN lays out plans for €21-billion supercollider. *Nature*, 2019. Accessed: 2021-06-02.
- [17] L. Bottura. Taming the superconductors of tomorrow. *CERN Cour.*, 60:34–38. 5 p, 2020.
- [18] H. Toshiyasu et al. Advances in X-band TW Accelerator Structures Operating in the 100 MV/m Regime. In *1st International Particle Accelerator Conference*, 2010.
- [19] J. M. Dawson. Nonlinear Electron Oscillations in a Cold Plasma. *Phys. Rev.*, 113:383–387, 1959.
- [20] F. F. Chen. *Introduction to Plasma Physics*. Springer-Verlag US, 1974.
- [21] I. Blumenfeld et al. Energy doubling of 42 GeV electrons in a metre-scale plasma wakefield accelerator. *Nature*, 445:741–744, 2007.
- [22] T. Tajima and J. M. Dawson. Laser Electron Accelerator. *Phys. Rev. Lett.*, 43:267–270, 1979.
- [23] P. Chen, J. M. Dawson, R. W. Huff, and T. Katsouleas. Acceleration of Electrons by the Interaction of a Bunched Electron Beam with a Plasma. *Phys. Rev. Lett.*, 54:693–696, 1985.
- [24] N. Kumar, A. Pukhov, and K. Lotov. Self-Modulation Instability of a Long Proton Bunch in Plasmas. *Phys. Rev. Lett.*, 104:255003, 2010.
- [25] J. J. Su, T. Katsouleas, J. M. Dawson, P. Chen, M. Jones, and R. Keinigs. Stability of the Driving Bunch in the Plasma Wakefield Accelerator. *IEEE Transactions on Plasma Science*, 15(2):192–198, 1987.
- [26] R. Assmann. A European Perspective on Plasma Acceleration, 2014. Accessed: 2021-08-16.
- [27] E. Kallos, T. Katsouleas, P. Muggli, I. Pavlishin, I. Pogorelsky, D. Stolyarov, V. Yakimenko, and W. D. Kimura. Plasma wakefield acceleration utilizing multiple electron bunches. In *2007 IEEE Particle Accelerator Conference (PAC)*, pages 3070–3072, 2007.

-
- [28] A. Caldwell and K. Lotov. Plasma Wakefield Acceleration with a Modulated Proton Bunch. *Phys. Plasmas*, 18(10):103101, 2011.
- [29] S. Lee, T. Katsouleas, R. G. Hemker, E. S. Dodd, and W. B. Mori. Plasma-wakefield acceleration of a positron beam. *Phys. Rev. E*, 64:045501, 2001.
- [30] P. Muggli. Beam Driven Systems , 2014. Lecture at the CERN Accelerator School on Plasma Wake Acceleration.
- [31] E. Esarey, C. B. Schroeder, and W. P. Leemans. Physics of laser-driven plasma-based electron accelerators. *Rev. Mod. Phys.*, 81:1229–1285, 2009.
- [32] D. Strickland and G. Mourou. Compression of amplified chirped optical pulses. *Optics Communications*, 55(6):447 – 449, 1985.
- [33] C. Danson et al. Petawatt and exawatt class lasers worldwide. *High Power Laser Science and Engineering*, 7, 2019.
- [34] Proceedings of the 4th European Advanced Accelerator Concepts Workshop 15-20 September 2019, Isola d’Elba, Italy, 2020. Journal of Physics: Conference Series.
- [35] A. Modena et al. Electron acceleration from the breaking of relativistic plasma waves. *Nature*, 377(6550):606, 1995.
- [36] A. Gonsalves et al. Petawatt laser guiding and electron beam acceleration to 8 GeV in a laser-heated capillary discharge waveguide. *Phys. Rev. Lett.*, 122(8):084801, 2019.
- [37] S. Mangles et al. Monoenergetic beams of relativistic electrons from intense laser-plasma interactions. *Nature*, 431(7008):535, 2004.
- [38] J. Faure et al. A laser-plasma accelerator producing monoenergetic electron beams. *Nature*, 431(7008):541, 2004.
- [39] C. Geddes et al. High-quality electron beams from a laser wakefield accelerator using plasma-channel guiding. *Nature*, 431(7008):538, 2004.
- [40] R. Weingartner et al. Ultralow emittance electron beams from a laser-wakefield accelerator. *Phys. Rev. ST Accel. Beams*, 15(11):111302, 2012.
- [41] W. P. Leemans et al. Multi-GeV Electron Beams from Capillary-Discharge-Guided Subpetawatt Laser Pulses in the Self-Trapping Regime. *Phys. Rev. Lett.*, 113:245002, 2014.

- [42] P. L. Poole et al. Laser-driven ion acceleration via target normal sheath acceleration in the relativistic transparency regime. *New Journal of Physics*, 20(1):013019, 2018.
- [43] J. B. Rosenzweig et al. Experimental Observation of Plasma Wake-Field Acceleration. *Phys. Rev. Lett.*, 61:98–101, 1988.
- [44] M. Litos et al. 9 GeV Energy Gain in a Beam-Driven Plasma Wakefield Accelerator. *Plasma Physics and Controlled Fusion*, 58, 2015.
- [45] M. Litos et al. High-efficiency acceleration of an electron beam in a plasma wakefield accelerator. *Nature*, 515:92–5, 2014.
- [46] A. Doche, C. Beekman, Sébastien Corde, S. Corde, et al. Acceleration of a trailing positron bunch in a plasma wakefield accelerator. *Nature Sci. Rep.*, 7:14180, 2017.
- [47] S. Corde et al. Multi-gigaelectronvolt acceleration of positrons in a self-loaded plasma wakefield. *Nature*, 524:442–5, 2015.
- [48] N. Doble, L. Gatignon, K. Hübner, and Ed. Wilson. The Super Proton Synchrotron (SPS): A Tale of Two Lives. *Adv. Ser. Direct. High Energy Phys.*, 27:135–177. 43 p, 2017.
- [49] E. Gschwendtner et al. (AWAKE Collaboration). AWAKE, The Advanced Proton Driven Plasma Wakefield Acceleration Experiment at CERN. *Nucl. Instr. and Meth. in Phys. Res. A: Accelerators, Spectrometers, Detectors and Associated Equipment*, 829:76 – 82, 2016. 2nd European Advanced Accelerator Concepts Workshop - EAAC 2015.
- [50] P. Muggli et al. (AWAKE Collaboration). AWAKE readiness for the study of the seeded self-modulation of a 400 GeV proton bunch. *Plasma Physics and Controlled Fusion*, 60(1):014046, 2017.
- [51] AWAKE Collaboration. Experimental Observation of Proton Bunch Modulation in a Plasma at Varying Plasma Densities. *Phys. Rev. Lett.*, 122:054802, 2019.
- [52] AWAKE Collaboration. Acceleration of electrons in the plasma wakefield of a proton bunch. *Nature*, 571:363–367, 2018.
- [53] M. Wing. Particle physics experiments based on the AWAKE acceleration scheme. *Phil. Trans. R. Soc. A.*, 61, 2019.
- [54] M. Hüther. Direct Observation of the Hosing Instability of a Long, Relativistic Proton Bunch in the AWAKE Experiment, Doctoral Thesis, Technical University Munich, 2020.

-
- [55] K. V. Lotov et al. Natural noise and external wakefield seeding in a proton-driven plasma accelerator. *Phys. Rev. ST Accel. Beams*, 16:041301, 2013.
- [56] A.-M. Bachmann. Self-Modulation Development of a Proton Bunch in Plasma, Doctoral Thesis, Technical University Munich, 2021.
- [57] K. V. Lotov. Controlled self-modulation of high energy beams in a plasma. *Physics of Plasmas*, 18(2):024501, 2011.
- [58] P. I. Morales Guzmán, P. Muggli et al. (AWAKE Collaboration). Simulation and experimental study of proton bunch self-modulation in plasma with linear density gradients. *Phys. Rev. Accel. Beams*, 24:101301, 2021.
- [59] F. Batsch. Interferometry-based white light measurement of neutral rubidium density and gradient for the AWAKE experiment at CERN", Master's Thesis, Technical University Munich, 2016.
- [60] F. Braunmüller, T. Nechaeva et al. (AWAKE Collaboration). Proton Bunch Self-Modulation in Plasma with Density Gradient. *Phys. Rev. Lett.*, 125:264801, 2020.
- [61] U. Stroth. *Plasmaphysik*. Vieweg+Teubner, 2011.
- [62] M. Turner. First Observation of the Seeded Proton Bunch Self-Modulation in Plasma, Doctoral Thesis, Technical University of Graz, 2017.
- [63] AWAKE Publication Committee. List of AWAKE Publications , 2021.
- [64] R. Keinigs and M. E. Jones. Two-dimensional dynamics of the plasma wakefields accelerators. *IEEE Transactions on Plasma Science*, 30(252), 1987.
- [65] C. B. Schroeder, C. Benedetti, E. Esarey, F. J. Grüner, and W. P. Leemans. Growth and Phase Velocity of Self-Modulated Beam-Driven Plasma Waves. *Phys. Rev. Lett.*, 107:145002, 2011.
- [66] A. Pukhov et al. Phase Velocity and Particle Injection in a Self-Modulated Proton-Driven Plasma Wakefield Accelerator. *Phys. Rev. Lett.*, 107:145003, 2011.
- [67] M. Turner et al. (AWAKE Collaboration). Experimental study of wakefields driven by a self-modulating proton bunch in plasma. *Phys. Rev. Accel. Beams*, 23:081302, 2020.
- [68] A. Caldwell, E. Gschwendtner, K. Lotov, P. Muggli, and M. Wing. AWAKE Design Report: A Proton-Driven Plasma Wakefield Acceleration Experiment

- at CERN. Technical Report CERN-SPSC-2013-013. SPSC-TDR-003, CERN, 2013.
- [69] E. Mobs. The CERN accelerator complex - August 2018. Complexe des accélérateurs du CERN - Août 2018, 2018. OPEN-PHO-ACCEL-2018-005. General Photo.
- [70] M. Turner et al. (AWAKE Collaboration). Experimental Observation of Plasma Wakefield Growth Driven by the Seeded Self-Modulation of a Proton Bunch. *Phys. Rev. Lett.*, 122:054801, 2019.
- [71] ISO View of the AWAKE Area. Accessed: 2020-08-17.
- [72] A. Caldwell, E. Gschwendtner, K. Lotov, P.c Muggli, and M. Wing. AWAKE Status Report. Technical Report CERN-SPSC-2014-026, SPSC-SR-143, CERN, Geneva, 2014.
- [73] H. Bartosik et al. SPS Operation and Future Proton Sharing scenarios for the SHiP experiment at the BDF facility. Technical Report CERN-ACC-NOTE-2018-0082, CERN, Geneva, 2018.
- [74] G. Arduini et al. The SPS beam parameters, the operational cycle, and proton sharing with the SHiP facility. Technical Report CERN-SHiP-NOTE-2015-004, CERN, Geneva, 2015.
- [75] S. Burger and E. Bravin. A new Control System for the CERN TV Beams Observation. Technical Report CERN-AB-Note-2008-041-BI, CERN, Geneva, 2008.
- [76] P. Forck, P. Kowina, and D. Liakin. Beam position monitors, 2009.
- [77] AWAKE Collaboration. AWAKE Status Report. Technical Report CERN-SPSC-2017-039. SPSC-SR-222, CERN, Geneva, 2017.
- [78] C. Bracco et al. Beam studies and experimental facility for the AWAKE experiment at CERN. *Nucl. Instr. and Meth. in Phys. Res. A: Accelerators, Spectrometers, Detectors and Associated Equipment*, 740:48 – 53, 2014. Proceedings of the first European Advanced Accelerator Concepts Workshop 2013.
- [79] V. Fedosseev et al. Integration of a Terawatt Laser at the CERN SPS Beam for the AWAKE Experiment on Proton-Driven Plasma Wake Acceleration. In *Proc. of International Particle Accelerator Conference (IPAC'16), Busan, Korea*, pages 2592–2595. JACoW, 2016.

-
- [80] A. Caldwell, E. Gschwendtner, K. Lotov, P. Muggli, and M. Wing. AWAKE Status Report. Technical Report CERN-SPSC-2015-032. SPSC-SR-169, CERN, Geneva, 2015.
- [81] J. T. Moody. AWAKE Laser. Technical Report AWK-TO-ES-0001, CERN, 2016.
- [82] A. Caldwell and (for the AWAKE Collaboration). AWAKE Status Report. Technical Report CERN-SPSC-2016-033. SPSC-SR-194, CERN, Geneva, 2016.
- [83] J. T. Moody. Private communication.
- [84] V. Fedosseev et al. Generation and Delivery of an Ultraviolet Laser Beam for the RF-Photoinjector of the Awake Electron Beam. In *Proc. 10th International Particle Accelerator Conference (IPAC'19), Melbourne, Australia, 19-24 May 2019*, pages 3709–3712. JACoW Publishing, 2019.
- [85] C. Barnes et al. Improvements for the third generation Plasma Wakefield experiment E-164 at SLAC. In *Proceedings of the 2003 Particle Accelerator Conference*, volume 3, pages 1530 – 1532 vol.3, 2003.
- [86] G. Plyushchev, R. Kersevan, A. Petrenko, and P. Muggli. A rubidium vapor source for a plasma source for AWAKE. *Journal of Physics D: Applied Physics*, 51(2):025203, 2017.
- [87] E. Öz and P. Muggli. A novel Rb vapor plasma source for plasma wakefield accelerators. *Nucl. Instrum. Meth. A*, 740:197–202, 2014.
- [88] F. Batsch, F. Braummüller, et al. Overview, Control & Status of AWAKE Plasma cell, 2018. internal presentation.
- [89] A.-M. Bachmann, M. Martyanov, J. Moody, A. Pukhov, and P. Muggli. Schlieren Imaging for the Determination of the Radius of an Excited Rubidium Column. *Nucl. Instrum. Meth. A*, 2017.
- [90] C. B. Alcock, V. P. Itkin, and M. K. Horrigan. Vapour Pressure Equations for the Metallic Elements: 298–2500K. *Canadian Metallurgical Quarterly*, 23(3):309–313, 1984.
- [91] F. Batsch. *AWAKE Wiki: Instructions on the use of the Rb vapor source*. Accessible only within CERN.
- [92] K. Rieger, A. Caldwell, O. Reimann, R. Tarkeshian, and P. Muggli. GHz modulation detection using a streak camera: Suitability of streak cameras in the AWAKE experiment. *Review of Scientific Instruments*, 88(2):025110, 2017.

- [93] Hamamatsu Photonics. Guide to Streak Cameras, 2008.
- [94] B. Gitter. Optical Transition Radiation. Technical Report CAA-TECH-NOTE-internal-#24, UCLA, Center For Advanced Accelerators, 1992.
- [95] J. D. Jackson. *Klassische Elektrodynamik*. Berlin New York: de Gruyter, 3rd edition, 2002.
- [96] CERN and Matterport. Interactive panorama of AWAKE by 360YourHouse, 2019.
- [97] S. Gessner et al. (AWAKE Collaboration). Evolution of a plasma column measured through modulation of a high-energy proton beam, 2020.
- [98] A.-M. Bachmann and P. Muggli. Determination of the Charge per Micro-Bunch of a Self-Modulated Proton Bunch using a Streak Camera. *Journal of Physics: Conference Series*, 1596:012005, 2020.
- [99] A.-M. Bachmann. Private communication.
- [100] F. Braunmüller, M. Martyanov, S. Alberti, and P. Muggli. Novel diagnostic for precise measurement of the modulation frequency of Seeded Self-Modulation via Coherent Transition Radiation in AWAKE. *Nucl. Instr. and Meth. in Phys. Res. A: Accelerators, Spectrometers, Detectors and Associated Equipment*, 909:76 – 79, 2018. 3rd European Advanced Accelerator Concepts workshop (EAAC2017).
- [101] R. J. Bauer, M. Cohn, J. M. Cotton, and R. F. Packard. Millimeter wave semiconductor diode detectors, mixers, and frequency multipliers. *Proceedings of the IEEE*, 54(4):595–605, 1966.
- [102] E. Bründermann, H.-W. Hübers, and M. F. Kimmitt. *Terahertz Techniques*, volume 151. Springer-Verlag Berlin Heidelberg, 2012.
- [103] K. Pepitone et al. The electron accelerator for the AWAKE experiment at CERN. *Nucl. Instr. and Meth. in Phys. Res. A: Accelerators, Spectrometers, Detectors and Associated Equipment*, 829:73 – 75, 2016. 2nd European Advanced Accelerator Concepts Workshop - EAAC 2015.
- [104] S.-Y. Kim et al. Commissioning of the electron injector for the AWAKE experiment. *Nucl. Instr. and Meth. in Phys. Res. A: Accelerators, Spectrometers, Detectors and Associated Equipment*, 953:163194, 2020.
- [105] A. Petrenko, C. Bracco, E. Gschwendtner, K. Lotov, and P. Muggli. Electron Injection Studies for the AWAKE Experiment at CERN. In *5th International Particle Accelerator Conference*, page TUPME078, 2014.

-
- [106] M. Turner et al. External Electron Injection for the AWAKE Experiment. In *18th Advanced Accelerator Concepts Workshop*, 2018.
- [107] F. Keeble et al. The AWAKE Electron Spectrometer. In *9th International Particle Accelerator Conference*, 2018.
- [108] F. Keeble. Measurement of the electron energy distribution at AWAKE, Doctoral Thesis, University College London, 2019.
- [109] W. Sliwinski. Controls middleware - overview & architecture, 2015.
- [110] F. Braunmüller. Private communication.
- [111] S. Gessner. Private communication.
- [112] The AWAKE fixed display.
- [113] F. Batsch. *AWAKE Wiki: Instructions on the use of the Rb vapor density measurement*. Accessible only within CERN.
- [114] M. Martyanov. OTR signal delay at 450nm vs. 775nm caused by an optical dispersion of bulk elements, 2018. Internal presentation.
- [115] F. Batsch. *AWAKE Wiki: Instructions on the use of the LRS*. Accessible only within CERN.
- [116] AWAKE Collaboration. AWAKE Status Report. Technical Report CERN-SPSC-2020-024. SPSC-SR-279, CERN, Geneva, 2020.
- [117] P. Muggli, A. Caldwell, E. Gschwendtner, . Lotov, and M. Wing. Physics Plan for AWAKE Run 2a. Technical Report CERN-SPSC-2020-020. SPSC-SR-275, CERN, Geneva, 2020.
- [118] P. Muggli and the AWAKE Collaboration. Physics to plan AWAKE Run 2. *Journal of Physics: Conference Series*, 1596:012008, 2020.
- [119] AWAKE Collaboration. AWAKE Status Report. Technical Report CERN-SPSC-2019-037. SPSC-SR-258, CERN, Geneva, 2019.
- [120] B. Buttenschön, N. Fahrenkamp, and O. Grulke. A high power, high density helicon discharge for the plasma wakefield accelerator experiment AWAKE. *Plasma Physics and Controlled Fusion*, 60(7):075005, 2018.
- [121] P. W. Draper, M. M. Taylor, and Allan A. A glossary of CCD terminology, 2011. Accessed: 2021-01-12.

- [122] F. Braunmüller, P. Muggli, et al. Overview, Control & Status of AWAKE Plasma cell, 2017.
- [123] M. Moreira, J. Vieira, and P. Muggli. Influence of proton bunch parameters on a proton-driven plasma wakefield acceleration experiment. *Phys. Rev. Accel. Beams*, 22(3):031301, 2019.
- [124] G. Zevi Della Porta. AWAKE Wiki on UV Timing, 2021. Accessed: 2021-07-27.
- [125] R. Fonseca et al. OSIRIS: A Three-Dimensional, Fully Relativistic Particle in Cell Code for Modeling Plasma Based Accelerators. In *Computational Science — ICCS 2002*, pages 342–351, 2002.